UC San Diego
UC San Diego Electronic Theses and Dissertations

Title
Studies of Nitrogen and Organic Carbon Cycling in the Eastern Pacific Ocean Using Natural Abundance Isotopes

Permalink
https://escholarship.org/uc/item/8zv5z8jf

Author
White, Margot Elizabeth

Publication Date
2021

Peer reviewed|Thesis/dissertation

eScholarship.org Powered by the California Digital Library
University of California

UNIVERSITY OF CALIFORNIA SAN DIEGO

Studies of Nitrogen and Organic Carbon Cycling in the Eastern Pacific Ocean Using Natural Abundance Isotopes

A dissertation submitted in partial satisfaction of the requirements for the degree
Doctor of Philosophy

in

Oceanography

by

Margot Elizabeth White

Committee in charge:

Professor Lihini Aluwihare, Chair
Professor Andreas Andersson
Professor Katherine Barbeau
Professor Christopher Charles
Professor Mark Thiemens

2021

Copyright

Margot Elizabeth White, 2021

All rights reserved.

The dissertation of Margot Elizabeth White is approved, and it is acceptable in quality and form for publication on microfilm and electronically.

University of California San Diego

2021

DEDICATION

To my mother, who was my first and most important teacher.

And to my father, who taught me to love the ocean.

TABLE OF CONTENTS

LIST OF ABBREVIATIONS

BDON	bioavailable dissolved organic nitrogen
CalCOFI	California Cooperative Oceanic Fisheries Investigations
CCE	California Current Ecosystem
CCS	California Current System
CDOM	colored/chromophoric dissolved organic matter
Chl	Chlorophyll *a*
CTD	Conductivity Temperature Depth sensor
DIC	dissolved inorganic carbon
DOC	dissolved organic carbon
DON	dissolved organic nitrogen
DOP	dissolved organic phosphorus
DOS	dissolved organic sulfur
ENSO	El Niño Southern Oscillation
ETNP	eastern tropical North Pacific
ETSP	eastern tropical South Pacific
FDOM	fluorescent dissolved organic matter
NPP	net primary production
ODZ	oxygen deficient zone
OM	organic matter
ONI	Oceanic Niño Index
PDO	Pacific Decadal Oscillation
PNM	primary nitrite maximum

POC	particulate organic carbon
POM	particulate organic matter
PON	particulate organic nitrogen
RPO	ramped pyrolysis/oxidation
SBB	Santa Barbara Basin
SCM	secondary chlorophyll maximum
SNM	secondary nitrite maximum
SPE	solid phase extracted
TDN	total dissolved nitrogen
TOC	total organic carbon

LIST OF FIGURES

LIST OF TABLES

ACKNOWLEDGEMENTS

I have so many people to thank not only for making this dissertation work possible, but for making it a source of tremendous joy and growth over the past several years. First and foremost, I would like to thank my advisor, Professor Lihini Aluwihare, who has always been an example of the best of what a scientist can be. Thank you also to my wonderful committee members, Professors Andreas Andersson, Katherine Barbeau, Christopher Charles, and Mark Thiemens. I also want to express my thanks to all of my undergraduate research mentors, particularly Professor Sarah Boyer at Macalester College and Professor Sarah Cohen at San Francisco State University, for helping to set me on this path.

I would like to express my gratitude to my many collaborators throughout this process. To Scott Wankel and the Wankel lab at WHOI-- thank you for welcoming me in summer 2016 and for working afterward to ensure that all my nitrate isotope measurements were complete and accurate. Thank you to Patrick Rafter for providing additional nitrate isotope data and for many useful discussions over the years and to Matt Mazloff for providing modeling data and physical oceanography advice. Thank you also to Shonna Dovel for collecting our nitrate isotope samples on CalCOFI cruises and to Bruce Deck for analyzing many POM and PPL DOM samples over the years. A big thank you as well to the captains and crews of the *R/V Oceanus* and to Mike Beman and the Beman lab at UC Merced for including us on two cruises to the ETNP region, as well as for allowing me my own CTD casts, a rare privilege. Many thanks to the captain and crew of the *R/V Western Flyer* and to Ken Smith of MBARI for bringing a CTD out to Station M just for me. I am so grateful for the staff and scientists at NOSAMS, particularly Mary Lardie Gaylord, Al Gagnon, and Mark Kurz for making the analyses in Chapter 5 possible. I am also very grateful to have had the opportunity to work with Steve Beaupre and Ann McNichol, who taught me how to think about and understand radiocarbon measurements.

Thank you as well to all members of the Aluwihare lab. It has been wonderful to work in such a supportive and collaborative environment. Particular thanks are due to Neal Arakawa and Brandon Stephens, who taught me the ways of the lab when I first joined. And, of course, to Irina Koester and Sara Rivera, with whom I was lucky enough to share almost all of my time in the lab. I also would like to thank Tran Nguyen and Ravleen Khalsa-Basra, who spent many hours helping me prepare samples of various types. In addition, I want to acknowledge the members of the Barbeau lab for always being there to provide trace metal advice and sympathy. And to the many others that I have failed, in the service of brevity, to mention here but who helped me in ways both great and small, my deepest thanks. To all my friends at SIO—I am going to miss you very much! I want to specifically acknowledge our MCG cohort and Team CTD.

Finally, I want to thank my family including my sister Nicole and my brother Alec, as well my parents, all of whom have been endlessly supportive. And last but never least, many thanks to my husband, Yury, who has been by my side no matter the challenge, and who is always enthusiastic, sometimes a bit too enthusiastic, about helping me code in Python.

Chapter 2 has been recently submitted as “Stable isotopes of nitrate reveal effects of ENSO on nitrogen cycling in the surface waters of the southern California Current” to *Limnology and Oceanography*. Margot White, Patrick Rafter, Brandon Stephens, Matthew Mazloff, Scott Wankel, and Lihini Aluwihare. The dissertation author was the primary investigator and author of this paper.

Chapter 3, in full, is a reprint of the material as it appears in “Recent Increases in Water Column Denitrification in the Seasonally Suboxic Bottom Waters of the Santa Barbara Basin” published in Geophysical Research Letters, 2019. Margot White, Patrick Rafter, Brandon Stephens, Scott Wankel, and Lihini Aluwihare. The dissertation author was the primary investigator and author of this paper.

Chapter 4 is currently being formulated into a manuscript that will be submitted for publication. “Organic matter composition across oxygen gradients in the eastern tropical North Pacific Ocean.” Margot White, Irina Koester, Tran Nguyen, Alexandra Phillips, Alex Sessions, Michael Beman, and Lihini Aluwihare. The dissertation author was the primary investigator and author of this study.

Chapter 5, is currently being formulated into a manuscript that will soon be submitted for publication. “It’s about time: a new perspective on dissolved organic radiocarbon”. Margot White, Tran Nguyen, Irina Koester, Mary C. Lardie Gaylord, J. Michael Beman, Kenneth Smith, Ann McNichol, Steven Beaupré, and Lihini Aluwihare. The dissertation author was the primary investigator and author of this paper.

VITA

EDUCATION

2014	B.A. in Chemistry and Biology, Macalester College, St. Paul, MN
2021	Ph.D. in Oceanography, Scripps Institution of Oceanography, UC San Diego

PUBLICATIONS

White, Margot E., Patrick A. Rafter, Brandon M. Stephens, Matthew R. Mazloff, Scott D. Wankel, and Lihini I. Aluwihare. 2021. "Stable isotopes of nitrate reveal effects of ENSO on nitrogen cycling in the surface waters of the California Current System." Submitted to *Limnology and Oceanography.*

White, Margot E., Patrick A. Rafter, Brandon M. Stephens, Scott D. Wankel, and Lihini I. Aluwihare. 2019. "Recent Increases in Water Column Denitrification in the Seasonally Suboxic Bottom Waters of the Santa Barbara Basin." *Geophysical Research Letters* 46 (12): 6786–95. https://doi.org/10.1029/2019GL082075.

FIELDS OF STUDY

Major Field: Oceanography

Studies in Isotope Biogeochemistry

Professor Lihini I. Aluwihare

ABSTRACT OF THE DISSERTATION

Studies of Nitrogen and Organic Carbon Cycling in the Eastern Pacific Ocean Using Natural Abundance Isotopes

by

Margot Elizabeth White

Doctor of Philosophy in Oceanography

University of California San Diego, 2021

Professor Lihini Aluwihare, Chair

This thesis uses a variety of natural abundance isotope measurements to expand our understanding of nitrogen and organic carbon cycling within the ocean. Chapters 2 & 3 use stable isotopes of nitrate to investigate recent trends in nitrogen cycling in the southern California Current System (sCCS). In Chapter 2 we show that surface ocean warming during the 2015-2016 El Niño event led to reduced nitrate supply and increased reliance on recycled nitrate produced via euphotic zone nitrification. We also identified spatial and temporal variability in euphotic zone nitrate utilization associated with iron limitation of phytoplankton. Chapter 3 uses a time series of stable isotopes of nitrate along with other physical and chemical measurements to examine recent biogeochemical changes in a partially isolated marine basin off the coast of California, whose bottom waters become deoxygenated between annual flushing events. Our data confirm an unprecedented increase in water column denitrification in basin bottom waters in recent years that was likely caused by a long-term trend of decreasing oxygen concentrations outside the basin. Chapter 4 uses a variety of chemical and isotopic measurements to characterize organic matter across oxygen gradients in the eastern tropical North Pacific (ETNP). This work describes unique organic matter dynamics along the oxycline and shows that optical properties of dissolved organic matter effectively identify locations where intense oxic remineralization takes place, whereas most other bulk measurements of organic matter do not provide insight into unique processes within these environments. We also document the impact of a passing hurricane on water column properties. Chapter 5 uses thermal oxidation in conjunction with a chemical processing method to show that the current paradigm of marine DOC cycling needs revision. Our results show that even the most ^{14}C-depleted DOC fraction exhibits a vertical ^{14}C gradient, suggesting the addition and removal of DOC from this reservoir on shorter timescales than current models predict. We propose a new hypothesis for marine DOC cycling that would revise the water column lifetime of marine DOC to only 2,300 years, approximately doubling the estimated flux of carbon through the deep ocean.

Chapter 1: Introduction

Natural abundance isotopes

The measurement of natural abundance isotopes has broad applicability across the earth sciences. In this thesis, isotopic measurements are applied across a variety of marine environments to address outstanding questions about nitrogen and organic carbon cycling in the eastern North Pacific Ocean. In the case of stable isotopes (e.g., $^{15}N/^{14}N$) in open ocean systems, insights are primarily provided by isotopic fractionation, whereby different physical and biological processes preferentially use either the heavy or light isotope, thus leaving behind a fingerprint of past influences on a sample or reservoir. Furthermore, measurement of multiple concurrent isotopes in the same sample or compound can help to deconvolute the impacts of different processes (e.g. Casciotti 2016). This dissertation makes use of nitrogen and oxygen isotope measurements of dissolved nitrate to examine the physical and biological controls on nitrogen cycling in the southern California Current System (sCCS).

In addition to stable isotopes, we can measure the presence of naturally occurring radioactive isotopes in a sample. Measurements of radiocarbon, for example, allow us to estimate the residence time of carbon within a particular reservoir, while also providing insight into the exchange of carbon between different reservoirs. Radiocarbon has proven to be an extremely useful tool for studying organic carbon cycling in the ocean (McNichol and Aluwihare 2007), and becomes even more powerful when paired with other chemical methods designed to uncover the distribution of radiocarbon signatures present within a sample. This dissertation uses a novel approach that combines ^{14}C measurements with a thermal oxidation method to examine the cycling of long-lived organic matter in the ocean.

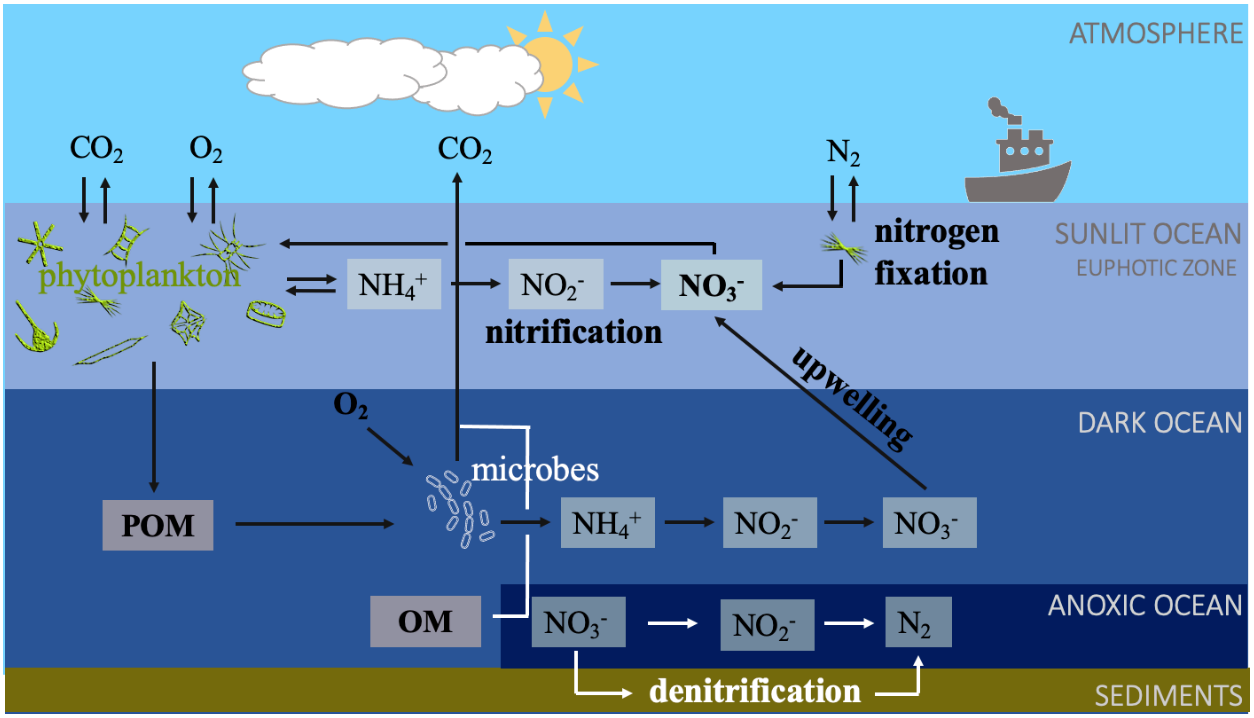

Figure 1.1 Nitrogen cycling in the southern California Current System. Nitrate is supplied to the euphotic zone via upwelling or recycling of organic nitrogen. Denitrification (the removal of fixed nitrogen) occurs mostly in anoxic sediments of borderland basins but can also occur in the low oxygen water column.

The marine nitrogen cycle

The first two chapters of this dissertation are focused on the marine nitrogen cycle and use stable isotopes of dissolved inorganic nitrogen species to study nitrogen cycling in the eastern Pacific Ocean. In much of the world's oceans, nitrogen is the most important nutrient limiting phytoplankton primary production, and thus constraining nitrogen sources and cycling is of particular interest (Moore et al. 2013). The vast majority of nitrogen in the atmosphere and in seawater is in the form of molecular nitrogen (N_2), and not biologically available to most organisms (Zehr and Ward 2002). The most common biologically available form of N in the ocean is nitrate (NO_3^-), which is proximally derived from the oxidation of ammonium and nitrite by archaea and bacteria. However, the main source of bioavailable N to the ocean is microbially mediated nitrogen fixation, which converts molecular nitrogen to ammonium. The input through nitrogen fixation is balanced by removal of nitrate in low oxygen environments via microbial denitrification and anammox (Figure 1.1). The eastern north Pacific Ocean hosts environments where nitrate is permanently removed from the ocean via denitrification (the conversion of nitrate through several intermediates including nitrite and nitrous oxide, to nitrogen gas). In the sCCS, nitrate removal takes place primarily in sediments of the borderland basins, though the possibility for water column denitrification and anaerobic ammonia oxidation exists in the Santa Barbara Basin (Sigman et al. 2003; Goericke et al. 2015). CCS nitrate concentrations, particularly upwelling concentrations, are also influenced by water column nitrate removal in the eastern tropical North Pacific (ETNP) because these two regions (the CCS and ETNP) are linked through the poleward travelling California Undercurrent (Castro et al. 2001; Bograd et al. 2015). These processes are of interest beyond their importance in the nitrogen budget due to their potential to produce N_2O, a powerful greenhouse gas (Babbin et al. 2015).

Nitrogen is supplied to phytoplankton in the surface ocean largely via the upwelling of nitrate from below the euphotic zone (Figure 1.1), and carbon export out of the euphotic zone is linked to this externally supplied or “new” nitrate (Dugdale and Goering 1967). The vertically transported nitrate has been produced from the regeneration of organic matter to ammonium and subsequent oxidation via nitrification. Both ammonium production and nitrification does occur in the surface ocean, but the importance of nitrification in sunlit waters is still in question (Wankel et al. 2007; Stephens et al. 2019; Laperriere et al. 2020). Overall, it is well established that nitrate availability and flux is an important control on primary productivity and carbon sequestration in marine environments. Factors controlling the inventory of nitrate, and therefore the nitrate supply to the euphotic zone, are particularly important in eastern boundary current systems such as the

California Current, where high productivity is supported by upwelled nutrients (Chan et al. 2008). The California Cooperative Oceanic Fisheries Investigation (CalCOFI) survey was established in the late 1940s to examine natural population fluctuations in commercially important planktivorous fish populations (McClatchie 2014). The spatial extent of the survey and the measurements made on its quarterly cruises have evolved over the decades, but since the early 1980s a core group of physical, chemical, and biological measurements have been maintained and provides a rich timeseries of the climatology and biogeochemistry of the region (www.calcofi.org). Both Chapters 2 & 3 make extensive use of the CalCOFI timeseries to place nitrate isotope measurements into a larger context.

Organic matter cycling in the ocean

Organic carbon is mostly produced in the surface ocean via photosynthesis and is transferred through the food web as particulate or dissolved organic matter. Organic matter, often after being processed through the food web, can be exported out of the euphotic as sinking organic matter and this is referred to as the biological carbon pump (Falkowski et al. 1998). However, both dissolved organic matter and suspended organic matter can be transported by subduction and lateral advection to be used at sites remote from where the organic matter was produced. These pathways constitute additional mechanisms of organic carbon export and have been shown to be important in the CCS (Stukel et al. 2017; Stephens et al. 2018).

Although much of the annually produced organic matter is respired over relatively short timescales, marine dissolved organic matter (DOM) has been shown to accumulate on a variety of timescales and $\Delta^{14}C$ measurements suggest that much of the 630±30 Pg dissolved organic carbon (DOC) reservoir in the ocean accumulates on timescales >5000 years (Williams and

Druffel 1987). This apparent long lifetime of organic carbon sourced from primary production in the surface ocean is an enigma in the marine carbon cycle. The average age of the marine DOC reservoir indicates that it should be well-mixed over several cycles of overturning circulation at a constant concentration. Building from this assumption and extending it to incorporate the additional assumption that the well-mixed (i.e., background) component has a fixed "age" of ~6000 years in the ocean, has led to a two-component mass and isotope mixing model. This model states that any variability in the $\Delta^{14}C$ of DOC can be explained by mixing the 'old' background component with different amounts of recently produced DOC. This model adequately recreates the well documented vertical decrease in the $\Delta^{14}C$ signature of marine DOC in the ocean (Beaupré et al. 2020) and fraction and compound-specific measurements in DOC do support the contribution of DOC from photosynthesis and the prevalence of aged DOC throughout the ocean (McNichol and Aluwihare 2007; Follett et al. 2014; Zigah et al. 2017; Broek et al. 2017). However, a key requirement of the two-component model, the background pool of ^{14}C-depleted DOC with a vertically uniform concentration and $\Delta^{14}C$ signature, has not been satisfied.

Linking the carbon and nitrogen cycles

Nitrate is linked to both carbon fixation in the surface ocean and subsequent carbon export into the deep ocean as discussed above. However, the loss of nitrate is also linked to carbon because denitrification is a heterotrophic process. Furthermore, in order for denitrification to take place, oxygen must be completely consumed, a process that is also mediated by the availability of organic matter. In certain areas of the subsurface ocean, highly productive overlying waters result in high rates of remineralization at depth which conspire with slow ventilation to deplete oxygen concentrations to nanomolar levels (Wyrtki 1962). These areas are known as anoxic marine zones, or AMZs. Mounting evidence suggests that the AMZs of the eastern Pacific Ocean will expand under future ocean warming, thus their role in nitrogen removal and the role of organic matter in modulating this removal in AMZs is of particular interest (Stramma et al. 2008; Oschlies et al. 2018). Organic matter processing in anoxic sediments has been the subject of much research, but the cycling of organic matter in the low oxygen water column is not as well-studied. Some studies have shown that organic matter flux is less attenuated within AMZs, but potentially subject to more intense remineralization in the upper oxycline (Keil et al., 2016, Pavia et al 2019). The potential expansion of AMZs highlights the importance of constraining the controls on and extent to which *aerobic* respiration is occurring near the boundaries (above and below) of the AMZ as this may further deplete oxygen concentrations in these areas as well (Deutsch et al. 2011; Beman and Carolan 2013). Furthermore, AMZ specific processes such as sulfurization reactions that can make organic matter more resistant to remineralization have been shown to occur in the ETNP AMZ (Raven et al. 2021) but their extent is still poorly understood.

Organization of dissertation

This dissertation focuses on the use of natural abundance isotopes to study nitrogen and organic carbon cycling in diverse marine environments. The first two chapters explore nitrogen cycling in the southern California Current System (sCCS) through the use of nitrogen and oxygen stable isotopes of nitrate. In **Chapter 2** we investigate sources and cycling of nitrate in the surface waters of the sCCS with a focus on the impact of the 2015-2016 El Niño on nitrogen sources for primary production. **Chapter 3** uses nitrate isotopes to constrain the extent and location of denitrification in the bottom waters of the seasonally suboxic Santa Barbara Basin over interannual and seasonal timescales. **Chapter 4** investigates the composition and cycling of organic matter in and around the eastern tropical North Pacific anoxic marine zone using isotopes in combination with other methods of characterization. **Chapter 5** moves away from stable isotopes and uses a thermal oxidation method to better constrain the distribution of radiocarbon signatures in marine dissolved organic carbon across depths. Together the chapters in this dissertation provide new information on the cycling of two of the elements most essential to life in the oceans - carbon and nitrogen.

References

Babbin, A. R., D. Bianchi, A. Jayakumar, and B. B. Ward. 2015. Rapid nitrous oxide cycling in the suboxic ocean. Science (80-.). **348**: 1127–1129. doi:10.1126/science.aaa8380

Beaupré, S. R., B. D. Walker, and E. R. M. Druffel. 2020. The two-component model coincidence: Evaluating the validity of marine dissolved organic radiocarbon as a stable-conservative tracer at Station M. Deep Sea Res. Part II Top. Stud. Oceanogr. 104737. doi:10.1016/j.dsr2.2020.104737

Beman, J. M., and M. T. Carolan. 2013. Deoxygenation alters bacterial diversity and community composition in the ocean's largest oxygen minimum zone. Nat. Commun. **4**: 1–11. doi:10.1038/ncomms3705

Bograd, S. J., M. P. Buil, E. Di Lorenzo, and others. 2015. Changes in source waters to the Southern California Bight. Deep. Res. Part II Top. Stud. Oceanogr. **112**: 42–52. doi:10.1016/j.dsr2.2014.04.009

Broek, T. A. B., B. D. Walker, T. P. Guilderson, and M. D. McCarthy. 2017. Coupled ultrafiltration and solid phase extraction approach for the targeted study of semi-labile high molecular weight and refractory low molecular weight dissolved organic matter. Mar. Chem. **194**: 146–157. doi:10.1016/J.MARCHEM.2017.06.007

Casciotti, K. L. 2016. Nitrogen and Oxygen Isotopic Studies of the Marine Nitrogen Cycle. Ann. Rev. Mar. Sci. **8**: 379–407. doi:10.1146/annurev-marine-010213-135052

Castro, C. G., F. P. Chavez, and C. A. Collins. 2001. Role of the California Undercurrent in the export of denitrified waters from the eastern tropical North Pacific. Global Biogeochem. Cycles **15**: 819–830. doi:10.1029/2000GB001324

Chan, F., J. A. Barth, J. Lubchenco, A. Kirincich, H. Weeks, W. T. Peterson, and B. A. Menge. 2008. Emergence of anoxia in the California current large marine ecosystem. Science **319**: 920. doi:10.1126/science.1149016

Deutsch, C., H. Brix, T. Ito, H. Frenzel, and L. A. Thompson. 2011. Climate-forced variability of ocean hypoxia. Science (80-.). **333**: 336–339. doi:10.1126/science.1202422

Dugdale, R. C., and J. J. Goering. 1967. UPTAKE OF NEW AND REGENERATED FORMS OF NITROGEN IN PRIMARY PRODUCTIVITY. Limnol. Oceanogr. **12**: 196–206. doi:10.4319/lo.1967.12.2.0196

Falkowski, P. G., R. T. Barber, and V. Smetacek. 1998. Biogeochemical controls and feedbacks on ocean primary production. Science (80-.). **281**: 200–206. doi:10.1126/science.281.5374.200

Follett, C. L., D. J. Repeta, D. H. Rothman, L. Xu, and C. Santinelli. 2014. Hidden cycle of dissolved organic carbon in the deep ocean. Proc. Natl. Acad. Sci. U. S. A. **111**: 16706–

16711. doi:10.1073/pnas.1407445111

Goericke, R., S. J. Bograd, and D. S. Grundle. 2015. Denitrification and flushing of the Santa Barbara Basin bottom waters. Deep. Res. Part II Top. Stud. Oceanogr. **112**: 53–60. doi:10.1016/j.dsr2.2014.07.012

Keil, R. G., J. A. Neibauer, C. Biladeau, K. van der Elst, and A. H. Devol. 2016. A multiproxy approach to understanding the “enhanced” flux of organic matter through the oxygen-deficient waters of the Arabian Sea. Biogeosciences **13**: 2077–2092.

Laperriere, S. M., M. Morando, D. G. Capone, T. Gunderson, J. M. Smith, and A. E. Santoro. 2020. Nitrification and nitrous oxide dynamics in the Southern California Bight. Limnol. Oceanogr. lno.11667. doi:10.1002/lno.11667

McClatchie, S. 2014. Regional fisheries oceanography of the california current system: The CalCOFI program, Springer Netherlands.

McNichol, A. P., and L. I. Aluwihare. 2007. The Power of Radiocarbon in Biogeochemical Studies of the Marine Carbon Cycle: Insights from Studies of Dissolved and Particulate Organic Carbon (DOC and POC). Chem. Rev. **107**: 443–466. doi:10.1021/cr050374g

Moore, C. M., M. M. Mills, K. R. Arrigo, and others. 2013. Processes and patterns of oceanic nutrient limitation. Nat. Geosci. **6**: 701–710. doi:10.1038/ngeo1765

Oschlies, A., P. Brandt, L. Stramma, and S. Schmidtko. 2018. Drivers and mechanisms of ocean deoxygenation. Nat. Geosci. **11**: 467–473. doi:10.1038/s41561-018-0152-2

Raven, M. R., R. G. Keil, and S. M. Webb. 2021. Microbial sulfate reduction and organic sulfur formation in sinking marine particles. Science (80-.). **371**: 178–181. doi:10.1126/science.abc6035

Sigman, D. M., R. Robinson, A. N. Knapp, A. van Geen, D. C. McCorkle, J. A. Brandes, and R. C. Thunell. 2003. Distinguishing between water column and sedimentary denitrification in the Santa Barbara Basin using the stable isotopes of nitrate. Geochemistry, Geophys. Geosystems **4**. doi:10.1029/2002GC000384

Stephens, B. M., M. Porrachia, S. Dovel, M. Roadman, R. Goericke, and L. I. Aluwihare. 2018. Nonsinking Organic Matter Production in the California Current. Global Biogeochem. Cycles **32**: 1386–1405. doi:10.1029/2018GB005930

Stephens, B. M., S. D. Wankel, J. M. Beman, A. J. Rabines, A. E. Allen, and L. I. Aluwihare. 2019. Euphotic zone nitrification in the California Current Ecosystem. Limnol. Oceanogr. lno.11348. doi:10.1002/lno.11348

Stramma, L., G. C. Johnson, J. Sprintall, and V. Mohrholz. 2008. Expanding Oxygen-Minimum Zones in the Tropical Oceans. Science (80-.). **320**: 655–658. doi:10.1126/science.1153847

Stukel, M. R., L. I. Aluwihare, K. A. Barbeau, and others. 2017. Mesoscale ocean fronts enhance carbon export due to gravitational sinking and subduction. Proc. Natl. Acad. Sci. U. S. A. **114**: 1252–1257. doi:10.1073/pnas.1609435114

Wankel, S. D., C. Kendall, J. T. Pennington, F. P. Chavez, and A. Paytan. 2007. Nitrification in the euphotic zone as evidenced by nitrate dual isotopic composition: Observations from Monterey Bay, California. Global Biogeochem. Cycles **21**. doi:10.1029/2006GB002723

Williams, P. M., and E. R. M. M. Druffel. 1987. Radiocarbon in dissolved organic matter in the central North Pacific Ocean. Nature **330**: 246–248. doi:10.1038/330246a0

Zehr, J. P., and B. B. Ward. 2002. Nitrogen cycling in the ocean: New perspectives on processes and paradigms. Appl. Environ. Microbiol. **68**: 1015–1024. doi:10.1128/AEM.68.3.1015-1024.2002

Zigah, P. K., A. P. McNichol, L. Xu, C. Johnson, C. Santinelli, D. M. Karl, and D. J. Repeta. 2017. Allochthonous sources and dynamic cycling of ocean dissolved organic carbon revealed by carbon isotopes. Geophys. Res. Lett. doi:10.1002/2016GL071348

Chapter 2: Stable isotopes of nitrate reveal effects of ENSO on nitrogen cycling in the surface waters of the southern California Current System

Abstract

The southern California Current System (sCCS) is a productive eastern boundary current system where strong coastal upwelling brings deep, nutrient-rich waters to the surface ocean. In this often nitrogen-limited environment, the supply of nitrate (NO_3^-) supports a productive food web. The NO_3^- load in water masses that supply the region can be impacted by a variety of climate-related processes that subsequently modulate primary productivity. In this study, stable isotopes of NO_3^- ($\delta^{15}N$ and $\delta^{18}O$) were used to examine NO_3^- biogeochemistry in the region, particularly in response to changes in NO_3^- supply to the euphotic zone. Two locations, encompassing two different coastal upwelling regimes in the sCCS, one to the north (Line 80) and one to the south (Line 93), were sampled seasonally over several years (2010-2016) on 14 California Cooperative Oceanic Fisheries Investigations (CalCOFI) cruises. The largest changes were associated with the El Niño conditions in late 2015 and early 2016, where upwelling NO_3^- supply was reduced, leading to increased isotopic enrichment, NO_3^- utilization, and reliance on nitrified (recycled) NO_3^-. The timeseries also revealed that the extent of NO_3^- utilization varied seasonally, interannually, and spatially and was sometimes linked to iron limitation of phytoplankton. Together, these data identify a dynamic euphotic zone NO_3^- cycle in the sCCS that is strongly impacted by climatic events that alter the thermal structure of the upper ocean.

Introduction

In the southern California Current System (sCCS), spring and summertime wind-driven upwelling of nutrient-rich waters sustains high levels of phytoplankton growth, which supports a productive ecosystem typical of Eastern Boundary Current systems worldwide (Chan et al. 2008). As such, understanding the bottom-up controls on phytoplankton productivity are of vital importance to the fisheries economy in the region. The California Cooperative Oceanic Fisheries Investigation (CalCOFI) survey was established in the late 1940s to examine natural population fluctuations in commercially important planktivorous fish populations (McClatchie 2014). The spatial extent of the survey and the measurements made on its quarterly cruises have evolved over the decades, but since the early 1980s a core group of physical, chemical, and biological measurements have been maintained and provides a rich timeseries of the climatology and biogeochemistry of the region (www.calcofi.org).

Data from the CalCOFI timeseries have demonstrated the central role of nitrate (NO_3^-) in maintaining the sCCS food web, though periodic iron limitation has been observed and results in excess surface nitrate in some regions of the California Current (Mantyla et al. 2007; Stukel et al. 2011; Brzezinski et al. 2015). Long-term NO_3^- variability, expressed in various ways including the nitracline depth (Aksnes and Ohman 2009) and NO_3^- concentration in upwelling source waters (Eppley and Peterson 1979; Stephens et al. 2018) has shown that Chlorophyll *a* concentrations in the sCCS are tightly controlled by NO_3^- delivery, which in turn is modulated by the region's varied climatology including pronounced influence by the El Niño Southern Oscillation (ENSO) (Kahru et al. 2009; Bograd et al. 2015, 2019; Jacox et al. 2016).

ENSO influences the sCCS via multiple mechanisms including atmospheric teleconnection that impacts vertical transport in the coastal sCCS, the deepening of the pycnocline due to the poleward propagation of coastally trapped waves originating in the tropical Pacific, and the anomalous northward advection of warm, saline subtropical water into the sCCS (Jacox et al. 2015). All of these mechanisms can profoundly impact the magnitude of NO_3^- delivered to the euphotic zone and thus primary production (Lilly et al. 2019). Nitrogen isotopes of archived zooplankton and sedimentary organic N have been used to provide insight into long term variations in the source and concentration of NO_3^- upwelling into the euphotic zone and indicate that indeed N supply is sensitive to climate variability such as ENSO (Ohman et al. 2012; Décima et al. 2013; Tems et al. 2015). For instance, nitrogen isotopes ($\delta^{15}N$) in zooplankton from the sCCS were significantly elevated during El Niño events (Rau et al. 2003; Ohman et al. 2012; Décima et al. 2013), which could result from a decrease in the supply of NO_3^-, an increase in the proportion of NO_3^- utilized (regardless of supply), and/or a shift in trophic position. Sediment trap studies also identified an increase in organic $\delta^{15}N$ of sinking particles during the recent El Niño (Davis et al. 2019), although this signal is typically attributed to a change in $\delta^{15}N$ of source NO_3^- rather than the proportion of N utilized.

In this study, we measured stable nitrogen and oxygen isotopes of NO_3^- along two CalCOFI lines (Figure 2.1), one in the northern region of the grid (Line 80.0, hereafter referred to as the northern line) where coastal upwelling is consistently observed in the spring and summer and which supports some of the highest primary production observed within the modern CalCOFI grid, and one in the southern end of the grid (Line 93.3, hereafter referred to as the southern line), off of San Diego where upwelling is more intermittent and iron supply is believed to be lower (King and Barbeau 2007). Along the southern line, inshore station 93.30 exhibits subsurface physical and chemical properties that are emblematic of the California Undercurrent, which connects the sCCS to the low oxygen waters of the eastern tropical North Pacific Ocean and brings nitrate isotopes enriched by denitrification to the CCS (Bograd et al. 2019). Several seasonal profiles of NO_3^- isotopes were examined from 2010-2016 at stations that were situated in the California Current or inshore. By considering these two lines, we were able to examine two very different regimes within the sCCS and their response to the El Niño event of 2015-2016. In particular, NO_3^- isotopes, in conjunction with other parameters measured during

CalCOFI cruises, make it possible to better quantify the degree of NO_3^- consumption in the sCCS as well as address other questions about nitrogen cycle dynamics for which NO_3^- concentration measurements alone are insufficient including the importance of euphotic zone nitrification. Importantly, this study also provides the first comprehensive spatial and temporal coverage of water column sCCS NO_3^- isotope values necessary for interpretation of measurements in marine organisms as well as isotope signals recorded in the sediments.

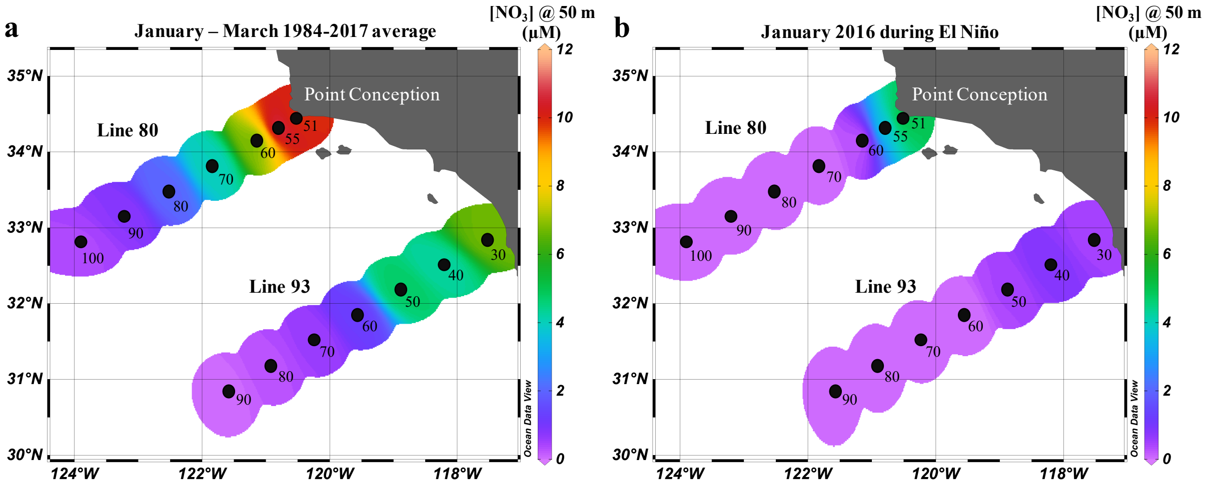

Figure 2.1. Locations of CalCOFI stations sampled for NO_3^- isotopes in this study. Two CalCOFI lines were sampled for NO_3^- isotopes- Line 80.0 off of Point Conception (northern line) and Line 93.3 off of San Diego (southern line). **(a)** The 1984-2017 average NO_3^- concentrations at 50 m in winter (January-March) highlighting the North-South and inshore-offshore gradients in NO_3^- concentration. **(b)** The NO_3^- concentrations at 50 m for winter 2016 during the El Niño event. Winter and early spring are when ENSO events are most strongly expressed in the sCCS. NO_3^-concentrations long both lines were much lower during the El Niño compared to the seasonal average. See Table S1 for a complete list of locations and time periods covered by this data set as well as seasonal designations.

Materials and methods

Sample collection

NO_3^- isotope samples were collected from Lines 80 and 93 of the CalCOFI grid (Figure 2.1, http://calcofi.org). Line 93 is the southernmost location sampled by CalCOFI while Line 80 is to the north, off of Point Conception. Most measurements were performed on stations 93.30 to

93.60 and 80.55 to 80.80 to better understand the more dynamic nature of the inshore stations, where wind-drive upwelling and the influence of the California Undercurrent are most likely to be observed (see Table S1 for a complete list of locations and time periods sampled). Samples were collected during fourteen CalCOFI cruises from 2010-2016 and include all measurements made above 150 m (Figure 2.2). Samples for NO_3^- isotopes were filtered through GF/F filters (0.7 μm pore size) directly from Niskin bottles mounted on a standard conductivity-temperature-depth rosette system (CTD) and frozen until analysis.

Nutrient concentrations and isotope analyses

Ancillary data were collected, analyzed and made publicly available through the CalCOFI program (http://calcofi.org/data.html). Accuracy and precision for NO_3^- concentrations are reported as 0.05 μmol/L. The detection limit is reported as 0.02 μmol/L for $NO_3^- + NO_2^-$. $\delta^{15}N_{NO3}$ and $\delta^{18}O_{NO3}$ were analyzed using the denitrifier method (Casciotti et al. 2002; Sigman et al. 2001), in which denitrifying bacteria quantitatively convert NO_3^- to N_2O for isotopic analysis. Sample N_2O was purified using a customized purge and trap system and analyzed on a continuous flow IsoPrime 100 isotope ratio mass spectrometer (IRMS). Nitrite concentrations greater than 2% of $NO_3^- + NO_2^-$ were removed by addition of sulfamic acid prior to injection (Granger and Sigman 2009). Corrections for drift, size and fractionation of O isotopes during bacterial conversion were carried out using NO_3^- reference materials USGS 32, USGS 34 and USGS 35 (McIlvin and Casciotti 2011).

Isotopic expressions and calculations

Delta notation is used to describe the isotopic composition of a sample expressed in units of permil (‰), where $\delta = [(R_{Sample}/R_{Standard}) - 1] \times 1000$ and R is the ratio of ^{15}N to ^{14}N or ^{18}O to ^{16}O in NO_3^-. The relative strength of isotopic discrimination is represented by the isotope effect or fractionation factor and is also expressed in per mil as $^{15}\varepsilon$ (where $\varepsilon = [(k^{heavy}/k^{light}) - 1] \times 1000$, and k represents the rate constant of the heavy or light isotope, respectively. N isotope fractionation factors for NO_3^-uptake by phytoplankton were calculated by fitting both open and closed system Rayleigh fractionation models. The closed system model is described by Equation 1 where:

$$\delta^{15}NO3 = \delta^{15}NO3_{initial} - {}^{15}\varepsilon \quad \times \ln\left(\frac{[NO3]}{[NO3]initial}\right) \qquad (1)$$

The open system model, where new water is supplied continuously, is described by a second equation where:

$$\delta^{15}NO3 = \delta^{15}NO3_{initial} + {}^{15}\varepsilon \quad \times \left(1 - \frac{[NO3]}{[NO3]initial}\right) \quad (2)$$

where $\delta^{15}N_{initial}$ and $[NO_3]_{initial}$ refer to immediate source waters to the EZ, the determination of which is described further below. Each profile was individually evaluated using both models. The model with the best least squares regression fit was selected based on r^2 values and the corresponding $^{15}\varepsilon$ value are reported (Table S2). In this way, $^{15}\varepsilon$ values for NO_3^- uptake were calculated for all stations with at least 3 measurements in the euphotic zone.

The nitrogen isotope data together with the appropriate Rayleigh fractionation model can be used to estimate the fraction of upwelled NO_3^- that is utilized at inshore stations (stations 51-70 for Line 80 and stations 30-60 for Line 93). A closed system Rayleigh fractionation model where $\delta^{15}N_{NO3} = \delta^{15}N_{NO3,\ initial} + {}^{15}\varepsilon * \ln(1-\%_{NO3\ utilized})$, was ultimately used to calculate the extent of NO_3^- utilization at each depth because more than 75 % of the profiles where a fractionation factor could be determined fit the closed system model better (Table S2). A consistent $^{15}\varepsilon$ value of 3 ‰ was used for all stations based on our average calculated fractionation factor and fractionation factors calculated from previous work conducted in the sCCS (Stephens et al., 2019). Uncertainty for fraction NO_3^- utilization was estimated from the standard deviation of $^{15}\varepsilon$ values. Upwelling source depth, needed to determine $\delta^{15}N_{NO3,\ initial}$ and the concentration of upwelling NO_3^-, was estimated from the NO_3^--temperature relationship for each station by fitting a line to NO_3^- concentration and temperature data below 150 m. The upwelling depth was assigned as the deepest depth where the measured NO_3^- value deviated below the concentration predicted from measured temperature (i.e., deviated from a simple water mass mixing relationship) by at least 2 μM, similar to the method used in Stephens et al. (2018). This method did not work for some stations, particularly during the El Niño period in 2015/2016 when surface waters were unusually warm. For stations where we were unable to use the NO_3^--temperature relationship to determine source water characteristics, NO_3^- and chlorophyll profiles were examined individually to estimate these parameters. In this case, the NO_3^- concentration at the deepest depth where chlorophyll concentrations began to exceed background values was used. Once the depth where NO_3^- concentrations representing pre-utilization characteristics was identified, the corresponding source NO_3^- isotope signature was determined. Since we did not make isotope measurements for every depth where nutrients were measured, the closest deepest depth with an isotope value was used (Table S3). Choosing the closest deepest depth ensured that isotope characteristics were uninfluenced by biological uptake.

NO_3^- assimilation by phytoplankton results in equivalent fractionation for both nitrogen and oxygen isotopes in the remaining NO_3^- pool (Granger et al., 2004). However, this is not always observed, and in fact, when $\delta^{15}N_{NO3}$ and $\delta^{18}O_{NO3}$ do not change in such a predicted 1:1 relationship, other processes apart from assimilation must be important, the relative magnitude which can be expressed using Δ(15,18), defined by Sigman et al., 2005 as:

$$\Delta(15{,}18) = [(\delta^{15}N_{NO3} - \delta^{15}N_{NO3,source}) - {}^{15}\varepsilon_p/{}^{18}\varepsilon_p(\delta^{18}O_{NO3} - \delta^{18}O_{NO3,source})] \quad (3)$$

${}^{15}\varepsilon_p/{}^{18}\varepsilon_p$ was assumed to be 1:1 since it has been demonstrated in culture that phytoplankton fractionate oxygen and nitrogen isotopes uniformly during NO_3^- uptake (Granger et al. 2004). In particular, deviation from the 1:1 relationship in surface waters has been attributed to active euphotic zone nitrification, supplying NO_3^- to the phytoplankton community. The contribution of locally nitrified NO_3^- to uptake by phytoplankton was calculated after Wankel et al., 2007 and Stephens et al., 2019 using a steady state box model, where:

$$\Delta(15,18) = f_n * \left(\varepsilon_p - f_a * f_w * (\varepsilon_{ntr} - \varepsilon_a)\right) - \left(\frac{\delta^{18}O_{source} - \delta^{18}O_{source} * f_w + (\varepsilon_p * f_n) + (\delta^{18}O_{ntr} * f_n * f_w)}{1 - f_w + (f_n * f_w)}\right) + \delta^{18}O_{source}, \tag{4}$$

Here f_n is the fraction of NO_3^- remaining relative to the source NO_3^-, ε_p is the fractionation factor for phytoplankton uptake of NO_3^- (here a constant value of 3 ‰ was used), f_a is the fraction of NH_4^+ assimilated by phytoplankton (with a value of 0.8 used here), f_w is the fraction of assimilated NO_3^- contributed by nitrification within the euphotic zone, ε_{ntr} is the net isotope effect of NH_4^+ and NO_2^- oxidation (with a value of 6 ‰ used here), ε_a is the isotope effect of NH_4^+ assimilation (with a value of 22 ‰ used here), and $\delta^{18}O_{ntr}$ is the $\delta^{18}O$ of NO_3^- resulting from nitrification (with a value of 0 ‰ used here) (Wankel et al. 2007; Buchwald and Casciotti 2010; Stephens et al. 2019). Upwelling water mass characteristics were determined as described above and values for the other parameters were assigned following Stephens et al., 2019. The effect of varying several of the poorly constrained parameters in equation (4) was previously examined in depth (Stephens et al., 2019) and is therefore not repeated here. Instead, we examine trends in f_w spatially and temporally, with less of a focus on interpreting each specific value. We note that many of the samples from 2010-2012 with lower NO_3^- concentrations were not analyzed for oxygen isotopes, and thus are not included in the f_w analysis.

To examine the relationship between nitrogen cycle parameters and upper ocean stratification, we computed a stratification strength index for each station and timepoint using the density at 200 m as a reference point and calculating the difference in density between each depth in the euphotic zone and the reference density at 200 m (Behrenfeld et al. 2006) (see Table S4 for complete list of density values used).

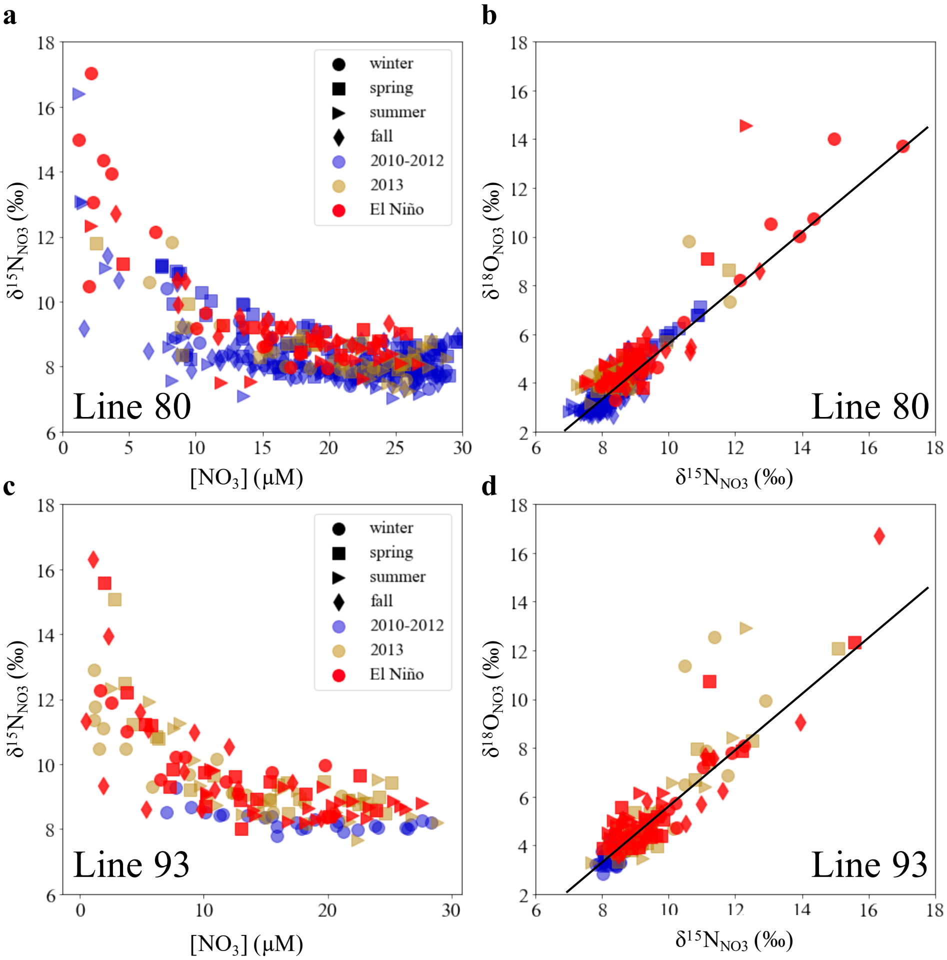

Figure 2.2. $\delta^{15}N_{NO3}$ and $\delta^{18}O_{NO3}$ measurements from two CalCOFI lines. $\delta^{15}N_{NO3}$ and $\delta^{18}O_{NO3}$ increase as NO_3^- is drawn down by phytoplankton in the surface ocean along the northern line (Line 80) (**a**) and the southern line (Line 93) (**c**). The range of $\delta^{15}N_{NO3}$ values observed at a given NO_3^- concentration demonstrate how isotopic measurements provide additional information. $\delta^{15}N_{NO3}$ and $\delta^{18}O_{NO3}$ along Line 80 (**b**) and Line 93 (**d**) generally increase in a ratio of 1:1 (indicated by the black line), but other processes such as euphotic zone nitrification can lead to deviations from this 1:1 trajectory. Season and year are indicated by the shape and color, respectively, of each point.

Results

Variability in $\delta^{15}N_{NO3}$ and $\delta^{18}O_{NO3}$

Assimilation of NO_3^- by phytoplankton in the euphotic zone results in one of the strongest signals in oceanic $\delta^{15}N_{NO3}$ and $\delta^{18}O_{NO3}$ (Figure 2.2). From 2010-2016, $\delta^{15}N_{NO3}$ and $\delta^{18}O_{NO3}$ above 150 m demonstrated considerable spatial and temporal variability in the sCCS (see Table S4.1 for a full list of time periods and locations sampled). $\delta^{15}N_{NO3}$ ranged from 7.1 up to 17.0 ‰ and $\delta^{18}O_{NO3}$ ranged from 2.7 to 16.7 ‰ (Figure 2.2). Values for both $\delta^{15}N_{NO3}$ and $\delta^{18}O_{NO3}$ were generally greatest where NO_3^- concentrations were drawn low as the result of uptake by phytoplankton (Figure 2.2). NO_3^- isotope ratios were generally higher deeper in the water column along the southern line compared to the northern line (Figure 2.3). Although in general both $\delta^{15}N$ and $\delta^{18}O$ increased with a ratio of 1:1, as would be expected for NO_3^- uptake, there was substantial deviation from 1:1, mostly where $\delta^{18}O$ values increased more relative to $\delta^{15}N$ values (Figure 2.2b and 2.2d).

In the sCCS, El Niño conditions, defined here as including fall 2015 – summer 2016 (Jacox et al. 2016; though effects of the event had most dissipated by spring 2016), resulted in greater density anomalies in the surface ocean (Figure S2.1), increased stratification (Figure S2.2) and decreased net primary production (NPP; Figure S2.3). At the more inshore stations, the highest $\delta^{15}N$ and $\delta^{18}O$ values were generally found in surface water during this time period, also coinciding with higher values deeper in the water column compared to non-El Niño years (Figure 2.3). In the shallow surface ocean, particularly in the offshore region along the northern line and for most of southern line, low NO_3^- concentrations prevailed and precluded isotopic measurements (Figures 2.4a and 2.5a). During 2013, values of $\delta^{15}N_{NO3}$ along the southern line were almost as high has during the El Niño, but fewer measurements before 2013 make it difficult to evaluate how anomalous these observations are for this section of the CalCOFI grid (Figure 2.5b).

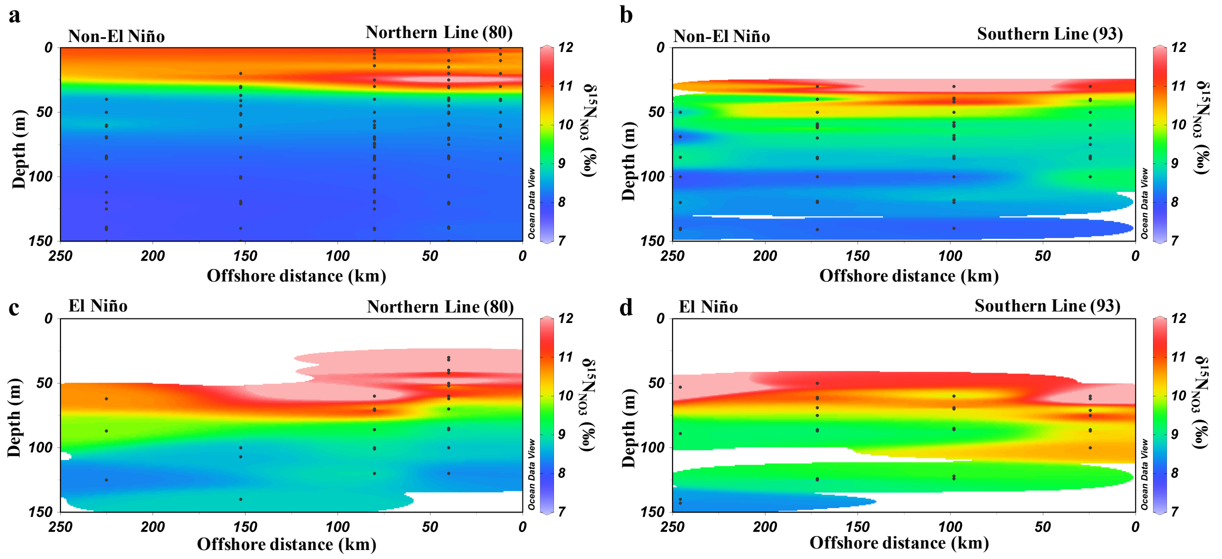

Figure 2.3. $\delta^{15}N_{NO3}$ values increased during the recent El Niño. $\delta^{15}N_{NO3}$ from 2010-2013 along the northern line is shown in (**a**), in contrast to the higher values observed during the El Niño (fall 2015-winter 2016) (**c**). A similar pattern was seen along the southern line (**b**), where $\delta^{15}N_{NO3}$ is higher deeper in the water column during the El Niño (**d**).

NO_3^- utilization

An accurate estimate of the fractionation factor associated with NO_3^- uptake by phytoplankton is necessary in order connect the isotopic signature of the remaining NO_3^- pool to the extent of utilization. Previous laboratory studies have shown that species composition and growth rate, among other factors can influence the $^{15}\varepsilon$ of phytoplankton uptake (Needoba et al., 2003; Granger et al., 2004). Here, $^{15}\varepsilon$ of phytoplankton uptake was calculated for 21 profiles. Five profiles fit the open system model better than the closed system, all at coastal stations during different cruises (spring 2010, fall 2010, spring 2011, summer 2013, and winter 2016). The remaining 16 profiles were better fit using a closed system model (Eq 1). Estimated fractionation factors from the closed system profiles ranged from 2.1 to 5.0 ‰ with an average of 3.2 ± 0.8 ‰ (Table S2). This is in good agreement with a previous study which estimated the average $^{15}\varepsilon$ for the inshore sCCS region at 3.0 ± 0.5 ‰ (Stephens et al., 2019), as well as a previous study examining $^{15}\varepsilon$ for various marine phytoplankton cultures (Needoba et al. 2003), but it is lower than what has been determined in several culture studies and other marine environments (e.g. Granger et al. 2004).

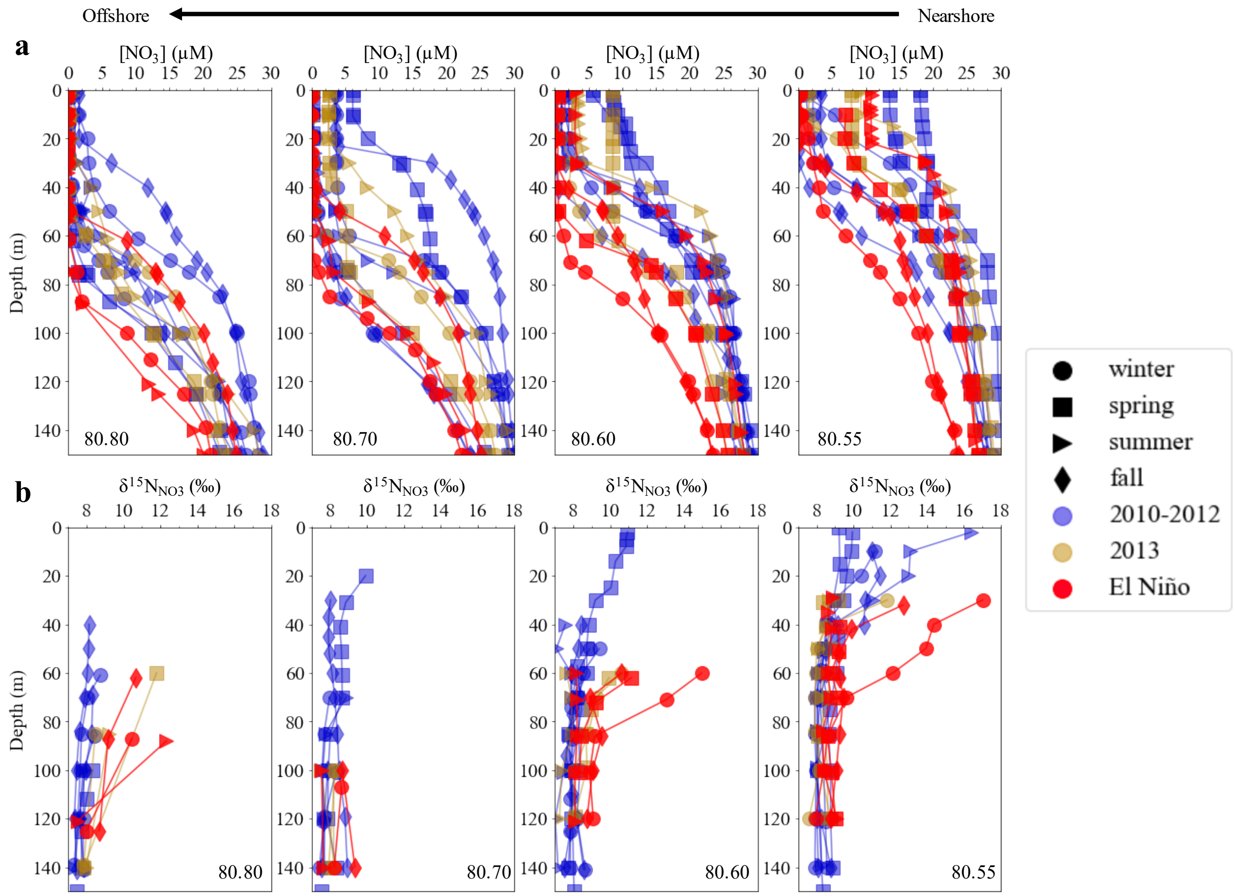

Figure 2.4. Profiles of NO_3^- concentrations and $\delta^{15}N_{NO3}$ along the northern line. NO_3^- concentrations are shown in **(a)**, with lower concentrations apparent during 2015-2016 (El Niño; red symbols). $\delta^{15}N_{NO3}$ values are plotted for all samples above 150 m (**b**) showing larger increases during 2015-2016 compared to earlier years. Season and year are indicated by the shape and color, respectively, of each point.

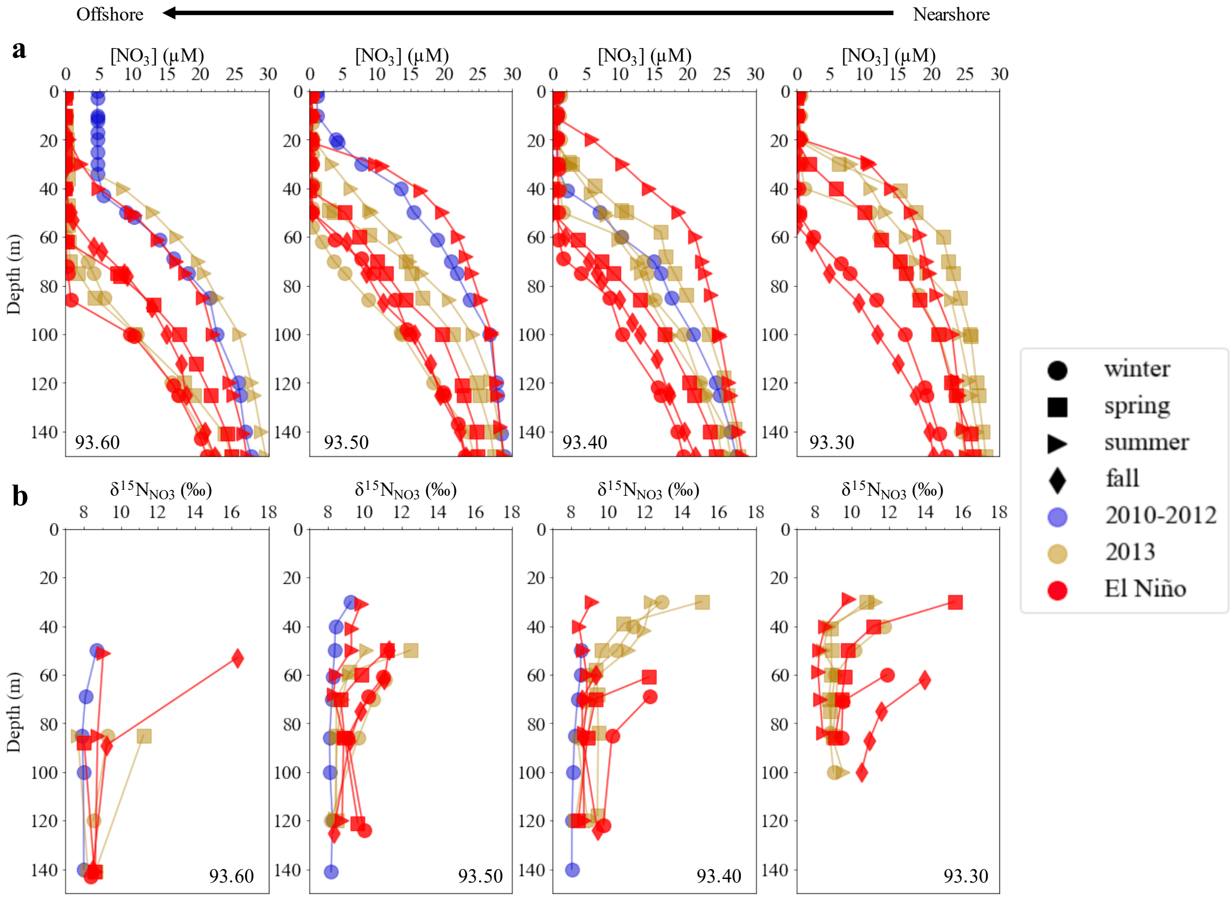

Figure 2.5. Profiles of NO_3^- concentrations and $\delta^{15}N_{NO3}$ along the southern line. NO_3^- concentrations are shown in **(a)**, with lower concentrations apparent during 2015-2016 (El Niño; red symbols). $\delta^{15}N_{NO3}$ values are plotted for all samples above 150 m (**b**) showing larger increases during 2015-2016 compared to earlier years. Season and year are indicated by the shape and color, respectively, of each point.

Calculated $^{15}\varepsilon$ values together with $\delta^{15}N_{NO3}$ profiles allowed us to estimate the fraction of NO_3^- utilized in the euphotic zone and provided insights into the balance between NO_3^- supply and demand. In general, higher $\delta^{15}N_{NO3}$ values reflect greater extent of NO_3^- drawdown (Altabet and Francois 1994) and lower values suggest that NO_3^- uptake may be limited by factors other than NO_3^- concentration. Depth profiles of the fraction of NO_3^- utilized varied greatly both spatially and temporally, across seasonal and interannual time scales (Figure 2.6), with values ranging from zero up to 0.94 at specific depths. A comparison of vertical NO_3^- utilization profiles also indicated that higher NO_3^- utilization began deeper in the water column at the southern line compared to the northern line (Figure 2.6).

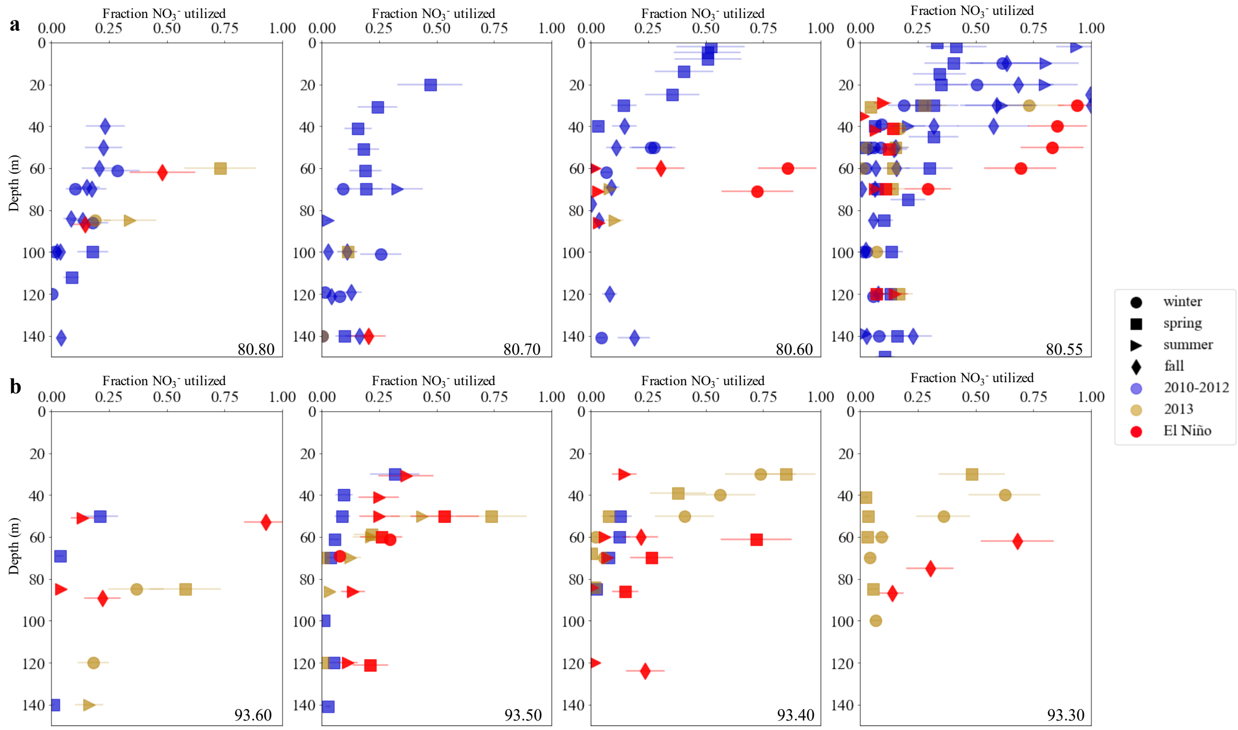

Figure 2.6. Fraction NO_3^- utilization increased during the recent El Niño. The fraction of NO_3^- that was utilized at individual depths in shown for the northern line (Line 80) **(a)** and southern line (Line 93) **(b)**. Error bars were calculated based on standard deviation of estimated $^{15}\varepsilon$. Season and year are indicated by the shape and color, respectively, of each point.

In general, $\delta^{15}N_{NO3}$ data indicated utilization was lowest during spring cruises (Figure 2.6). With the exception of the El Niño year (spring 2016), the fraction of NO_3^- utilized did not rise above 0.50 for spring cruises, and surface NO_3^-concentrations remained elevated at inshore stations (Figure 2.4a). A similar observation was made in the equatorial upwelling region of the Pacific Ocean (Altabet 2001) .

For most other seasons, NO_3^- was below the detection limit in surface waters suggesting near complete utilization, however, where NO_3^- was present, the shape of the NO_3^- utilization profile often differed significantly. For winter cruises, January 2016 (the winter of El Niño) saw the greatest fraction of NO_3^- utilization; whereas for all summer cruises, the fraction of NO_3^- utilized remained below 0.50 where NO_3^- was detectable (deeper than 20 m), and the El Niño year was indistinguishable from the others, consistent with the event having mostly dissipated by this time (Jacox et al. 2016). In the fall, at the start of the El Niño year (1511), we saw a greater fraction of NO_3^- utilized at every depth compared to previous years.

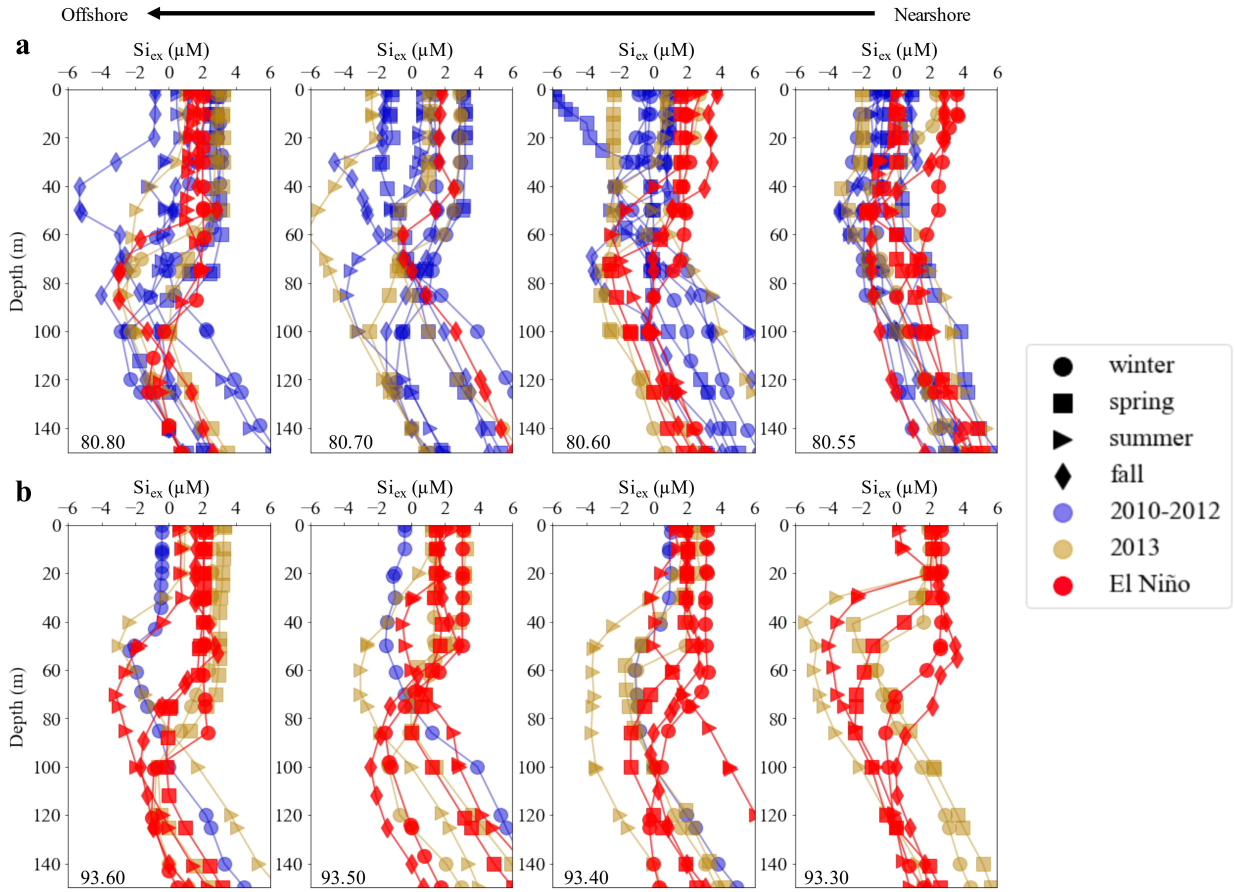

Figure 2.7. Silica excess (Si_{ex}) as a proxy for iron limitation along northern and southern Lines. Profiles of Si_{ex} are shown here for the northern line (Line 80) (**a**) and southern line (Line 93) **(b)** for each station. Season and year are indicated by the shape and color, respectively, of each point. Along the northern line, values become more negative as we move offshore. Along the southern line, the more inshore stations exhibit strong mid-depth minima in $Si_{ex.}$

Iron limitation estimates via silica excess

Differences in the proportion of NO_3^- utilized at each depth indicated that other factors besides NO_3^- availability could prevent phytoplankton from fully utilizing euphotic zone NO_3^-. Iron limitation of phytoplankton productivity has been shown to occur intermittently in the sCCS (King and Barbeau 2007; Hogle et al. 2018; Stukel and Barbeau 2020) and could be responsible for limiting NO_3^- utilization. The proxy Si_{ex}, where $Si_{ex} = [Si(OH)_4] – (R_{Si:NO3} \times [NO_3^-])$, has been previously used in the sCCS as an indicator of possible iron limitation (King and Barbeau 2011; Hogle et al. 2018; Stukel and Barbeau 2020). Negative values of Si_{ex} are thought to result from Fe-limited diatoms taking up excess silicic acid ($Si(OH)_4$) relative to NO_3^- (Hutchins and Bruland 1998). For this calculation, the ratio of these two macronutrients in the upwelling source water ($R_{Si:NO3}$) was determined in the same way as upwelling NO_3^- isotope signatures (as described above). Profiles of Si_{ex} for the northern line and the southern line are shown for each station in Figure 2.7. As is apparent if we compare the Si_{ex} profiles to the NO_3^- concentration profiles, Si_{ex} invariably becomes positive in the surface ocean when all of the NO_3^- has been consumed (Figures 2.4a, 2.5a, and 2.7). Positive values show that excess silica accumulates at these depths (relative to upwelling values) and are indicative of NO_3^- uptake by phytoplankton with low or no silica requirements. Along the northern line Si_{ex} often becomes negative in the upper ocean as we move offshore, developing primarily in the spring and summer, but also occasionally in the fall for stations offshore. For the southern line, it is the inshore stations that display the strongest Si_{ex} minimum, which develops primarily during the spring and summer (Figure 2.6: e.g., station 93.30). Overall, positive Si_{ex} values seem to occur when smaller phytoplankton, likely with no silica requirement, are more abundant, as reflected in size-fractionated chlorophyll data (Figures S2.4-5).

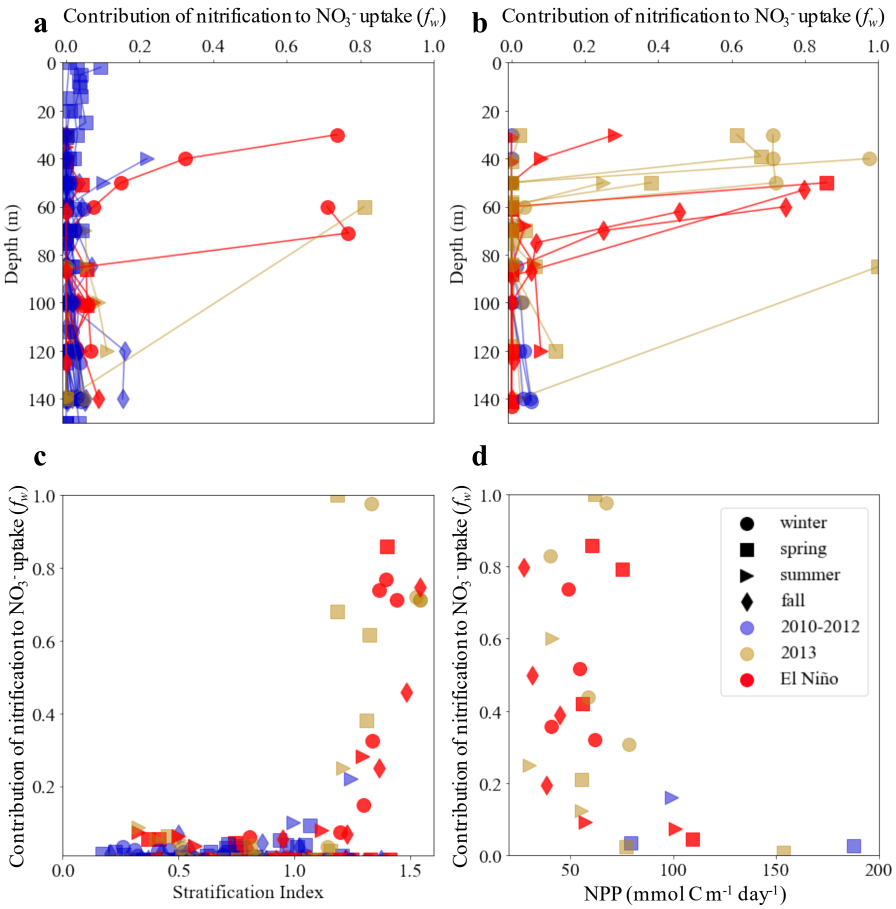

Figure 2.8. Contribution of recycled NO_3^- varies greatly in the sCCS. The proportion of NO_3^- taken up by phytoplankton that originated from nitrification in the euphotic zone (f_w) by depth (northern line: (**a**), southern line: (**b**)) and as compared to the stratification strength index (**c**) and satellite estimates of net primary production (NPP) (**d**). f_w was greater during warm periods when the water column was more stratified, and upwelling was reduced. Higher f_w values were also associated with lower NPP. Season and year are indicated by the shape and color, respectively, of each point.

Euphotic zone nitrification

While NO_3^- uptake by phytoplankton results in a closely coupled fractionation of the two isotope systems in a ratio of 1:1, the N and O isotope systems are decoupled in other processes, such as nitrification (Wankel et al. 2007; Granger and Wankel 2016). NO_3^- most commonly enters the surface ocean via the upwelling of deeper waters, where NH_4^+ has been converted to NO_3^- via nitrification. However, nitrification can also occur in the surface ocean, where locally nitrified NO_3^- can contribute to primary production (Smith et al. 2014; Laperriere et al. 2020). Here we estimate the f_w parameter, which is an integrated indicator of the proportion of NO_3^- uptake by phytoplankton that has been supplied via upper ocean nitrification as opposed to being delivered via upwelling.

In order to examine the influence of surface ocean nitrification, we calculated Δ(15,18) for all samples, and used this to estimate f_w. For all samples above 100 m, Δ(15,18) ranged from -5.9 to 1.6 ‰ (Figure S2.6). Negative values signify that either the nitrogen isotopic signature is anomalously low, or that the oxygen signature is anomalously elevated (Casciotti, 2016; Wankel et al., 2007). Here we assume that negative deviations are due to the presence of NO_3^- produced via local (euphotic zone) nitrification, which has the effect of elevating $\delta^{18}O_{NO3}$ but not $\delta^{15}N_{NO3}$, relative to assimilation alone. The fractional contribution of nitrification to NO_3^- uptake by phytoplankton (f_w) varied spatially and temporally, ranging from 0 to more than 0.9 at individual depths (Figures 2.8a and b).

Increased contribution from euphotic zone nitrification occurred when ocean waters were warmer and more stratified (per the stratification strength index) and NO_3^- concentrations in the euphotic zone were lower (Figures 2.4-5, 2.8c). We noted that f_w was also elevated when NPP was low (Figure 2.8d). It is difficult to estimate an average f_w value due to variations in spatial sampling, but in general, contribution from nitrification was low for most time periods, with values above 0.2 appearing mainly along the southern line (Figure 2.8b) and during winter 2016 for the northern line (Figure 2.8a). Because the majority of data points on the southern line are from 2013 and 2015-2016, when euphotic zone waters were anomalously warm and stratified, we cannot determine whether we would always observe high f_w in this location. In fact, a time series of satellite-based NPP estimates for inshore stations shows an extended period of low NPP along the southern line from 2013 to mid 2016 (Figure S2.3) indicating that this time period was anomalous and may have indeed seen decreased NO_3^- input from vertical transport. Such episodes could favor NPP supported primarily by recycled nutrients, including NO_3^- derived from euphotic zone nitrification. All elevated f_w values occurred at a relatively narrow depth range of 30-70 m (Figures 2.8a and b).

Discussion

Influence of ENSO on N cycling in the sCCS

This timeseries of NO_3^- isotopes enabled us to examine the response of the sCCS nitrogen cycle to the 2015-2016 El Niño. El Niño conditions resulted in increased stratification (Figure S2.2), decreased surface NO_3^- concentrations (Figures 2.1, 2.4a and 2.5a) and decreased NPP (Figure S2.3). We observed large differences between $\delta^{15}N_{NO3}$ measured during El Niño and non-El Niño periods both in the magnitude of the values (Figures 2.2-2.5) as well as in the NO_3^- dynamics inferred from the isotope compositions (Figured 2.6 and 2.8-9). The fraction of NO_3^- that was utilized by upper ocean ecosystems increased and extended to deeper depths during El Niño cruises (Figure 2.6), indicating an overall decrease in NO_3^- supply to the euphotic zone consistent with a deeper nitracline and reduced upwelling (Jacox et al. 2016; Bograd et al. 2019). Greater utilization at inshore stations probably also had important implications for productivity elsewhere in the sCCS because inshore partial NO_3^- utilization is a relatively common feature in this region and makes excess NO_3^- available for both alongshore and offshore export (Figure 2.6). Estimates of greater utilization confirm that the observed enrichment in NO_3^- isotopes during the 2015-2016 El Niño was linked to decreased supply and not simply elevated source nitrate $\delta^{15}N$.

The large fraction of NO_3^- assimilated by phytoplankton (>75%; f_w) that was derived from recycled nitrogen (i.e., euphotic zone nitrification; Figure 2.8a and b), particularly along the southern line, also reflects the importance of euphotic zone nitrification during the 2015-2016 El Niño. The apparent increased reliance on NO_3^- from surface nitrification during these time periods was likely linked to decreased supply of NO_3^-, decreased competition from phytoplankton for NH_4^+ (the substrate for nitrification), and the potentially longer residence time of NH_4^+ and suspended particulate organic nitrogen (PON) in the euphotic zone, all associated with decreased vertical mixing and a deeper pycnocline (Figure S2.2). One thing we cannot assess is whether relatively greater NPP or changes in the distribution of phytoplankton size classes occurred as a result of this nitrified NO_3^- supply, or whether or not or to what extent absolute nitrification rates were elevated during this time period. Overall, the increased contribution from recycled nitrogen reported here is consistent with previous studies in the sCCS that have reported decreased new production during El Niño years (Hernández-de-la-Torre et al. 2003; Kelly et al. 2018). There is a tendency for NPP to decrease alongside the f-ratio, and so, lower NO_3^- supply has important ramifications for higher trophic level productivity and carbon export in the sCCS (Eppley et al., 1977; Eppley & Peterson, 1979).

Warming increases the importance of local nitrification

Elevated reliance on nitrified NO_3^- by phytoplankton has been previously reported for the sCCS, and generally occurred at times of low net primary production (Figures 2.8d and S2.3), indicating the importance of recycled NO_3^- in maintaining sCCS food webs during these periods (Wankel et al. 2007; Stephens et al. 2019; Laperriere et al. 2020). As noted in previous studies (Wankel et al., 2007; Stephens et al. 2019), new production estimates that rely on NO_3^- uptake measurements would be impacted if a significant fraction of NO_3^- in the euphotic zone were derived from nitrified NO_3^-, as seen here during warm, stratified periods in the sCCS. In addition to the El Niño, we also observed elevated f_w along the southern line in 2013 (Figure 2.8b). Although our data only showed increased f_w and NO_3^- utilization in 2013 and 2015-2016, it is likely that the warm anomaly years between 2013-2015 exhibited similar conditions (e.g., Stephens et al. 2019) particularly in the southern sCCS. Such episodes could favor production supported primarily by recycled nutrients, including NO_3^- derived from euphotic zone nitrification. Across our entire dataset, we observed that f_w is higher when the water column is more stratified (Fig. 8c), and when the stratification index was >1.4 in our dataset more than half of the NO_3^- used by phytoplankton came from euphotic zone nitrification.

Considering the longer CalCOFI time series of maximum chlorophyll concentrations, it appears that the 2000-2012 period may have seen anomalously high primary production along the southern line compared to the period immediately before. Whereas, we noted earlier that the time period between 2013-2016 exhibited anomalously low NPP (Figure S2.3). The timing of these transitions suggests a possible relation to both interannual climate variability (ENSO) and indices of decadal climate variability (Newman et al. 2016).

All f_w values above 0.25 (or 25 % of utilized NO_3^- coming from nitrification) occurred when Si_{ex}, our proxy for iron limitation, was positive (i.e., no iron limitation). This could be explained by an oligotrophic community dominated by non-diatom phytoplankton, consistent with the observed trends in size-fractionated chlorophyll (Figures S2.4 and S2.5). The CalCOFI timeseries of flow cytometry-based phytoplankton community composition (Nagarkar et al. 2021) also indicated that warm periods, when we expect greater f_w values, are correlated with a phytoplankton community of smaller cells including autotrophic cyanobacteria. Another recent study observed lower biogenic silica to Chlorophyll *a* ratios during the period of the warm anomaly, suggesting a decrease in the abundance of siliceous phytoplankton at that time (Closset et al. 2021). It has also been shown that nitrifiers can experience iron limitation in the surface ocean, and thus may not be as active when they are having to compete with phytoplankton for scarce iron (Shafiee et al. 2019). This could help to explain why f_w values appear elevated only when we do not see indicators of iron limitation.

Since we do not have measurements of NO_3^- or NH_4^+ uptake from CalCOFI cruises, we are unable to say how nitrification rates or NH_4^+ uptake rates varied here. Thus, we are unable to determine whether nitrification rates are actually elevated during the time periods when we observed high f_w, or whether the increase in f_w is more a result of lower NO_3^- supply from upwelling. It is also unclear how f_w is related to the f-ratio, as it has been suggested that phytoplankton and nitrifiers may compete for access to NH_4^+ (Zakem et al. 2018). It is possible that higher temperatures in the sCCS resulted in higher organic matter recycling rates and therefore, higher nitrification rates, parameters that should be more closely investigated further in future studies.

Incomplete NO_3^- utilization in the sCCS

Recent studies in the sCCS have indicated that both Ekman transport associated with coastal upwelling as well as iron limitation in the California Current can limit NO_3^- utilization in nearshore waters, allowing excess NO_3^- and nitrogen biomass to be transported offshore or subducted at fronts (Plattner 2005; Frischknecht et al. 2018; Hogle et al. 2018; Stukel and Barbeau 2020). Capturing these events of incomplete NO_3^- utilization is also important for interpreting isotope studies of non-nitrate N reservoirs. The value of N isotope fractionation factor is essential to the determination of NO_3^- utilization. Here, there appears to be a correspondence between $^{15}\varepsilon$ and NPP as estimated from satellite measurements (Kahru et al.

2009) where greater NPP is associated with a larger fractionation effect (Figure S2.7). This could be explained by higher euphotic zone NO_3^- concentrations leading to higher NPP and greater expression of the fractionation factor for NO_3^- uptake. It is also possible that factors such as iron limitation, or luxury uptake and storage of NO_3^- by diatoms may lead to variability in the expressed $^{15}\varepsilon$ (Karsh et al. 2003).

Except for the periods of high utilization associated with the 2015-2016 El Niño, incomplete NO_3^- utilization was commonly observed, especially at our inshore stations (Figures 2.4-2.6). Rapid upwelling coupled with a lag in phytoplankton response could result in low local NO_3^- utilization and subsequent export through offshore Ekman transport. In this way, unutilized NO_3^- that is transferred offshore may fuel productivity elsewhere in the region (Eppley and Peterson 1979; Plattner 2005; Frischknecht et al. 2018). In our dataset, inshore stations along the northern line off Point Conception, which are characterized by some of the strongest upwelling in the sCCS (Sherrell et al. 1998), likely experienced low fraction NO_3^- utilization for this reason (Fig. 6). This is evident in a few depth profiles along the northern line where NO_3^- concentrations decrease toward the surface ocean but marked isotope fractionation is not discernable. This could be because of open system isotope dynamics, where the constant addition of new NO_3^- from upwelling dilutes any isotope effect imparted on the NO_3^- reservoir during uptake (Figure 2.4 e.g. at 80.55).

When NO_3^- remains unutilized in otherwise favorable conditions, it can point to the importance of other factors, for example iron limitation (King and Barbeau 2007; Hogle et al. 2018). In this study, we used the diatom iron limitation proxy, Si_{ex}, to examine the interplay between iron limitation and NO_3^- utilization. Inshore, upwelling conditions lead to nutrient replete surface waters necessary to support diatom blooms, and with their higher iron quotas and requirements for silica, diatoms will influence the Si:NO_3 ratio, and thus Si_{ex}, when iron is scarce (King and Barbeau 2007; Brzezinski et al. 2015). Negative values of Si_{ex} indicate that phytoplankton are using more Si relative to NO_3^-, as is the case with iron-limited diatoms. Our dataset indicates that NO_3^- utilization and Si_{ex} interact in the sCCS in a few different ways. For example, some regions exhibit high NO_3^- utilization, low chlorophyll and positive Si_{ex} (Figure 2.9a), whereas other regions are iron limited (negative Si_{ex}) but can have either high NO_3^- utilization and high chlorophyll (Figure 2.9b) or low NO_3^- utilization and low chlorophyll (Fig. 9c). Water masses with positive Si_{ex} values but low chlorophyll (Figure 2.9a) are likely nitrate-limited and oligotrophic. In these environments, NO_3^- has been drawn down, but the overall limited supply of NO_3^- keeps chlorophyll concentrations low. We can see from the size-fractionated chlorophyll data that these communities tend to host smaller phytoplankton, potentially with either no or limited silica requirements (Figures S2.4-5). Although it is possible that these communities are also experiencing iron limitation, it will not be reflected in the Si_{ex} proxy used here. However, iron limitation of both phytoplankton and heterotrophic bacteria has been shown to be less common in oligotrophic regimes (Kirchman et al. 2000). These conditions generally describe what was commonly observed during the 2015-2016 El Nino (Figure 2.3;2.4a and 2.5a).

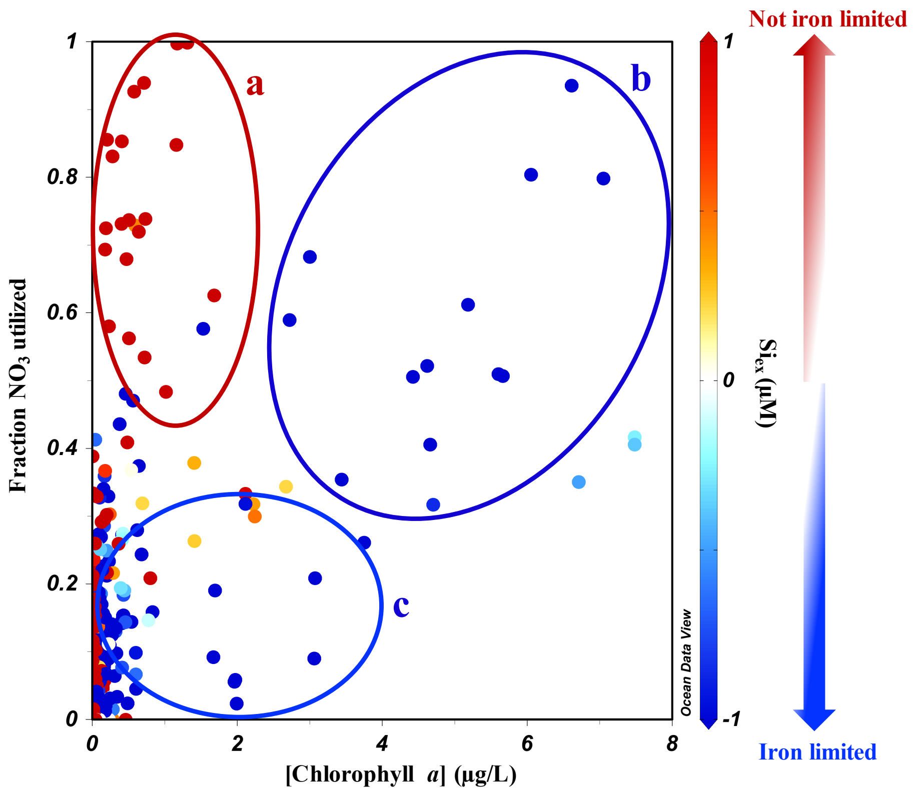

Figure 2.9. Iron limitation may influence NO_3^- utilization in the sCCS. A comparison of Chlorophyll *a* concentration, the fraction of NO_3^- utilized, and the proxy for diatom iron limitation Si_{ex} (color bar). Negative values of Si_{ex} indicate potential iron limitation (blue). Three different groups of data points, identifying different ecosystem conditions (iron replete: (**a**), and iron limited: (**b**) and (**c**)), were identified and discussed further in the text.

Any unutilized iron supplied from sediments or from external sources is oxidized or scavenged quickly unless chelated by iron-binding ligands (Gledhill and Buck 2012), and so, upwelled waters moving offshore can rapidly tend toward iron limitation. Indeed this has been previously demonstrated specifically for Point Conception (Firme et al. 2003; King et al. 2012). In regions with high NO_3^- utilization, high chlorophyll concentrations, and negative Si_{ex} values indicative of potential iron limitation (Figure 2.9b), we propose that developing iron limitation in offshore moving water masses may be responsible for the negative Si_{ex} values at stations 80.60, 80.70 and 80.80 (Figure 2.6a). Iron limitation offshore along the northern line has previously been identified in other studies (e.g. Brzezinski et al., 2015).

Finally, negative Si_{ex} values indicative of iron limitation were found to coincide with lower chlorophyll and lower NO_3^- utilization (as indicated by the $\delta^{15}N_{NO3}$) most often inshore, along the southern line (Figure 2.9c). At these locations, negative Si_{ex} values appeared deeper in the water column and under more stratified conditions (Figures 2.7 and S2.2). Subsurface, negative Si_{ex} values are consistent with previous studies that have identified subsurface chlorophyll maxima as important sites of iron limitation in the sCCS (Hopkinson and Barbeau 2008; Hogle et al. 2018). At these depths, diatoms experiencing light limitation may produce a greater number of photosystems (Strzepek et al. 2019), resulting in even greater iron requirements. Long-term records of CalCOFI Si_{ex} suggest that diatoms are becoming increasingly iron limited in the sCCS, consistent with a secular surface ocean warming trend and increased stratification leading to development of iron limitation at the base of the euphotic zone (Hogle et al. 2018). It is possible that this will result in a reapportionment of nutrients, and thus productivity, in the region, as unutilized NO_3^- may become available for export elsewhere.

Conclusions

The NO_3^- isotope data presented here reveal the sCCS to be a dynamic eastern boundary current system with a strong response to the 2015-2016 El Niño. Whether this response is typical of other El Niño events remains to be seen, especially because this particular event occurred during a pronounced marine heatwave: the North Pacific warm anomaly of 2014-2015 (Jacox et al. 2016; Di Lorenzo and Mantua 2016). The El Niño conditions of late 2015 and early 2016 resulted in reduced NO_3^- supply, leading to elevated NO_3^- isotopic compositions, greater percent utilization, and decreased primary production. This period of warm surface waters also resulted in greater stratification, which increased the relative reliance of the phytoplankton community on recycled NO_3^-. These trends may be expected to become increasingly relevant as surface oceans continue to warm. Our larger dataset also revealed significant variability in upper ocean NO_3^- isotopic composition tied to differences in the extent of euphotic zone NO_3^- utilization. The degree of utilization in the sCCS is likely influenced by iron limitation at southern, inshore stations (Line 93) and within the California Current along our northern line (Line 80), where progressive nutrient drawdown along upwelling filaments can result in both iron and NO_3^- limitation, but high biomass. Some inshore Line 80 stations also showed low NO_3^- utilization that was not tied to iron limitation but was likely driven by rapid Ekman transport of unused NO_3^- offshore and replacement with newly upwelled NO_3^-.

Acknowledgements

We thank the technicians and crew of the CalCOFI program, and Shonna Dovel in particular for sample collection. We are grateful to Zoe Sandwith and Jennifer Karolewski for help with NO_3^- isotope analyses and Yury Kiselev for help with data analysis. Additional thanks to Daniel Sigman and the Sigman Lab at Princeton University for assistance with sample analysis. Data sets presented here were supported in part by CCE-LTER augmented funding (NSF grant OCE-1026607). Additional funding came from the Edna Bailey Sussman Foundation and NSF grant OCE-1736656.

Additional acknowledgements

Chapter 2 has been recently submitted as “Stable isotopes of nitrate reveal effects of ENSO on nitrogen cycling in the surface waters of the southern California Current” to *Limnology and Oceanography*. Margot White, Patrick Rafter, Brandon Stephens, Matthew Mazloff, Scott Wankel, and Lihini Aluwihare. The dissertation author was the primary investigator and author of this paper.

Data availability

All data produced by the CalCOFI program are available at http://calcofi.org. Nitrate isotope data can be found at https://oceaninformatics.ucsd.edu/datazoo/catalogs/ccelter/datasets. Upwelling velocities and other model data are available at http://www.ecco.ucsd.edu/case.html.

References

Aksnes, D. L., and M. D. Ohman. 2009. Multi-decadal shoaling of the euphotic zone in the southern sector of the California Current System. Limnol. Oceanogr. **54**: 1272–1281. doi:10.4319/lo.2009.54.4.1272

Altabet, M. A. 2001. Nitrogen isotopic evidence for micronutrient control of fractional NO_3^- utilization in the equatorial Pacific. Limnol. Oceanogr. **46**: 368–380. doi:10.4319/lo.2001.46.2.0368

Altabet, M. A., and R. Francois. 1994. Sedimentary nitrogen isotopic ratio as a recorder for surface ocean nitrate utilization. Global Biogeochem. Cycles **8**: 103–116. doi:10.1029/93GB03396

Behrenfeld, M. J., R. T. O'Malley, D. A. Siegel, and others. 2006. Climate-driven trends in contemporary ocean productivity. Nature **444**. doi:10.1038/nature05317

Bograd, S. J., M. P. Buil, E. Di Lorenzo, and others. 2015. Changes in source waters to the Southern California Bight. Deep. Res. Part II Top. Stud. Oceanogr. **112**: 42–52. doi:10.1016/j.dsr2.2014.04.009

Bograd, S. J., I. D. Schroeder, and M. G. Jacox. 2019. A water mass history of the Southern California current system. Geophys. Res. Lett. **46**. doi:10.1029/2019GL082685

Brzezinski, M. A., J. W. Krause, R. M. Bundy, K. A. Barbeau, P. Franks, R. Goericke, M. R. Landry, and M. R. Stukel. 2015. Enhanced silica ballasting from iron stress sustains carbon export in a frontal zone within the California Current. J. Geophys. Res. Ocean. **120**: 4654–4669. doi:10.1002/2015JC010829

Buchwald, C., and K. L. Casciotti. 2010. Oxygen isotopic fractionation and exchange during bacterial nitrite oxidation. Limnol. Oceanogr. **55**: 1064–1074. doi:10.4319/lo.2010.55.3.1064

Casciotti, K. L. 2016. Nitrogen and Oxygen Isotopic Studies of the Marine Nitrogen Cycle. Ann. Rev. Mar. Sci. **8**: 379–407. doi:10.1146/annurev-marine-010213-135052

Casciotti, K. L., D. M. Sigman, M. G. Hastings, J. K. Böhlke, and A. Hilkert. 2002. Measurement of the oxygen isotopic composition of nitrate in seawater and freshwater using the denitrifier method. Anal. Chem. **74**: 4905–4912. doi:10.1021/ac020113w

Chan, F., J. A. Barth, J. Lubchenco, A. Kirincich, H. Weeks, W. T. Peterson, and B. A. Menge. 2008. Emergence of anoxia in the California current large marine ecosystem. Science **319**: 920. doi:10.1126/science.1149016

Closset, I., H. M. McNair, M. A. Brzezinski, J. W. Krause, K. Thamatrakoln, and J. L. Jones. 2021. Diatom response to alterations in upwelling and nutrient dynamics associated with climate forcing in the California Current System. Limnol. Oceanogr. lno.11705.

doi:10.1002/lno.11705

Davis, C. V., J. F. Ontiveros-Cuadras, C. Benitez-Nelson, A. Schmittner, E. J. Tappa, E. Osborne, and R. C. Thunell. 2019. Ongoing Increase in Eastern Tropical North Pacific Denitrification as Interpreted Through the Santa Barbara Basin Sedimentary δ15N Record. Paleoceanogr. Paleoclimatology **34**: 1554–1567. doi:10.1029/2019PA003578

Décima, M., M. R. Landry, and B. N. Popp. 2013. Environmental perturbation effects on baseline δ^{15}N values and zooplankton trophic flexibility in the southern California Current Ecosystem. Limnol. Oceanogr. **58**: 624–634. doi:10.4319/lo.2013.58.2.0624

Eppley, R. W., and B. J. Peterson. 1979. Particulate organic matter flux and planktonic new production in the deep ocean. Nature **282**: 677–680. doi:10.1038/282677a0

Eppley, R. W., J. H. Sharp, E. H. Renger, M. J. Perry, and W. G. Harrison. 1977. Nitrogen assimilation by phytoplankton and other microorganisms in the surface waters of the central North Pacific Ocean. Mar. Biol. **39**: 111–120. doi:10.1007/BF00386996

Firme, G. F., E. L. Rue, D. A. Weeks, K. W. Bruland, and D. A. Hutchins. 2003. Spatial and temporal variability in phytoplankton iron limitation along the California coast and consequences for Si, N, and C biogeochemistry. Global Biogeochem. Cycles **17**. doi:10.1029/2001GB001824

Frischknecht, M., M. Münnich, and N. Gruber. 2018. Origin, Transformation, and Fate: The Three-Dimensional Biological Pump in the California Current System. J. Geophys. Res. Ocean. **123**: 7939–7962. doi:10.1029/2018JC013934

Gledhill, M., and K. N. Buck. 2012. The organic complexation of iron in the marine environment: A review. Front. Microbiol. **3**: 69. doi:10.3389/fmicb.2012.00069

Granger, J., and D. M. Sigman. 2009. Removal of nitrite with sulfamic acid for nitrate N and O isotope analysis with the denitrifier method. Rapid Commun. Mass Spectrom. **23**: 3753–3762. doi:10.1002/rcm.4307

Granger, J., D. M. Sigman, J. A. Needoba, and P. J. Harrison. 2004. Coupled nitrogen and oxygen isotope fractionation of nitrate during assimilation by cultures of marine phytoplankton. Limnol. Oceanogr. **49**: 1763–1773. doi:10.4319/lo.2004.49.5.1763

Granger, J., and S. D. Wankel. 2016. Isotopic overprinting of nitrification on denitrification as a ubiquitous and unifying feature of environmental nitrogen cycling. Proc. Natl. Acad. Sci. U. S. A. **113**: E6391–E6400. doi:10.1073/pnas.1601383113

Hernández-de-la-Torre, B., G. Gaxiola-Castro, S. Alvarez-Borrego, J. Gómez-Valdés, and S. Nájera-Martínez. 2003. Interannual variability of new production in the southern region of the California Current. Deep. Res. Part II Top. Stud. Oceanogr. **50**: 2423–2430. doi:10.1016/S0967-0645(03)00129-2

Hogle, S. L., C. L. Dupont, B. M. Hopkinson, and others. 2018. Pervasive iron limitation at subsurface chlorophyll maxima of the California Current. Proc. Natl. Acad. Sci. U. S. A. **115**: 13300–13305. doi:10.1073/pnas.1813192115

Hopkinson, B. M., and K. A. Barbeau. 2008. Interactive influences of iron and light limitation on phytoplankton at subsurface chlorophyll maxima in the eastern North Pacific. Limnol. Oceanogr. **53**: 1303–1318. doi:10.4319/lo.2008.53.4.1303

Hutchins, D. A., and K. W. Bruland. 1998. Iron-limited diatom growth and Si:N uptake ratios in a coastal upwelling regime. Nature **393**: 561–564. doi:10.1038/31203

Jacox, M. G., J. Fiechter, A. M. Moore, and C. A. Edwards. 2015. ENSO and the California Current coastal upwelling response. J. Geophys. Res. Ocean. **120**: 1691–1702. doi:10.1002/2014JC010650

Jacox, M. G., E. L. Hazen, K. D. Zaba, D. L. Rudnick, C. A. Edwards, A. M. Moore, and S. J. Bograd. 2016. Impacts of the 2015-2016 El Niño on the California Current System: Early assessment and comparison to past events. Geophys. Res. Lett. **43**: 7072–7080. doi:10.1002/2016GL069716

Kahru, M., R. Kudela, M. Manzano-Sarabia, and B. G. Mitchell. 2009. Trends in primary production in the California Current detected with satellite data. J. Geophys. Res. Ocean. **114**. doi:10.1029/2008JC004979

Karsh, K. L., T. W. Trull, M. J. Lourey, and D. M. Sigman. 2003. Relationship of nitrogen isotope fractionation to phytoplankton size and iron availability during the Southern Ocean Iron RElease Experiment (SOIREE). Limnol. Oceanogr. **48**: 1058–1068. doi:10.4319/lo.2003.48.3.1058

Kelly, T. B., R. Goericke, M. Kahru, H. Song, and M. R. Stukel. 2018. CCE II: Spatial and interannual variability in export efficiency and the biological pump in an eastern boundary current upwelling system with substantial lateral advection. Deep. Res. Part I Oceanogr. Res. Pap. **140**: 14–25. doi:10.1016/j.dsr.2018.08.007

King, A. L., and K. Barbeau. 2007. Evidence for phytoplankton iron limitation in the southern California Current System. Mar. Ecol. Prog. Ser. **342**: 91–103. doi:10.3354/meps342091

King, A. L., and K. A. Barbeau. 2011. Dissolved iron and macronutrient distributions in the southern California Current System. J. Geophys. Res. **116**: C03018. doi:10.1029/2010JC006324

King, A. L., K. N. Buck, and K. A. Barbeau. 2012. Quasi-Lagrangian drifter studies of iron speciation and cycling off Point Conception, California. Mar. Chem. **128–129**: 1–12. doi:10.1016/j.marchem.2011.11.001

Kirchman, D. L., B. Meon, M. T. Cottrell, D. A. Hutchins, D. Weeks, and K. W. Bruland. 2000. Carbon versus iron limitation of bacterial growth in the California upwelling regime. Limnol. Oceanogr. **45**: 1681–1688. doi:10.4319/lo.2000.45.8.1681

Laperriere, S. M., M. Morando, D. G. Capone, T. Gunderson, J. M. Smith, and A. E. Santoro. 2020. Nitrification and nitrous oxide dynamics in the Southern California Bight. Limnol. Oceanogr. lno.11667. doi:10.1002/lno.11667

Lilly, L. E., U. Send, M. Lankhorst, T. R. Martz, R. A. Feely, A. J. Sutton, and M. D. Ohman. 2019. Biogeochemical Anomalies at Two Southern California Current System Moorings During the 2014–2016 Warm Anomaly-El Niño Sequence. J. Geophys. Res. Ocean. **124**: 6886–6903. doi:10.1029/2019JC015255

Di Lorenzo, E., and N. Mantua. 2016. Multi-year persistence of the 2014/15 North Pacific marine heatwave. Nat. Clim. Chang. **6**. doi:10.1038/nclimate3082

Mantyla, A. W., S. J. Bograd, and E. L. Venrick. 2007. Patterns and controls of chlorophyll-a and primary productivity cycles in the Southern California Bight.doi:10.1016/j.jmarsys.2007.08.001

McClatchie, S. 2014. Regional fisheries oceanography of the california current system: The CalCOFI program, Springer Netherlands.

McIlvin, M. R., and K. L. Casciotti. 2011. Technical Updates to the Bacterial Method for Nitrate Isotopic Analyses. Anal. Chem. **83**: 1850–1856. doi:10.1021/ac1028984

Nagarkar, M., M. Wang, B. Valencia, and B. Palenik. 2021. Spatial and temporal variations in *Synechococcus* microdiversity in the Southern California coastal ecosystem. Environ. Microbiol. **23**: 252–266. doi:10.1111/1462-2920.15307

Needoba, J., N. Waser, P. Harrison, and S. Calvert. 2003. Nitrogen isotope fractionation in 12 species of marine phytoplankton during growth on nitrate. Mar. Ecol. Prog. Ser. **255**: 81–91. doi:10.3354/meps255081

Newman, M., M. A. Alexander, T. R. Ault, and others. 2016. The Pacific decadal oscillation, revisited. J. Clim. **29**: 4399–4427. doi:10.1175/JCLI-D-15-0508.1

Ohman, M. D., G. H. Rau, and P. M. Hull. 2012. Multi-decadal variations in stable N isotopes of California Current zooplankton. Deep. Res. Part I Oceanogr. Res. Pap. **60**: 46–55. doi:10.1016/j.dsr.2011.11.003

Plattner, G.-K. 2005. Decoupling marine export production from new production. Geophys. Res. Lett. **32**: L11612. doi:10.1029/2005GL022660

Rau, G. H., M. D. Ohman, and A. Pierrot-Bults. 2003. Linking nitrogen dynamics to climate variability off central California: a 51 year record based on 15 N/ 14 N in CalCOFI zooplankton. Deep. Res. II **50**: 2431–2447. doi:10.1016/S0967-0645(03)00128-0

Shafiee, R. T., J. T. Snow, Q. Zhang, and R. E. M. Rickaby. 2019. Iron requirements and uptake strategies of the globally abundant marine ammonia-oxidising archaeon, Nitrosopumilus maritimus SCM1. ISME J. **13**: 2295–2305. doi:10.1038/s41396-019-0434-8

Sherrell, R. M., P. M. Field, and Y. Gao. 1998. Temporal variability of suspended mass and composition in the Northeast Pacific water column: Relationships to sinking flux and lateral advection. Deep. Res. Part II Top. Stud. Oceanogr. **45**: 733–761. doi:10.1016/S0967-0645(97)00100-8

Sigman, D. M., K. L. Casciotti, M. Andreani, C. Barford, M. Galanter, and J. K. Böhlke. 2001. A Bacterial Method for the Nitrogen Isotopic Analysis of Nitrate in Seawater and Freshwater. Anal. Chem. **73**: 4145–4153. doi:10.1021/ac010088e

Smith, J. M., F. P. Chavez, and C. A. Francis. 2014. Ammonium Uptake by Phytoplankton Regulates Nitrification in the Sunlit Ocean C. Lovejoy [ed.]. PLoS One **9**: e108173. doi:10.1371/journal.pone.0108173

Stephens, B. M., M. Porrachia, S. Dovel, M. Roadman, R. Goericke, and L. I. Aluwihare. 2018. Nonsinking Organic Matter Production in the California Current. Global Biogeochem. Cycles **32**: 1386–1405. doi:10.1029/2018GB005930

Stephens, B. M., S. D. Wankel, J. M. Beman, A. J. Rabines, A. E. Allen, and L. I. Aluwihare. 2019. Euphotic zone nitrification in the California Current Ecosystem. Limnol. Oceanogr. lno.11348. doi:10.1002/lno.11348

Strzepek, R. F., P. W. Boyd, and W. G. Sunda. 2019. Photosynthetic adaptation to low iron, light, and temperature in Southern Ocean phytoplankton. Proc. Natl. Acad. Sci. U. S. A. **116**: 4388–4393. doi:10.1073/pnas.1810886116

Stukel, M. R., and K. A. Barbeau. 2020. Investigating the Nutrient Landscape in a Coastal Upwelling Region and Its Relationship to the Biological Carbon Pump. Geophys. Res. Lett. **47**. doi:10.1029/2020GL087351

Stukel, M. R., M. R. Landry, C. R. Benitez-Nelson, and R. Goericke. 2011. Trophic cycling and carbon export relationships in the California current ecosystem. Limnol. Oceanogr. **56**: 1866–1878. doi:10.3354/meps010257

Tems, C. E., W. M. Berelson, and M. G. Prokopenko. 2015. Particulate ??15N in laminated marine sediments as a proxy for mixing between the California Undercurrent and the California Current: A proof of concept. Geophys. Res. Lett. **42**: 419–427. doi:10.1002/2014GL061993

Wankel, S. D., C. Kendall, J. T. Pennington, F. P. Chavez, and A. Paytan. 2007. Nitrification in the euphotic zone as evidenced by nitrate dual isotopic composition: Observations from

Monterey Bay, California. Global Biogeochem. Cycles **21**. doi:10.1029/2006GB002723

Zakem, E. J., A. Al-Haj, M. J. Church, and others. 2018. Ecological control of nitrite in the upper ocean. Nat. Commun. **9**: 1206. doi:10.1038/s41467-018-03553-w

Table S2.1. Dates and locations of nitrate isotope measurements from this study. Included in this study are all measurements from these locations above 150 m depth. Locations for each station can be seen on the map in Fig. 1 or found online at calcofi.org. Samples from 2010-2012 were measured by Patrick Rafter in Daniel Sigman's laboratory at Princeton University. Samples from 2013-2016 were measured in Scott Wankel's laboratory at Woods Hole Oceanographic Institution.

Cruise	Year	Season	Dates	Line 80.0 Stations	Line 93.3 Stations
1004	2010	Spring	11 Apr – 17 May	51-60	-
1011	2010	Fall	28 Oct - 15 Nov	51-100	-
1101	2011	Winter	12 Jan - 06 Feb	55-100	40-90
1104	2011	Spring	08 - 26 Apr	55-100	-
1108	2011	Summer	27 Jul - 13 Aug	55-100	-
1110	2011	Fall	16 Oct - 02 Nov	55-100	-
1202	2012	Winter	27 Jan - 13 Feb	55-70	-
1301	2013	Winter	10 Jan - 02 Feb	55-80	30-60
1304	2013	Spring	06 - 30 Apr	55-80	30-60
1307	2013	Summer	6 - 22 July	55-80	30-60
1511	2015	Fall	25 Oct - 13 Nov	55-80	30-60
1601	2016	Winter	06 - 30 Jan	55-80	30-60
1604	2016	Spring	01 - 23 Apr	55-60	30-60
1607	2016	Summer	10 - 27 July	55-80	30-60

Table S2.2. Estimated fractionation factors for nitrate uptake by phytoplankton. Fractionation factors could not be calculated for all profiles; thus, this table does not include all profiles for which we have isotope data. The average ***ε*** was 3.3 ± 0.8 ‰ for all profiles and slightly lower, 3.2 ± 0.8 ‰ when looking only at closed system results.

Station	Cruise	EZ Depth (m)	n	Open ***ε***	Open r^2	Closed ***ε***	Closed r^2	Rayleigh Model	Best fit ***ε***
080.0 051.0	1004	30	5	3.7	0.86	2.4	0.9278	closed	2.4
080.0 055.0	1004	75	5	2.9	0.97	2.7	0.9648	open	2.9
080.0 055.0	1011	75	7	3.9	0.92	1.7	0.9158	open	3.9
080.0 055.0	1101	50	5	3.9	0.97	2.3	0.994	closed	2.3
080.0 055.0	1104	40	5	4.3	0.99	3.6	0.9933	closed	3.6
080.0 055.0	1108	60	7	7.1	0.73	2.5	0.8823	closed	2.5
080.0 055.0	1301	60	4	7.5	0.96	5.0	0.9852	closed	5.0
080.0 055.0	1511	52	3	4.9	0.88	2.9	0.9676	closed	2.9
080.0 055.0	1601	70	5	7.9	0.91	4.2	0.959	closed	4.2
080.0 060.0	1104	30	6	4.7	0.99	3.7	0.99	open	4.7
093.3 030.0	1511	87	3	3.7	0.80	2.1	0.9316	closed	2.1
093.3 030.0	1604	50	3	8.9	0.90	3.6	0.9898	closed	3.6
093.3 030.0	1607	50	3	4.7	0.93	3.5	0.9599	closed	3.5
093.3 040.0	1304	50	3	10.4	0.85	4.1	0.9562	closed	4.1
093.3 040.0	1307	61	4	3.9	0.85	1.9	0.6965	open	3.9
093.3 040.0	1604	86	3	4.3	0.73	2.7	0.8702	closed	2.7
093.3 050.0	1304	70	3	6.3	0.88	3.0	0.969	closed	3.0
093.3 050.0	1307	70	3	5.0	0.98	2.8	0.9936	closed	2.8
093.3 050.0	1511	87	3	3.8	0.97	2.8	0.9936	closed	2.8
093.3 050.0	1601	86	3	2.8	0.99	1.6	0.96	open	2.8
093.3 050.0	1604	70	3	7.4	0.98	3.9	0.99	closed	3.9

Table S2.3. Characteristics of upwelling water. This table shows the depth, density, nitrate concentration, and nitrate isotope signature of upwelling water used for the analyses presented here.

Station	Cruise	Depth (m)	STheta	[NO_3] (uM)	$\delta^{15}N$ (‰)	$\delta^{18}O$ (‰)
080.0 055.0	1004	100	26.102	25.4	8.00	3.71
080.0 060.0	1004	75	25.799	20.3	8.45	3.99
080.0 055.0	1011	100	26.087	26.1	7.98	3.06
080.0 060.0	1011	71	25.783	21.5	7.94	3.66
080.0 070.0	1011	85	26.226	27.8	8.41	4.07
080.0 080.0	1011	120	26.224	25.6	7.33	2.77
080.0 055.0	1101	85	26.129	25.8	8.30	3.80
080.0 060.0	1101	60	25.707	18.1	8.51	3.87
080.0 070.0	1101	85	25.814	22	7.68	2.88
080.0 080.0	1101	85	25.885	22.3	7.72	2.95
093.3 040.0	1101	100	25.82	20.7	8.11	3.37
093.3 050.0	1101	86	26.002	23.8	8.11	3.63
093.3 060.0	1101	100	25.897	22.4	7.97	3.18
093.3 070.0	1101	120	25.699	18.2	8.05	3.28
080.0 055.0	1104	60	26.129	25.4	8.33	4.17
080.0 060.0	1104	60	25.802	17.8	8.73	4.47
080.0 070.0	1104	85	25.967	22.1	8.02	3.82
080.0 080.0	1104	140	25.986	22.5	7.72	3.20
080.0 055.0	1108	120	26.236	27	8.21	3.86
080.0 060.0	1108	70	25.895	24	7.87	3.29
080.0 070.0	1108	120	26.182	27	7.64	3.03
080.0 080.0	1108	100	25.631	16.4	7.80	3.10
080.0 055.0	1110	120	26.093	24.9	8.02	3.59
080.0 060.0	1110	110	26.057	25.5	7.96	3.26
080.0 070.0	1110	140	25.992	21.5	7.53	2.94
080.0 080.0	1110	140	26.114	24.7	7.84	3.18
080.0 055.0	1202	120	26.126	25.7	7.94	3.20
080.0 060.0	1202	87	26.083	25.1	7.93	3.41
080.0 070.0	1202	140	25.986	21.6	7.43	2.87
080.0 080.0	1202	141	26.11	25.5	7.81	3.39
080.0 055.0	1301	84	26.0088	23.3	7.92	4.52
080.0 060.0	1301	120	26.029	23.3	7.99	4.23
080.0 070.0	1301	100	25.857	20.4	8.20	3.81
080.0 080.0	1301	139	26.095	22.4	7.84	4.02
093.3 030.0	1301	84	25.7337	18.1	8.81	3.94

093.3 050.0	1301	120	25.8141	18.3	8.16	3.88
093.3 060.0	1301	120	25.7081	15.6	8.53	3.93
080.0 055.0	1304	100	26.2646	26.3	8.22	4.66
080.0 060.0	1304	119	26.22525	25.3	8.09	3.80
080.0 070.0	1304	140	26.22098	25.2	7.93	3.88
093.3 030.0	1304	75	25.99776	23.1	8.81	4.64
093.3 040.0	1304	118	26.18654	25.2	9.42	5.30
093.3 050.0	1304	85	25.71972	16.8	8.47	3.35
093.3 060.0	1304	141	26.09072	23.5	8.62	3.80
080.0 055.0	1307	30	25.72118	18.6	8.67	4.90
080.0 060.0	1307	60	26.02079	23.1	7.65	3.18
080.0 070.0	1307	140	26.33463	28.9	8.25	4.67
080.0 080.0	1307	140	26.20945	27.5	7.98	4.05
093.3 030.0	1307	100	26.0464	24.1	9.51	4.85
093.3 040.0	1307	120	26.0332	21.8	8.23	3.66
093.3 050.0	1307	86	25.87227	20.7	8.51	3.78
093.3 060.0	1307	85	25.96297	22.4	7.68	3.30
080.0 055.0	1511	120	25.91232	20.58	8.78	4.62
080.0 060.0	1511	86	25.43757	13.26	9.55	5.28
080.0 070.0	1511	100	25.94812	21.69	8.67	4.52
080.0 080.0	1511	125	26.06965	23.5	8.69	3.78
093.3 030.0	1511	100	25.35411	12	10.52	4.89
093.3 040.0	1511	86	25.24222	9.8	8.62	3.70
093.3 050.0	1511	125	25.85791	19.42	8.32	3.77
093.3 060.0	1511	140	25.95753	20.61	8.49	3.60
080.0 055.0	1601	86	25.51694	15.01	8.60	4.30
080.0 060.0	1601	86	25.24526	10.05	9.18	4.44
080.0 080.0	1601	125	25.63499	17.09	7.98	3.93
093.3 030.0	1601	86	25.27975	11.78	9.46	4.66
093.3 040.0	1601	122	25.48657	15.5	9.74	5.24
093.3 050.0	1601	124	25.94343	19.82	9.97	5.47
093.3 060.0	1601	143	25.84862	19.99	8.36	3.86
080.0 055.0	1604	60	25.84335	18.94	8.81	4.88
080.0 060.0	1604	101	25.87056	20.91	8.35	4.19
093.3 030.0	1604	86	25.68145	18.19	9.09	3.92
093.3 040.0	1604	120	25.90811	20.13	8.39	4.42
093.3 050.0	1604	86	25.46248	14.26	8.93	4.59
093.3 060.0	1604	141	26.04172	23.88	8.57	5.57
080.0 055.0	1607	60	25.94931	22.52	8.59	4.46

080.0 060.0	1607	101	26.13377	25.41	8.10	4.71
080.0 080.0	1607	121	25.4062	11.89	7.51	4.07
093.3 030.0	1607	84	25.89854	20.74	8.43	4.11
093.3 040.0	1607	50	25.6537	18.51	8.65	4.20
093.3 050.0	1607	60	25.90622	22.06	8.43	4.83
093.3 060.0	1607	141	26.2401	26.29	8.62	4.80

Table S2.4. Stratification and densities for all depths with isotope measurements. Stratification was calculated by subtracting the density at each relevant depth from the density at 200 m at that station (Behrenfeld et al. 2006).

Station	Cruise	Depth (m)	Temperature (˚C)	Salinity (psu)	STheta	STheta at 200 m	Stratification Index
080.0 055.0	1004	0	10.82	33.698	25.794	26.516	0.722
080.0 055.0	1004	15	10.44	33.667	25.837	26.516	0.679
080.0 055.0	1004	30	10.39	33.685	25.860	26.516	0.656
080.0 055.0	1004	45	10.42	33.704	25.870	26.516	0.646
080.0 055.0	1004	60	10.34	33.727	25.902	26.516	0.614
080.0 055.0	1004	75	10.23	33.815	25.990	26.516	0.526
080.0 060.0	1004	57	10.27	33.36	25.627	26.521	0.894
080.0 060.0	1004	75	10.48	33.626	25.799	26.521	0.722
080.0 055.0	1011	50	11.11	33.262	25.404	26.425	1.021
080.0 055.0	1011	60	10.09	33.471	25.745	26.425	0.680
080.0 055.0	1011	70	9.73	33.567	25.880	26.425	0.545
080.0 055.0	1011	85	9.61	33.6	25.926	26.425	0.499
080.0 060.0	1011	50	11.41	33.4	25.457	26.524	1.067
080.0 060.0	1011	60	10.57	33.474	25.665	26.524	0.859
080.0 060.0	1011	71	10.2	33.544	25.783	26.524	0.741
080.0 060.0	1011	85	9.75	33.715	25.992	26.524	0.532
080.0 070.0	1011	30	11.22	33.442	25.524	26.502	0.978
080.0 070.0	1011	37	10.31	33.475	25.710	26.502	0.792
080.0 070.0	1011	45	10.04	33.586	25.842	26.502	0.660
080.0 070.0	1011	52	10	33.689	25.930	26.502	0.572
080.0 070.0	1011	60	9.85	33.772	26.020	26.502	0.482
080.0 070.0	1011	70	9.67	33.879	26.134	26.502	0.368
080.0 070.0	1011	85	9.53	33.968	26.226	26.502	0.276

080.0 080.0	1011	40	12.03	33.256	25.231	26.521	1.290
080.0 080.0	1011	50	11.34	33.269	25.368	26.521	1.153
080.0 080.0	1011	60	10.05	33.216	25.552	26.521	0.969
080.0 080.0	1011	70	9.65	33.345	25.719	26.521	0.802
080.0 080.0	1011	84	9.26	33.523	25.922	26.521	0.599
080.0 090.0	1011	72	10.68	33.07	25.331	26.473	1.142
080.0 090.0	1011	86	10.36	33.153	25.451	26.473	1.022
080.0 055.0	1101	50	10.82	33.61	25.727	26.442	0.715
080.0 055.0	1101	59	10.18	33.724	25.927	26.442	0.515
080.0 055.0	1101	71	9.84	33.787	26.033	26.442	0.409
080.0 055.0	1101	85	9.64	33.866	26.129	26.442	0.313
080.0 060.0	1101	50	11.58	33.513	25.514	26.558	1.044
080.0 060.0	1101	60	10.89	33.6	25.707	26.558	0.851
080.0 060.0	1101	70	10.01	33.772	25.993	26.558	0.565
080.0 060.0	1101	85	9.69	33.836	26.097	26.558	0.461
080.0 070.0	1101	70	10.85	33.333	25.506	26.526	1.020
080.0 070.0	1101	85	9.77	33.491	25.814	26.526	0.712
080.0 080.0	1101	61	11.02	33.133	25.320	26.512	1.192
080.0 080.0	1101	70	9.87	33.181	25.555	26.512	0.957
080.0 080.0	1101	85	9.63	33.552	25.885	26.512	0.627
080.0 090.0	1101	69	10.16	33.189	25.513	26.472	0.959
080.0 090.0	1101	85	9.73	33.392	25.743	26.472	0.729
093.3 040.0	1101	50	12.99	33.301	25.081	26.468	1.387
093.3 040.0	1101	60	12.15	33.287	25.233	26.468	1.235
093.3 040.0	1101	70	10.83	33.313	25.494	26.468	0.974
093.3 040.0	1101	85	10.33	33.388	25.640	26.468	0.828
093.3 050.0	1101	30	12.55	33.392	25.237	26.550	1.313
093.3 050.0	1101	40	11.79	33.434	25.414	26.550	1.136
093.3 050.0	1101	50	11.4	33.459	25.505	26.550	1.045
093.3 050.0	1101	61	10.7	33.531	25.686	26.550	0.864
093.3 050.0	1101	70	10.32	33.585	25.795	26.550	0.755
093.3 050.0	1101	86	9.77	33.732	26.002	26.550	0.548
093.3 060.0	1101	50	12.2	33.34	25.264	26.506	1.242
093.3 060.0	1101	69	11.11	33.431	25.536	26.506	0.970
093.3 060.0	1101	85	10.13	33.569	25.815	26.506	0.691
080.0 055.0	1104	2	11.06	33.721	25.769	26.538	0.769
080.0 055.0	1104	10	11.06	33.721	25.770	26.538	0.768
080.0 055.0	1104	20	11.01	33.722	25.780	26.538	0.758
080.0 055.0	1104	30	10.73	33.725	25.832	26.538	0.706

080.0 055.0	1104	40	10.29	33.717	25.902	26.538	0.636
080.0 055.0	1104	50	9.9	33.79	26.025	26.538	0.513
080.0 055.0	1104	60	9.61	33.861	26.129	26.538	0.409
080.0 055.0	1104	70	9.31	33.985	26.275	26.538	0.263
080.0 055.0	1104	85	9.23	34.014	26.311	26.538	0.227
080.0 060.0	1104	2	11.8	33.498	25.461	26.527	1.066
080.0 060.0	1104	5	11.7	33.502	25.482	26.527	1.045
080.0 060.0	1104	8	11.56	33.513	25.517	26.527	1.010
080.0 060.0	1104	14	11.44	33.542	25.562	26.527	0.965
080.0 060.0	1104	25	11.45	33.581	25.590	26.527	0.937
080.0 060.0	1104	30	11.32	33.595	25.625	26.527	0.902
080.0 060.0	1104	40	11.04	33.619	25.694	26.527	0.833
080.0 060.0	1104	50	10.85	33.649	25.752	26.527	0.775
080.0 060.0	1104	60	10.71	33.682	25.802	26.527	0.725
080.0 060.0	1104	70	10.27	33.718	25.907	26.527	0.620
080.0 060.0	1104	85	9.49	33.752	26.064	26.527	0.463
080.0 070.0	1104	20	12.43	33.443	25.299	26.505	1.206
080.0 070.0	1104	31	11.15	33.488	25.573	26.505	0.932
080.0 070.0	1104	41	10.82	33.531	25.665	26.505	0.840
080.0 070.0	1104	51	10.63	33.604	25.755	26.505	0.750
080.0 070.0	1104	61	10.58	33.634	25.788	26.505	0.717
080.0 070.0	1104	70	10.57	33.637	25.792	26.505	0.713
080.0 070.0	1104	85	9.9	33.714	25.967	26.505	0.538
080.0 090.0	1104	85	10.35	33.097	25.409	26.430	1.021
080.0 055.0	1108	40	12.93	33.519	25.261	26.456	1.195
080.0 055.0	1108	51	11.3	33.432	25.502	26.456	0.954
080.0 055.0	1108	60	10.53	33.463	25.663	26.456	0.793
080.0 055.0	1108	70	10.04	33.692	25.926	26.456	0.530
080.0 055.0	1108	84	9.9	33.75	25.995	26.456	0.461
080.0 055.0	1108	99	9.72	33.786	26.053	26.456	0.403
080.0 060.0	1108	40	12.86	33.566	25.311	26.554	1.243
080.0 060.0	1108	50	11.75	33.608	25.557	26.554	0.997
080.0 060.0	1108	60	10.77	33.686	25.795	26.554	0.759
080.0 060.0	1108	70	10.35	33.72	25.895	26.554	0.659
080.0 060.0	1108	86	9.49	33.786	26.091	26.554	0.463
080.0 070.0	1108	70	11.02	33.137	25.323	26.493	1.170
080.0 070.0	1108	85	9.88	33.414	25.736	26.493	0.757
080.0 055.0	1110	40	14.79	33.406	24.791	26.452	1.661
080.0 055.0	1110	51	13.33	33.383	25.077	26.452	1.375

080.0 055.0	1110	60	12.37	33.335	25.228	26.452	1.224
080.0 055.0	1110	70	11.07	33.473	25.576	26.452	0.876
080.0 055.0	1110	85	10.25	33.534	25.767	26.452	0.685
080.0 055.0	1110	99	9.97	33.65	25.905	26.452	0.547
080.0 060.0	1110	69	11.44	33.338	25.404	26.437	1.033
080.0 060.0	1110	77	10.68	33.411	25.597	26.437	0.840
080.0 060.0	1110	84	10.2	33.52	25.765	26.437	0.672
080.0 060.0	1110	94	9.5	33.572	25.922	26.437	0.515
080.0 080.0	1110	69	12.17	33.277	25.221	26.429	1.208
080.0 080.0	1110	85	11.59	33.311	25.356	26.429	1.073
080.0 090.0	1110	50	12.99	33.412	25.167	26.510	1.343
080.0 090.0	1110	60	12.02	33.37	25.322	26.510	1.188
080.0 090.0	1110	70	10.91	33.478	25.608	26.510	0.902
080.0 090.0	1110	85	9.64	33.596	25.918	26.510	0.592
080.0 100.0	1110	86	10.45	33.458	25.673	26.465	0.792
080.0 055.0	1202	50	11.01	33.54	25.638	26.449	0.811
080.0 055.0	1202	60	10.64	33.575	25.731	26.449	0.718
080.0 055.0	1202	70	10.4	33.605	25.796	26.449	0.653
080.0 055.0	1202	85	9.95	33.677	25.929	26.449	0.520
080.0 060.0	1202	50	11.89	33.448	25.406	26.519	1.113
080.0 060.0	1202	62	10.59	33.58	25.744	26.519	0.775
080.0 060.0	1202	74	9.79	33.692	25.968	26.519	0.551
080.0 060.0	1202	87	9.54	33.787	26.083	26.519	0.436
080.0 080.0	1202	86	11.2	33.203	25.343	26.412	1.069
080.0 090.0	1202	85	11.16	33.345	25.461	26.413	0.952
080.0 100.0	1202	85	11.17	33.168	25.321	26.381	1.060
080.0 055.0	1301	30	11.693	33.379	25.389	26.400	1.011
080.0 055.0	1301	41	10.362	33.4188	25.658	26.400	0.742
080.0 055.0	1301	50	10.287	33.4742	25.713	26.400	0.687
080.0 055.0	1301	60	10.073	33.5329	25.797	26.400	0.603
080.0 055.0	1301	70	9.794	33.6058	25.901	26.400	0.499
080.0 055.0	1301	84	9.585	33.6993	26.009	26.400	0.391
080.0 060.0	1301	60	12.014	33.3371	25.299	26.394	1.095
080.0 060.0	1301	70	11.301	33.3791	25.463	26.394	0.931
080.0 060.0	1301	85	10.591	33.5282	25.706	26.394	0.688
080.0 080.0	1301	85	10.706	33.4432	25.619	26.424	0.804
093.3 030.0	1301	40	13.751	33.5078	25.089	26.418	1.330
093.3 030.0	1301	50	11.853	33.3982	25.376	26.418	1.042
093.3 030.0	1301	60	11.529	33.4082	25.444	26.418	0.974

093.3 030.0	1301	70	11.3	33.5242	25.576	26.418	0.842
093.3 030.0	1301	84	10.85	33.6226	25.734	26.418	0.684
093.3 040.0	1301	30	14.596	33.5143	24.916	26.458	1.541
093.3 040.0	1301	40	14.585	33.5077	24.914	26.458	1.544
093.3 040.0	1301	50	14.46	33.4956	24.932	26.458	1.526
093.3 040.0	1301	60	12.191	33.4002	25.314	26.458	1.144
093.3 040.0	1301	70	11.65	33.4861	25.483	26.458	0.975
093.3 040.0	1301	86	10.861	33.4896	25.628	26.458	0.830
093.3 050.0	1301	62	13.911	33.4922	25.045	26.485	1.440
093.3 050.0	1301	70	13.471	33.4654	25.114	26.485	1.371
093.3 050.0	1301	86	12.379	33.4368	25.308	26.485	1.177
093.3 060.0	1301	85	11.626	33.1586	25.233	26.388	1.155
080.0 055.0	1304	30	11.66	33.5599	25.536	26.561	1.025
080.0 055.0	1304	31	11.561	33.5653	25.559	26.561	1.003
080.0 055.0	1304	50	10.786	33.7103	25.812	26.561	0.749
080.0 055.0	1304	60	10.424	33.7322	25.892	26.561	0.669
080.0 055.0	1304	70	9.964	33.774	26.004	26.561	0.558
080.0 055.0	1304	86	9.218	33.8537	26.189	26.561	0.372
080.0 060.0	1304	62	11.407	33.5698	25.592	26.535	0.943
080.0 060.0	1304	75	10.163	33.5772	25.817	26.535	0.718
080.0 060.0	1304	85	10.251	33.6846	25.886	26.535	0.649
080.0 060.0	1304	99	9.485	33.6783	26.009	26.535	0.526
080.0 080.0	1304	60	13.12	33.216	24.991	26.387	1.396
093.3 030.0	1304	30	12.548	33.544	25.356	26.513	1.157
093.3 030.0	1304	41	11.586	33.5627	25.552	26.513	0.960
093.3 030.0	1304	50	11.157	33.6057	25.664	26.513	0.848
093.3 030.0	1304	60	10.638	33.6953	25.827	26.513	0.686
093.3 030.0	1304	70	10.278	33.7765	25.953	26.513	0.560
093.3 030.0	1304	75	10.245	33.827	25.998	26.513	0.515
093.3 030.0	1304	85	10.086	33.874	26.062	26.513	0.451
093.3 040.0	1304	30	13.088	33.4736	25.195	26.518	1.323
093.3 040.0	1304	39	12.465	33.4936	25.333	26.518	1.185
093.3 040.0	1304	50	11.857	33.4957	25.451	26.518	1.068
093.3 040.0	1304	58	10.954	33.5399	25.650	26.518	0.869
093.3 040.0	1304	68	10.777	33.5555	25.694	26.518	0.825
093.3 040.0	1304	84	10.39	33.6482	25.834	26.518	0.685
093.3 050.0	1304	50	13.079	33.4326	25.166	26.477	1.311
093.3 050.0	1304	59	11.932	33.4334	25.389	26.477	1.088
093.3 050.0	1304	70	10.757	33.516	25.666	26.477	0.811

093.3 050.0	1304	85	10.547	33.5366	25.720	26.477	0.757
093.3 060.0	1304	85	12.435	33.3396	25.222	26.404	1.182
080.0 055.0	1307	30	11.1	33.6667	25.721	26.432	0.711
080.0 055.0	1307	41	10.363	33.7189	25.892	26.432	0.540
080.0 055.0	1307	50	10.287	33.7235	25.909	26.432	0.523
080.0 055.0	1307	60	9.838	33.7953	26.041	26.432	0.391
080.0 055.0	1307	70	9.756	33.8469	26.095	26.432	0.337
080.0 055.0	1307	86	9.544	33.9184	26.187	26.432	0.245
080.0 060.0	1307	60	9.56	33.7105	26.021	26.583	0.562
080.0 060.0	1307	70	9.427	33.7583	26.080	26.583	0.503
080.0 060.0	1307	85	9.28	33.8557	26.181	26.583	0.402
080.0 080.0	1307	85	11.48	33.3354	25.397	26.476	1.079
093.3 030.0	1307	30	12.792	33.5025	25.276	26.443	1.167
093.3 030.0	1307	40	12.516	33.5539	25.370	26.443	1.073
093.3 030.0	1307	50	11.45	33.5176	25.543	26.443	0.901
093.3 030.0	1307	60	10.743	33.5221	25.673	26.443	0.770
093.3 030.0	1307	70	10.347	33.5531	25.766	26.443	0.677
093.3 030.0	1307	86	10.162	33.7545	25.956	26.443	0.488
093.3 040.0	1307	30	14.639	33.5515	24.936	26.466	1.531
093.3 040.0	1307	42	13.521	33.5258	25.149	26.466	1.317
093.3 040.0	1307	50	13.034	33.518	25.241	26.466	1.225
093.3 040.0	1307	61	12.224	33.4879	25.376	26.466	1.091
093.3 040.0	1307	71	11.453	33.4842	25.517	26.466	0.949
093.3 040.0	1307	86	10.945	33.5054	25.626	26.466	0.841
093.3 050.0	1307	50	12.485	33.4868	25.325	26.535	1.210
093.3 050.0	1307	60	11.886	33.533	25.475	26.535	1.060
093.3 050.0	1307	70	11.21	33.5327	25.599	26.535	0.936
093.3 050.0	1307	86	10.078	33.6293	25.872	26.535	0.663
093.3 060.0	1307	85	9.836	33.6936	25.963	26.534	0.571
080.0 055.0	1511	32	14.552	33.2964	24.758	26.343	1.586
080.0 055.0	1511	42	12.797	33.3377	25.148	26.343	1.195
080.0 055.0	1511	52	11.688	33.4291	25.430	26.343	0.913
080.0 055.0	1511	62	11.37	33.4821	25.530	26.343	0.813
080.0 055.0	1511	70	11.279	33.4941	25.556	26.343	0.787
080.0 055.0	1511	85	10.845	33.5365	25.668	26.343	0.676
080.0 060.0	1511	60	12.807	33.3278	25.139	26.356	1.216
080.0 060.0	1511	70	12.111	33.3507	25.291	26.356	1.064
080.0 060.0	1511	86	11.591	33.4134	25.438	26.356	0.918
080.0 080.0	1511	62	11.948	33.2187	25.219	26.391	1.172

080.0 080.0	1511	87	10.237	33.2757	25.570	26.391	0.821
093.3 030.0	1511	62	15.387	33.374	24.639	26.122	1.483
093.3 030.0	1511	75	14.6	33.4857	24.896	26.122	1.226
093.3 030.0	1511	87	13.387	33.521	25.175	26.122	0.947
093.3 040.0	1511	60	14.55	33.289	24.754	26.297	1.543
093.3 040.0	1511	70	13.795	33.3126	24.930	26.297	1.367
093.3 040.0	1511	86	12.049	33.2714	25.242	26.297	1.055
093.3 050.0	1511	50	14.705	33.1254	24.594	26.340	1.745
093.3 050.0	1511	62	12.924	33.1574	24.985	26.340	1.355
093.3 050.0	1511	75	12.058	33.1436	25.141	26.340	1.199
093.3 050.0	1511	87	11.39	33.2076	25.314	26.340	1.025
093.3 060.0	1511	53	14.222	33.1304	24.700	26.402	1.702
093.3 060.0	1511	89	11.308	33.3456	25.437	26.402	0.966
080.0 055.0	1601	30	14.194	33.5047	24.994	26.358	1.364
080.0 055.0	1601	40	14.009	33.493	25.024	26.358	1.334
080.0 055.0	1601	50	13.851	33.4981	25.061	26.358	1.297
080.0 055.0	1601	60	13.305	33.4847	25.162	26.358	1.196
080.0 055.0	1601	70	12.658	33.4689	25.278	26.358	1.079
080.0 055.0	1601	86	10.457	33.2565	25.517	26.358	0.841
080.0 060.0	1601	60	14.224	33.4134	24.919	26.361	1.443
080.0 060.0	1601	71	14.099	33.4414	24.967	26.361	1.394
080.0 060.0	1601	86	12.617	33.415	25.245	26.361	1.116
080.0 080.0	1601	87	13.666	33.1167	24.806	26.289	1.482
093.3 030.0	1601	60	15.341	33.4489	24.707	26.311	1.604
093.3 030.0	1601	71	13.11	33.225	25.001	26.311	1.310
093.3 030.0	1601	86	12.745	33.4916	25.280	26.311	1.031
093.3 040.0	1601	69	16.664	33.6888	24.593	26.105	1.512
093.3 040.0	1601	85	15.434	33.6712	24.859	26.105	1.246
093.3 050.0	1601	61	14.846	33.4995	24.853	26.322	1.469
093.3 050.0	1601	69	13.824	33.4411	25.024	26.322	1.298
093.3 050.0	1601	86	11.931	33.4405	25.396	26.322	0.926
080.0 055.0	1604	41	11.486	33.4	25.444	26.436	0.992
080.0 055.0	1604	51	11.142	33.6403	25.694	26.436	0.742
080.0 055.0	1604	60	10.72	33.7353	25.843	26.436	0.593
080.0 055.0	1604	70	10.472	33.8207	25.954	26.436	0.483
080.0 055.0	1604	86	10.297	33.8692	26.022	26.436	0.414
080.0 060.0	1604	62	12.733	33.3472	25.169	26.421	1.252
080.0 060.0	1604	72	11.272	33.3607	25.454	26.421	0.967
080.0 060.0	1604	86	10.386	33.441	25.673	26.421	0.748

093.3 030.0	1604	30	14.24	33.3875	24.894	26.432	1.538
093.3 030.0	1604	40	14.054	33.4758	25.001	26.432	1.430
093.3 030.0	1604	50	13.301	33.4928	25.169	26.432	1.263
093.3 030.0	1604	61	12.641	33.5076	25.311	26.432	1.121
093.3 030.0	1604	70	11.98	33.5428	25.465	26.432	0.967
093.3 030.0	1604	86	10.941	33.5761	25.681	26.432	0.750
093.3 040.0	1604	61	13.919	33.3553	24.937	26.347	1.410
093.3 040.0	1604	70	12.973	33.3161	25.098	26.347	1.249
093.3 040.0	1604	86	11.23	33.3104	25.423	26.347	0.924
093.3 050.0	1604	50	13.686	33.4554	25.062	26.459	1.397
093.3 050.0	1604	60	13.345	33.4556	25.132	26.459	1.327
093.3 050.0	1604	70	12.699	33.4728	25.273	26.459	1.186
093.3 050.0	1604	86	11.424	33.4062	25.462	26.459	0.996
093.3 060.0	1604	88	11.654	33.4086	25.422	26.400	0.978
080.0 055.0	1607	29	11.096	33.6102	25.678	26.451	0.773
080.0 055.0	1607	35	10.746	33.6253	25.752	26.451	0.699
080.0 055.0	1607	42	10.495	33.6417	25.809	26.451	0.642
080.0 055.0	1607	60	10.047	33.7226	25.949	26.451	0.502
080.0 055.0	1607	70	9.991	33.7921	26.013	26.451	0.438
080.0 055.0	1607	84	9.822	33.8289	26.071	26.451	0.380
080.0 060.0	1607	60	10.858	33.5978	25.712	26.535	0.823
080.0 060.0	1607	71	10.003	33.6471	25.898	26.535	0.637
080.0 060.0	1607	86	9.752	33.7301	26.005	26.535	0.529
080.0 080.0	1607	88	13.158	32.962	24.789	26.296	1.507
093.3 030.0	1607	29	12.482	33.4439	25.291	26.370	1.079
093.3 030.0	1607	40	11.741	33.4349	25.424	26.370	0.945
093.3 030.0	1607	50	11.159	33.495	25.578	26.370	0.792
093.3 030.0	1607	59	10.702	33.5277	25.685	26.370	0.685
093.3 030.0	1607	70	10.499	33.5497	25.738	26.370	0.632
093.3 030.0	1607	84	10.011	33.6486	25.899	26.370	0.471
093.3 040.0	1607	30	12.47	33.4176	25.273	26.568	1.295
093.3 040.0	1607	40	11.805	33.4821	25.449	26.568	1.119
093.3 040.0	1607	50	10.855	33.5229	25.654	26.568	0.914
093.3 040.0	1607	60	10.465	33.6384	25.812	26.568	0.756
093.3 040.0	1607	70	10.06	33.6861	25.919	26.568	0.649
093.3 040.0	1607	84	9.68	33.7955	26.068	26.568	0.499
093.3 050.0	1607	31	12.608	33.5524	25.351	26.552	1.201
093.3 050.0	1607	41	11.348	33.5985	25.624	26.552	0.928
093.3 050.0	1607	50	10.89	33.6562	25.751	26.552	0.801

093.3 050.0	1607	60	10.205	33.7017	25.906	26.552	0.646
093.3 050.0	1607	68	9.94	33.7393	25.981	26.552	0.571
093.3 050.0	1607	86	9.551	33.8627	26.142	26.552	0.410
093.3 060.0	1607	51	11.789	33.2678	25.286	26.484	1.198
093.3 060.0	1607	85	10.235	33.5834	25.810	26.484	0.674

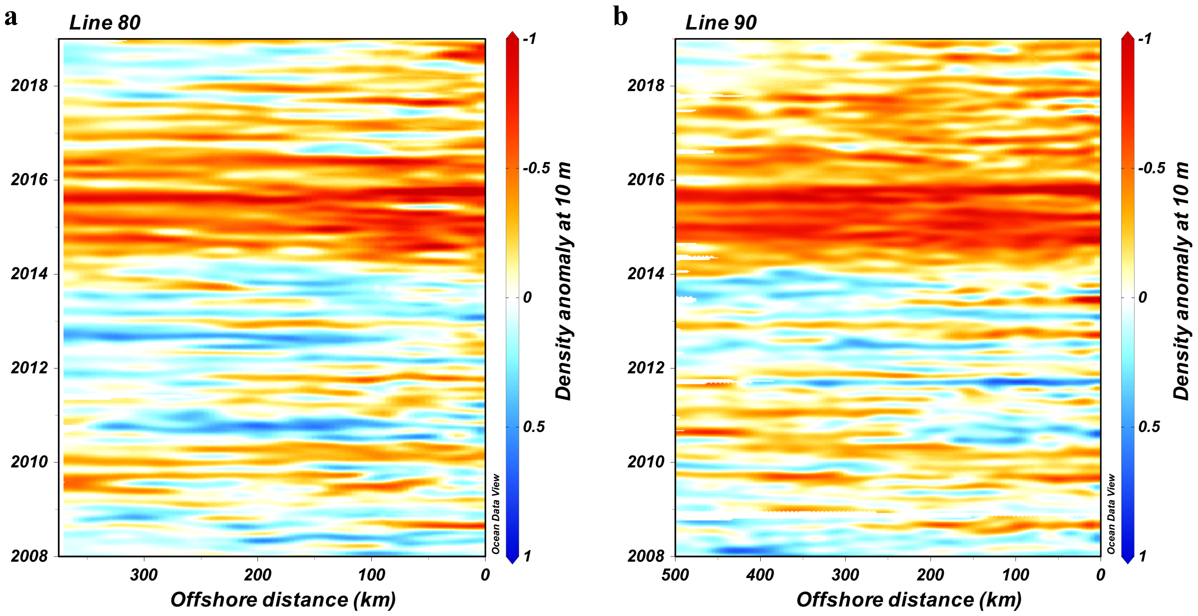

Figure S2.1. Density anomaly at 10 m along line 80 and line 90 of the CalCOFI grid. Density data from (https://spraydata.ucsd.edu/climCUGN/) (Rudnick et al. 2017). In (**a**) we see the effects of the warm anomaly and El Nino in along Line 80. Since there is no glider data from Line 93, we used data from Line 90 in (**b**) to illustrate conditions in the southern CalCOFI region during this time period.

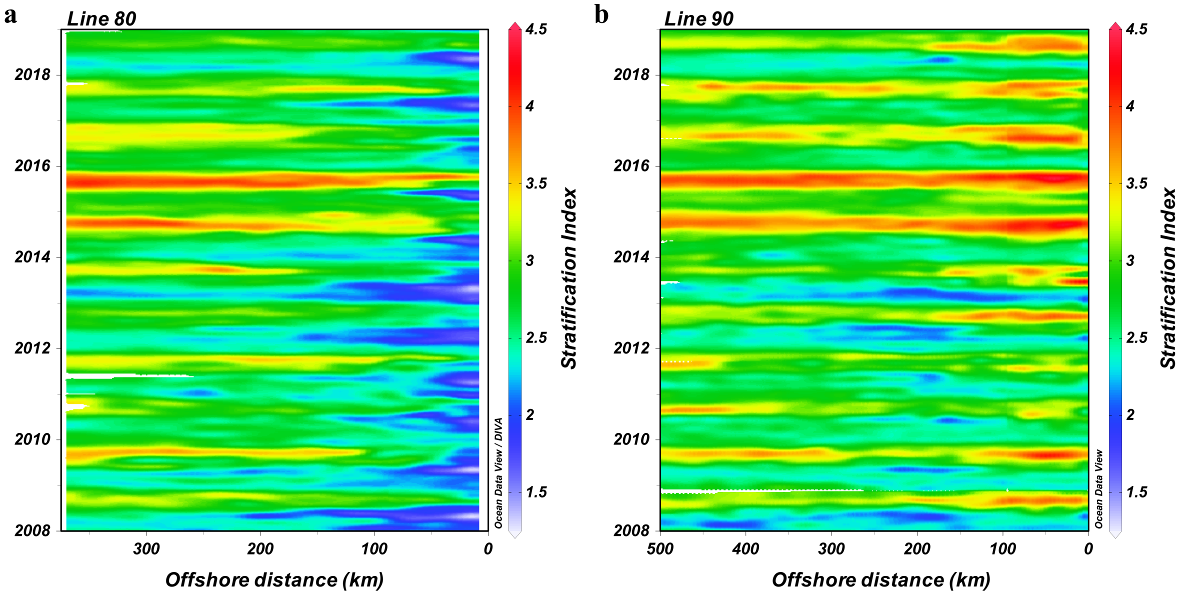

Figure S2.2. Surface stratification along line 80 and line 90 of the CalCOFI grid. Stratification was calculated from glider data (https://spraydata.ucsd.edu/climCUGN/) by subtracting the surface density from the density at 200 m (Behrenfeld et al. 2006; Rudnick et al. 2017). In (**a**) we see the effects of the warm anomaly and El Nino in increased stratification along Line 80. Since there is no glider data from Line 93, we used data from Line 90 in (**b**) to illustrate conditions in the southern CalCOFI region during this time period.

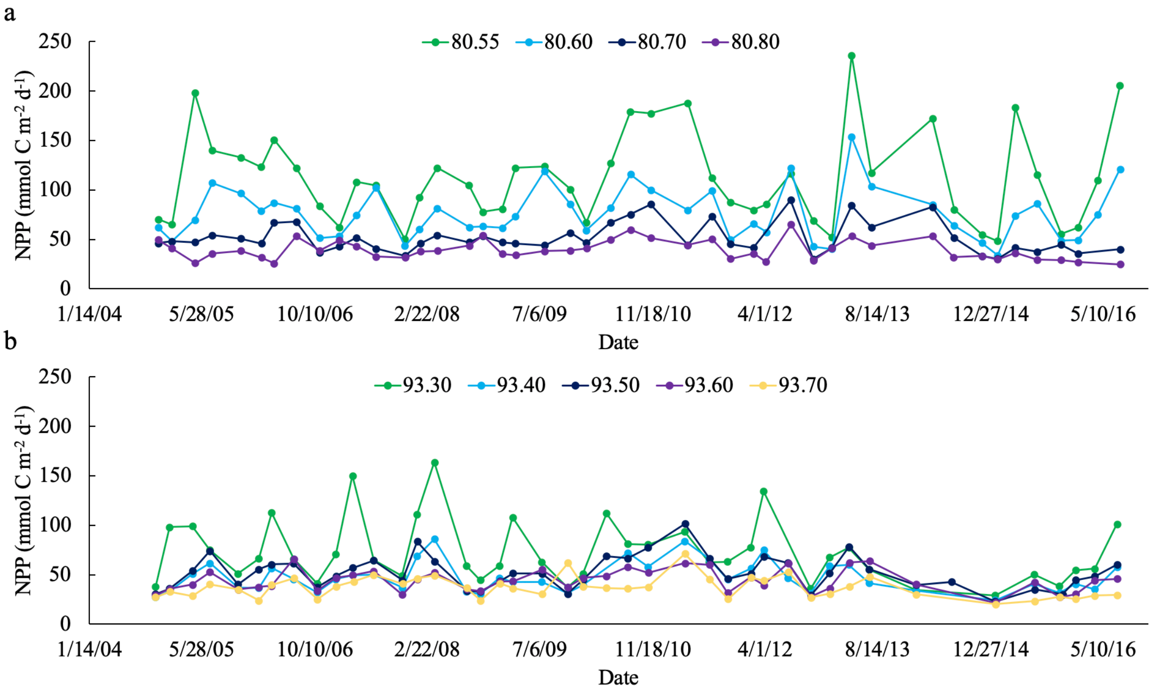

Figure S2.3. Satellite-based net primary production (NPP) for Lines 80 and 93. Net primary production as estimated from satellite data is shown from 2005-2016 for line 80 (**a**) and line 93 (**b**) (Kahru et al. 2009).

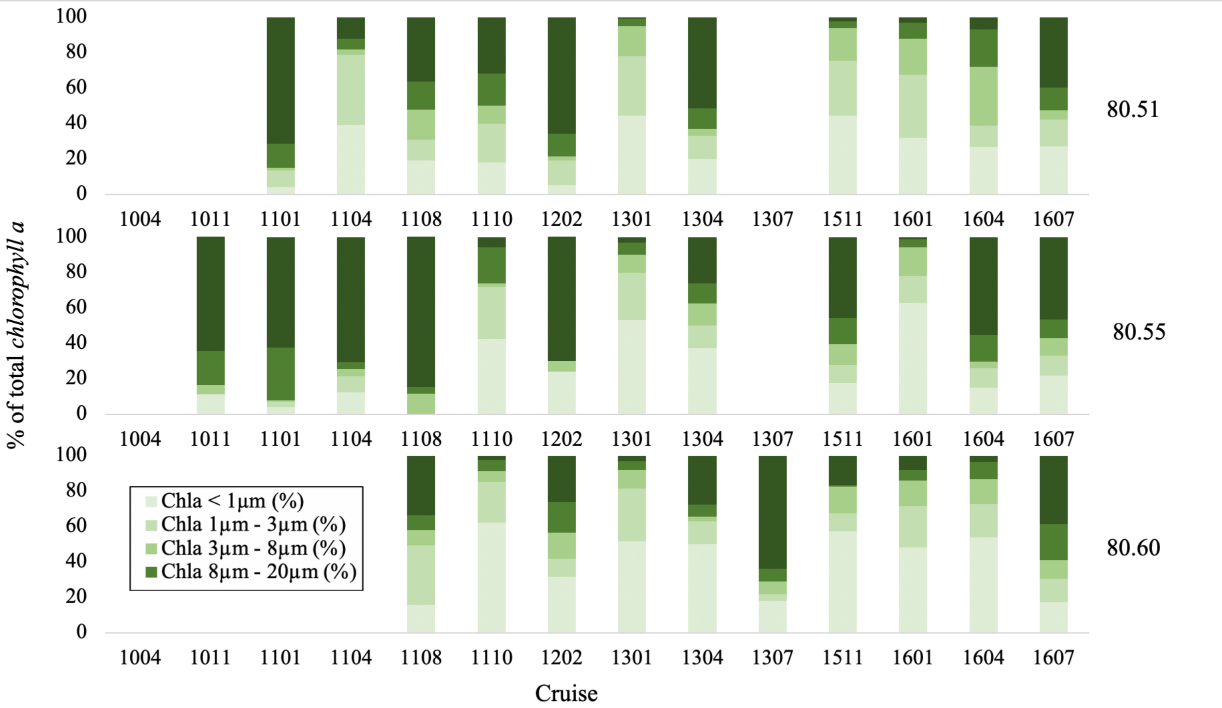

Figure S2.4. Size fractionated chlorophyll along Line 80 for cruises with nitrate isotope data. Percent of total chlorophyll a in each size fraction at 10 m depth is shown for three station along Line 80. Each sampling is labeled by cruise number (year and month, e.g. 1004 for April 2010). Darker green indicates larger size.

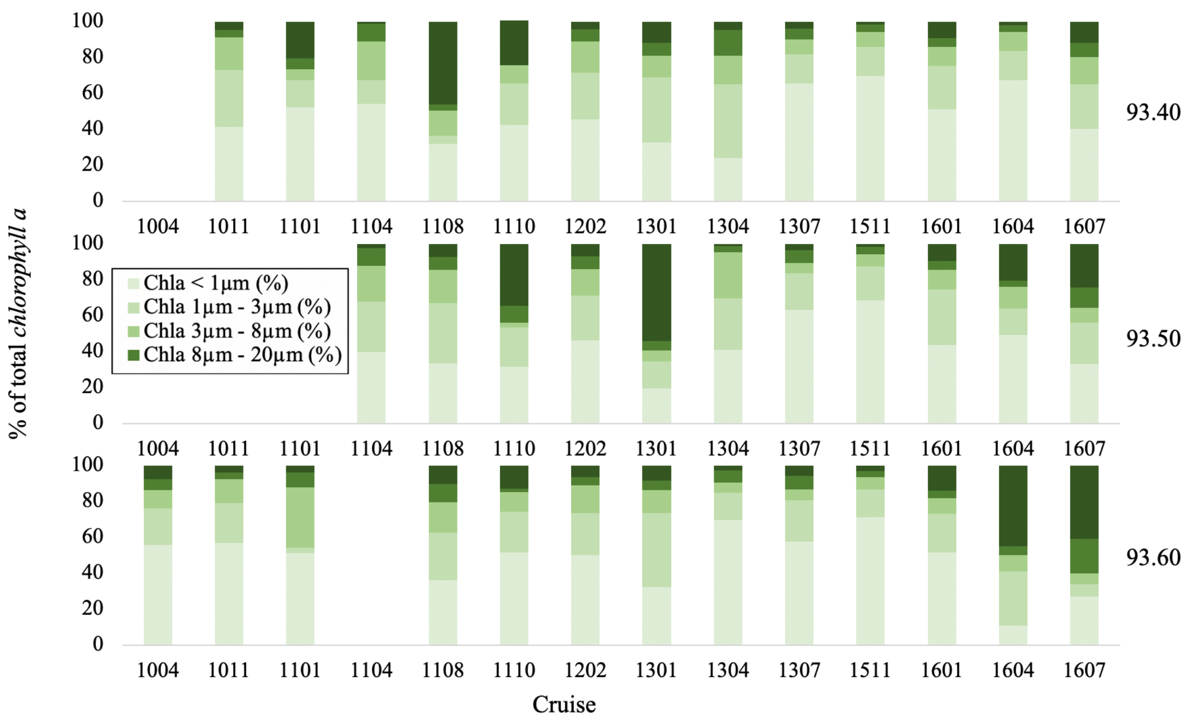

Figure S2.5. Size fractionated chlorophyll along Line 93 for cruises with nitrate isotope data. Percent of total chlorophyll a in each size fraction at 10 m depth is shown for three station along Line 93. Each sampling is labeled by cruise number (year and month, e.g. 1004 for April 2010). Darker green indicates larger size.

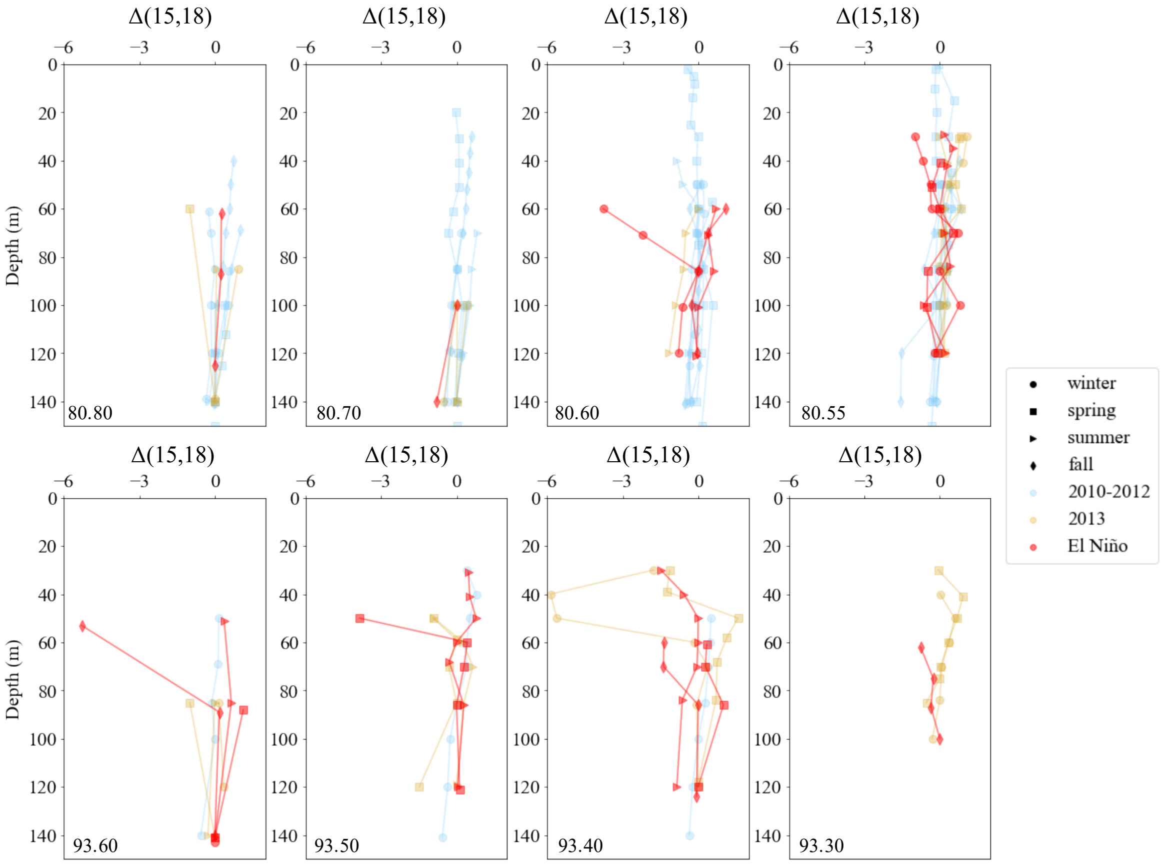

Figure S2.6. Δ(15,18) profiles for stations along Line 80 (top) and Line 93 (bottom).

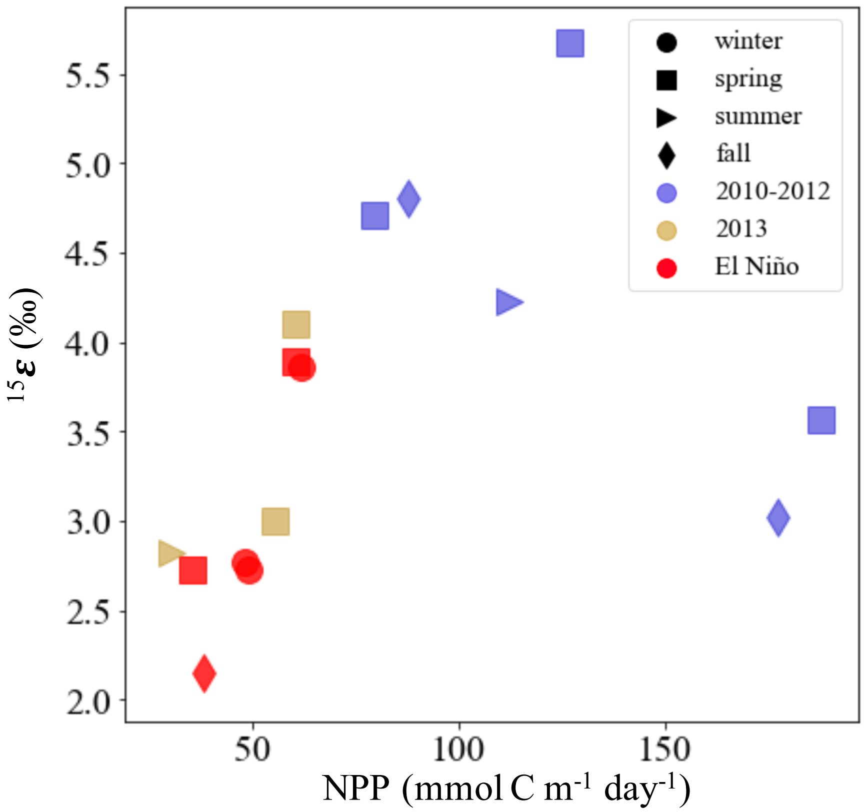

Figure S2.7. Comparison between NPP and N isotope fractionation factor for nitrate uptake. Net primary production as estimated from satellite data is shown compared to the nitrogen isotope fractionation factor for nitrate uptake by phytoplankton. (Pearson's *r* = 0.408, p-value = 0.116)

References

Behrenfeld, M. J., R. T. O’Malley, D. A. Siegel, and others. 2006. Climate-driven trends in contemporary ocean productivity. Nature **444**. doi:10.1038/nature05317

Kahru, M., R. Kudela, M. Manzano-Sarabia, and B. G. Mitchell. 2009. Trends in primary production in the California Current detected with satellite data. J. Geophys. Res. Ocean. **114**. doi:10.1029/2008JC004979

Rudnick, D. L., K. D. Zaba, R. E. Todd, and R. E. Davis. 2017. A climatology of the California Current System from a network of underwater gliders. Prog. Oceanogr. **154**: 64–106. doi:10.1016/j.pocean.2017.03.002

Rudnick, D. L., K. D. Zaba, R. E. Todd, and R. E. Davis, 2017: A climatology using data from the California Underwater Glider Network - Dataset [Downloaded 1/16/2021]. Scripps Institution of Oceanography, Instrument Development Group. doi: 10.21238/S8SPRAY7292

Chapter 3: Recent increases in water column denitrification in the seasonally suboxic bottom waters of the Santa Barbara Basin

Geophysical Research Letters

RESEARCH LETTER
10.1029/2019GL082075

Key Points:

- Stable isotopes of nitrate confirm an unprecedented increase in water column denitrification in the Santa Barbara Basin since 2004
- Reoxidation of water column nitrite alters the oxygen and nitrogen isotopic signatures of nitrate
- Changes in the bottom water nitrogen cycle are linked to longer-term deoxygenation and warming of the California Current Ecosystem

Supporting Information:

- Supporting Information S1

Correspondence to:
M. E. White,
mew070@ucsd.edu

Citation:
White, M. E., Rafter, P. A., Stephens, B. M., Wankel, S. D., & Aluwihare, L. I. (2019). Recent increases in water column denitrification in the seasonally suboxic bottom waters of the Santa Barbara Basin. *Geophysical Research Letters*, *46*. https://doi.org/10.1029/2019GL082075

Received 15 JAN 2019
Accepted 4 JUN 2019
Accepted article online 11 JUN 2019

©2019. American Geophysical Union. All Rights Reserved.

Recent Increases in Water Column Denitrification in the Seasonally Suboxic Bottom Waters of the Santa Barbara Basin

Margot E. White[1], Patrick A. Rafter[2], Brandon M. Stephens[3], Scott D. Wankel[4], and Lihini I. Aluwihare[1]

[1]Scripps Institution of Oceanography, University of California, San Diego, San Diego, CA, USA, [2]Department of Earth System Science, University of California, Irvine, Irvine, CA, USA, [3]Marine Science Institute and Department of Ecology, Evolution, and Marine Biology, University of California, Santa Barbara, Santa Barbara, CA, USA, [4]Woods Hole Oceanographic Institution, Woods Hole, MA, USA

Abstract Denitrification in the anoxic sediments of the Santa Barbara Basin has been well documented in the historic and modern record, but the regulation of and frequency with which denitrification occurs in the overlying water column are less understood. Since 2004, the magnitude and speciation of redox active nitrogen species in bottom waters have changed markedly. Most notable are periods of decreased nitrate and increased nitrite concentrations. Here we examine these changes in nitrogen cycling as recorded by the stable isotopes of dissolved nitrate from 2010–2016. When compared to previous studies, our data identify an increase in water column denitrification in the bottom waters of the basin. Observations from inside the basin as well as data from the wider California Current Ecosystem implicate a long-term trend of decreasing oxygen concentrations as the driver for these observed changes, with ramifications for local benthic communities and regional nitrogen loss.

Plain Language Summary The current chemical environment of the deep Santa Barbara Basin is unprecedented in the 30 years since measurements began, suggesting that a regional change in ocean chemistry has occurred over this time period. Here we use stable isotope measurements of nitrate to examine how the nitrogen cycle in the deep part of the basin has changed, documenting a recent increase in the amount of nitrate being removed from the water column at this location. Nitrogen removal in the dark ocean, known as denitrification, occurs when microbes utilize nitrate for respiration in the absence of oxygen. Such a process is consistent with the extremely low or absent oxygen concentrations that accompany the altered nitrate isotope signatures we measured in this study. Denitrification in sediments is common in the Santa Barbara Basin, but extensive water column denitrification has not been previously documented. Loss of nitrate from the water column can have important consequences for the balance of nutrients that support primary production in the ocean. These changes appear to be an effect of decreasing oxygen concentrations observed on a regional scale in the North Pacific Ocean, a trend which is likely to continue as the oceans warm.

1. Introduction

The Santa Barbara Basin (SBB) is located southeast of Point Conception, where strong upwelling of nutrients fuels primary productivity in local surface waters. Bound by the Channel Islands to the south and shallow sills to the east and west, the bottom waters of the basin are isolated from intensive circulation. This reduced ventilation combined with the remineralization of organic matter results in the rapid removal of oxygen from water depths below the 475 m sill (Goericke et al., 2015). During the winter or spring, when upwelling is strongest, denser oxygen-rich waters are brought up over the sill, temporarily reoxygenating bottom waters (Reimers et al., 1990; Roach et al., 2013; Figure 1). However, reoxygenation is often short-lived—within a few months oxygen has again been completely utilized, returning the basin to a suboxic state (Goericke et al., 2015; Reimers et al., 1990). Drawdown of oxygen within the basin plays an important role in regulating the redox regime and, by extension, the geochemical cycling of elements in both sediments and the water column. The 30-year, quarterly time series of the SBB provided by the California Cooperative Fisheries Investigation (CalCOFI) program has delivered important insights into the dynamics of the basin environment (Goericke et al., 2015; Reimers et al., 1990). One prominent feature in the CalCOFI

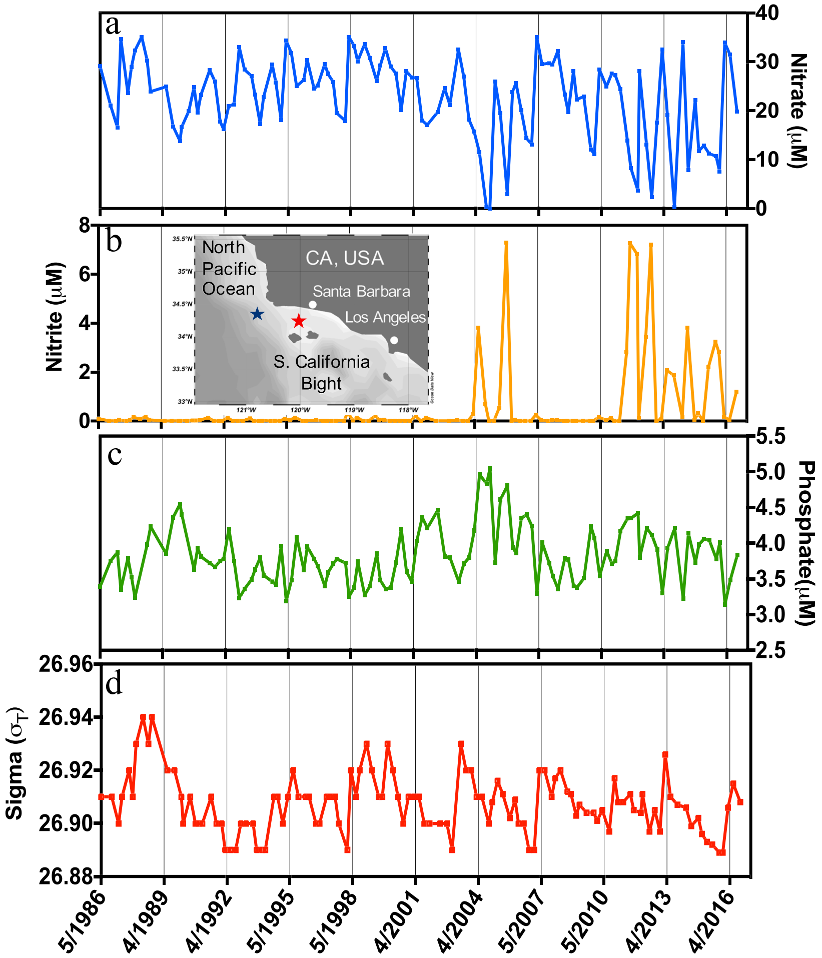

Figure 1. Time series of CalCOFI data at 570 m in the Santa Barbara Basin. The inset map shows the location of the Santa Barbara Basin in red and CalCOFI station 80.55 in blue. Starting in 2004 there are time periods where nitrate (a) is close to zero, corresponding with periodic large increases in nitrite (b). Phosphate concentrations (c) are broadly representative of time since last flushing, where phosphate accumulates between flushing events. Density (d) also provides a history of flushing events, where increases in density identify periods of flushing.

time series is the removal of nitrate (NO_3^-) from bottom waters due to denitrification (Goericke et al., 2015)—where NO_3^- is used as the terminal electron acceptor of the microbial electron transport chain, typically in support of heterotrophic remineralization of organic carbon (Körner & Zumft, 1989). By converting bioavailable NO_3^- to nitrogen gas, denitrification represents an important sink in the global nitrogen cycle (Brandes & Devol, 2002; Gruber & Sarmiento, 1997).

Previous studies of the SBB document significant changes in biogeochemistry since the time series began in the 1980s (Bograd et al., 2008; Goericke et al., 2015; Wang et al., 2017). The most pronounced of these changes has been in bottom water nitrite (NO_2^-) concentrations, which in recent years have increased by over an order of magnitude (Goericke et al., 2015; Figure 1b). In general, accumulation of nitrite to this degree in the ocean is rare—occurring most commonly in water column oxygen-deficient zones (Buchwald & Casciotti, 2013; Casciotti, 2016a; Casciotti et al., 2013; Gaye et al., 2013; Peters et al., 2016). Nitrite is an intermediate in both the nitrification and denitrification pathways, and under low-oxygen conditions, one or both processes may contribute to its accumulation (Goericke et al., 2015; Peng et al., 2016).

Denitrification can occur in both sediments and the water column and observed changes in water column NO_3^- and NO_2^- concentration do not necessarily reflect the location of denitrification. However, well-established differences in the extent of nitrate isotope fractionation during water column denitrification relative to sediment-hosted denitrification have proven useful for apportioning their relative roles in the NO_3^- budget of the SBB and elsewhere (e.g., Sigman et al., 2003). Biological transformations often impart strong isotopic fractionation, where the more rapid reaction of lighter isotopes enriches heavier isotopes (^{15}N or ^{18}O) in the reactant pool relative to their starting distribution. The relative strength of this isotopic discrimination is represented by the isotope effect or fractionation factor and is expressed (in units of per mil, ‰) as ε (where $\varepsilon = [1 - (k^{heavy}/k^{light})] \times 1{,}000$, and k represents the reaction rate constant of the light or heavy isotope as denoted). The isotope effect associated with water column denitrification (ε_{wc}), is usually estimated to be between 20‰ and 30‰ (Barford et al., 1999; Brandes et al., 1998; Lehmann et al., 2003; Marconi et al., 2017), though recent work suggests that values may be lower (~15‰) under conditions typical of the open ocean (Kritee et al., 2012; Marconi et al., 2017; Sigman et al., 2009). In contrast, sedimentary denitrification (ε_{sed}) has been found to exhibit very small net fractionation, where complete utilization results in little to no NO_3^- returning to the water column after entering the sediments (Brandes & Devol, 1997). This anticipated difference between ε_{wc} and ε_{sed} was used as a framework to interpret $\delta^{15}N_{NO3}$ and $\delta^{18}O_{NO3}$ measurements from the SBB between 1995 and 1999 and indicated a dominant contribution from sedimentary denitrification (Sigman et al., 2003). That study found that water column denitrification in the SBB accounted for less than 15% of total N loss. During the same time period, CalCOFI observed no NO_2^- accumulation and bottom water NO_3^- concentrations remained above 12 μM.

In order to more definitively determine whether an increase in water column denitrification was underlying recent changes in SBB nitrogen cycling, we measured $\delta^{15}N_{NO3}$ and $\delta^{18}O_{NO3}$ in seawater samples taken during CalCOFI cruises from 2010–2016. In the SBB, where restricted circulation exacerbates biogeochemical changes occurring elsewhere in the region, an altered N Cycle may be the “canary in the coal mine” for long-term trends of warming and deoxygenation in the source waters of the productive California Current Ecosystem.

2. Materials and Methods

Samples were collected during CalCOFI cruises from 2010-2016 at station 081.8 046.9 in the center of the SBB (approximately 34.28°N and 120.02°W). Typically, three depths below the 475m sill were included—nominally 515, 540, and 570 m. Samples for nitrate and nitrite isotopes were filtered through GF/F filters (0.7 μm pore size) directly from Niskin bottles mounted on a standard conductivity-temperature-depth rosette system, and frozen until analysis. Ancillary physical and chemical data (Figure 1) were collected and analyzed by the CalCOFI program as described at http://calcofi.org. Nutrient concentrations were measured immediately or else refrigerated and measured within 16 hr. Accuracy and precision for NO_3^- and NO_2^- concentration are 0.05 and 0.01 μM, respectively. The detection limit is 0.02 μM for nitrate plus nitrite. Estimated precision for oxygen concentration measurements is 0.9 μM, though in the presence of nitrite greater than 1 μM, oxygen measurements can be erroneously high (Bograd et al., 2008). For this reason, oxygen measurements from below the sill are not discussed here as they lack the necessary precision.

Nitrogen and oxygen isotopes of NO_3^- were analyzed using the denitrifier method (Casciotti et al., 2002; Sigman et al., 2001). Samples from 2010–2012 were measured according to Rafter & Sigman, 2016. Those from 2013–2015 were measured according to Buchwald et al., 2018. Briefly, sample N_2O was purified using a customized purge and trap system and analyzed on a continuous flow IsoPrime 100 isotope ratio mass spectrometer. NO_2^- concentrations greater than 2% of $NO_3^- + NO_2^-$ were removed by addition of sulfamic acid prior to injection (Granger & Sigman, 2009). Corrections for drift, size, and fractionation of O isotopes during bacterial conversion were carried out using NO_3^- reference materials USGS 32, USGS 34, and USGS

35 (McIlvin & Casciotti, 2011). Typical reproducibility for $\delta^{15}N_{NO3}$ and $\delta^{18}O_{NO3}$ measurements was ±0.2‰ and 0.4‰, respectively. Samples with less than 1-μM N were not analyzed.

Nitrogen isotopes of NO_2^- were analyzed using the sodium azide method, in which NO_2^- is quantitatively converted to N_2O by addition of an acetic acid buffered sodium azide solution (McIlvin & Altabet, 2005). Reported $\delta^{15}N_{NO2}$ values were normalized against internal nitrite isotope reference standards WILIS 10 (−1.7‰) and WILIS 11 (+57.1‰) (Wankel et al., 2017). Typical reproducibility for $\delta^{15}N_{NO2}$ is ±0.1‰.

3. Results

Measured NO_3^- isotope values increased as NO_3^- concentrations were drawn down, from values as low as +9.9‰ up to +44.3‰ for $\delta^{15}N_{NO3}$ and +6.6‰ up to +29.3‰ for $\delta^{18}O_{NO3}$ (Figures 2c and 3a). We also calculated Δ(15,18), where $\Delta(15,18) = (\delta^{15}N - \delta^{15}N_{source}) - (\delta^{18}O - \delta^{18}O_{source})$. The source isotopic signature of NO_3^- was assigned as +8.5‰ for $\delta^{15}N$ and +4.6‰ for $\delta^{18}O$ based on the average signature between 300 and 500 m outside the basin (Figure 1). Values of Δ(15,18) varied between −1.6‰ and +11.9‰ (Figure 2).

Example water column NO_3^- profiles from 2011–2012 identify the progression of denitrification as the basin becomes isolated between flushing events (Figure 3a). At depths below 500 m, NO_3^- isotope values increase as NO_3^- concentration decreases from Spring 2011 to Fall 2012. Flushing in Spring 2012 with waters rich in NO_3^- then resets concentrations and isotope signatures by diluting the denitrification signal. As evidenced from time series (Figure 2) and depth profiles (Figure 3a) NO_3^- isotope values changed in parallel across several depths, and the most enriched values at each depth accompanied maximum NO_2^- and minimum NO_3^- concentrations. For the five samples where both were measured, $\delta^{15}N_{NO2}$ was between 24.4‰ and 33.3‰ lighter than the companion $\delta^{15}N_{NO3}$ and largely changed in parallel with $\delta^{15}N_{NO3}$ (Table S1 in the supporting information).

To identify mechanisms responsible for N removal in the basin, we calculated apparent isotope fractionation factors (e.g. $^{15}\varepsilon_{app}$) from NO_3^- isotope data using a closed system, Rayleigh fractionation model, where

$$\delta^{15}N = \delta^{15}N_{source} - {}^{15}\varepsilon_{app} \times \ln\left([NO_3^-]/[NO_3^-]_{initial}\right)$$

Assuming a unidirectional transformation occurring in a closed system, a single, linear relationship would be expected in a plot of $\ln[NO_3^-]$ versus $\delta^{15}N_{NO3}$ or $\delta^{18}O_{NO3}$. Across our data set several different slopes were observed (Figures 3b and 3c), which indicated that ε_{app} varied. To examine the range, we focused on $^{15}\varepsilon_{app}$ and calculated a value for each NO_3^- isotope data point according to the rearranged equation:

$$^{15}\varepsilon_{app} = -\left(\delta^{15}N - \delta^{15}N_{source}\right) / \ln\left([NO_3^-]/[NO_3^-]_{initial}\right)$$

The $[NO_3^-]_{initial}$ was calculated from N* (Gruber & Sarmiento, 1997) according to $[NO_3^-]_{initial} = [PO_4^{3-}] \times \frac{N}{P}$; where N:P was 12.6:1 based on the NO_3^-:PO_4^{3-} ratio outside the basin (CalCOFI station 80.55) at depths between 300 and 500 m. Initial $\delta^{15}N_{NO3}$ corresponded to the source values discussed previously, +8.5‰ for $\delta^{15}N$ and +4.6‰ for $\delta^{18}O$. Fractionation factors ranged from 2.7‰ to 13.3‰ for $^{15}\varepsilon_{app}$.

The variability in these ε_{app} values, which integrate all N loss processes over the time since the last flushing, likely resulted from differing contributions of sedimentary and water column denitrification to N removal from SBB bottom waters. If we assume that sedimentary denitrification consumes NO_3^- with an $^{15}\varepsilon$ of 1.5‰, while water column denitrification exhibits an $^{15}\varepsilon$ of 25‰, then the relative contribution of water column and sedimentary denitrification to each calculated ε_{app} value can be estimated from a two end-member isotope mixing model, assuming no other processes altered NO_3^- (Peters et al., 2018; Sigman et al., 2003; SI). This calculation suggested that the percent of nitrate loss occurring in the water column ranged from 0% up to 50% from 2010–2016.

We additionally estimated ε_{app} by isolating consecutive cruises where the concentration and isotopic signature of NO_3^- appeared to be unaffected by flushing (e.g., Figure 3a). During such time periods, NO_3^- continuously decreased from one cruise to the next, presumably due to denitrification, while its isotopic signature increased (Table S2). We isolated 12 such periods in the time series and calculated 12 $^{15}\varepsilon_{app}$

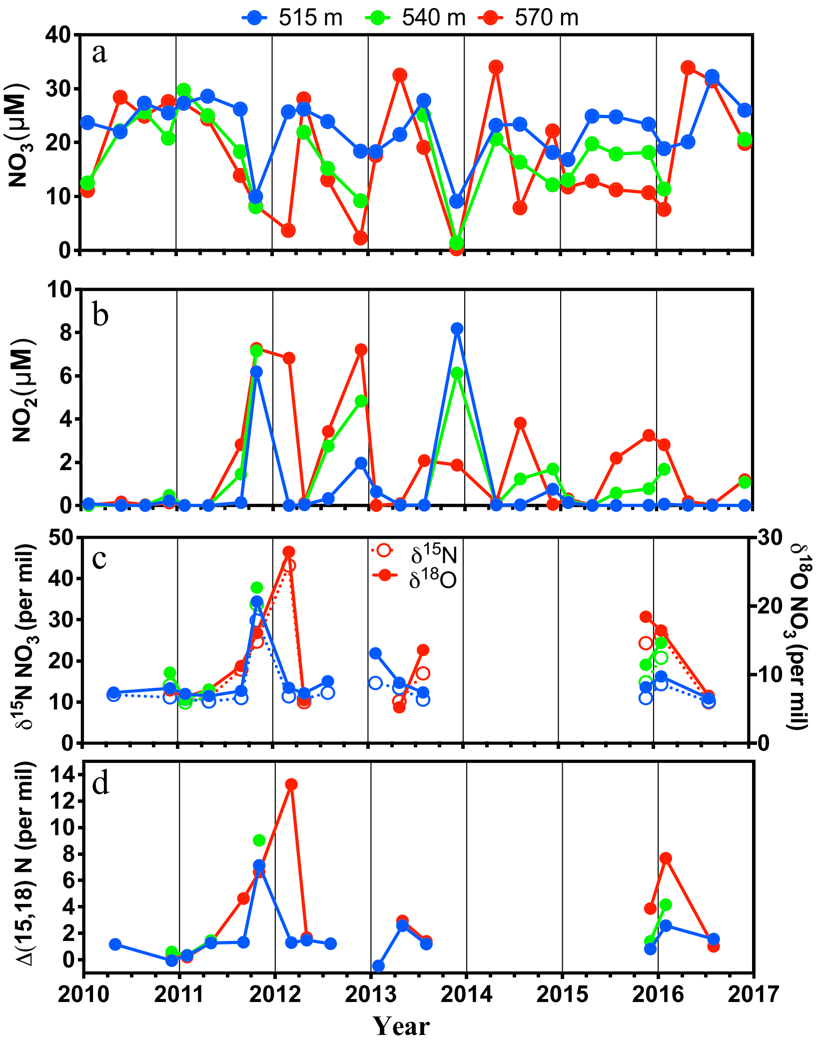

Figure 2. Nitrate and nitrite concentrations and nitrate isotope measurements from three depths. Time periods of low nitrate (a) and high nitrite (b) correspond to increased enrichment in isotope values (c) as well as greater deviation between nitrogen and oxygen isotopes of nitrate (d).

values. These values ranged from 8.1‰ to 24.3‰ (Table S2). Applying the same isotopic mass balance for *ε* as above, we found that **in situ** nitrogen loss in the water column ranged from 28% to 97% of the total, for these time periods.

Values of Δ(15,18) are expected to be close to 0‰ if denitrification is the primary process altering NO_3^- concentrations and isotopes. However, this value increased together with $\delta^{15}N_{NO3}$ and $\delta^{18}O_{NO3}$ (Figure 2d) suggesting that NO_2^- reoxidation could influence NO_3^- isotopes. To test this hypothesis, we adopted a previously described dual nitrate isotope model framework (Granger & Wankel, 2016), which explicitly

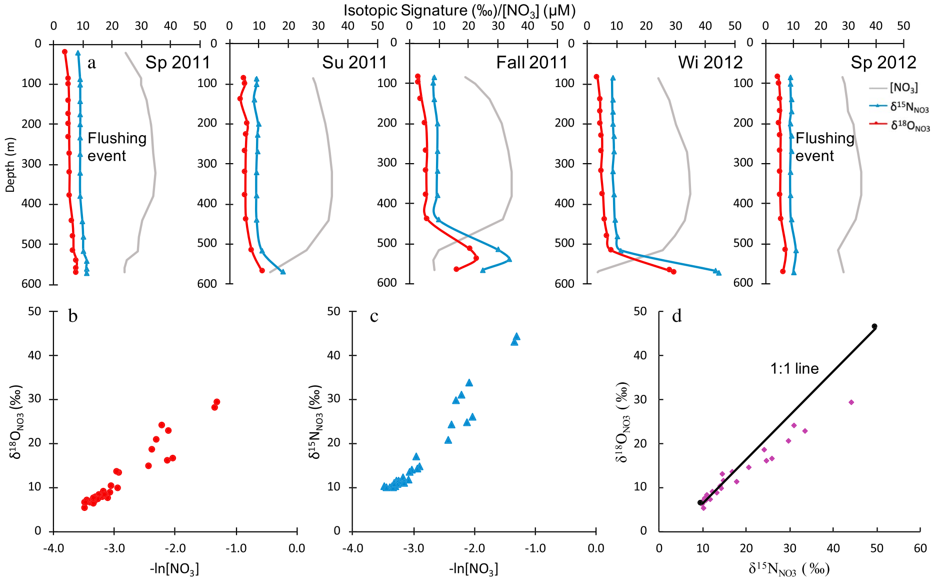

Figure 3. Profiles from five cruises are shown in (3a) beginning with a flushing event in the spring of 2011. Following the flushing, the basin becomes deoxygenated and nitrogen is removed as isotopes become progressively more enriched until another flushing event in the following spring. Figure 3b shows $\delta^{18}O_{NO3}$ for all samples below the sill depth versus the negative natural log of nitrate concentration. Unidirectional consumption of nitrate in a closed system yields a straight line with the slope reflecting the apparent $^{18}\varepsilon$. Figure 3c shows the same, but for $\delta^{15}N_{NO3}$. Figure 3d plots $\delta^{18}O_{NO3}$ versus $\delta^{15}N_{NO3}$ with the black line showing a 1:1 relationship between the two.

includes nitrate reduction (**NAR**), nitrite reduction (**NIR**) and nitrite reoxidation to nitrate (**NXR**), to identify processes influencing the isotopic signature of the standing NO_3^- pool. Pooling data from all sampling time points, the model iterates to minimize differences from observed NO_3^- concentrations and isotopic signatures by optimizing $^{15}\varepsilon$ values for NO_3^- reduction ($^{15}\varepsilon_{NAR}$; assuming the $^{15}\varepsilon_{NAR} = {}^{18}\varepsilon_{NAR}$; Granger et al., 2008), NO_2^- reduction ($^{15}\varepsilon_{NIR}$) and NO_2^- reoxidation ($^{15}\varepsilon_{NXR}$), as well as the relative flux of NO_2^- reoxidation to NO_3^- reduction (NXR/NAR), in a series of governing isotope mass balance equations (Granger & Wankel, 2016). Values for the inverse kinetic oxygen isotope effect of NO_2^- oxidation ($^{18}\varepsilon_{NXR}$) and the normal kinetic isotope effect for incorporation of O from water during NO_2^- oxidation ($^{18}\varepsilon_{,k,H2O}$) were assumed to be −4‰ and +14‰, respectively (Buchwald & Casciotti, 2010) and the $\delta^{18}O_{NO2}$ was assumed to reflect a 13.5‰ higher equilibrium isotope composition (Casciotti et al., 2007) with respect to seawater ($\delta^{18}O_{SW} = 0$‰). Results of optimized model fits yielded values of 8.8 ± 0.7‰ for $^{15}\varepsilon_{NAR}$, 9.7 ± 4.9‰ for $^{15}\varepsilon_{NIR}$, −32.9 ± 16.8‰ for $^{15}\varepsilon_{NXR}$ and 0.10 ± 0.05 for NXR/NAR. If $^{15}\varepsilon_{NAR,}$ the fractionation factor for the integrated (i.e., water column and sedimentary) process of NO_3^- reduction reflected in the pooled NO_3^- samples, is treated like $^{15}\varepsilon_{app}$, then revisiting the mass balance calculation from above suggests an average of 37 ± 3% of nitrate loss attributable to water column denitrification during our study period.

4. Discussion

Patterns of increased nitrogen loss and elevated NO_2^- in SBB bottom waters are consistent with regional (and global) progression toward expanding oxygen depletion in nearshore environments. Below we discuss our isotope data and argue that water column denitrification has greatly increased in the years since 2004, resulting in periodic accumulation of NO_2^- to levels unprecedented in the context of the CalCOFI record and a pronounced enrichment in $\delta^{15}N_{NO3}$ and $\delta^{18}O_{NO3}$. Furthermore, we posit that these trends are the result of decreased oxygen delivery to the basin.

4.1. Evidence of Water Column Denitrification

The accumulation of NO_2^- in the SBB (up to 8.19 μM, Figures 1 and 2) contrasts markedly with previous basin records (since 1986; Goericke et al., 2015) and is consistent with, or at times greater than, observations from open ocean oxygen deficient zones (Casciotti, 2016a; Gaye et al., 2013; Martin & Casciotti, 2017). Similarly, periods of low NO_3^- have increased in frequency in recent years (Figure 1; Goericke et al., 2015). The combined time series clearly shows that periods of low NO_3^- correspond temporally with elevated NO_2^- (Figure 1) and greater enrichment in $\delta^{15}N_{NO3}$ and $\delta^{18}O_{NO3}$ (Figure 2). These records are all consistent with greater incidence of water column denitrification since ~2004.

We calculated the relative importance of water column denitrification using three different approaches. First, we used ε_{app} values calculated using a closed system, Rayleigh model to estimate percent water column denitrification since last flushing. We found that up to 50% of N removal was mediated by water column denitrification. However, one limitation of this calculation is the use of PO_4^{3-} concentrations in the basin to estimate initial NO_3^-. In low-oxygen environments, respiration is not the only source of PO_4^{3-} as PO_4^{3-} bound to iron particles can be released from reducing sediments into the water column (Bourbonnais et al., 2013; King & Barbeau, 2011; Peters et al., 2018; Reimers et al., 1990). Thus, it is possible that the N:P approach taken here overestimated $[NO_3^-]_{initial}$ at times, as has been concluded elsewhere (Hu et al., 2016; Peters et al., 2018). For this reason, we also estimated ε_{app} using the change in isotopic composition internal to the basin between two time points where NO_3^- continued to decrease. With this approach, the initial NO_3^- concentration is that measured at the first time point. Using this method, we found that on occasion, up to 97% of NO_3^- loss in the basin resulted from water column denitrification (Table S2). Time periods with such high N loss from water column denitrification are typically accompanied by very low NO_3^-. For example, for this time period, the NO_3^- at 570 m was 3.7 μM and sedimentary denitrification would have been limited due to low diffusion from the water column. The two estimates are distinct because the former examines the time period since the basin was flushed, whereas the latter captures the shorter time period between two cruises. Furthermore, a model that examined the influence of processes other than denitrification on NO_3^- isotopes estimated that an average of $37 \pm 3\%$ of nitrate loss could be attributed to water column denitrification during our study period. Despite the different assumptions, processes, and time periods captured in each method, they all identify the importance of water column denitrification and exceed the previous estimate of around 15% reported in Sigman et al., 2003.

Many processes can act to dilute the observed ε_{app}, including partial flushing and nitrite reoxidation (see below). However, increasing ε_{app} with decreasing NO_3^- can only be explained by greater influence of water column denitrification. Thus, our data require extensive water column denitrification, in addition to sedimentary denitrification, to be taking place in the basin when NO_3^- is drawn down to its lowest levels. Nitrogen isotopes of NO_2^- were significantly depleted compared to $\delta^{15}N_{NO3}$ (by 24.4‰ to 33.3‰), and they increased in tandem, indicating that NO_3^- reduction is the most likely source of NO_2^- in the system (Table S1).

4.2. Evidence of Nitrite Reoxidation

If denitrification is the only process affecting NO_3^- then equal increases in both $\delta^{15}N$ and $\delta^{18}O$ are expected (Granger et al., 2008). While earlier observations noted a consistent 1:1 relationship between $\delta^{15}N_{NO3}$ and $\delta^{18}O_{NO3}$ in the SBB, these were restricted to conditions of limited NO_3^- consumption (Sigman et al., 2003). Here, we observe higher relative increases in $\delta^{15}N$ values compared to corresponding $\delta^{18}O$ values when NO_3^- loss was greater, as is visible in $\Delta(15,18)$ values exceeding 0‰ (Figures 2d) and a slope <1 in a plot of $\delta^{15}N_{NO3}$ versus $\delta^{18}O_{NO3}$ (Figure 3d). The departure from the expected relationship between $\delta^{15}N_{NO3}$ and $\delta^{18}O_{NO3}$ is most prominent during periods of NO_2^- accumulation in the water column. Such deviations are commonly observed in oxygen-deficient zones and have generally been interpreted as evidence for the influence of NO_2^- reoxidation to NO_3^- (Casciotti, 2016a; Granger & Wankel, 2016; Sigman et al., 2005).

The observed deviation from 1:1 can be linked to several interrelated mechanisms (Casciotti, 2016b; Granger & Wankel, 2016). Foremost, if NO_2^- becomes reoxidized to NO_3^-, one of the required oxygen atoms derives from the surrounding water, contributing to a difference between $\delta^{15}N_{NO3}$ and $\delta^{18}O_{NO3}$ (Buchwald & Casciotti, 2010). Indeed, our data reflect lower than expected $\delta^{18}O_{NO3}$ relative to observed $\delta^{15}N_{NO3}$, as might be predicted as a progressive consequence of the incorporation of low $\delta^{18}O$ from seawater (~0‰;Buchwald & Casciotti, 2010 ; Casciotti, 2016a). Previous work has described a phenomenon similar to that observed here, under conditions where NO_3^- consumption is extensive and $\delta^{15}N_{NO3}$ is significantly elevated (Casciotti et al., 2013; Granger & Wankel, 2016). As presented in Granger and Wankel (2016), the disparity from 1:1 is also partially explained by the inverse isotope effect imparted on NO_2^- during oxidation to NO_3^-, in which heavier isotopes preferentially accumulate in the product NO_3^- pool and the effect on N isotopes is greater than on O isotopes (Buchwald & Casciotti, 2010; Casciotti, 2016a). Overall, existing studies confirm that $\delta^{15}N_{NO3}$ should become more enriched than $\delta^{18}O_{NO3}$ during nitrite reoxidation. Thus, it seems likely that NO_2^- re-oxidation is contributing to the measured isotopic composition of NO_3^-. This effect becomes more prominent at higher degrees of NO_3^- consumption, NO_2^- accumulation and associated extremes in isotopic composition. Indeed, model fits to the dual isotope trajectories presented here suggest that as much as 10% of the standing NO_3^- pool may derive from a reoxidative NO_2^- flux.

Notably, the model results fail to adequately reproduce the observed low $\delta^{15}N_{NO2}$ values (Table S1). One possible explanation for this may be the presence of a source of NO_2^- not linked to nitrate reduction, such as ammonia oxidation, although accumulation of ammonium is rarely observed in the basin. Overall, the important consequence of any nitrite reoxidation is that accurate estimates of the exact extent of water column denitrification cannot be made with these isotope data alone. Furthermore, the added perspective of $\delta^{18}O_{NO3}$ drew attention to the fact that $\delta^{15}N_{NO3}$ in the bottom waters of the SBB likely does not reflect the singular process of NO_3^- reduction, but rather the confluence of an active redox cycling between NO_3^- and NO_2^-.

4.3. External Influences on Bottom Water Biogeochemistry

Our data unequivocally support the importance of water column denitrification as the cause of the observed NO_2^- accumulation and NO_3^- deficit. We conclude that water column denitrification rates remained fairly low during the time period from 1986 to 2004 when NO_2^- accumulation was not observed. This is supported by the relatively higher NO_3^- concentrations during that time (Figure 1a). Goericke et al. (2015) also noted that NO_3^- removal rates appeared to increase when NO_3^- was below 15 μM, an observation that is consistent with water column denitrification rates being generally faster than sedimentary rates (Groffman et al., 2006). Those authors hypothesized that a decrease in either the frequency of flushing events or in the strength of that flushing was altering N cycling in the basin. Based on observed time series of bottom water properties, flushing events in the SBB appear to have occurred at a similar frequency over the course of the time series (Figure 1d). Furthermore, lowest NO_3^- concentrations are not consistently accompanied by the highest PO_4^{3-} concentrations, where PO_4^{3-} accumulation in bottom waters is considered to be a proxy for time since flushing (Figure 1; Goericke et al., 2015). Thus, the observed anomalous NO_2^- accumulation does not appear to be definitively related to the frequency of flushing events.

As proposed in Goericke et al. (2015), it seems that observed changes in N cycling stem from a reduction in the extent of reoxygenation during more recent flushing events, as demonstrated by decreasing oxygen concentrations at shallower basin depths (Wang et al., 2017; Figure S1). There is strong evidence that the overall internal oxygen content of the basin has decreased over the last two decades (Wang et al., 2017), which is likely related to decreasing oxygen concentrations in the CCE as a whole (Bograd et al., 2008) and the mesopelagic North Pacific more generally (Ito et al., 2017). A shoaling of the hypoxic boundary has been observed outside the basin, suggesting that each flushing event would introduce less oxygen. It has also been noted that decreases in oxygen outside the basin appeared to be more pronounced during January to March (Bograd et al., 2008), which is the time period immediately preceding the detection of spring flushing events in the CalCOFI time series. Thus, the seasonality of deep water deoxygenation may have an outsized effect on the basin. A recent analysis of oxygen trends in the global ocean concluded that oxygen has decreased in the ocean's interior due to greater apparent oxygen utilization, which points to changes in biology or ocean physics as the primary cause of this decrease rather than decreased solubility in the surface ocean (Ito et al., 2017). Finally, paleoceanographic evidence using Fe/Ti ratios from sediment cores collected in the basin suggest oxygen concentrations in the bottom waters over the past 15 years are the lowest observed over the last 200 years (Wang et al., 2017).

5. Conclusions

Time periods of high NO_3^- loss in the SBB appear to have increased in frequency and intensity beginning in the early 2000s, accompanied by a large periodic increase in NO_2^-. The evidence from $\delta^{15}N_{NO3}$ and $\delta^{18}O_{NO3}$ presented here shows that this increase is almost entirely due to episodic increases in water column denitrification. However, we find that the isotope values cannot be definitively used to quantify the NO_3^- loss because NO_2^- reoxidation plays a role in modifying the isotopic composition of NO_3^-. These large changes in the extent of water column denitrification appear to be linked to decreased oxygen concentrations in waters entering the basin. Thus, extreme changes in the biogeochemistry of the SBB may serve as an indicator of the state of the CCE at large, and the changes that a warming climate may bring to the region. With the shallowest sills of any of the California Borderland Basins, the current state of the SBB may foreshadow how conditions in other basins are likely to change in the future as deoxygenation and warming continue. Further work should focus on continued monitoring of this basin, perhaps including denitrification rate measurements and/or measurements of N_2/Ar. A more complete understanding of the dynamics and timing of basin flushing would also be beneficial, as well as additional modeling efforts aimed at a better constraining the effects of mixing on the complex isotope dynamics of nitrogen cycling in the anoxic bottom waters.

Acknowledgments
We thank CalCOFI and Shonna Dovel for sample collection and two anonymous reviewers for improving the manuscript. Thanks also to Daniel Sigman for useful discussions, and Zoe Sandwith and Jen Karolewski for help with sample analysis. Data sets presented here were supported in part by CCE-LTER augmented funding (NSF grant OCE-1026607). Additional funding came from the Edna Bailey Sussman Foundation and the San Diego Foundation Blasker Environment grant. All data can be accessed at http://calcofi.org and https://oceaninformatics.ucsd.edu/datazoo/catalogs/ccelter/datasets. SDW acknowledges the support of a fellowship through the Hanse-Wissenschaftskolleg (Institute for Advanced Studies).

References

Barford, C. C., Montoya, J. P., Altabet, M. A., & Mitchell, R. (1999). Steady-state nitrogen isotope effects of N_2 and N_2O production in Paracoccus denitrificans. *Applied and Environmental Microbiology*, *65*(3), 989–994. Retrieved from http://www.ncbi.nlm.nih.gov/pubmed/10049852

Bograd, S. J., Castro, C. G., Di Lorenzo, E., Palacios, D. M., Bailey, H., Gilly, W., & Chavez, F. P. (2008). Oxygen declines and the shoaling of the hypoxic boundary in the California Current. *Geophysical Research Letters*, *35*, L12607. https://doi.org/10.1029/2008GL034185

Bourbonnais, A., Lehmann, M. F., Hamme, R. C., Manning, C. C., & Juniper, S. K. (2013). Nitrate elimination and regeneration as evidenced by dissolved inorganic nitrogen isotopes in Saanich Inlet, a seasonally anoxic fjord. *Marine Chemistry*, *157*, 194–207. https://doi.org/10.1016/j.marchem.2013.09.006

Brandes, J. A., & Devol, A. H. (1997). Isotopic fractionation of oxygen and nitrogen in coastal marine sediments. *Geochimica et Cosmochimica Acta*, *61*(9), 1793–1801. https://doi.org/10.1016/S0016-7037(97)00041-0

Brandes, J. A., & Devol, A. H. (2002). A global marine-fixed nitrogen isotopic budget: Implications for Holocene nitrogen cycling. *Global Biogeochemical Cycles*, *16*(4), 1120. https://doi.org/10.1029/2001GB001856

Brandes, J. A., Devol, A. H., Yoshinari, T., Jayakumar, D. A., & Naqvi, S. W. A. (1998). Isotopic composition of nitrate in the central Arabian Sea and eastern tropical North Pacific: A tracer for mixing and nitrogen cycles. *Limnology and Oceanography*, *43*(7), 1680–1689. https://doi.org/10.4319/lo.1998.43.7.1680

Buchwald, C., & Casciotti, K. L. (2010). Oxygen isotopic fractionation and exchange during bacterial nitrite oxidation. *Limnology and Oceanography*, *55*(3), 1064–1074. https://doi.org/10.4319/lo.2010.55.3.1064

Buchwald, C., & Casciotti, K. L. (2013). Isotopic ratios of nitrite as tracers of the sources and age of oceanic nitrite. *Nature Geoscience*, *6*(4), 308–313. https://doi.org/10.1038/ngeo1745

Buchwald, C., Homola, K., Spivack, A. J., Estes, E. R., Murray, R. W., & Wankel, S. D. (2018). Isotopic constraints on nitrogen transformation rates in the deep sedimentary marine biosphere. *Global Biogeochemical Cycles*, *32*, 1688–1702. https://doi.org/10.1029/2018GB005948

Casciotti, K. L. (2016a). Nitrite isotopes as tracers of marine N cycle processes. *Philosophical Transactions of the Royal Society A: Mathematical, Physical and Engineering Sciences*, *374*(2081). https://doi.org/10.1098/rsta.2015.0295

Casciotti, K. L. (2016b). Nitrogen and oxygen isotopic studies of the marine nitrogen cycle. *Annual Review of Marine Science*, *8*(1), 379–407. https://doi.org/10.1146/annurev-marine-010213-135052

Casciotti, K. L., Böhlke, J. K., McIlvin, M. R., Mroczkowski, S. J., & Hannon, J. E. (2007). Oxygen Isotopes in Nitrite: Analysis, Calibration, and Equilibration. *Analytical Chemistry*, *79*(6), 2427–2436. https://doi.org/10.1021/AC061598H

Casciotti, K. L., Buchwald, C., & McIlvin, M. (2013). Implications of nitrate and nitrite isotopic measurements for the mechanisms of nitrogen cycling in the Peru oxygen deficient zone. *Deep Sea Research Part I: Oceanographic Research Papers*, *80*, 78–93. Retrieved from https://www.sciencedirect.com/science/article/pii/S0967063713001155

Casciotti, K. L., Sigman, D. M., Hastings, M. G., Böhlke, J. K., & Hilkert, A. (2002). Measurement of the oxygen isotopic composition of nitrate in seawater and freshwater using the denitrifier method. *Analytical Chemistry*, *74*(19), 4905–4912. https://doi.org/10.1021/ac020113w

Gaye, B., Nagel, B., Dähnke, K., Rixen, T., & Emeis, K.-C. (2013). Evidence of parallel denitrification and nitrite oxidation in the ODZ of the Arabian Sea from paired stable isotopes of nitrate and nitrite. *Global Biogeochemical Cycles*, *27*, 1059–1071. https://doi.org/10.1002/2011GB004115

Goericke, R., Bograd, S. J., & Grundle, D. S. (2015). Denitrification and flushing of the Santa Barbara Basin bottom waters. *Deep-Sea Research Part II: Topical Studies in Oceanography*, *112*, 53–60. https://doi.org/10.1016/j.dsr2.2014.07.012

Granger, J., & Sigman, D. M. (2009). Removal of nitrite with sulfamic acid for nitrate N and O isotope analysis with the denitrifier method. *Rapid Communications in Mass Spectrometry*, *23*(23), 3753–3762. https://doi.org/10.1002/rcm.4307

Granger, J., Sigman, D. M., Lehmann, M. F., & Tortell, P. D. (2008). Nitrogen and oxygen isotope fractionation during dissimilatory nitrate reduction by denitrifying bacteria. *Limnology and Oceanography*, *53*(6), 2533–2545. https://doi.org/10.4319/lo.2008.53.6.2533

Granger, J., & Wankel, S. D. (2016). Isotopic overprinting of nitrification on denitrification as a ubiquitous and unifying feature of environmental nitrogen cycling. *Proceedings of the National Academy of Sciences of the United States of America*, *113*(42), E6391–E6400. https://doi.org/10.1073/pnas.1601383113

Groffman, P. M., Altabet, M. A., Böhlke, J. K., Butterbach-Bahl, K., David, M. B., Firestone, M. K., et al. (2006). Methods for measuring denitrification: Diverse approaches to a difficult problem. *Ecological Applications: A Publication of the Ecological Society of America*, *16*(6), 2091–2122. Retrieved from http://www.ncbi.nlm.nih.gov/pubmed/17205891, https://doi.org/10.1890/1051-0761(2006)016[2091:MFMDDA]2.0.CO;2

Gruber, N., & Sarmiento, J. L. (1997). Global patterns of marine nitrogen fixation and denitrification. *Global Biogeochemical Cycles*, *11*(2), 235–266. https://doi.org/10.1029/97GB00077

Hu, H., Bourbonnais, A., Larkum, J., Bange, H. W., & Altabet, M. A. (2016). Nitrogen cycling in shallow low-oxygen coastal waters off Peru from nitrite and nitrate nitrogen and oxygen isotopes. *Biogeosciences*, *13*(5), 1453–1468. https://doi.org/10.5194/bg-13-1453-2016

Ito, T., Minobe, S., Long, M. C., & Deutsch, C. (2017). Upper ocean O_2 trends: 1958–2015. *Geophysical Research Letters*, *44*, 4214–4223. https://doi.org/10.1002/2017GL073613

King, A. L., & Barbeau, K. A. (2011). Dissolved iron and macronutrient distributions in the southern California Current System. *Journal of Geophysical Research*, *116*, C03018. https://doi.org/10.1029/2010JC006324

Körner, H., & Zumft, W. G. (1989). Expression of denitrification enzymes in response to the dissolved oxygen level and respiratory substrate in continuous culture of Pseudomonas stutzeri. *Applied and Environmental Microbiology*, *55*(7), 1670–1676. Retrieved from http://www.ncbi.nlm.nih.gov/pubmed/2764573

Kritee, K., Sigman, D. M., Granger, J., Ward, B. B., Jayakumar, A., & Deutsch, C. (2012). Reduced isotope fractionation by denitrification under conditions relevant to the ocean. *Geochimica et Cosmochimica Acta*, *92*, 243–259. https://doi.org/10.1016/j.gca.2012.05.020

Lehmann, M. F., Reichert, P., Bernasconi, S. M., Barbieri, A., & McKenzie, J. A. (2003). Modelling nitrogen and oxygen isotope fractionation during denitrification in a lacustrine redox-transition zone. *Geochimica et Cosmochimica Acta*, *67*(14), 2529–2542. https://doi.org/10.1016/S0016-7037(03)00085-1

Marconi, D., Kopf, S., Rafter, P. A., & Sigman, D. M. (2017). Aerobic respiration along isopycnals leads to overestimation of the isotope effect of denitrification in the ocean water column. *Geochimica et Cosmochimica Acta*, *197*, 417–432. https://doi.org/10.1016/J.GCA.2016.10.012

Martin, T. S., & Casciotti, K. L. (2017). Paired N and O isotopic analysis of nitrate and nitrite in the Arabian Sea oxygen deficient zone. *Deep Sea Research Part I: Oceanographic Research Papers*, *121*, 121–131. https://doi.org/10.1016/j.dsr.2017.01.002

McIlvin, M. R., & Altabet, M. A. (2005). Chemical conversion of nitrate and nitrite to nitrous oxide for nitrogen and oxygen isotopic analysis in freshwater and seawater. *Analytical Chemistry*, *77*(17), 5589–5595. https://doi.org/10.1021/AC050528S

McIlvin, M. R., & Casciotti, K. L. (2011). Technical updates to the bacterial method for nitrate isotopic analyses. *Analytical Chemistry*, *83*(5), 1850–1856. https://doi.org/10.1021/ac1028984

Peng, X., Fuchsman, C. A., Jayakumar, A., Warner, M. J., Devol, A. H., & Ward, B. B. (2016). Revisiting nitrification in the Eastern Tropical South Pacific: A focus on controls. *Journal of Geophysical Research: Oceans*, *121*, 1667–1684. https://doi.org/10.1002/2015JC011455

Peters, B., Horak, R., Devol, A., Fuchsman, C., Forbes, M., Mordy, C. W., & Casciotti, K. L. (2018). Estimating fixed nitrogen loss and associated isotope effects using concentration and isotope measurements of NO3-, NO2-, and N2 from the Eastern Tropical South Pacific oxygen deficient zone. *Deep Sea Research Part II: Topical Studies in Oceanography*, *156*, 121–136. https://doi.org/10.1016/J.DSR2.2018.02.011

Peters, B. D., Babbin, A. R., Lettmann, K. A., Mordy, C. W., Ulloa, O., Ward, B. B., & Casciotti, K. L. (2016). Vertical modeling of the nitrogen cycle in the eastern tropical South Pacific oxygen deficient zone using high-resolution concentration and isotope measurements. *Global Biogeochemical Cycles*, *30*, 1661–1681. https://doi.org/10.1002/2016GB005415

Rafter, P. A., & Sigman, D. M. (2016). Spatial distribution and temporal variation of nitrate nitrogen and oxygen isotopes in the upper equatorial Pacific Ocean. *Limnology and Oceanography*, *61*(1), 14–31. https://doi.org/10.1002/lno.10152

Reimers, C. E., Lange, C. B., Tabak, M., & Bernhard, J. M. (1990). Seasonal spillover and varve formation in the Santa Barbara Basin, California. *Limnology and Oceanography*, *35*(7), 1577–1585. https://doi.org/10.4319/lo.1990.35.7.1577

Roach, L. D., Charles, C. D., Field, D. B., & Guilderson, T. P. (2013). Foraminiferal radiocarbon record of northeast Pacific decadal subsurface variability. *Journal of Geophysical Research: Oceans*, *118*, 4317–4333. https://doi.org/10.1002/jgrc.20274

Sigman, D. M., Casciotti, K. L., Andreani, M., Barford, C., Galanter, M., & Böhlke, J. K. (2001). A bacterial method for the nitrogen isotopic analysis of nitrate in seawater and freshwater. *Analytical Chemistry*, *73*(17), 4145–4153. https://doi.org/10.1021/ac010088e

Sigman, D. M., Granger, J., DiFiore, P. J., Lehmann, M. M., Ho, R., Cane, G., & van Geen, A. (2005). Coupled nitrogen and oxygen isotope measurements of nitrate along the eastern North Pacific margin. *Global Biogeochemical Cycles*, *19*, GB4022. https://doi.org/10.1029/2005GB002458

Sigman, D. M., Karsh, K. L., & Casciotti, K. L. (2009). Nitrogen isotopes in the ocean. In *Encyclopedia of ocean sciences* (pp. 40–54). https://doi.org/10.1016/B978-012374473-9.00632-9

Sigman, D. M., Robinson, R., Knapp, A. N., van Geen, A., McCorkle, D. C., Brandes, J. A., & Thunell, R. C. (2003). Distinguishing between water column and sedimentary denitrification in the Santa Barbara Basin using the stable isotopes of nitrate. *Geochemistry, Geophysics, Geosystems*, *4*(5), 1040. https://doi.org/10.1029/2002GC000384

Wang, Y., Hendy, I., & Napier, T. J. (2017). Climate and anthropogenic controls of coastal deoxygenation on interannual to centennial timescales. *Geophysical Research Letters*, *44*, 11,528–11,536. https://doi.org/10.1002/2017GL075443

Wankel, S. D., Ziebis, W., Buchwald, C., Charoenpong, C., de Beer, D., Dentinger, J., et al. (2017). Evidence for fungal and chemodenitrification based N2O flux from nitrogen impacted coastal sediments. *Nature Communications*, *8*(1), 15595. https://doi.org/10.1038/ncomms15595

Additional Acknowledgements

Chapter 3, in full, is a reprint of the material as it appears in “Recent Increases in Water Column Denitrification in the Seasonally Suboxic Bottom Waters of the Santa Barbara Basin” published in Geophysical Research Letters, 2019. Margot White, Patrick Rafter, Brandon Stephens, Scott Wankel, and Lihini Aluwihare. The dissertation author was the primary investigator and author of this paper.

Geophysical Research Letters

Supporting Information for

Recent Increases in Water Column Denitrification in the Seasonally Suboxic Bottom Waters of the Santa Barbara Basin

Margot E. White[1], Patrick A. Rafter[2], and Brandon M. Stephens[3], Scott D. Wankel[4], Lihini I. Aluwihare[1]

[1]Scripps Institution of Oceanography, University of California, San Diego.

[2]University of California, Irvine.

[3]University of California, Santa Barbara.

[4]Woods Hole Oceanographic Institution.

Contents of this file

Text S1
Tables S1 to S2
Figure S1

Introduction

Presented here is the isotope fractionation factor ($^{15}\varepsilon$) mass balance used to interpret observed temporal variations in the apparent fractionation (ε_{app}) factor for denitrification in our dataset. We also include the nitrite isotope data (Table S1) and the calculated ε_{app} for closed system nitrate reduction between consecutive flushing events (Table S2; see body of paper for method description). Finally, we provide a timeseries demonstrating the secular decrease in oxygen concentrations at 450 m depth in the Santa Barbara Basin (Figure S1), which we use as an index for decreasing oxygen concentrations in intermediate waters of the North Pacific Ocean.

Text S1: Isotope Mass Balance

After estimating $^{15}\varepsilon_{app}$ as described in the paper, we used the following isotope mass balance equation to apportion N loss via denitrification between the sediments and the water column. If we assume that the apparent fractionation factor is a combination of sedimentary and water column denitrification processes, then:

$$^{15}\varepsilon_{app} = {}^{15}\varepsilon_{wc} \text{ x } \%WC + {}^{15}\varepsilon_{sed} \text{ x } \%Sed$$

Using a value of 25 ‰ for the water column fractionation factor and 1.5 ‰ for the sedimentary fractionation factor we calculated the percent of N loss that had occurred in each environment (Sigman et al. 2003). Based on this approach, more water column denitrification is accompanied by a larger $^{15}\varepsilon_{app}$.

Date	Depth (m)	$[NO_3]$ (μM)	$[NO_2]$ (μM)	$\delta^{15}N_{NO3}$ (‰)	$\delta^{18}O_{NO3}$ (‰)	$\delta^{15}N_{NO2}$ (‰)	$\Delta\delta^{15}N$ (‰)
7/2013	570	19.10	2.08	16.97	13.58	-16.34	33.31
11/2013	515	9.10	8.19	31.02	23.97	4.44	26.58
11/2015	570	10.70	3.24	24.32	18.45	-1.87	26.19
1/2016	540	11.40	1.68	20.79	14.63	-7.91	28.70
1/2016	570	7.60	2.80	26.11	16.44	1.68	24.43

Table S1. Nitrogen isotopes of nitrite from the Santa Barbara Basin

Initial date	Final date	Depth (m)	$[NO_3]_{initial}$ (μM)	$[NO_3]_{final}$ (μM)	$[NO_2]_{initial}$ (μM)	$[NO_2]_{final}$ (μM)	$\delta^{15}N_{NO3,\ initial}$ (‰)	$\delta^{15}N_{NO3,\ final}$ (‰)	$^{15}\varepsilon$ (‰)	$denitr_{WC}$ %
1/2011	4/2011	540	29.70	25.00	0	0	9.89	11.29	8.13	28
1/2011	4/2011	570	27.30	24.40	0	0	10.18	11.68	8.06	28
4/2011	7/2011	515	28.60	26.20	0	0.14	10.15	10.98	9.32	33
4/2011	7/2011	570	24.40	13.90	0	2.82	11.08	17.91	12.14	45
7/2011	10/2011	515	26.20	10.00	0.40	6.19	10.98	29.81	19.55	77
10/2011	2/2012	570	8.50	3.70	7.27	6.82	24.68	44.32	24.31	97
3/2012	7/2012	515	26.20	23.90	0.04	0.32	10.77	12.26	16.18	63
4/2013	7/2013	570	32.50	19.10	0.09	2.08	10.18	16.97	12.78	48
7/2013	11/2013	515	27.80	9.10	0.02	8.19	10.61	31.02	18.28	71
11/2015	1/2016	515	23.43	18.08	0.01	0.07	10.99	14.33	15.50	60
11/2015	1/2016	540	18.19	11.37	0.78	1.68	14.82	20.79	12.70	48

Table S2. Estimated nitrogen isotope fractionation factors for nitrate reduction between subsequent periods when no flushing has occurred. Fractionation factors were calculated by finding the slope of a linear fit to a closed system Rayleigh model.

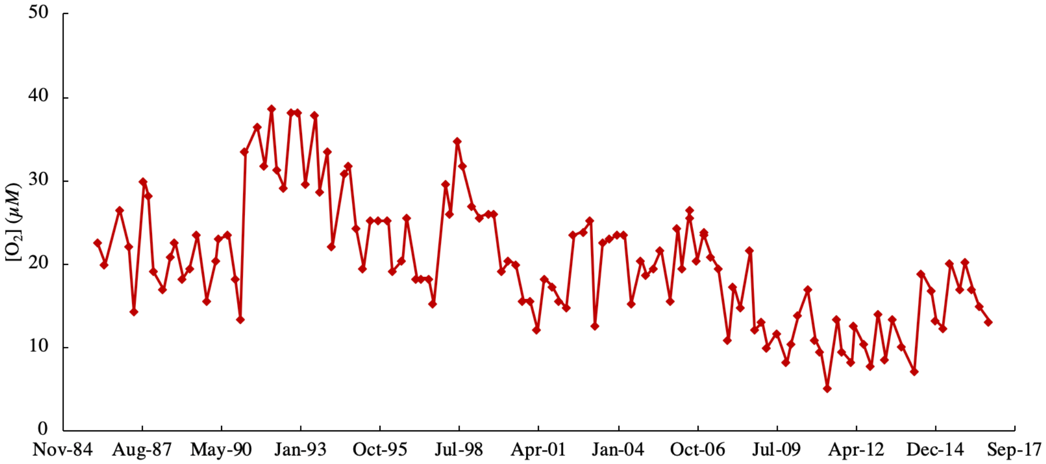

Figure S1. Time series of oxygen concentration at 450m in the Santa Barbara Basin

References

Sigman DM, Robinson R, Knapp AN, et al. Distinguishing between water column and sedimentary denitrification in the Santa Barbara Basin using the stable isotopes of nitrate. *Geochemistry, Geophys Geosystems*. 2003;4(5):n/a-n/a. doi:10.1029/2002GC000384.

Chapter 4: Organic matter composition across oxygen gradients in the eastern tropical North Pacific Ocean

Abstract

As a result of high surface productivity and slow ventilation, the eastern tropical North Pacific (ETNP) "shadow zone" is home to one of the largest anoxic marine zones (AMZs) in the global ocean. AMZs play an essential role in the biogeochemical cycling of a variety of elements due to the diverse metabolisms that can occur when oxygen is depleted. One prominent example is the removal of fixed nitrogen via denitrification and anammox. All of these biogeochemical processes are directly or indirectly related to the supply and subsequent degradation of organic matter, yet the composition of organic matter within and around these regions remains understudied. The aim of this project was to use a variety of measurements to examine the quantity and quality of organic matter across horizontal and vertical oxygen gradients in the ETNP, and to compare these findings with rates of oxygen consumption. We found that the majority of the observed trends in our data can be best explained by the gradient of production and remineralization processes both vertically in the water column and along the oxygen gradient, rather than by differences in oxygen concentration alone. Fluorescent dissolved organic matter (FDOM) appeared to vary along the oxycline above AMZs and oxygen consumption rates could be linked to differences in DOM composition as reflected by its optical properties. In our dataset, other bulk organic matter properties such as C, N, and P concentrations, and elemental ratios did not differ significantly inside the AMZ compared to more oxygenated waters. We also provide evidence via the use of a novel technique to measure stable isotopes of sulfur that sulfurization reactions appear to be unimportant in the dissolved organic sulfur pool within the ETNP AMZ. In 2018, a category 4 hurricane passed through our study region which resulted in increased vertical mixing and shoaling of low oxygen waters, which altered the local biogeochemistry.

Introduction

In certain areas of the subsurface ocean, highly productive overlying waters result in high rates of remineralization at depth which conspire with slow ventilation to deplete oxygen concentrations to nanomolar levels (Wyrtki 1962). These anoxic marine zones (AMZs) usually occur between 200 and 1000 m, and can be seasonal or permanent (Oschlies et al. 2018). When oxygen is depleted, the absence of this key ingredient in aerobic respiration results in a radically altered microbial community capable of using a variety of substrates to fuel their metabolisms (Canfield et al. 2010; Lam and Kuypers 2011; Wakeham 2020). Heterotrophic organisms first turn to nitrate, and via a process known as denitrification are responsible for the removal of a major fraction of bioavailable nitrogen from the oceans (Christensen et al. 1987; Devol 2015). Incomplete denitrification can result in nitrite accumulation in the AMZ as well as a significant flux of nitrous oxide, a potent greenhouse gas, into the atmosphere (Babbin et al. 2015).

Anammox, another specialized metabolism restricted to AMZs, is also implicated in fixed nitrogen removal, but as an autotrophic mechanism it is only dependent on organic matter because the reductant ammonium is produced from organic nitrogen degradation and the oxidant nitrite is produced during incomplete denitrification, which as described above is a heterotrophic metabolism (Thamdrup and Dalsgaard 2002; Kuypers et al. 2003).

The three largest, permanent AMZs are located in the eastern tropical North Pacific, eastern tropical South Pacific, and Arabian Sea and nitrogen loss from these regions is estimated to comprise up to half of all fixed nitrogen loss from the oceans (Codispoti et al. 2001). The ETNP in particular is also subject to periodic disruption by tropical storms and hurricanes, which have been shown to impact the water column down to 200 m and are predicted to increase in intensity under climate change (Bhatia et al. 2019).

An additional and perhaps unexpected, distinguishing feature of AMZs is the presence of a secondary chlorophyll maximum (SCM) where cyanobacteria produce oxygen and organic matter within the low oxygen water column via photosynthesis (Goericke et al. 2000; Lavin et al. 2010; Garcia-Robledo et al. 2017). This can result in cryptic oxygen cycling as well as the co-occurrence of aerobic and anaerobic processes, and varying oxygen concentrations will determine which nitrogen loss processes occur when and where (Kalvelage et al. 2011). The potential for AMZs to expand with future global warming highlights the importance of constraining the controls on and extent to which *aerobic* respiration is occurring near the boundaries (above and below) of the AMZ as this may further deplete oxygen concentrations in these areas as well (Deutsch et al. 2011; Beman and Carolan 2013). In addition to respiration of organic matter, other oxygen consuming processes such as nitrite and ammonia oxidation have been shown to occur even at very low oxygen concentrations, potentially contributing to the maintenance of the AMZ (Bristow et al. 2016; White et al. 2019).

While it is well known that organic matter (OM) availability plays an important role in structuring microbial communities and elemental cycles within the AMZ, less is known about how OM is altered as it transits via vertical export or horizontal advection through AMZs. Studies have shown that OM flux is poorly attenuated within AMZs (Keil et al., 2016, Pavia et al 2019) but potentially processed to a greater extent at shallower depths; i.e., greater remineralization in the upper oxycline but lower remineralization in the AMZ (e.g., Pavia et al. 2019). The decreased attenuation of particle flux within AMZs reported in some studies (e.g., Keil et al. 2016) mimics the enhanced OM preservation observed in anoxic sediments (Hartnett et al. 1998; Burdige 2007; Schimmelmann et al. 2016) . Indeed it has been shown that certain compounds that are readily degraded under oxic conditions remain intact when subjected to anoxic remineralization processes (Bonaglia et al. 2016; Harvey et al.1995). In contrast, other studies have observed preferential degradation of nitrogen-containing compounds in these regions (Maßmig et al. 2020) that could be linked to the nitrogen-loss processes described above. These dynamics contribute to the potential complexity of low oxygen OM cycling.

Low oxygen waters are also relevant to the marine sulfur cycle, as sulfate in addition to nitrate can be used as an electron acceptor during the respiration of organic matter. Previous studies have demonstrated that sulfate reduction to sulfide occurs in the low oxygen water column (Canfield et al. 2010; Carolan et al. 2015), sometimes in the presence of measurable nitrate (Carolan et al. 2015), but organic sulfur remains hard to access analytically due its low concentration relative to sulfate. Recently, Raven et al. 2021 showed that once sulfide is produced it can participate in sulfurization reactions - abiotic reactions between dissolved sulfides and OM that can decrease OM lability- on sinking particles, perhaps within nitrate free microenvironments, within the ETNP AMZ. This sulfurized organic matter was found to be resistant to acid hydrolysis, suggesting that it could contribute to long term storage of OM matter in sediments underlying AMZs. It is unclear to what extent sulfurization reactions in the low oxygen water column may impact the dissolved organic matter (DOM) pool, given the presence of other potential sulfur oxidants in the water column.

Under most climate change scenarios, it is predicted that AMZs and OMZs will expand (Stramma et al. 2008). As such, it will become even more important to understand their role in carbon flux modulation either though decreased degradation or through structural modifications such as sulfurization or preferential organic nitrogen removal, that may enhance preservation. In order to better understand organic matter cycling in the low oxygen water column, we used a wide variety of characterization methods and isotope measurements to study OM composition along vertical and horizontal oxygen gradients in the eastern tropical North Pacific's permanent AMZ, with a particular emphasis on the traditionally understudied DOM pool. We use these results in combination with measurements of oxygen consumption to build a more comprehensive picture of the biogeochemistry of these unique oceanic environments.

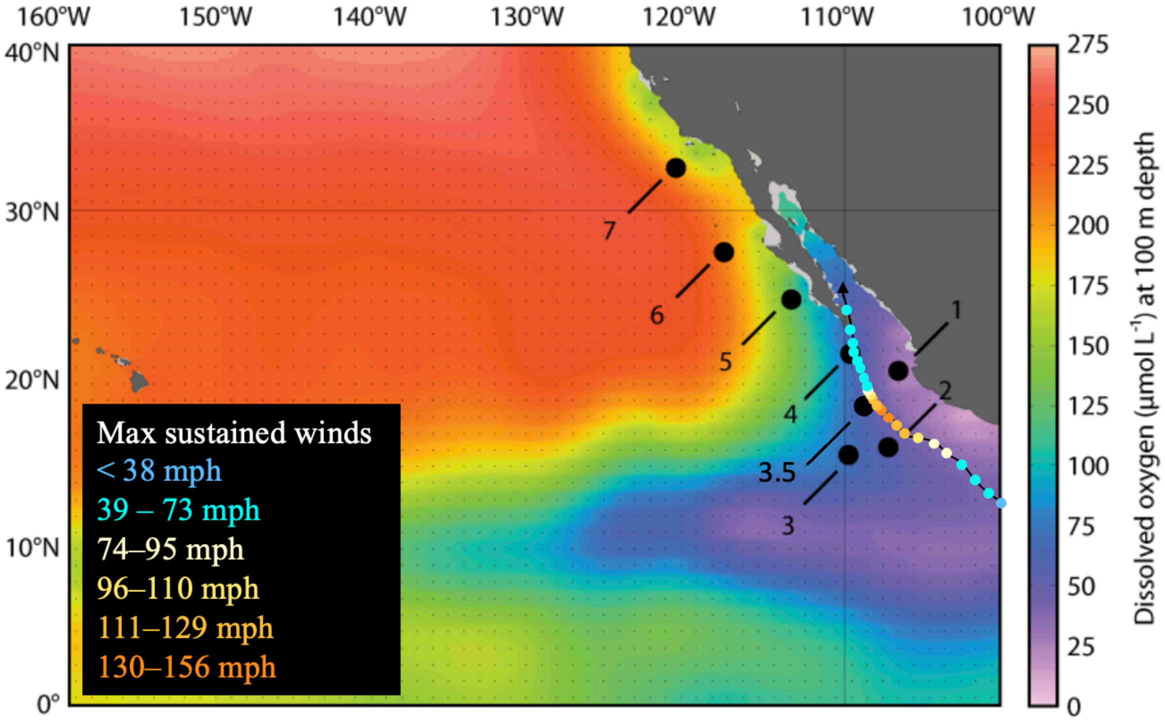

Figure 4.1. Station locations in the eastern tropical North Pacific (ETNP) plotted over dissolved oxygen concentrations (in μM) at 100 m depth from the World Ocean Atlas. Stations 1-7 were sampled in 2017 and Stations 1-5 plus Station 3.5 were sampled in 2018 (Table S4.1). All of these stations have an oxygen minimum zone (OMZ), but not all of them see oxygen concentrations drop low enough to be classified as anoxic marine zones (AMZs). The colored dots show the path of Hurricane Bud, which passed through the region in June 2018, traveling northwest, after the sampling at Station 1 and before the remainder of the cruise. Colors indicate the intensity of the storm based on the Saffir-Simpson scale (data from the National Hurricane Center).

Methods

Sample Collection

Samples were collected aboard the *R/V Oceanus* on two cruises to the ETNP region off the coast of Mexico in April 2017 and June 2018. Our first cruise began at Station 7 and ended at

Station 1. The second cruise began at Station 1 and ended at Station 5 with an additional Station (3.5) added between Stations 3 and 4 (Figure 4.1). The goal was to capture variations across the ETNP by sampling locations chosen to capture both horizontal and vertical oxygen gradients (Figures 4.1, S4.1). Sampling for the 2018 cruise was briefly interrupted by Hurricane Bud (June 9-15, 2018; Figure 4.1), a category 4 storm which passed through the region (Stewart 2019). At each station, conductivity/salinity, temperature, depth, pressure, chlorophyll fluorescence, and photosynthetically active radiation (PAR) were measured by a SeaBird SBE 9 CTD, SBE 43 DO sensor, WetLabs Fluorometer, and Biospheric PAR sensor. Initial casts at each Station were used to determine DO concentrations and measure nutrient profiles to guide subsequent sampling (Figures 4.2 and S4.2). At each Station, water samples were collected at depths along a gradient targeting a range of oxygen concentrations (200, 100, 50, 20, 10, 5, 1, 0.5, 0.1, and 0.05 μM) in order to examine biogeochemical variations along the sharp oxygen gradients found in this region. Samples in addition to those along this oxygen gradient were collected on the 2018 cruise in order to improve the resolution of profiles. Seawater for [TOC] analysis was collected directly from Niskin bottles mounted on a standard conductivity-temperature-depth rosette system (CTD) into combusted 40-mL borosilicate vials and sealed using acid-washed vial caps with septa. DOC samples were collected the same way except water was first filtered through pre-combusted GF/F filters (0.7 μm pore size). Samples were immediately acidified to pH 2 using trace metal grade 12N HCl (Fisher Scientific). Fluorescent and colored dissolved organic matter (FDOM/CDOM) samples were filtered through pre-combusted GF/F filters and collected directly into combusted amber 40-mL borosilicate vials before being sealed using acid-washed vial caps with septa and refrigerated until analysis. Samples for DON/DOP were filtered through GF/F filters (0.7 μm pore size) and frozen until analysis. Samples for bioavailable dissolved organic nitrogen (BDON) analysis were collected in the same way as DON/DOP. Particulate organic matter (POM) was collected onto pre-combusted GF/F filters via filtration under low vacuum of 5 L of seawater collected from Niskin bottles. Filters were kept in frozen storage until analysis. DOM was concentrated via solid-phase extraction (PPL resin) from 5 L of seawater acidified to pH 2 using 12N HCl at Stations 2-3 and 4-5 during the 2018 cruise. Extraction was done via gravity, but largely after Dittmar et al. 2008.

TOC and DOC analyses

Acidified samples were stored at room temperature in the dark until analyzed via high-temperature combustion on a Shimadzu 500 V-CSN/TNM-1 (Shimadzu Corp, Kyoto, Japan) that was modified from the manufacturer's design. The Shimadzu combustion oven contained a quartz column filled with platinum (Pt) catalyst beads. Combustion columns were pre-conditioned on 40 - 100 injections of filtered (0.2 μm) seawater until the baseline of measured carbon was stable. A magnesium perchlorate water-trap was placed prior to the halogen trap and changed daily. CO_2-free carrier gas was used to pre-condition the column, and ultra-high purity grade O_2 gas was delivered to the instrument as the carrier gas during sample analysis.

Each acidified TOC sample was sparged for two minutes and measured following high-temperature combustion at 680˚ C. During analysis, five 100 μL injections were made from a single sample reservoir, and samples were reanalyzed when the %CV of the best 3 injections was >5%. TOC measurements were calibrated using an 8-point calibration curve between 10 and 100 μM C of potassium phthalate in Milli-Q water. Milli-Q water and a reference water sample were analyzed every 10 samples. Reference standards were obtained from NSF-supported deep Florida Strait (Batch 6FS – 2006; Dennis Hansell, RSMAS, University of Miami). The expected concentration range for Batch reference materials is provided at http://www.rsmas.miami.edu/groups/biogeochem/. Further details of sample analysis details and data verification protocols can be found at cce.lternet.edu/research.

Nutrient Concentration Measurements

Nutrient samples were analyzed for NH_4^+ and NO_2^- aboard the ship, with additional shore-based analyses of combined NO_3^- + NO_2^- and PO_4^{3-} at the University of California Santa Barbara Marine Science Institute (UCSB MSI) Analytical Lab. Samples were analyzed at sea for NH_4^+ using the fluorescent method of Holmes et al. (1999) and for NO_2^- using the sulfanilamide method, both on a Trilogy Laboratory Fluorometer (Turner Designs; San Jose, CA, USA) equipped with the NH_4^+ or NO_2^- module. For more details, see Beman et al. 2020a. Organic nutrient concentrations were measured at the SOEST Laboratory for Analytical Biogeochemistry at the University of Hawaii at Manoa using a Seal Analytical AA3 HR Nutrient Autoanalyzer (http://www.soest.hawaii.edu/S-LAB/equipment/slab_autoanalyzer.htm). The reported relative standard deviation was 1.4 % for total nitrogen (TN), and 1.5 % for total phosphorus (TP). Relative standard deviation for NO_3^- + NO_2^- was 0.5 % and 0.4 % for PO_4^{3-}. For NH_4^+ the reported relative standard deviation was 1.3 %. Dissolved organic nitrogen (DON) concentrations were calculated by subtracting NO_3^- + NO_2^- and NH_4^+ from TN, and uncertainty was propagated accordingly. Dissolved organic phosphorus (DOP) concentrations were calculated by subtracting PO_4^{3-} from TP. DOP as defined here may contain inorganic P species such as pyrophosphate and other condensed P-containing polymers. Dissolved C:N ratios were calculated by dividing the DOC concentration by the DON concentration. C:N ratios where the propagated error was greater than 20 % of the value were excluded from subsequent analysis.

BDON (bioavailable dissolved organic nitrogen) was measured by proxy using a procedure known as the primary amine method, recently developed by R. Letscher and L.

Aluwihare. Briefly, samples were thawed and then hydrolyzed using HCl at concentration of 1 M. Acid was removed using a centrivap and the sample re-suspended in a bicarbonate buffer. Following the addition of OPA (o-Phtalaldehyde), samples were excited at 350 nm and fluorescence measured at 450 nm. Results were compared to a standard curve of known glycine concentrations to estimate concentration of primary amines. Each sample was run in triplicate and reported uncertainties are the standard deviation of these replicates. Percent bioavailable DON was calculated by dividing the BDON concentration by the DON concentration, and error was propagated accordingly.

FDOM and CDOM Analyses

FDOM samples were measured on a Horiba FluoroMax for FDOM on emission (Em) wavelengths 280-550 nm and excitation (Ex) wavelengths 250-450nm. For each day of analysis, the instrument was warmed up at least one hour before making the first measurement. At least two milliQ (~18 ohms) blanks were collected for each day for blank correction purposes. Raw data were exported from the instrument and corrected for a signal to response ratio by dividing the sample (S1) by the filter (R1) signal.

Methods for PARAFAC followed after Stedmon et al. 2008 and was used in order to identify the primary fluorescent components of DOM. FDOM data were first imported into Matlab for the entire Ex/Em range measured; however, preliminary use of PARAFAC demonstrated that instrument artifacts were overwhelming the spectra at excitation wavelengths <275 nm, and so these wavelengths were then excluded from further analyses. Tuckers congruence analysis identified four principal components to effectively model observations at a statistically significant level (more components than this failed the split-half analysis test). The

Ex/Em for the four components are as follows: Component 1 (Ex, Em: 320, 390), Component 2 (275, 485), Component 3 (255, 460), and Component 4 (280, 290).

CDOM samples were measured in a 10 cm cuvette by scanning in a dual-beam spectrophotometer (Cary 300 Agilent). Prior to each sample analysis, cuvette was rinsed with purified water (MilliQ) and then conditioned with sample water; MilliQ was used as the reference material. α_{CDOM} is derived from OD_s based on Helms et al. 2008. Open ocean waters show only very low absorbance at wavelengths of 400–600 nm, so absorption at 325 nm (α_{CDOM} (325)) was used as a proxy for open ocean CDOM concentrations (Nelson and Siegel 2013). Spectral slopes for the intervals 275–295 nm ($S_{275\text{–}295}$) and 350–400 nm ($S_{350\text{–}400}$) were calculated based on Helms et al. 2008 . The CDOM alteration indicator, slope ratio (S_R), was also calculated after Helms et al. 2008 as the ratio of $S_{275\text{–}295}$ and $S_{350\text{–}400}$.

POM Analyses

For POM analysis, inorganic carbon was removed by acidifying the filters with HCl vapor, followed by oven drying, overnight. One half of the filter was transferred to a pre-weighed tin cup for analysis. Blank filters were prepared in the same way to constrain any process contamination. Filter material was analyzed for C and N mass and stable isotopes on an elemental analyzer (Costech, model ECS 2010) coupled to an isotope ratio mass spectrometer (Thermo, model Delta Plus XP) at Scripps Institution of Oceanography’s unified laboratory facility. The measured isotope value varies as a function of the area response of the sample, and at low N concentrations the response deviates dramatically from a linear relationship. To correct for this bias, nine different quantities of finely powdered acetanilide standards (Baker A068-03) of constrained isotopic value were dispersed throughout each run. Standards were cross-calibrated to NBS-19 limestone in terms of Vienna Pee Dee Belemnite and IAEA-N1 ammonium sulfate in terms of pure nitrogen gas from air. The isotopic error for each measurement was then determined as a function of area response and was approximately 0.3 ‰ for $\delta^{13}C$ and 0.5 ‰ for $\delta^{15}N$.

SPE Analyses

One fourth to a third of each SPE DOM extract was transferred to pre-weighed tin cups and dried in an oven over multiple days to remove any residual methanol or water. The material was analyzed for C and N mass and stable isotopes on an elemental analyzer (Costech, model ECS 2010) coupled to an isotope ratio mass spectrometer (Thermo, model Delta Plus XP) as detailed above for POM. The remainder of each SPE DOM extract was used for measurements of C:S and stable sulfur isotope values ($\delta^{34}S$). This work was done by collaborators at the California Institute of Technology using a recently developed method after Phillips et al. 2021. Briefly, SPE-DOM was concentrated to 100 µL and aliquots corresponding to ~350 µg DOC were transferred to ultra clean smooth walled tin capsules (6 x 2.9 mm, OEA Labs). Tin capsules were combusted in an Elemental Analyzer Isolink (Thermo) coupled to an IRMS (Thermo, Delta V). Evolved gases were separated on a ramped GC column that allows SO_2 gas to be trapped at lower temperatures and later eluted at higher temperature, improving signal to noise ratios ~50x compared to previous EA-IRMS methods.

Rate measurements

Rate measurements were performed by collaborators at UC Merced, and a detailed description of the methods used to calculate oxygen consumption rates is available in Beman et al. 2020b. Briefly, oxygen consumption rates were measured at Stations 1-7 using 5 replicates at each depth, including one each with tracer level (5-10% *in situ* concentration) addition of $^{15}NH_4^+$ or $^{15}NO_2^-$ to measure ammonia or nitrite oxidation respectively (nitrite and ammonia oxidation rates were not measured at Station 7). Loligo sensor spots (Fibox, Loligo Systems, Viborg, Denmark) were attached to the inside of 300 mL Wheaton BOD glass bottles using silicone glue. Bottles were filled to at least three times overflowing, rapidly capped and transferred to the cold van, for initial DO measurements. After incubation, endpoint DO measurements were taken.

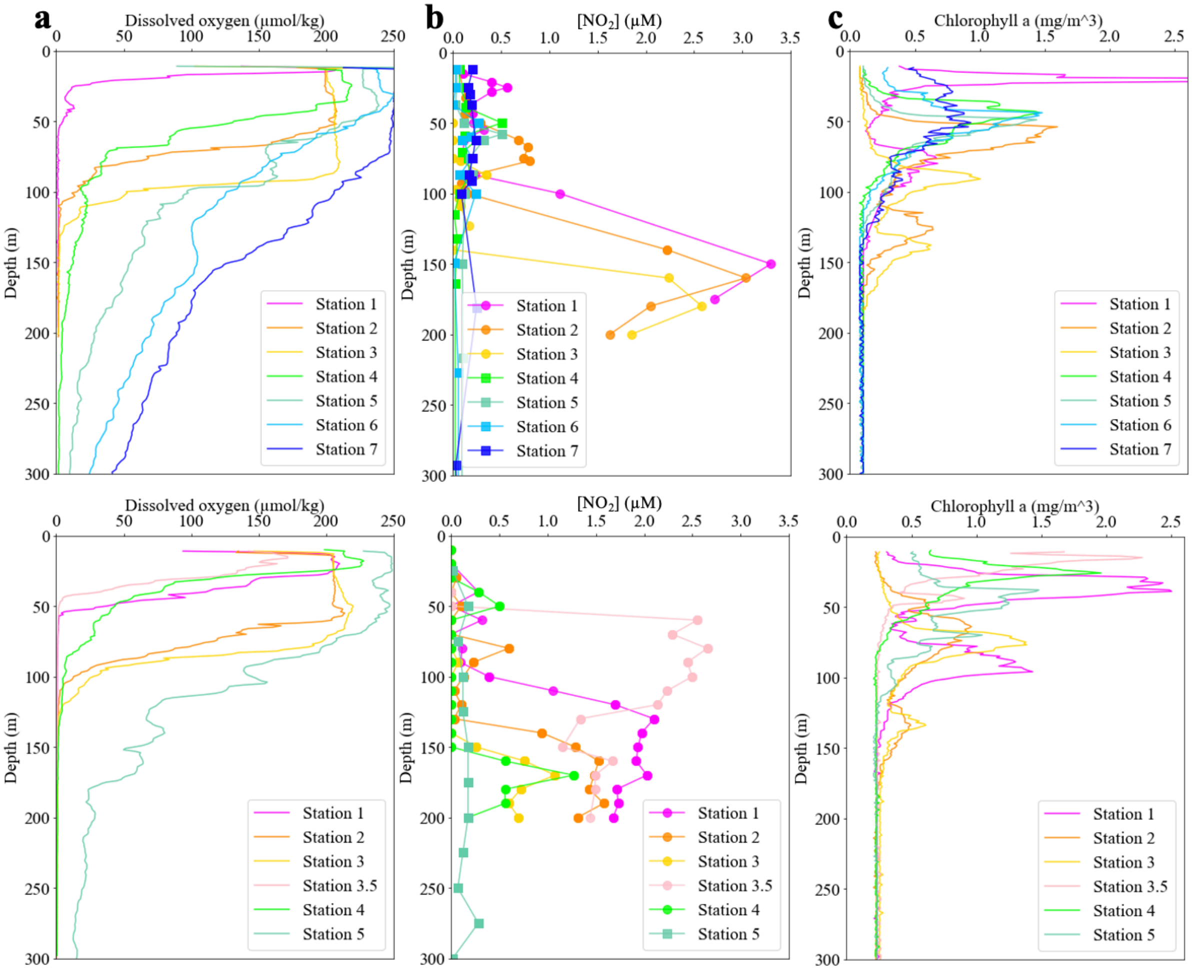

Figure 4.2. General station characteristics from the ETNP. In (**a**) dissolved oxygen is plotted with increasing depth. In (**b**) nitrite concentrations are shown. Circles indicate stations designated as 'AMZ' while squares show 'non-AMZ' stations. In panel (**c**), chlorophyll concentration is plotted with depth for all stations sampled. The top row shows data from the April 2017 cruise, and the bottom row from the June 2018 cruise.

Results

Oceanographic context

Stations sampled for this study span oxygen gradients both with depth and across space (Figures 4.1, 4.2a, S4.1). The June 2018 cruise was impacted by Hurricane Bud, a category 4 storm that passed through the region from June 9-15, and interrupted sampling between Stations 1 and 2 (Stewart 2019). This large storm seems to have had an impact on water column properties, and thus conditions for some stations sampled during the 2018 cruise may have been anomalous. In order to facilitate comparison, samples were divided into one of four categories based on the oxygen concentration where they were collected. Designations are based on Wakeham (2020) where anoxic corresponds to oxygen concentrations less than 2 µM, suboxic is between 2 and 20 µM, dysoxic is 20 to 90 µM, and concentrations above 90 µM are considered oxygenated.

Figure 4.2 shows oxygen, nitrite, and chlorophyll profiles for all stations. For 2017, Stations 1-3 are considered to be 'AMZ' stations, with oxygen concentrations decreasing to below 2 µM around 60 m at Station 1, and closer to 150 m at Stations 2 & 3. Oxygen concentrations at Station 4 decreased to 2 µM, but Station 4 did not exhibit the other characteristics associated with a true AMZ (see below). Stations 5-7 were more typical of open ocean conditions where O_2 concentrations in the OMZ remained greater than 5 µM and captured a horizontal gradient where OMZ oxygen concentrations increase from Station 4 through Station 7 at densities between ~1026 and 1031 kg/m^3 (Figure S4.1). In June 2018, the AMZ region had expanded, such that oxygen concentrations reached levels below 2 µM at Station 4 (Figure 4.2a). Oxygen concentrations at Station 1 decreased rapidly in the upper 60 m, similar to what was observed in 2017. In 2018, Stations 3.5 and 4 also had shallow, steep, oxyclines.

The secondary nitrite maximum (SNM) is the product of nitrate reduction within the low oxygen water column, and a greater accumulation of nitrite is associated with higher rates of denitrification (Casciotti 2016). Stations were designated as AMZ or non-AMZ based on the presence of a SNM (Figure 4.2b). We see that for Stations 1-3, the maximum nitrite concentration was greater in 2017 (up to 3.3 μM) compared to 2018 (up to ~2 μM). In 2018, the nitrite maxima are broader suggesting higher integrated water column nitrification rates in 2018, however, this cannot be confirmed because of the much sparser depth coverage in 2017, which may have missed the true extent of the nitrite maximum. While Station 4 does not have a SNM in 2017, we do see one in 2018 with nitrite accumulating to concentrations above 1 μM. When comparing both years, the shallowest expression of the AMZ and SNM (starting at ~ 50 m) was detected at Station 3.5, sampled only in 2018. The SNM remained high down to 200 m, the deepest depth that was sampled at this Station. The vertical extent of the AMZ and SNM marks a potentially important difference in conditions between Station 1, sampled prior to Hurricane Bud and more closely resembling conditions observed at this location in 2017, and Station 3.5 sampled in 2018 following the hurricane.

We see that the majority of AMZ stations exhibited a secondary chlorophyll maximum (SCM) in both years (Figure 4.2c), although we do not see one at Station 4 in 2018 despite low water column oxygen concentrations and the presence of an SNM (Figure 4.2a). Chlorophyll concentrations exceeded 2.0 mg m^{-3} at Station 1 in both 2017 and 2018 and at Station 3.5 in 2018; but Station 1 in 2018 had higher integrated chlorophyll concentrations due to the much broader primary and secondary maxima. In 2018, Station 4 the maximum chlorophyll concentration was higher and present shallower in the water column than in 2017, but again, integrated chlorophyll concentrations were more comparable. In both years, Station 2 and 3 had deeper primary and secondary chlorophyll maxima, consistent with their more offshore locations. There is no clear productivity gradient but based on chlorophyll and POM concentrations Stations 1 and 3.5 were generally the most productive.

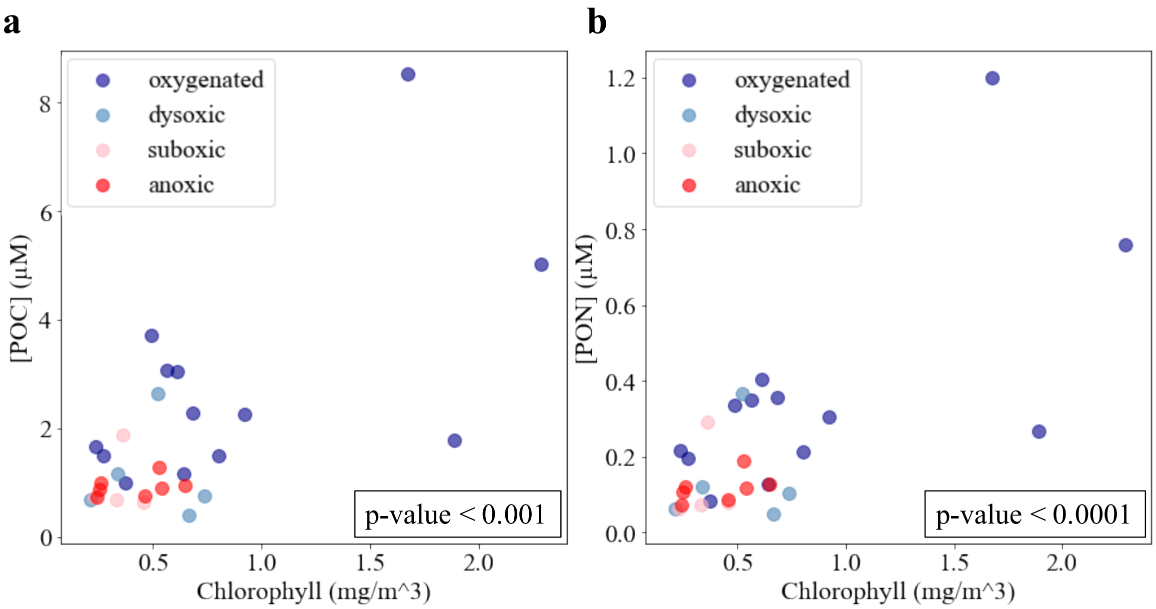

Figure 4.3. Concentrations of particulate organic carbon (a) and nitrogen (b) from the 2018 cruise plotted against chlorophyll. Both POC and PON were significantly related to chlorophyll (p-value < 0.001) with Pearson r values of 0.624 and 0.702 respectively. The color of each point indicates the oxygen concentration.

Organic matter concentrations

In 2018, particulate organic carbon and nitrogen (POC and PON) concentrations generally decreased with increasing depth (p-values for Pearson correlation both < 0.001) consistent with production in the euphotic zone (Figure S4.3). For both POC and PON, there was a significant correlation with chlorophyll (Figure 4.3) and the depth profiles of both POC and PON are very similar (Figure S4.3). However, the relationship between PON and chlorophyll was stronger than between POC and chlorophyll (p-value < 0.0001 vs. p-value < 0.001), primarily because there are near surface accumulations of POC at Station 4 and 5 that are not correlated with high chlorophyll concentrations. No clear difference was apparent between POC or PON concentrations for AMZ versus non-AMZ samples (Figure 4.3), but our limited dataset did not allow us to test this conclusively (Table S4.2; n = 7).

Dissolved organic carbon (DOC) concentration profiles demonstrate the expected trend of decreasing concentrations deeper in the water column and have a tight relationship with density suggestive of the importance of water mass mixing. Higher DOC concentrations that fall off the mixing line can be attributed to surface ocean production (Figure 4.4a). Typically, we observed that depths with higher chlorophyll concentrations supported higher DOC concentrations (e.g., Stations 1, 2 and 3). However, Stations 3.5 and 4 (Figure S4.4) showed the lowest near-surface DOC concentrations in 2018 despite high chlorophyll. Note that DOC concentrations are as low as 46-56 µM C near 50 m as these sites, indicating that upwelling or intense vertical mixing delivered low DOC water to the surface at this site, resulting in overall low concentrations. However, the addition of new DOC at these sites are indicated by the steep gradient in DOC profiles in the upper 50 m at Stations 3.5 and 4. Recent upwelling at this site is further supported by relatively lower surface water temperatures (21-24ºC) at Stations 3.5 and 4 versus Stations 1-3 (26-29ºC) (Figure S4.2a). Station 5 exhibited the lowest surface water temperature in 2018 and had low DOC concentrations (intermediate between Station 3.5 and 4) as well, suggestive of local upwelling.

Compared with DOC, depth profiles of DON (4.4b) and DOP (4.4c) from 2017 and 2018 were much more dynamic. Concentrations of DON ranged from approximately 0.4 µM up to 11.5 µM with an average of 3.4 ± 2.6 µM. Concentrations were generally higher in the surface ocean, decreasing with increasing density (Pearson $r = -0.609$, p-value < 0.0001). The relationship between DON and chlorophyll was also significant (p-value < 0.01) but was less direct than was expected likely because the complex interactions between production, removal, and mixing obscure the net DON production signal. Depth profiles of DOP were also highly variable, ranging from effectively zero up to 1.3 µM with an average of 0.26 ± 0.27 µM. Variation was higher in 2018 (Figure S4.6), and particularly high concentrations of DOP were observed throughout the water column at Stations 3.5-5 in 2018 that were not reflected in increased DOC or DON concentrations (Figure S4.4 and S4.5). Average DOP concentrations between 100 and 400 m were 0.14 ± 0.12 µM in April 2017 compared to 0.33 ± 0.37 µM in June 2018. When comparing samples from the AMZ to those of more oxygenated waters at a similar depth, no significant difference was observed for DOC, DON, or DOP concentration, and means and standard deviations were remarkably similar (Table S4.2).

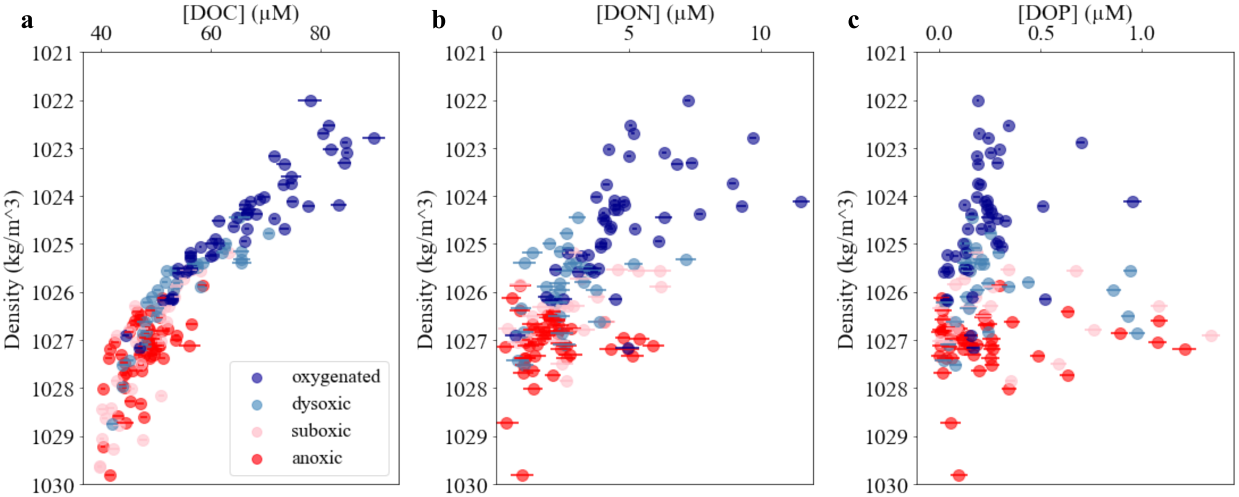

Figure 4.4. Concentrations of dissolved organic nutrients. In (**a**) dissolved organic carbon concentration is plotted with increasing density. In (**b**) dissolved organic nitrogen, and in (**c**) dissolved organic phosphorus. The color indicates oxygen concentration. Anoxic is less than 2 µM, suboxic is 2-20 µM, dysoxic is 20-90 µM, and oxygenated is greater than 90 µM. Error bars are based on the standard deviation.

To date, only four stations (1-2 and 4-5 in 2018) have been analyzed for bioavailable dissolved organic nitrogen (BDON), with concentrations ranging from close to zero up to almost 1.5 µM (Figure 4.5a). We anticipated that this assay may be able to identify any preferential removal of labile N compounds within the AMZ. Overall, concentrations of BDON decreased with increasing density (Pearson *r* = -0.564, p-value < 0.0001), but the relationship with chlorophyll concentration was less pronounced (Pearson *r* = 0.254, p-value = 0.062) as was the relationship with DON concentration itself (Pearson *r* = 0.315, p-value = 0.019). Considering the percent of DON which is bioavailable (Figure 4.5b) we found that BDON was generally below 50 % of total DON. There were some higher values deeper in the water column at Stations 1 and 2, but these seem to be driven largely by a decrease in DON concentration, and the error bars are correspondingly large (Figure 4.5b). This is also reflected in the strong correlation between %BDON and TOC:DON ratios (Pearson *r* = 0.923, p-value < 0.0001), which suggests that both parameters are largely controlled by the concentration of DON, which appears to be more dynamic.

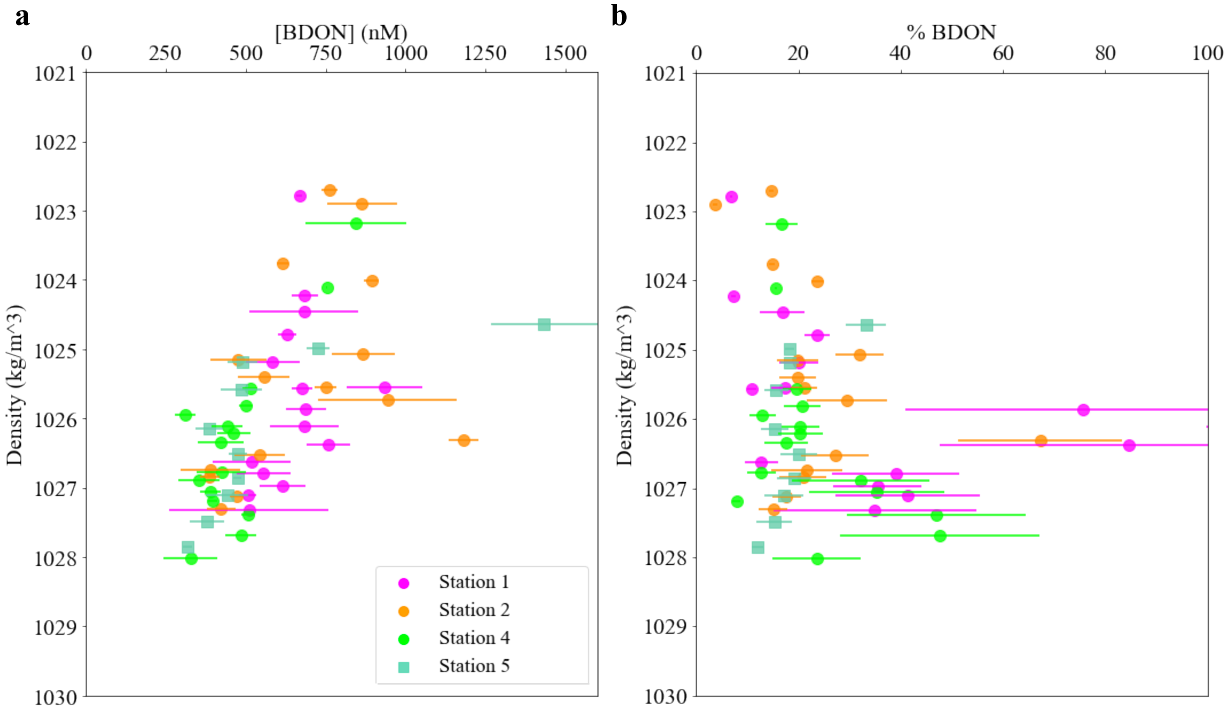

Figure 4.5 Bioavailable dissolved organic nitrogen (BDON). In (**a**) BDON concentration for four Stations from June 2018 is plotted with increasing density. In (**b**) the percent of all dissolved organic nitrogen that is considered ‘bioavailable’ is shown with density. Circles indicate Stations designated as ‘AMZ’ and squares show ‘non-AMZ’ Stations.

FDOM and CDOM

Bulk DOM can also be interrogated using its fluorescence and absorbance characteristics. Although light absorbing and fluorescent components of DOM represent only a small fraction of total DOM these measurements have provided insights into DOM cycling in various environments (Nelson and Gauglitz 2016). The PARAFAC analysis of FDOM spectra yielded four primary components: C1 (Ex, Em: 320, 390), which is referred to in the literature as "marine humic", and is generally described as being the products of bacterial reworking of marine DOM (Loginova et al. 2016); C2 (275, 485) and C3 (255, 460) are considered "humic-like"; and C4 (280, 290), which is characterized as "protein-" or "amino acid-like" (Stedmon and Bro 2008).

The distribution and abundance of C1 (marine humic) differed between stations with an AMZ and those with more oxygenated intermediate waters. This component was also identified in the only previous study looking at FDOM within an AMZ (Loginova et al. 2016). Although profiles for all stations show the characteristic increase at depth that led to the designation of this signal as 'marine humic-like', there are more pronounced maxima above 150 m at Stations 1-4 in 2017 and 2018 (Fig. 4.6). The depth of this maximum for each AMZ Station was positively correlated with the depth of the greatest change in oxygen concentrations with depth ($R^2 = 0.92$), indicating that it is likely a product of the remineralization gradient (Figure 4.6c)

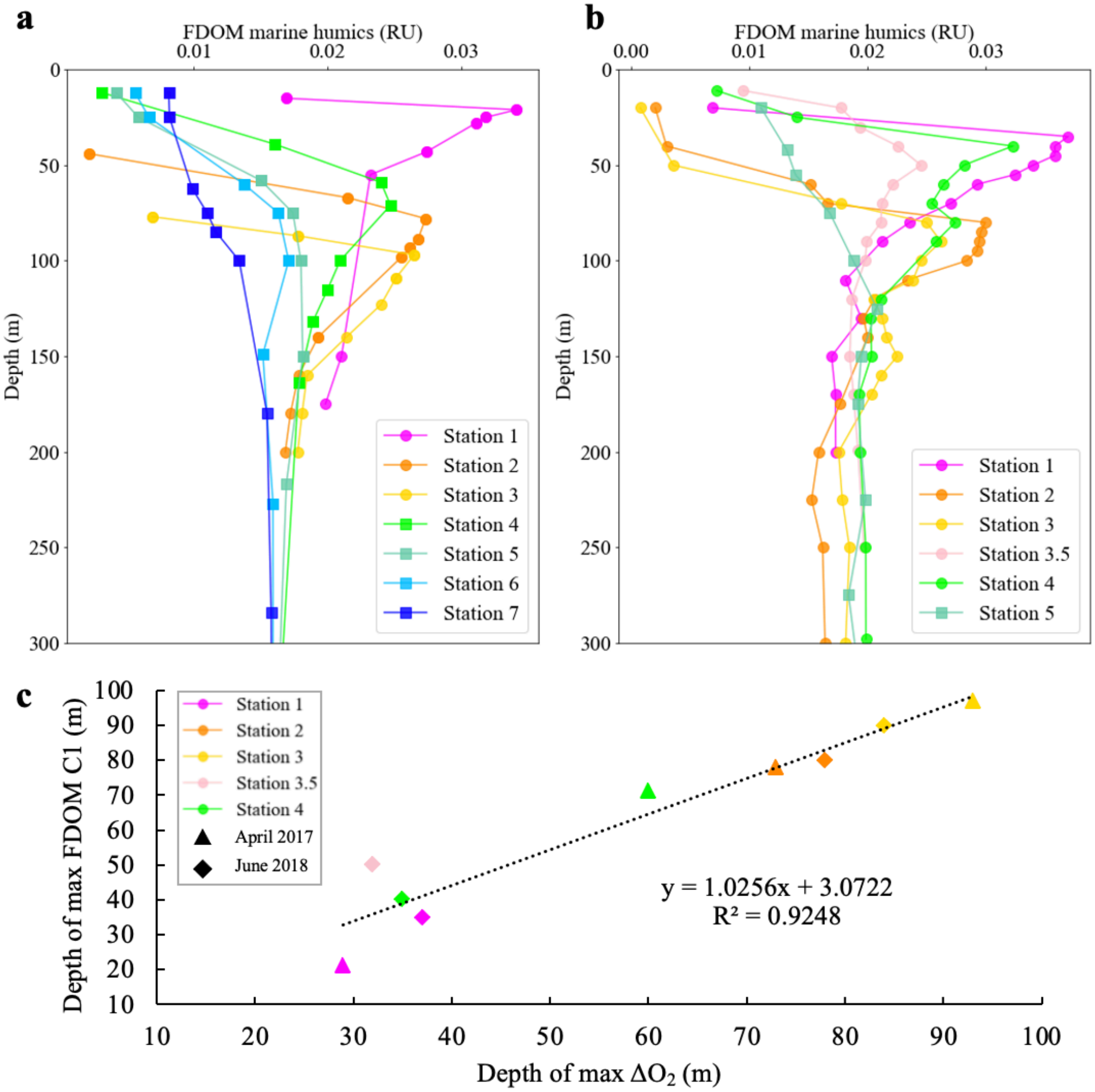

Figure 4.6. The FDOM "marine humic" component reaches a maximum where the oxycline is steepest. Concentrations of FDOM C1 for the April 2017 cruise (**a**) and the June 2018 cruise (**b**) plotted with increasing depth. Circles indicate Stations designated as 'AMZ' and squares show 'non-AMZ' Stations. For AMZ Stations, the marine humic component of FDOM reaches a maximum along the oxycline (**c**), where the rate of oxygen changes with depth reaches a maximum.

C2 and C3 (humic-like) of the PARAFAC model, which absorb in the UV and emit in the visible range, have similar profiles at all stations, showing an increase with depth (Figure S4.7). Overall, the distinguishing feature is the "bleaching of this signal near the surface. Station 1 during 2017 and Stations 1 and 4 sampled in 2018, do show distinctly different profiles consistent with near surface production. In 2018, Station 3.5, though it had high chlorophyll concentrations at the surface showed a relatively lower signal for C2 and C3. We attribute this lower signal to enhanced upwelling or vertical mixing at this site, such that the signal had not had a chance to grow in (from primary production) by the time of sampling as it may have done at Station 4. Both C2 and C3 are lower in the surface ocean at Stations 2-3. Stations 2 and 3 have nearly identical depth profiles for C2 and C3, reflecting their nearly identical water mass characteristics (Figure S4.2). Strong bleaching of this signal in the upper 50 m, with no subsequent production (i.e., low chlorophyll concentrations) may be indicated by the low values for C2 and C3 observed at Stations 2 and 3 in both years.

C4, identified as 'protein-like', shows a greater range of values at depth (Figure S4.7), but is generally positively correlated with chlorophyll fluorescence (Pearson $r = 0.327$, p-value < 0.0001). C4 was also highly correlated with POC and PON concentrations (Pearson $r = 0.711$, p-value < 0.0001; Pearson $r = 0.701$, p-value < 0.0001), consistent with recent production and particulate organic matter being a source for this fluorescence signal (Coble 1996; Loginova et al. 2016).

The spectral slope for light absorption by DOM in the interval 275-295 nm, $S_{275\text{-}295}$, showed a similar range to what has previously been reported for the eastern tropical South Pacific (ETSP) and typically decreased with depth even though the relationship to chlorophyll concentrations was not direct (Figure S4.8; Loginova et al. 2016). None of the optical measurements showed a difference between AMZ and non-AMZ samples (Table S4.4)

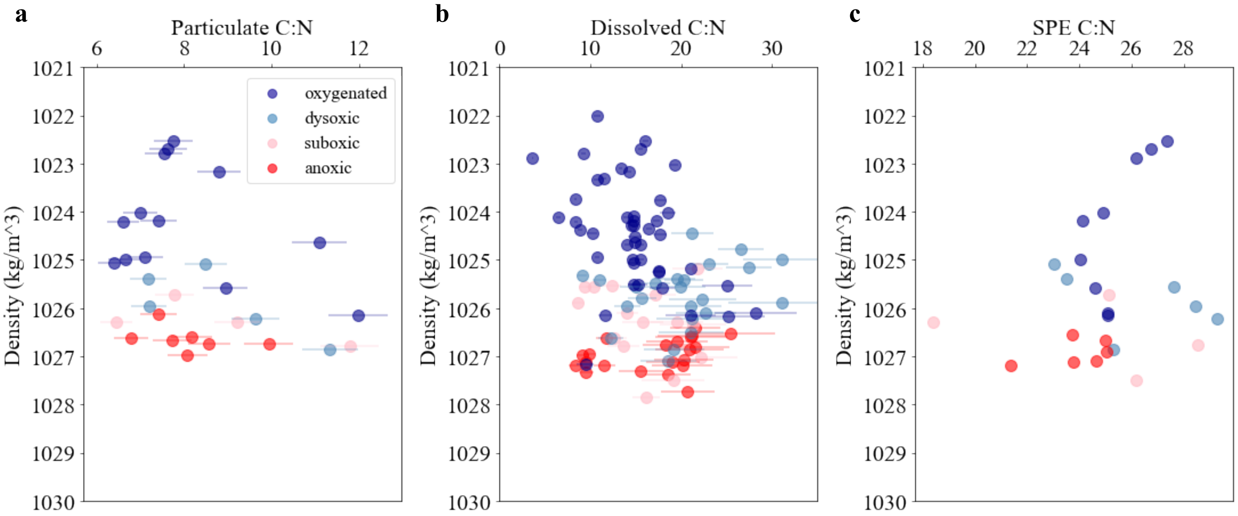

Figure 4.7. Carbon to nitrogen molar ratios. In (**a**) particulate organic C:N is plotted with increasing density. In (**b**) dissolved C:N, and in (**c**) solid-phase extracted C:N. The color indicates concentration of dissolved oxygen.

Elemental ratios in particulate and dissolved organic matter

Particulate C:N ratios can be used to examine preferential removal of nitrogen with depth if it is assumed that the change in this ratio with depth is driven by the loss of N and not the addition of new C (Figure 4.7a). In fact, particulate C:N increased with depth from close to the Redfield ratio to up to 12, with the highest values observed deeper in the water column. Particulate C:N ratios were lower within the AMZ compared to outside (Table S4.3), but a small sample size (n = 7) makes this result inconclusive. Dissolved C:N ratios were lowest in the surface ocean and increased with density ranging from 6.5 to 31 (Figure4.7b), however, most values in excess of 20 were accompanied by high error bars, increasing uncertainty for these samples. The average dissolved C:N ratio was not different between AMZ vs non-AMZ samples (Table S4.3). We also examined the C:N ratio of solid phase extracted (SPE) DOC. SPE DOC represents approximately 35-60 % of total DOC, and extraction efficiency for other elements such as nitrogen and sulfur may be even lower (Broek et al. 2017). These samples were collected only on the 2018 cruise at Stations 2-3 and 4-5 (Figure 4.7c). In general we see that the range of C:N for these samples is much narrower than what was observed for bulk DOC:DON. We also measured C:S ratios in SPE DOM (Figure 4.12a). There was no relationship between C:S and C:N (data not shown), but when considering the our larger dataset of SPE DOM from the ETNP across a broader range of depths we notice that C:S values are consistently higher with depths below 500 m. However, it is difficult to draw robust conclusions from this dataset where deep samples are extremely limited (Figure S4.9b).

Isotopic measurements of POM and SPE DOM

We measured stable C and N isotopes of POM and SPE DOM for a limited number of stations. We found $PO^{15}N$ was more depleted in the surface ocean and more enriched at depth ranging from 3.4 to 11.0 ‰ (Pearson $r = 0.470$, p-value = 0.01). Of the three ^{15}N-depleted PON samples at densities of ~1025 kg m^{-3}, two are from Stations 3.5 and 4 in 2018 and are near the surface but exhibit high density because these waters must have been recently upwelled. For SPE DOM, the range of $\delta^{15}N$ values was significantly smaller than for POM, ranging from 3.3 to 5.9 ‰ (Figure 4.8b) and showed the opposite relationship with density (Pearson $r = -0.568$, p-value < 0.01). $\delta^{13}C$ of SPE DOM had a relatively narrow range (-22.7 to -21.7 ‰) but had a strong positive relationship with density (Figure 4.8c; Pearson $r = 0.705$, p-value < 0.0001). None of these parameters differed significantly between AMZ vs. non-AMZ waters (Table S4.3).

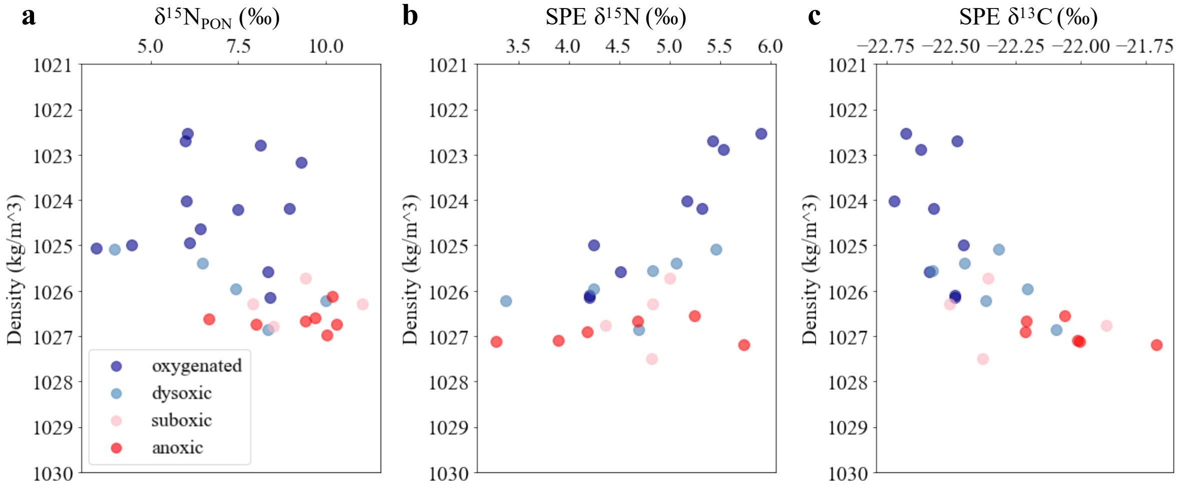

Figure 4.8. Carbon and nitrogen isotope measurements. In (**a**) δ^{15}N (‰) of particulate organic matter is shown with increasing density. In (**b**) we have δ^{15}N (‰) of solid-phase extracted dissolved organic matter and panel (**c**) shows δ^{13}C (‰) of solid-phase extracted dissolved organic matter. The color of each point indicates the concentration of dissolved oxygen.

δ^{34}S values in the ETNP ranged from 16.1 – 19.7 ‰. Values in the surface ocean were variable and exhibited no clear trend with density for this dataset. When considering deeper samples from this region we see that the lowest values are at depth, however, the data are variable and too sparse for any clear conclusions to be drawn (Figure S4.9a). When comparing δ^{34}S with C:S ratios, higher δ^{34}S values are associated with lower C:S (Figure S4.9c; Pearson *r* = -0.599, p- value < 0.001). There was no relationship between δ^{34}S and oxygen concentration (Figure 4.12b; Pearson *r* = -0.097, p-value = 0.67).

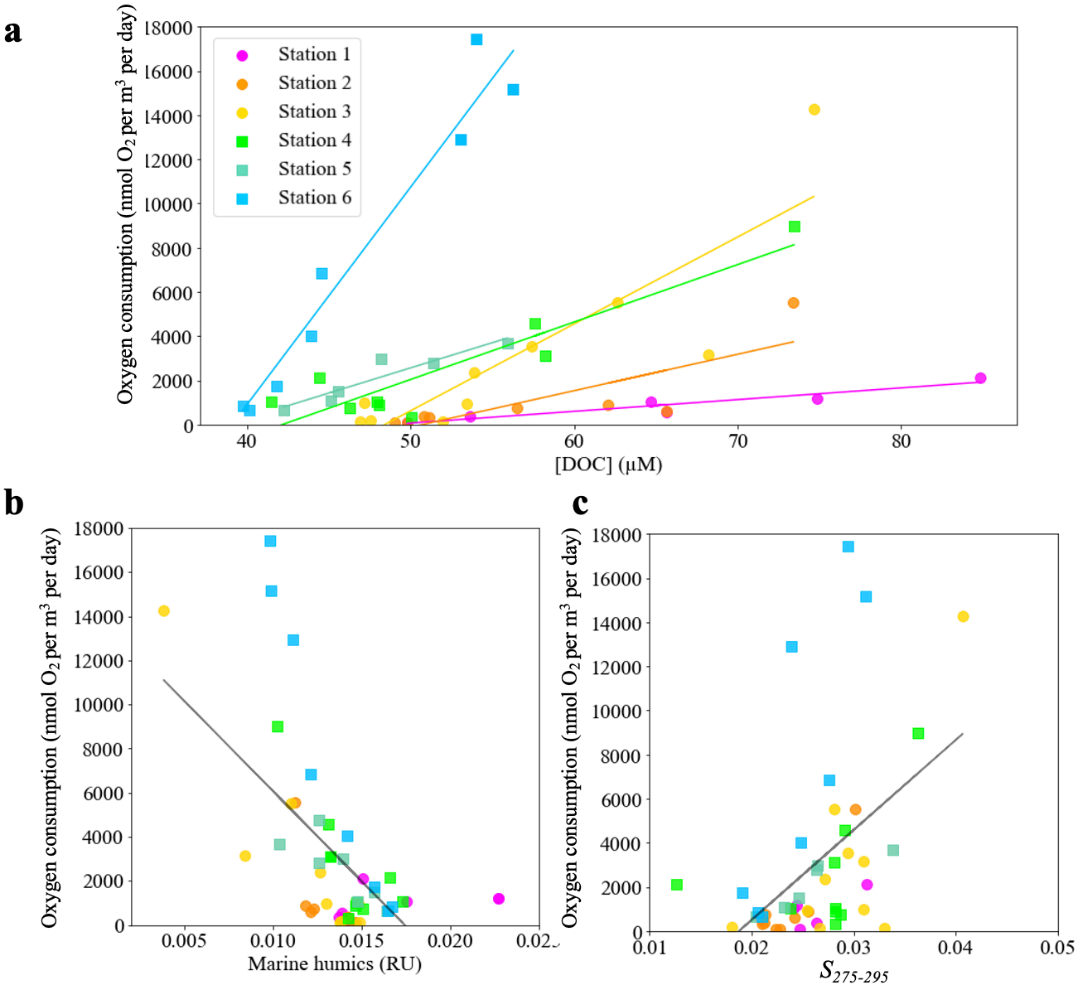

Figure 4.9. Oxygen consumption rates varied widely for stations sampled during the April 2017 cruise. Concentration of dissolved organic carbon is shown against the oxygen consumption rate corrected for nitrite and ammonia oxidation (**a**). Each line shows the linear best fit for each station. Of all organic parameters measured, two were shown to have the most significant relationship with oxygen consumption rates across all stations. In (**b**) the FDOM humics component is plotted against oxygen consumption and in (**c**) CDOM spectral slope. Circles indicate stations designated as ‘AMZ’ and squares show ‘non-AMZ’ stations. For both (a) and (b) the black line shows the best fit linear relationship for all data.

Rates of oxygen consuming processes

Oxygen consumption rates varied greatly across stations with the highest rates observed at Station 6 and the lowest rates at Station 1 (Figure 4.9a), and rates were highest in the upper water column and decreased depth (Figure S4.10). Considering each station individually, oxygen consumption rates were strongly and positively correlated with DOC concentrations. However, the slope of the linear relationship varied between stations (Figure 4.9a) and decreased from its highest value at Station 6 to its lowest value at Station 1. When considering all organic matter parameters measured in this study, those most correlated with oxygen consumption rates (once corrected for ammonia and nitrite oxidation) were the ‘humic-like’ C2 of FDOM (Figure 4.9b) and the CDOM spectral slope between 275-295 nm ($S_{275-295}$) (Figure 4.9c).

Discussion

Impact of Hurricane Bud

By reoccupying the same stations during a different month and year we hoped to establish the permanence of AMZ related OM parameters in the region. This goal was somewhat undermined by the appearance of Hurricane Bud, a category 4 storm with sustained winds up to 140 mph which passed through our study region during our cruise (Figure 4.1). A previous storm, category 4 Hurricane Arletta, also passed over Station 3 at the beginning of June (Stewart 2019). Thus, we unexpectedly had the opportunity to sample the ETNP region in the wake of intense hurricane activity. Hurricanes of this strength have been previously shown to impact the upper 200 m of the water column, resulting in intense vertical mixing (Sanford et al. 2007). Sea surface cooling following a hurricane has been extensively documented and is likely to be the cause of the observed differences in upper ocean temperatures between 2017 and 2018 (Figures 4.10a and S4.2). This is in contrast to Station 1, which was sampled before the hurricane and was about 4ºC warmer in June 2018 than in April 2017 (Figure S4.2). We also saw low SST at Station 3.5 in 2018 and although we did not have a companion station in 2017 (Figure 4.10a), it was clear from the path of the hurricane (Figure 4.1) that this station was strongly impacted by the storm. The intense vertical mixing that accompanies the passage of a major hurricane has also been shown to increase productivity by bringing deep, nutrient-rich waters up unto the euphotic zone (Pedrosa-Pàmies et al. 2019). This may be particularly relevant at Station 3.5, which we might not expect to be so productive based on its location alone, but which likely experienced the highest winds during the storm (Figure 4.1). At Station 3.5, 4 and 5, high chlorophyll levels (Figure 4.2c), a shallow AMZ (Figure 4.2a), and higher concentrations of POC and PON (Figure S4.3) all support the idea of increased water column productivity, whereas lower DOC concentrations (Figure S4.4), like lower surface water temperatures, confirm that this productivity was linked to vigorous vertical mixing at these sites. This vertical mixing also likely explains the shallow and broad nitrite maximum at Station 3.5 in 2018 (Figure 4.2b). In 2018, Station 4 was classified as an AMZ station but was the only such station sampled in both 2017 and 2018 that did not exhibit an SCM (Figure 4.2c). The uplifting of isopycnals at Station 4 may have happened too recently to allow time for the SCM to develop, but an SNM had developed and was detected. At Station 4, shoaling of the oxycline together with increased particle flux, inferred from increased chlorophyll concentrations, may have increased oxygen consumption rates within the oxycline and led to the development of the AMZ in 2018 (which was absent in 2017 at this site).

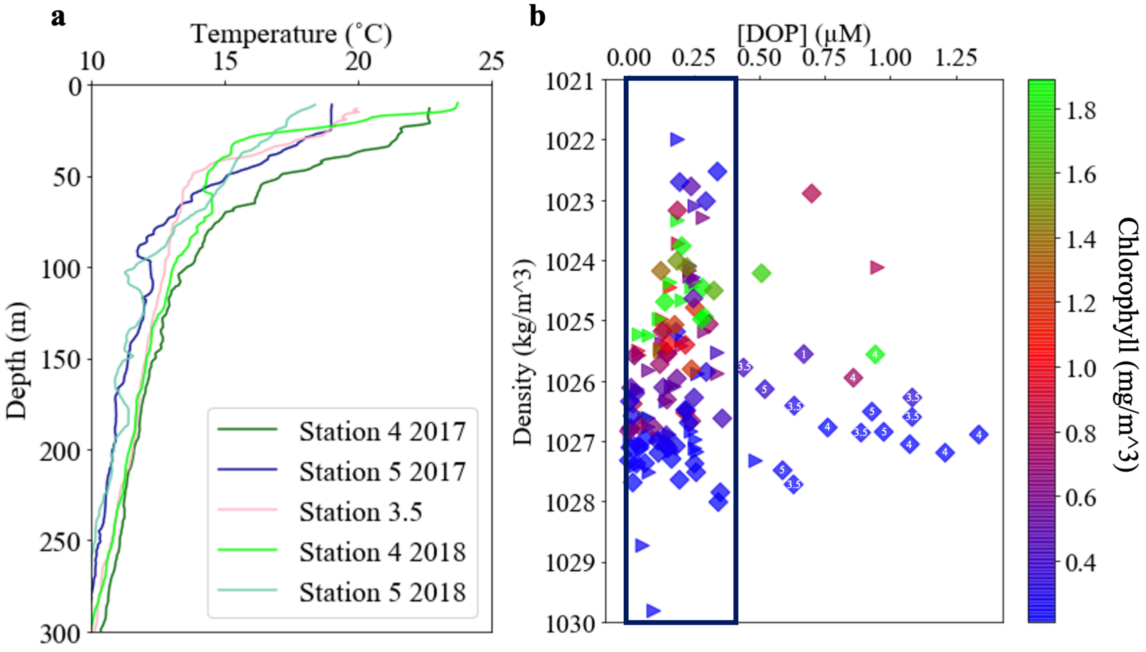

Figure 4.10. Possible effects of Hurricane Bud. In (**a**) we compare upper ocean temperatures between 2017 and 2018. In (**b**) concentrations of DOP are plotted with increasing density. Typical DOP concentrations are inside the rectangle, and the color bar shows chlorophyll concentration. Samples from 2017 are shown as triangles and those from 2018 as diamonds.

The most notable difference between 2017 and 2018 was in concentrations of DOP (Figure 4.10b). In 2018, DOP concentrations at Stations 3.5-5 reached 1.35 μM at depths below 100 m. Typical DOP concentrations for these depths are in the range of 0.2 – 0.4 μM. Some of the elevated DOP concentrations co-occur with high chlorophyll concentrations, and so could be explained by a productivity signal, but those deeper in the water column cannot be a product of local primary production (Figure 4.10b). Previous studies have demonstrated that hurricanes can resuspend sedimentary organic matter (Xu et al. 2016; Bianucci et al. 2018), but the >1000 m water-depths at Stations 3.5 and 4 (Table S4.1) and their distance from the shelf (Figure 4.1) exclude the local resuspension of DOP from sediments as the source of these elevated concentrations. Other explanations include the agitation and potential advection of remote shelf sediment plumes (“nepheloid layers”) extending from the Baja California peninsula, for example, and the release of DOP from freshly produced sinking particles (Pedrosa-Pàmies et al. 2019). Long-range (10s - 1000s km) advection of dissolved iron and/or long-lived radioisotopes sourced from low oxygen, shelf sediments have been reported for the eastern Pacific Ocean (Severmann et al. 2010; John et al. 2012; Sanial et al. 2018), and such a process could be invoked to support the hypothesis that DOP released from remote benthic environments can accumulate in the water column (Kim et al. 2007). Alternatively, if high concentrations of DOP present in the AMZ were derived from the disaggregation or reworking of sinking particles then one third and sometimes more, of the phosphate consumed by phytoplankton in the surface ocean would have to be released as DOP at depth. Regardless, if these unusually high DOP concentrations were the result of Hurricane Bud, this is to our knowledge the first time such a phenomenon has been documented.

Organic matter cycling along oxygen gradients

The existing literature provides conflicting evidence concerning the extent to which low oxygen conditions in the marine water column may reduce the rate or extent of organic matter remineralization (Bonaglia et al., 2016; Maßmig et al., 2020; Harvey et al., 1995). In this study, we try to consider evidence from both the dissolved and the particulate pool as to whether there is selective preservation of organic matter under low oxygen. However, the observed trends are influenced by production, remineralization, water mass mixing and oxygen concentrations, so teasing apart the role of oxygen alone is difficult. We used the average and standard deviation of our organic matter measurements to compare AMZ samples with non-AMZ samples between 100-400 m. With one exception, we found no significant differences between the AMZ and more oxygenated waters of a similar depth (Tables S4.2-S4.4). Higher TOC and DOC concentrations are observed above the AMZ region, consistent with high levels of productivity in these waters

(Figure S4.4). However, DOC concentrations are not always positively correlated with chlorophyll concentrations because vertical mixing can dilute surface ocean DOC concentrations, the build-up of DOC can lag chlorophyll, and warm, stratified waters can accumulate DOC even though chlorophyll concentrations are low (Stephens et al. 2018). In contrast to DOC, which showed a tight relationship with density, DON and DOP values are variable, suggesting more dynamic cycling of these components. However, for DON and DOP in addition to DOC there was no difference between AMZ vs. non-AMZ samples on average (Table S4.2). We did observe elevated DON concentrations at densities of ~1027 kg/m^3 (Figure 4.4b) that correspond to depths of the SNM (Figure 4.2b) and may be the result of microbial processes occurring within the low oxygen water column. The fact that high DON concentrations were not seen for every station at the SNM is likely due to the dynamic nature of the DON pool.

In general, organic matter with a lower C:N ratio is considered to be fresher and potentially more bioavailable. For instance, we see that for POM and DOM, C:N increases with increasing density as would be expected for the productivity gradient decreasing from the surface to depth (Figure 4.7). We hypothesized that we might see lower C:N ratios within the AMZ if fresh OM was preserved, or possibly higher C:N ratios if nitrogen was being preferentially removed for use in denitrification or anammox. Particulate C:N inside the AMZ was lower than outside the AMZ, but our relatively small number of samples (n = 7) precludes any robust conclusions (Table S4.3). This difference could be due to preservation within the AMZ, or it could be related to production at the SCM. Previous studies that documented attenuated flux through low oxygen waters were generally sampling deeper in the water column than we were able to do here. We saw no significant differences in C:N ratios of the dissolved pool when comparing AMZ and non-AMZ samples (Table S4.3). We also looked for differences in isotopic composition in POM and DOM, but again AMZ and non-AMZ samples were remarkably similar (Table S4.3). Here again, we were somewhat data limited due to the fact that only one of the stations sampled in 2018 was classified as 'non-AMZ', and other stations seem to have been influenced by Hurricane Bud, which in some cases resulted in significant shoaling of low oxygen waters (Figure 4.2a).

One of the strongest signals in our organic matter composition data comes from the FDOM signatures, and C1 specifically (the operationally defined "marine humics"). This component reaches a maximum above each AMZ, a signal that is notably absent from non-AMZ profiles (Figure 4.6). Further exploration of these profiles showed that the depth of the fluorescence maximum is strongly, positively correlated with the depth where oxygen concentrations change the most (i.e., the steepest part of the oxycline) (Figure 4.6c; $R^2 = 0.92$). The appearance of this signal during both cruises at similar depths suggests that it is a stable feature of this region, and its relationship to the oxycline points to the release or reworking of DOM during heterotrophic respiration as the source of this signal. As noted in Loginova et al. 2016, this component has appeared in a number of different FDOM studies, generally increasing with depth. Similar to our results, Loginova et al. observed that this component reached a maximum 10-100 m above the ETSP AMZ. Previous work by Beman and Carolan., 2013 has suggested that bacterial community diversity is greatest along the oxycline, indicating rapid and varied degradation processes are taking place at this depth. The fact that the C1 component of FDOM shows a similar distribution in both the ETSP and ETNP AMZ further confirms that it is a robust feature in these environments. None of the optical parameters measured were significantly different between AMZ and non-AMZ samples (Table S4.4).

Organic matter and oxygen consumption rates

For this study, our collaborators quantified the rates of three different oxygen consuming processes: aerobic respiration of carbon, ammonia oxidation, and nitrite oxidation (Beman et al. 2020b). Although oxygen concentrations decrease rapidly along the oxycline, we observed that rates of oxygen consumption were highest in the surface ocean, decreasing with depth and dissolved oxygen concentrations (Figure S4.10). We observed a relationship between DOC concentration and oxygen consumption rates, where higher DOC concentrations were associated with higher oxygen consumption rates on a per station basis (Figure 4.9a). Slopes were similar for Stations 2-5, despite significant differences in DOC concentrations and oxygen consumption rates across stations. This suggests a strong coupling between organic matter availability and microbial respiration. However, it is not clear why oxygen consumption rates were so low at Station 1, where in addition to high DOC concentrations, there was plenty of dissolved oxygen (Figure 4.2a). In contrast, Station 6 in particular saw very high rates of oxygen consumption, even though DOC concentrations were low compared to Stations 1-3 (Figure 4.9a).

In an attempt to explain the observed relationship between O_2 consumption rates and DOC, we performed a multiple linear regression with all measured organic matter properties to identify those most highly correlated with oxygen consumption across all stations. We identified a negative correlation between the FDOM "humics" fraction (C2) and oxygen consumption rates (Figure 4.9b; Pearson $r = -0.613$, p-value < 0.0001). The C2 component of FDOM has been shown to increase with depth and to be removed in the surface ocean via photoreactions. Here, a larger signal from C2 is correlated with a lower rate of oxygen consumption. Perhaps the humic-like FDOM signal identifies a component of DOM that is removed only at slow rates in the ocean and therefore, co-occurs with lower rates of OC oxidation. Alternatively, if the highest oxygen consumption rates in our dataset are always at the surface then the observed correlation may instead be driven by a surface ocean sink for C2 (Station 1 is an exception, as described above, but high particle concentrations at this site may have attenuated light penetrations even at very shallow depths and minimized photobleaching). Even with this relationship it is clear that the high oxygen consumption rates at Station 6 are outliers as they are higher than would be predicted based on the relationship with FDOM component C2 (Figure 4.9b). To date, no study has successfully assigned chemical structures to these FDOM components, and so, we unable to assign any specific sources to C2 at this time.

The multiple linear regression also identified a positive correlation between the spectral slope $S_{275\text{-}295}$ and oxygen consumption rates (Figure 4.9c; Pearson $r = 0.487$, p-value = 0.00052) Greater values of $S_{275\text{-}295}$ have been associated with lower average molecular weight as well as lower aromatic content (Helms et al. 2008; Helms 2012), which would suggest that higher oxygen utilization rates (and presumably rates of organic carbon oxidation) are correlated with those DOM properties. However, these relationships are still speculative. Overall, the relationship of oxygen consumption rates with FDOM and CDOM components identifies either the influence of DOM composition (as coarsely captured by optical properties) on oxidation rates or the result of oxidation processes on the DOM composition, and lend support to the measured oxidation rates. As noted above, the measured oxidation rates at Station 6 appear abnormally high, however, the concentrations of DOC (S4.4) at this station and at Station 7, which also had high uncorrected oxygen consumption rates (Figure S4.10) are some of the lowest measured in either 2017 or 2018, and together with temperature data (Figure S4.1) indicate strong vertical mixing in the upper 75 m at these sites. Therefore, very labile DOC may indeed be cycling rapidly at this site and contributing to high oxidation rates, but its presence is not captured by our concentration measurement.

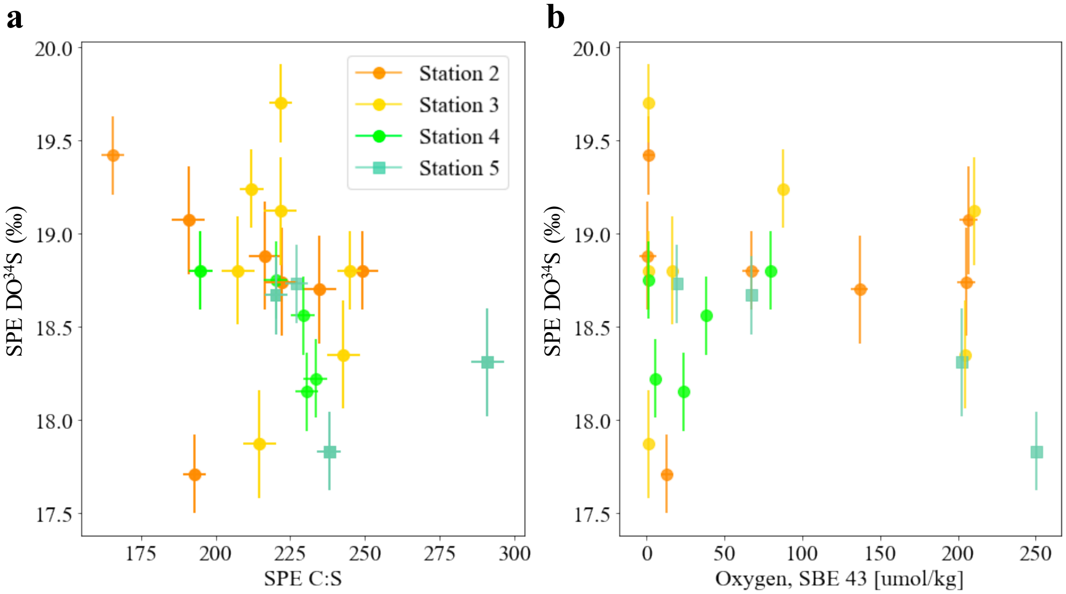

Figure 4.11. Measurements of dissolved organic sulfur. Panel (**a**) shows $\delta^{34}S$ (‰) vs. C:S of SPE DOM. In (**b**), $\delta^{34}S$ (‰) is shown against oxygen concentrations. For all, error bars are the standard error. Circles indicate Stations designated as 'AMZ' and squares show 'non-AMZ' Stations.

Dissolved organic sulfur cycling

Marine organic sulfur is thought to primarily originate from assimilation of marine sulfate, which has a $\delta^{34}S$ of approximately 21 ‰ (Paris et al. 2013). Assimilatory sulfate reduction has only been minimally studied, with work in aquatic plants suggesting a fractionation factor ($^{34}\varepsilon$) between +0.5 to -4.4 ‰ (Mekhtieva and Pankina 1968). More recently, studies of DMSP suggest a narrower range for at least one metabolite, with $^{34}\varepsilon$ between -1.4 and -2.8 ‰ (Oduro et al. 2012). The results presented here show that organic sulfur in the surface ocean (<100 m, n=12) is 1.9 to 2.8 ‰ depleted compared to sulfate (Figure 4.11) suggesting that fractionation associated with biological sulfate utilization for DMSP (-1.4 and -2.8 ‰) can be generalized to other organic sulfur metabolites. One caveat here of course is that the SPE DOS represents only a fraction of bulk DOS. As we have seen from comparing C:N in the bulk vs.

SPE (Figure 4.7), these ratios can be quite different in the bulk reservoir (Ksionzek et al. 2016; Longnecker et al. 2020).

Recent work has shown that sulfurization is occurring on sinking particles within the ETNP AMZ (Raven et al. 2021). We used measurements of $\delta^{34}S$ in SPE DOM to examine whether sulfurization reactions, whether occurring on sinking particles or in other locations, impact the marine DOS pool. Sulfurization reactions result in organic matter that is very depleted in ^{34}S, down to -20 ‰ (Raven et al. 2019). Our data show no relationship between oxygen concentrations and $\delta^{34}S$ (Figure 4.11b; Table S4.2), suggesting that sulfurization reactions are not impacting the DOS pool within AMZs. This is perhaps expected because the same types of microenvironments that develop on particles may not be relevant for the DOS reservoir. These results further suggest that there is less exchange between sulfurized particulate and dissolved reservoirs, which is consistent with Raven et al.'s finding that sulfurized organic matter is insoluble. However, this does not preclude the exchange of other organic sulfur compounds between these phases. This is an important finding as it has been suggested that sulfurization could contribute to the long-term storage of DOM in the oceans.

Conclusions

The remineralization and respiration of organic matter is a process essential not only to the creation of AMZs, but to the many processes that make them such unique biogeochemical environments. In this study, we showed that oxygen consumption rates across a range of oxygen concentrations in and around the ETNP AMZ are related not only to organic matter abundance, but potentially also to organic matter composition as reflected by its optical properties. We did not identify any consistent differences in organic matter properties between AMZ waters and more oxygenated waters of a similar depth. Some of these results were influenced by a storm event, showing that tropical storms can have a large impact on the biogeochemistry of the ETNP region. Finally, the novel use of sulfur isotope measurements on SPE DOS suggests that sulfurization reactions do not have a large impact on the marine DOS pool within the ETNP AMZ.

Acknowledgements

We would like to thank the captains and crews of the *R/V Oceanus*. Thanks also to all the members of the Beman lab at UC Merced. Additional thanks to Jennifer Karolewski and Scott Wankel at WHOI and Bruce Deck at SIO. Data sets presented here were supported in part by NSF grants OCE 1736656 and OCE 1555375 as well as the UC San Diego Academic Senate. JMB was supported by NSF CAREER grant 1555375.

Chapter 4, is currently being formulated into a manuscript that will be submitted for publication. “Organic matter composition across oxygen gradients in the eastern tropical North Pacific Ocean”. Margot White, Tran Nguyen, Irina Koester, Alexandra Phillips, Alex Sessions, J. Michael Beman, and Lihini Aluwihare. The dissertation author was the primary investigator and author of this paper.

References

Babbin, A. R., D. Bianchi, A. Jayakumar, and B. B. Ward. 2015. Rapid nitrous oxide cycling in the suboxic ocean. Science (80-.). **348**: 1127–1129. doi:10.1126/science.aaa8380

Beman, J. M., and M. T. Carolan. 2013. Deoxygenation alters bacterial diversity and community composition in the ocean's largest oxygen minimum zone. Nat. Commun. **4**: 1–11. doi:10.1038/ncomms3705

Beman, J. M., S. M. Vargas, S. Vazquez, J. M. Wilson, A. Yu, A. Cairo, and E. Perez-Coronel. 2020a. Biogeochemistry and hydrography shape microbial community assembly and activity in the eastern tropical North Pacific Ocean oxygen minimum zone. Environ. Microbiol. 1462-2920.15215. doi:10.1111/1462-2920.15215

Beman, J. M., S. M. Vargas, J. M. Wilson, A. E. Cairo, J. S. Karolewski, and S. D. Wankel. 2020b. Constraining oxygen consumption by nitrite oxidation in oceanic oxygen minimum zones. bioRxiv 2020.05.26.115402. doi:10.1101/2020.05.26.115402

Bhatia, K. T., G. A. Vecchi, T. R. Knutson, H. Murakami, J. Kossin, K. W. Dixon, and C. E. Whitlock. 2019. Recent increases in tropical cyclone intensification rates. Nat. Commun. **10**: 1–9. doi:10.1038/s41467-019-08471-z

Bianucci, L., K. Balaguru, R. W. Smith, L. R. Leung, and J. M. Moriarty. 2018. Contribution of hurricane-induced sediment resuspension to coastal oxygen dynamics. Sci. Rep. **8**: 1–10. doi:10.1038/s41598-018-33640-3

Bonaglia, S., I. Klawonn, L. De Brabandere, B. Deutsch, B. Thamdrup, and V. Brüchert. 2016. Denitrification and DNRA at the Baltic Sea oxic–anoxic interface: Substrate spectrum and kinetics. Limnol. Oceanogr. **61**. doi:10.1002/lno.10343

Bristow, L. A., T. Dalsgaard, L. Tiano, and others. 2016. Ammonium and nitrite oxidation at nanomolar oxygen concentrations in oxygen minimum zone waters. Proc. Natl. Acad. Sci. U. S. A. **113**: 10601–6. doi:10.1073/pnas.1600359113

Broek, T. A. B., B. D. Walker, T. P. Guilderson, and M. D. McCarthy. 2017. Coupled ultrafiltration and solid phase extraction approach for the targeted study of semi-labile high molecular weight and refractory low molecular weight dissolved organic matter. Mar. Chem. **194**: 146–157. doi:10.1016/J.MARCHEM.2017.06.007

Burdige*, D. J. 2007. Preservation of Organic Matter in Marine Sediments: Controls, Mechanisms, and an Imbalance in Sediment Organic Carbon Budgets?doi:10.1021/CR050347Q

Canfield, D. E., F. J. Stewart, B. Thamdrup, L. De Brabandere, T. Dalsgaard, E. F. Delong, N. P. Revsbech, and O. Ulloa. 2010. A cryptic sulfur cycle in oxygen-minimum-zone waters off the Chilean coast. Science (80-.). **330**: 1375–1378. doi:10.1126/science.1196889

Carolan, M. T., J. M. Smith, and J. M. Beman. 2015. Transcriptomic evidence for microbial sulfur cycling in the eastern tropical North Pacific oxygen minimum zone. Front. Microbiol. **06**: 334. doi:10.3389/fmicb.2015.00334

Casciotti, K. L. 2016. Nitrite isotopes as tracers of marine N cycle processes. Philos. Trans. R. Soc. A Math. Phys. Eng. Sci. **374**. doi:10.1098/rsta.2015.0295

Christensen, J. P., J. W. Murray, A. H. Devol, and L. A. Codispoti. 1987. Denitrification in continental shelf sediments has major impact on the oceanic nitrogen budget. Global Biogeochem. Cycles **1**: 97–116. doi:10.1029/GB001i002p00097

Coble, P. G. 1996. Characterization and Tracking DOM in the Ocean Using Total Fluorescence Spectroscopy.

Codispoti, L. A., J. A. Brandes, J. P. Christensen, A. H. Devol, S. W. A. Naqvi, H. W. Paerl, T. Yoshinari, and T. Yoshinari. 2001. The oceanic fixed nitrogen and nitrous oxide budgets: Moving targets as we enter the anthropocene? Sci. Mar. **65**: 85–105. doi:10.3989/scimar.2001.65s285

Deutsch, C., H. Brix, T. Ito, H. Frenzel, and L. A. Thompson. 2011. Climate-forced variability of ocean hypoxia. Science (80-.). **333**: 336–339. doi:10.1126/science.1202422

Devol, A. H. 2015. Denitrification, anammox, and N2 production in marine sediments. Ann. Rev. Mar. Sci. **7**. doi:10.1146/annurev-marine-010213-135040

Dittmar, T., B. Koch, N. Hertkorn, and G. Kattner. 2008. A simple and efficient method for the solid-phase extraction of dissolved organic matter (SPE-DOM) from seawater. Limnol. Oceanogr. Methods **6**: 230–235. doi:10.4319/lom.2008.6.230

Garcia-Robledo, E., C. C. Padilla, M. Aldunate, F. J. Stewart, O. Ulloa, A. Paulmier, G. Gregori, and N. P. Revsbech. 2017. Cryptic oxygen cycling in anoxic marine zones. Proc. Natl. Acad. Sci. U. S. A. **114**: 8319–8324. doi:10.1073/pnas.1619844114

Goericke, R., R. J. Olson, and A. Shalapyonok. 2000. A novel niche for Prochlorococcus sp. in low-light suboxic environments in the Arabian Sea and the Eastern Tropical North Pacific. Deep. Res. Part I Oceanogr. Res. Pap. **47**: 1183–1205. doi:10.1016/S0967-0637(99)00108-9

Helms, J. 2012. Spectroscopic Characterization of Dissolved Organic Matter: Insights into Composition, Photochemical Transformation and Carbon Cycling. Chem. Biochem. Theses Diss. doi:10.25777/1y3p-e444

Helms, J. R., A. Stubbins, J. D. Ritchie, E. C. Minor, D. J. Kieber, and K. Mopper. 2008. Absorption spectral slopes and slope ratios as indicators of molecular weight, source, and photobleaching of chromophoric dissolved organic matter. Limnol. Oceanogr. **53**: 955–969. doi:10.4319/lo.2008.53.3.0955

John, S. G., J. Mendez, J. Moffett, and J. Adkins. 2012. The flux of iron and iron isotopes from San Pedro Basin sediments. Geochim. Cosmochim. Acta **93**: 14–29. doi:10.1016/j.gca.2012.06.003

Kalvelage, T., M. M. Jensen, S. Contreras, and others. 2011. Oxygen Sensitivity of Anammox and Coupled N-Cycle Processes in Oxygen Minimum Zones J.A. Gilbert [ed.]. PLoS One **6**: e29299. doi:10.1371/journal.pone.0029299

Keil, R. G., J. A. Neibauer, C. Biladeau, K. van der Elst, and A. H. Devol. 2016. A multiproxy approach to understanding the "enhanced" flux of organic matter through the oxygen-deficient waters of the Arabian Sea. Biogeosciences **13**: 2077–2092.

Kim, C., Y. Nishimura, and T. Nagata. 2007. High potential activity of alkaline phosphatase in the benthic nepheloid layer of a large mesotrophic lake: implications for phosphorus regeneration in oxygenated hypolimnion. Aquat. Microb. Ecol. **49**: 303–311. doi:10.3354/ame01137

Ksionzek, K. B., O. J. Lechtenfeld, S. L. McCallister, P. Schmitt-Kopplin, J. K. Geuer, W. Geibert, and B. P. Koch. 2016. Dissolved organic sulfur in the ocean: Biogeochemistry of a petagram inventory. Science (80-.). **354**: 456–459. doi:10.1126/science.aaf7796

Kuypers, M. M. M., A. O. Silekers, G. Lavik, and others. 2003. Anaerobic ammonium oxidation by anammox bacteria in the Black Sea. Nature **422**: 608–611. doi:10.1038/nature01472

Lam, P., and M. M. M. Kuypers. 2011. Microbial Nitrogen Cycling Processes in Oxygen Minimum Zones. Ann. Rev. Mar. Sci. **3**: 317–345. doi:10.1146/annurev-marine-120709-142814

Lavin, P., B. González, J. F. Santibáñez, D. J. Scanlan, and O. Ulloa. 2010. Novel lineages of Prochlorococcus thrive within the oxygen minimum zone of the eastern tropical South Pacific. Environ. Microbiol. Rep. **2**: 728–738. doi:10.1111/j.1758-2229.2010.00167.x

Loginova, A. N., S. Thomsen, and A. Engel. 2016. Chromophoric and fluorescent dissolved organic matter in and above the oxygen minimum zone off Peru. J. Geophys. Res. Ocean. **121**: 7973–7990. doi:10.1002/2016JC011906

Longnecker, K., L. Oswald, M. C. Kido Soule, G. A. Cutter, and E. B. Kujawinski. 2020. Organic sulfur: A spatially variable and understudied component of marine organic matter. Limnol. Oceanogr. Lett. **5**: 305–312. doi:10.1002/lol2.10149

Maßmig, M., J. Lüdke, G. Krahmann, and A. Engel. 2020. Bacterial degradation activity in the eastern tropical South Pacific oxygen minimum zone. Biogeosciences **17**: 215–230. doi:10.5194/bg-17-215-2020

Mekhtieva, V. L., and R. G. Pankina. 1968. Isotopic composition of sulfur in aquatic plants and dissolved sulfates. Geochem. Int. 624–627.

Nelson, N. B., and J. M. Gauglitz. 2016. Optical Signatures of Dissolved Organic Matter Transformation in the Global Ocean. Front. Mar. Sci. **2**: 118. doi:10.3389/fmars.2015.00118

Nelson, N. B., and D. A. Siegel. 2013. The Global Distribution and Dynamics of Chromophoric Dissolved Organic Matter. Ann. Rev. Mar. Sci. **5**: 447–476. doi:10.1146/annurev-marine-120710-100751

Oduro, H., K. L. Van Alstyne, and J. Farquhar. 2012. Sulfur isotope variability of oceanic DMSP generation and its contributions to marine biogenic sulfur emissions. Proc. Natl. Acad. Sci. U. S. A. **109**: 9012–9016. doi:10.1073/pnas.1117691109

Oschlies, A., P. Brandt, L. Stramma, and S. Schmidtko. 2018. Drivers and mechanisms of ocean deoxygenation. Nat. Geosci. **11**: 467–473. doi:10.1038/s41561-018-0152-2

Paris, G., A. L. Sessions, A. V. Subhas, and J. F. Adkins. 2013. MC-ICP-MS measurement of δ34S and Δ33S in small amounts of dissolved sulfate. Chem. Geol. **345**: 50–61. doi:10.1016/j.chemgeo.2013.02.022

Pedrosa-Pàmies, R., M. H. Conte, J. C. Weber, and R. Johnson. 2019. Hurricanes Enhance Labile Carbon Export to the Deep Ocean. Geophys. Res. Lett. **46**: 10484–10494. doi:10.1029/2019GL083719

Phillips, A. A., F. Wu, and A. L. Sessions. 2021. Sulfur isotope analysis of cysteine and methionine via preparatory liquid chromatography and elemental analyzer isotope ratio mass spectrometry. Rapid Commun. Mass Spectrom. **35**. doi:10.1002/rcm.9007

Raven, M. R., D. A. Fike, M. L. Gomes, and S. M. Webb. 2019. Chemical and Isotopic Evidence for Organic Matter Sulfurization in Redox Gradients Around Mangrove Roots. Front. Earth Sci. **7**: 98. doi:10.3389/feart.2019.00098

Raven, M. R., R. G. Keil, and S. M. Webb. 2021. Microbial sulfate reduction and organic sulfur formation in sinking marine particles. Science (80-.). **371**: 178–181. doi:10.1126/science.abc6035

Rodger Harvey, H., J. H. Tuttle, and J. Tyler Bell. 1995. Kinetics of phytoplankton decay during simulated sedimentation: Changes in biochemical composition and microbial activity under oxic and anoxic conditions. Geochim. Cosmochim. Acta **59**: 3367–3377. doi:10.1016/0016-7037(95)00217-N

Sanford, T. B., J. F. Price, J. B. Girton, and D. C. Webb. 2007. Highly resolved observations and simulations of the ocean response to a hurricane. Geophys. Res. Lett. **34**. doi:10.1029/2007GL029679

Sanial, V., L. E. Kipp, P. B. Henderson, and others. 2018. Radium-228 as a tracer of dissolved trace element inputs from the Peruvian continental margin. Mar. Chem. **201**: 20–34.

doi:10.1016/j.marchem.2017.05.008

Schimmelmann, A., C. B. Lange, J. Schieber, P. Francus, A. E. K. Ojala, and B. Zolitschka. 2016. Varves in marine sediments: A review. Earth-Science Rev. **159**: 215–246. doi:10.1016/j.earscirev.2016.04.009

Severmann, S., J. McManus, W. M. Berelson, and D. E. Hammond. 2010. The continental shelf benthic iron flux and its isotope composition. Geochim. Cosmochim. Acta **74**: 3984–4004. doi:10.1016/j.gca.2010.04.022

Stedmon, C. A., and R. Bro. 2008. Characterizing dissolved organic matter fluorescence with parallel factor analysis: a tutorial. Limnol. Oceanogr. Methods **6**: 572–579. doi:10.4319/lom.2008.6.572

Stephens, B. M., M. Porrachia, S. Dovel, M. Roadman, R. Goericke, and L. I. Aluwihare. 2018. Nonsinking Organic Matter Production in the California Current. Global Biogeochem. Cycles **32**: 1386–1405. doi:10.1029/2018GB005930

Stewart, S. R. 2019. The 2018 Eastern North Pacific Hurricane Season: An Active Season Brings Third-Highest Accumulated Cyclone Energy on Record. Weatherwise **72**: 22–31. doi:10.1080/00431672.2019.1612202

Stramma, L., G. C. Johnson, J. Sprintall, and V. Mohrholz. 2008. Expanding Oxygen-Minimum Zones in the Tropical Oceans. Science (80-.). **320**: 655–658. doi:10.1126/science.1153847

Thamdrup, B., and T. Dalsgaard. 2002. Production of N2 through anaerobic ammonium oxidation coupled to nitrate reduction in marine sediments. Appl. Environ. Microbiol. **68**: 1312–1318. doi:10.1128/AEM.68.3.1312-1318.2002

Wakeham, S. G. 2020. Organic biogeochemistry in the oxygen-deficient ocean: A review. Org. Geochem. **149**: 104096. doi:10.1016/j.orggeochem.2020.104096

White, M. E., P. A. Rafter, B. M. Stephens, S. D. Wankel, and L. I. Aluwihare. 2019. Recent Increases in Water Column Denitrification in the Seasonally Suboxic Bottom Waters of the Santa Barbara Basin. Geophys. Res. Lett. **46**: 6786–6795. doi:10.1029/2019GL082075

Xu, K., R. C. Mickey, Q. Chen, C. K. Harris, R. D. Hetland, K. Hu, and J. Wang. 2016. Shelf sediment transport during hurricanes Katrina and Rita. Comput. Geosci. **90**: 24–39. doi:10.1016/j.cageo.2015.10.009

Supplementary Information

Table S4.1. Locations of stations sampled in the ETNP.

Station	Latitude	Longitude	Approx. water depth (m)	Year sampled	AMZ
1	20.5 N	106.5 W	3500	2017, 2018	Yes
2	16.5 N	107.2 W	4000	2017, 2018	Yes
3	16.0 N	110.0 W	3200	2017, 2018	Yes
3.5	18.5 N	108.5 W	3200	2018	Yes
4	21.5 N	109.5 W	3000	2017, 2018	No 2017 Yes 2018
5	24.7 N	113.3 W	3700	2017, 2018	No
6	27.4 N	117.5 W	3800	2017	No
7	32.5 N	120.5 W	3700	2017	No

Table S4.2. Mean and standard deviation of organic matter concentrations from the ETNP. All samples between 100 and 400 m were included in the analysis.

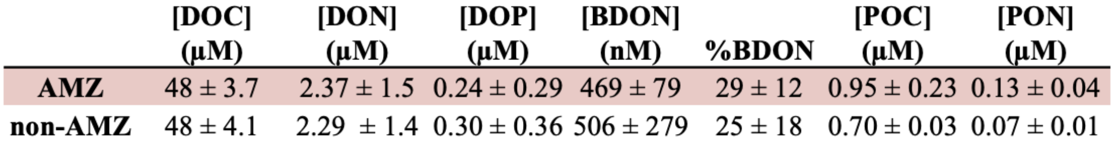

	[DOC] (µM)	[DON] (µM)	[DOP] (µM)	[BDON] (nM)	%BDON	[POC] (µM)	[PON] (µM)
AMZ	48 ± 3.7	2.37 ± 1.5	0.24 ± 0.29	469 ± 79	29 ± 12	0.95 ± 0.23	0.13 ± 0.04
non-AMZ	48 ± 4.1	2.29 ± 1.4	0.30 ± 0.36	506 ± 279	25 ± 18	0.70 ± 0.03	0.07 ± 0.01

Table S4.3. Mean and standard deviation of organic matter elemental ratios and stable isotope measurements from the ETNP. All samples between 100 and 400 m were included in the analysis.

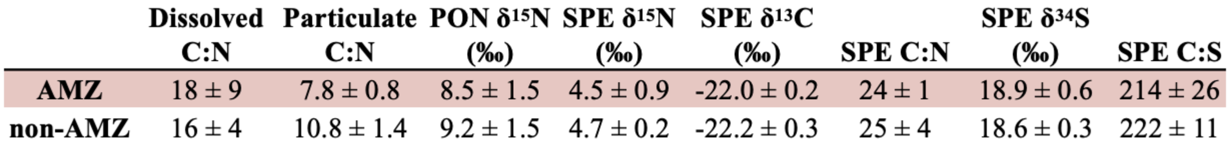

	Dissolved C:N	Particulate C:N	PON $\delta^{15}N$ (‰)	SPE $\delta^{15}N$ (‰)	SPE $\delta^{13}C$ (‰)	SPE C:N	SPE $\delta^{34}S$ (‰)	SPE C:S
AMZ	18 ± 9	7.8 ± 0.8	8.5 ± 1.5	4.5 ± 0.9	-22.0 ± 0.2	24 ± 1	18.9 ± 0.6	214 ± 26
non-AMZ	16 ± 4	10.8 ± 1.4	9.2 ± 1.5	4.7 ± 0.2	-22.2 ± 0.3	25 ± 4	18.6 ± 0.3	222 ± 11

Table S4.4. Mean and standard deviation of organic matter optical measurements from the ETNP. All samples between 100 and 400 m were included in the analysis.

	FDOM C1 (RU)	**FDOM C2 (RU)**	**FDOM C3 (RU)**	**FDOM C4 (RU)**	$S_{275\text{-}295}$
AMZ	0.019 ± 0.002	0.017 ± 0.002	0.027 ± 0.003	0.007 ± 0.015	0.020 ± 0.005
non-AMZ	0.019 ± 0.003	0.015 ± 0.002	0.025 ± 0.003	0.006 ± 0.003	0.024 ± 0.003

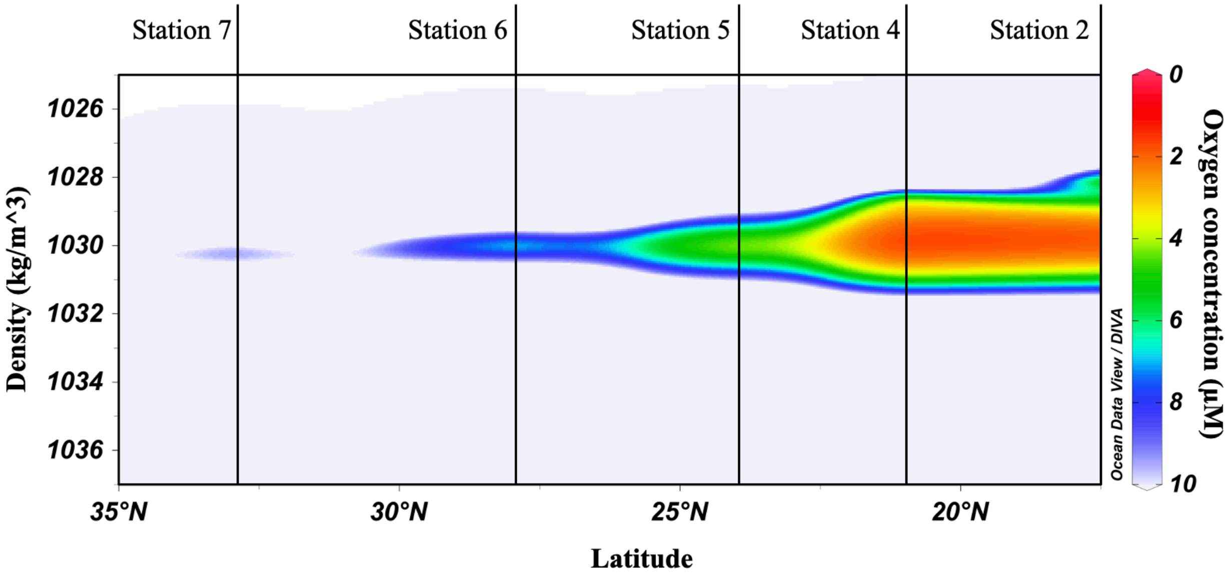

Figure S4.1. Horizontal oxygen gradient in the ETNP. Locations for the stations included in this section plot are shown (see Table S4.1).

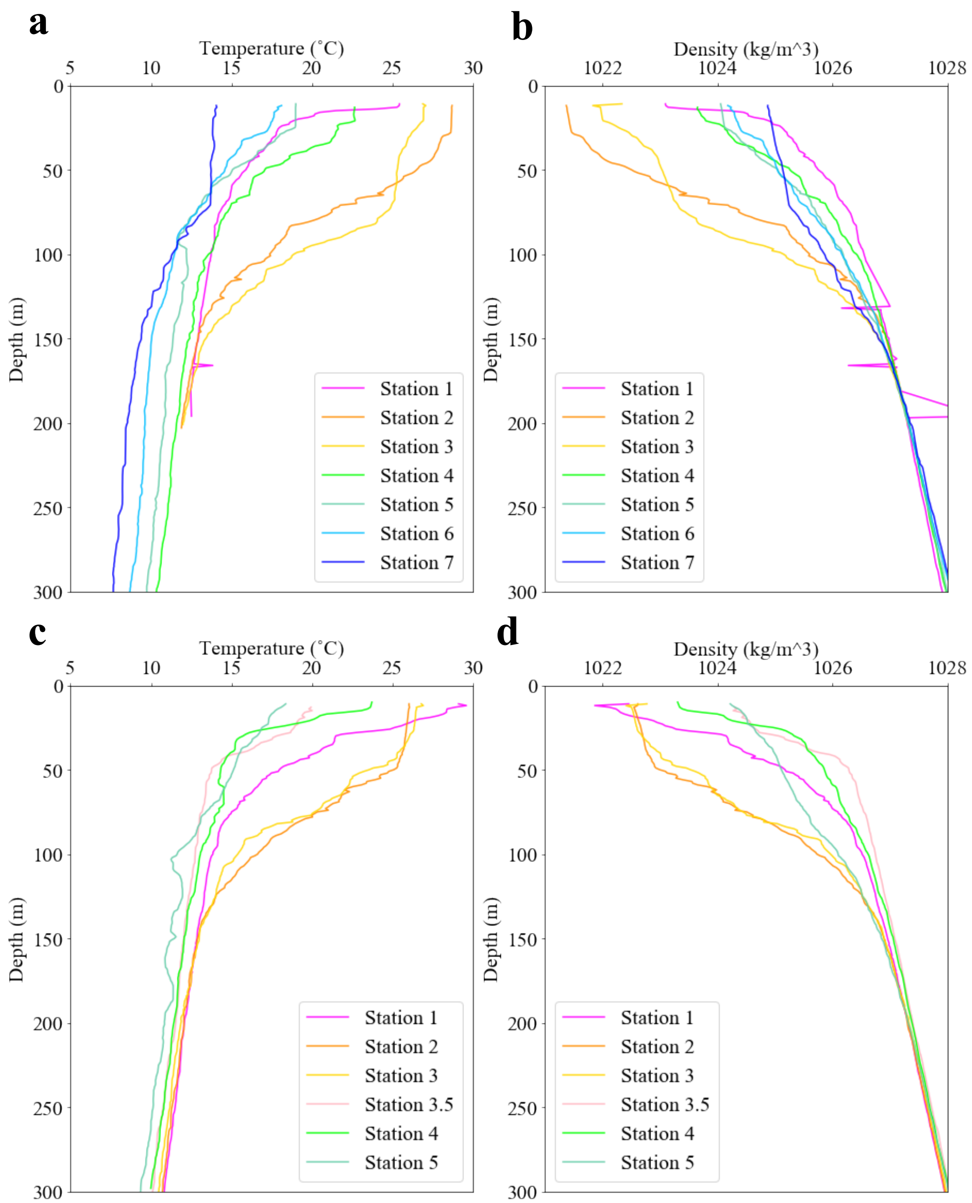

Figure S4.2. Temperatures and densities for sampled stations in ETNP. Temperature (**a**) and density (**b**) vs depth from the April 2017 cruise are in the top row. Temperature (**c**) and density (**d**) from June 2018 are in the bottom row.

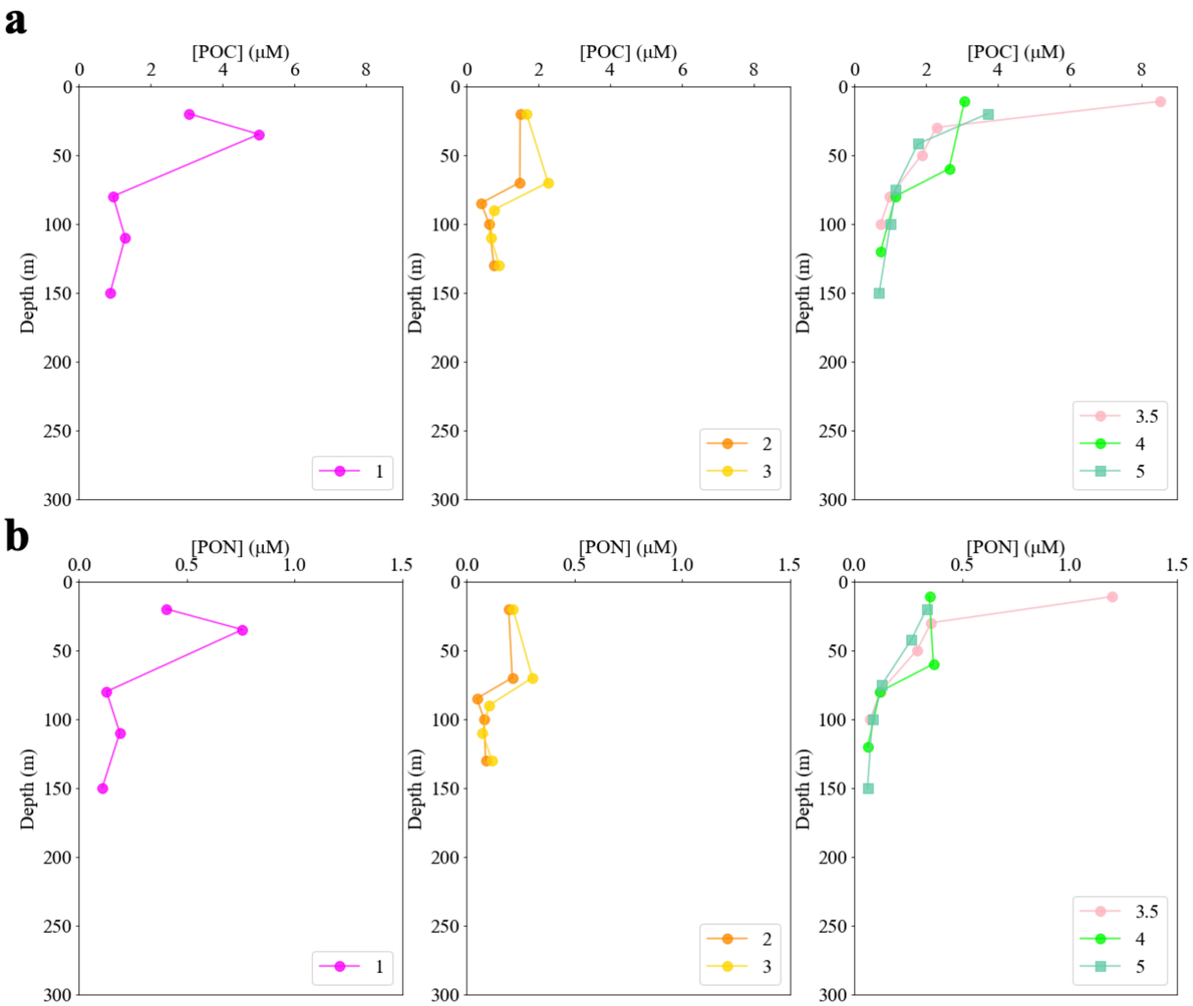

Figure S4.3. Particulate organic matter concentrations in the ETNP from the June 2018 cruise. Particulate organic carbon concentrations are shown in (**a**) and particulate organic nitrogen concentrations in (**b**).

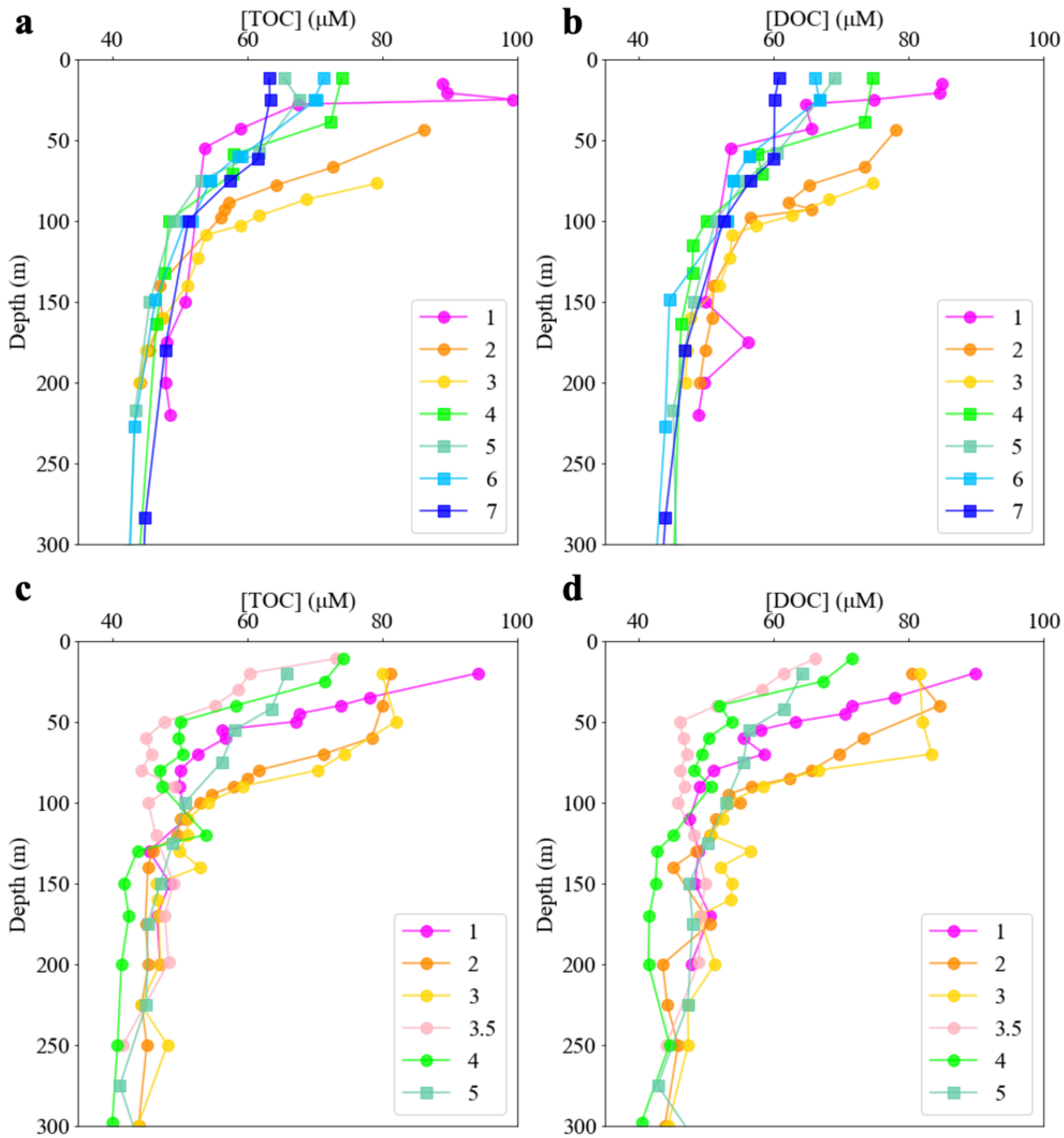

Figure S4.4. Total organic carbon and dissolved organic carbon concentrations at sampled stations in the ETNP. TOC (**a**) and DOC (**b**) concentrations from the April 2017 cruise are in the top row. TOC (**c**) and DOC (**d**) concentrations from June 2018 are in the bottom row. Circles designate 'AMZ' stations and squares are 'non-AMZ' stations.

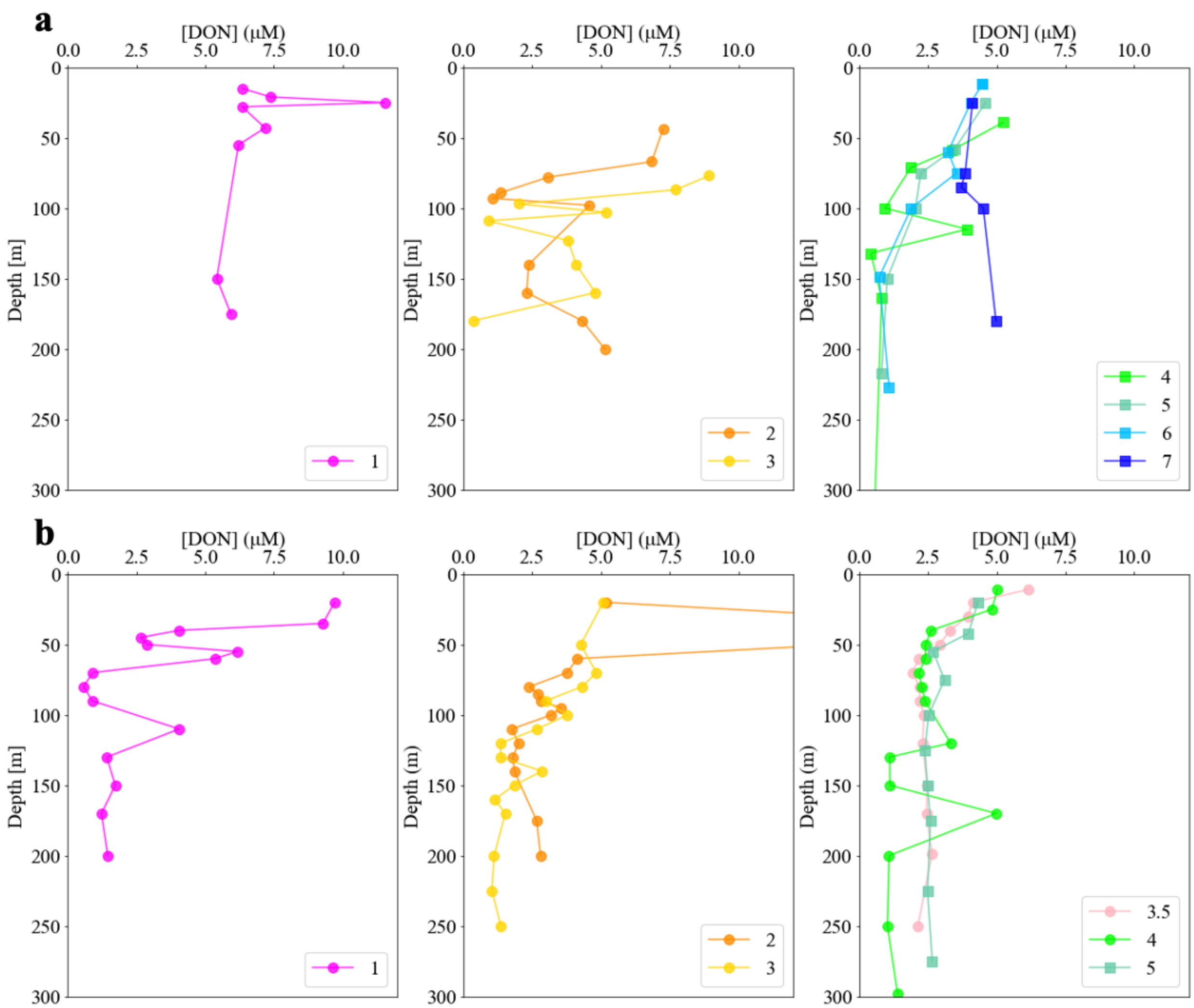

Figure S4.5. Dissolved organic nitrogen concentrations at sampled stations in the ETNP. Panel (**a**) has profiles from April 2017 and panel (**b**) shows profiles from June 2018. Circles designate 'AMZ' stations and squares are 'non-AMZ' stations.

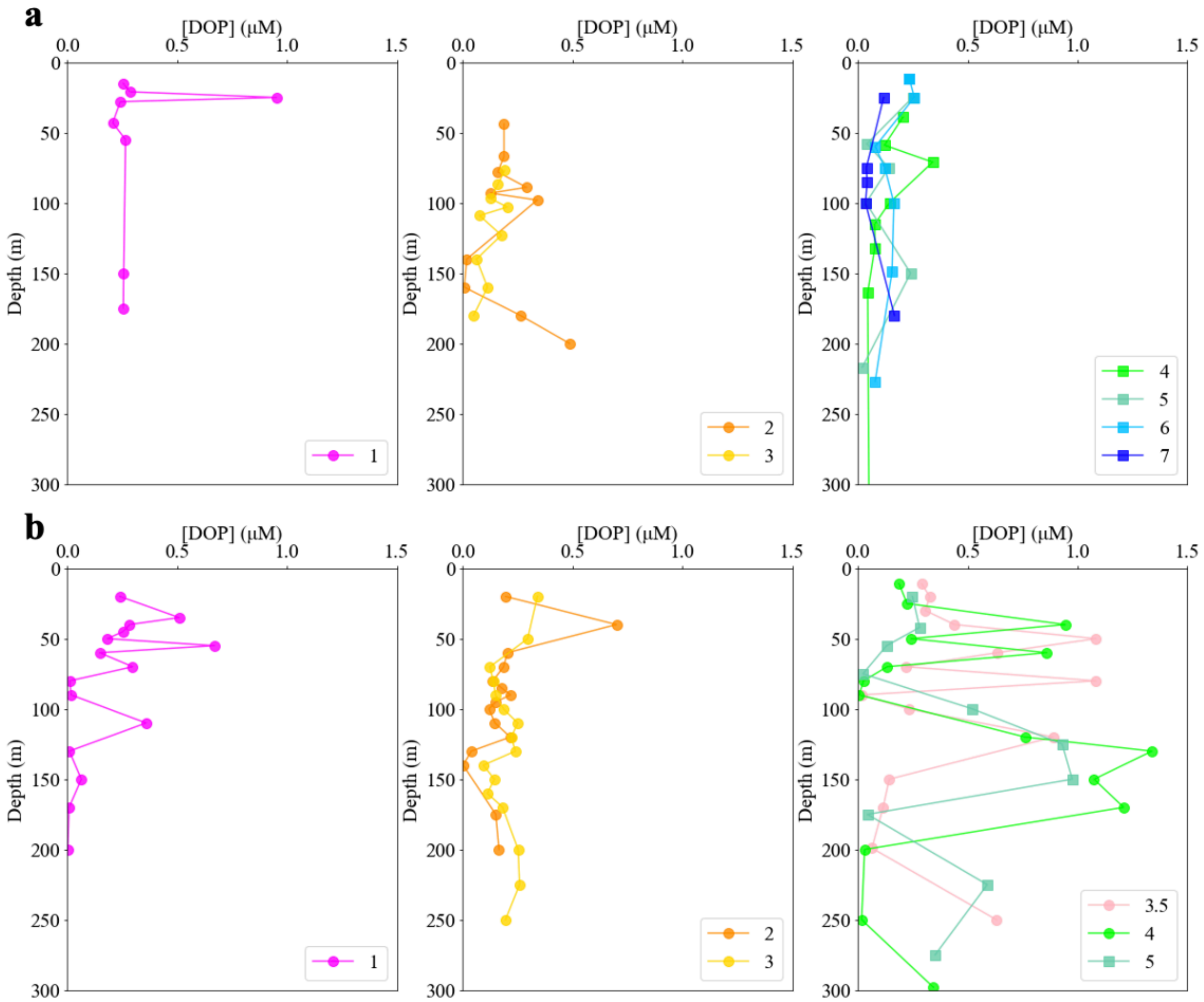

Figure S4.6. Dissolved organic phosphorus concentrations at sampled stations in the ETNP. Panel (**a**) has profiles from April 2017 and panel (**b**) shows profiles from June 2018. Circles designate 'AMZ' stations and squares are 'non-AMZ' stations.

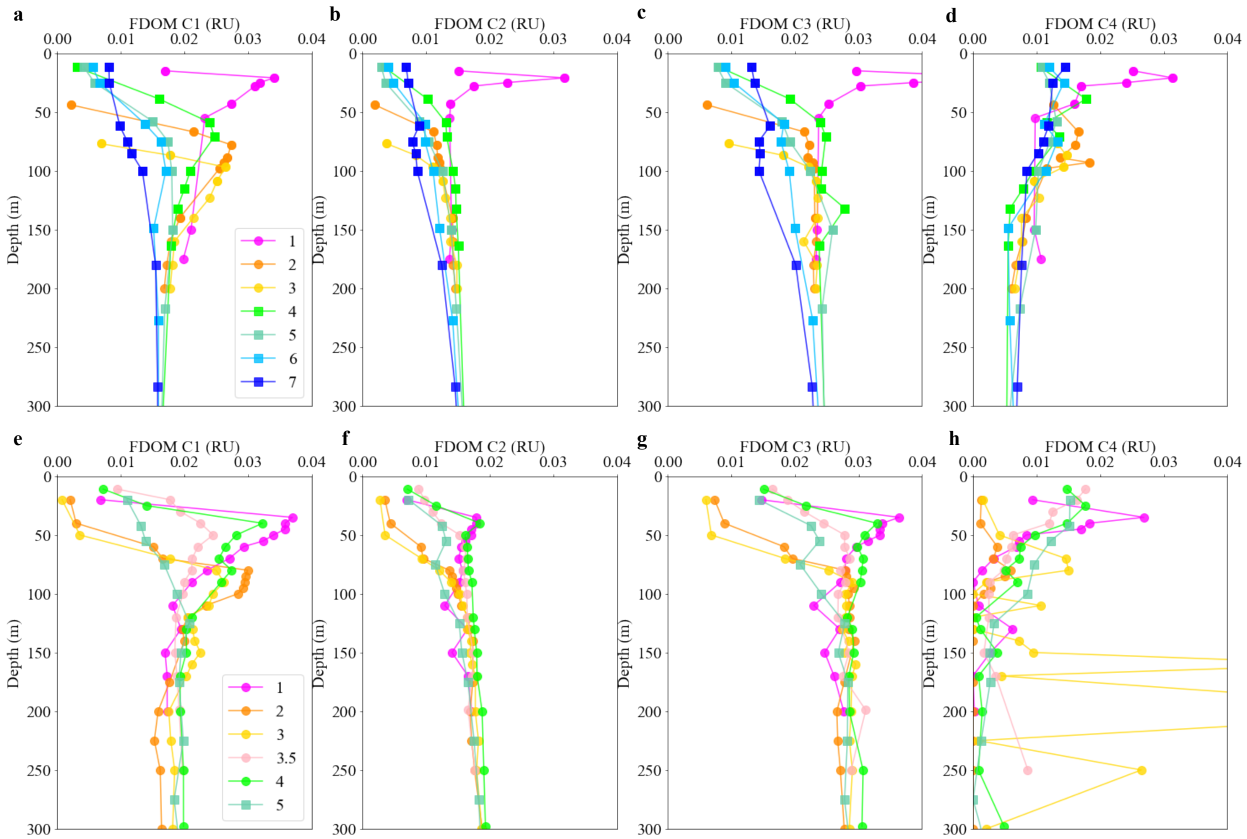

Figure S4.7. Fluorescent dissolved organic matter (FDOM) components at sampled stations in the ETNP. Profiles from April 2017 are in (**a-d**) and profiles from June 2018 are in (**e-h**). C1 (**a, e**) has been identified as characteristic of 'marine humics', C2 and C3 (**b-c, f-g**) are 'humic-like' and C4 (**d, h**) is 'protein-like'.

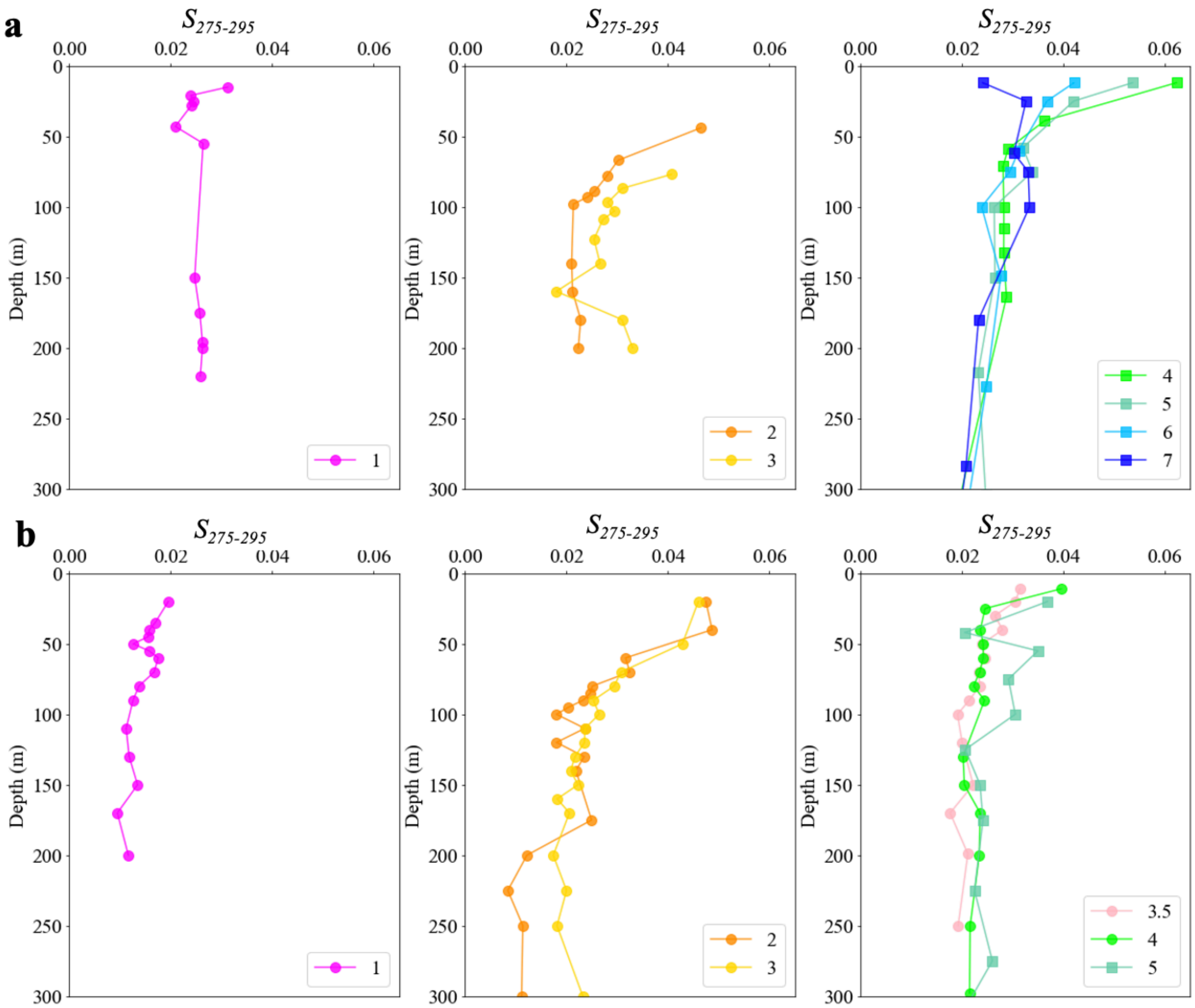

Figure S4.8. CDOM spectral slope from 275 to 295 nm at sampled stations in the ETNP. Panel (**a**) has profiles from April 2017 and panel (**b**) shows profiles from June 2018. Circles designate ‘AMZ’ stations and squares are ‘non-AMZ’ stations.

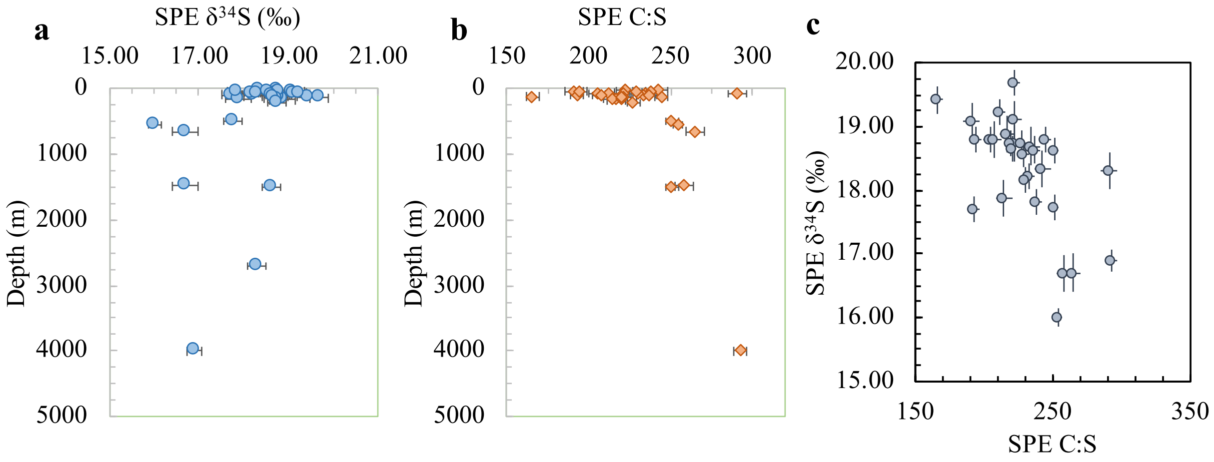

Figure S4.9. SPE C:S ratios and δ^{34}S from the ETNP across a range of depths. C:S (**a**) increases slightly with increasing depth. SPE δ^{34}S (**b**) shows a slight decrease with depth and is negatively correlated with SPE C:S (**c**).

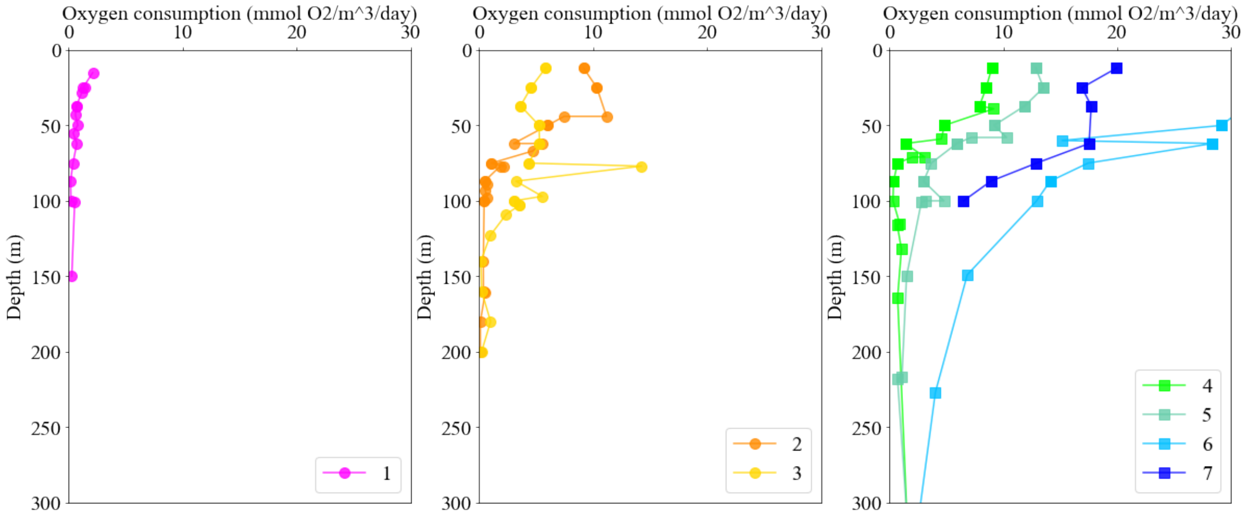

Figure S4.10. Oxygen consumption rates measured on the April 2017 cruise to the ETNP. These rates have not been corrected for nitrite or ammonium oxidation. Circles designate 'AMZ' stations and squares are 'non-AMZ' stations.

Chapter 5: It’s about time: a new perspective on marine dissolved organic radiocarbon

Abstract

The >5000-year radiocarbon age of much of the 630±30 Pg marine dissolved organic carbon (DOC) reservoir remains an enigma in the marine carbon cycle. Current models dictate that the most radiocarbon (^{14}C) depleted DOC is present as a uniform reservoir throughout the water column and cycles passively, with the observed vertical ^{14}C and concentration gradient modulated by the addition and removal of DOC from contemporary photosynthesis. Using a thermal oxidation method to constrain the ^{14}C distribution within a representative fraction of DOC, we show that the most ^{14}C-depleted fraction that we isolate from the surface ocean is not as depleted as deep ocean DOC, yet they share similar chemical features. Our new results show that even the most ^{14}C-depleted DOC fraction exhibits a vertical ^{14}C gradient, requiring the addition and removal of DOC from this reservoir on shorter timescales than current models predict. In fact, a revision of the water column lifetime of marine DOC to only 2,300 years is indicated by the data, which approximately doubles the flux of carbon through the deep ocean.

Introduction

The reservoir of dissolved organic carbon (DOC) in the ocean is similar in magnitude to that of atmospheric CO_2 and thus of significant importance to global cycling (Hedges and Oades 1997). Radiocarbon ($\Delta^{14}C$) measurements have revealed that $\Delta^{14}C$-DOC decreases along the path of global thermohaline circulation, similar to marine dissolved inorganic carbon (DIC). The enigma, however, is that DOC is older than *in situ* DIC by several thousand years (Druffel et al. 1992, 2019; Druffel and Bauer 2000). The average age of DOC in the deep North Pacific Ocean is approximately 6400 ^{14}C years (a $\Delta^{14}C$ signature of -550 ‰), which is significantly older than the circulation time of the ocean (~1000-2000 years) (Stuiver et al. 1983). These observations, together with a stable carbon isotope signature ($\delta^{13}C$) that suggests a photosynthetic source and a $\Delta^{14}C$ signature that varies linearly with the inverse DOC concentration, have produced the popular ~35 year-old paradigm: that of a homogenous background, 'refractory' reservoir of ^{14}C-depleted DOC present throughout the water column, to which is added varying concentrations of ^{14}C-enriched DOC from photosynthesis (Williams and Druffel 1987; Hansell et al. 2009). The longevity of this two-component isotope and concentration mixing model can be attributed to its ability to reproduce the observed $\Delta^{14}C$ distribution in DOC. However, the paradigm provides no mechanistic insight into the source and true residence time of the most ^{14}C-depleted components. For example, background refractory DOC with a constant $\Delta^{14}C$ signature throughout the water column is difficult to explain without invoking a DOC component of infinite age (^{14}C-dead) (Beaupré and Aluwihare 2010; Follett et al. 2014; Beaupré et al. 2020). Yet, there is currently no evidence for a quantitatively significant fraction of ^{14}C-dead DOC in the ocean (Beaupré and Aluwihare 2010; Follett et al. 2014; Zigah et al. 2017; Broek et al. 2017; Beaupré et al. 2020).

A few studies have measured the $\Delta^{14}C$ distribution within marine DOC and have concluded that a heterogeneous $\Delta^{14}C$ distribution exists (Aluwihare and Repeta 1999; Loh et al. 2004; Repeta and Aluwihare 2006; Follett et al. 2014; Zigah et al. 2015, 2017; Coppola and Druffel 2016; Broek et al. 2017, 2020). ^{14}C-enriched compounds consistent with recent production have been observed in both high molecular weight (HMW) DOC (Repeta and Aluwihare 2006) (Figure S5.1) and solid phase extracted DOC (de Jesus 2008) in the surface ocean, and ^{14}C-depleted fractions have been detected throughout the water column (Druffel et al. 1992; Loh et al. 2004; Repeta and Aluwihare 2006; de Jesus 2008; Beaupré and Druffel 2012; Follett et al. 2014; Coppola and Druffel 2016; Zigah et al. 2017; Broek et al. 2017, 2020). Taken together, these data support the contribution of DOC from photosynthesis and the prevalence of aged DOC throughout the ocean, but a key requirement of the two-component model, the background pool of refractory DOC with a vertically uniform concentration and $\Delta^{14}C$ signature, has not been satisfied.

In this study, we test the hypothesis that a chemically similar DOC fraction with the same ^{14}C-depleted signature is present in both the surface and deep ocean, as is required by the current paradigm (Williams and Druffel 1987; Beaupré and Aluwihare 2010; Beaupré et al. 2020). We applied a technique called ramped pyrolysis/oxidation (RPO) (Rosenheim et al. 2008; Hemingway et al. 2017b) to serially oxidize DOC to CO_2 and capture the evolved gas for $\Delta^{14}C$ measurements. The DOC examined here was isolated from seawater using PPL solid phase extraction resin (PPL-DOC) (Dittmar et al. 2008) and both bulk PPL-DOC and its acid hydrolyzed counterpart were examined by RPO. Our experiments did identify a chemically similar component of DOC throughout the water column that was depleted in ^{14}C. However, the $\Delta^{14}C$-DOC of this component was higher in the surface ocean (-385 ± 6‰) than in the deep ocean (-506 ± 14 to -537 ± 7‰), calling into question the existence of an isotopically uniform, background DOC pool and requiring a revision of the current paradigm.

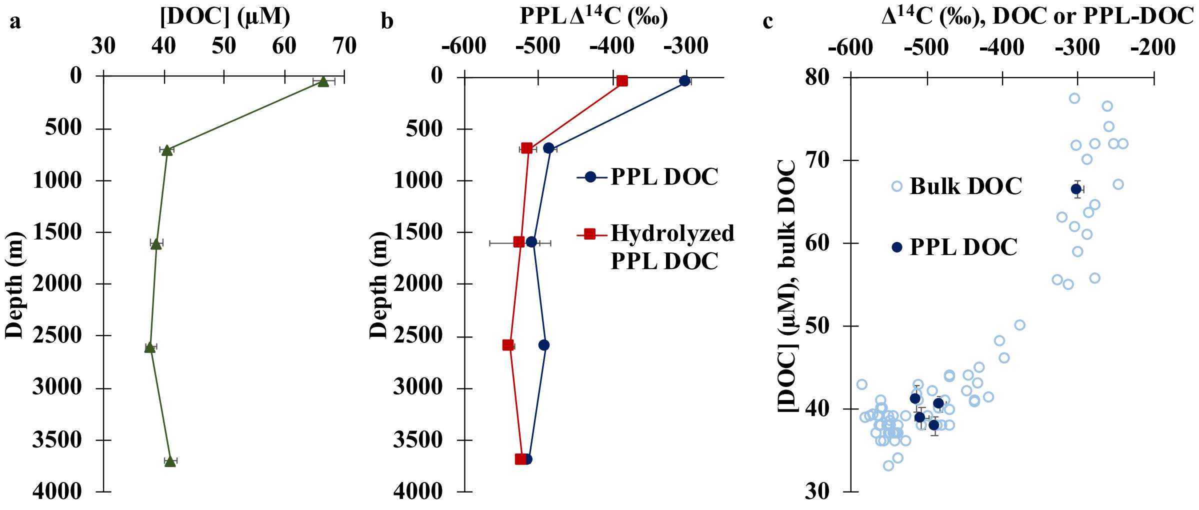

Figure 5.1. DOC concentration and PPL-DO^{14}C measurements from Station M. Organic carbon concentrations (this study) (**a**) decrease with depth. Error bars represent measurement uncertainty. A similar trend is seen in Δ^{14}C of SPE PPL-DOC (**b**), where PPL-DOC measurements are shown with blue circles. Acid hydrolyzed PPL-DOC Δ^{14}C values are shown as red squares. Error bars represent uncertainty in radiocarbon measurements. A plot of bulk DOC Δ^{14}C and [DOC] from previous Station M cruises 1991 – 2004 AD (n = 76) is shown in (**c**) reproduced from Beaupré et al. 2020. Bulk DOC values are shown in open circles and PPL-DOC values from this study are shown in closed circles. [DOC] values for PPL-DOC are the water column bulk [DOC] from where samples were collected. This demonstrates that radiocarbon values for PPL-DOC are not very different from what would be expected for bulk DOC at this location and DOC concentration.

Thermal oxidation reflects chemical differences but reveals limited ^{14}C diversity

PPL-DOC was isolated from five depths at Station M (34° 50’N, 123° 00’W; 4100 meters depth) in the Eastern North Pacific Ocean for RPO. Sampling depths were chosen to encompass the major currents and water masses of the region, which are well represented at Station M, and include the ocean’s oldest water mass, North Pacific Deep Water (~2000-4000 m) (Bauer et al. 1998). Overall, water column DOC concentrations (Figure 5.1a) as well as Δ^{14}C and δ^{13}C of PPL-DOC (Figure 5.1b, Table S5.1) from the current study are consistent with previous reports from Station M (Beaupré and Druffel 2009; Druffel and Griffin 2015). For example, both Δ^{14}C

PPL-DOC and Δ^{14}C-DOC from Station M show a similar relationship with bulk DOC concentration (Figure 5.1c), despite PPL-DOC representing approximately 35-55% of the total DOC mass (Lechtenfeld et al. 2014). Based on this simple comparison we expect PPL-DOC to encompass the range of Δ^{14}C-DOC values observed for bulk DOC and contain its most ^{14}C-enriched and ^{14}C-depleted components (see Supplementary Information).

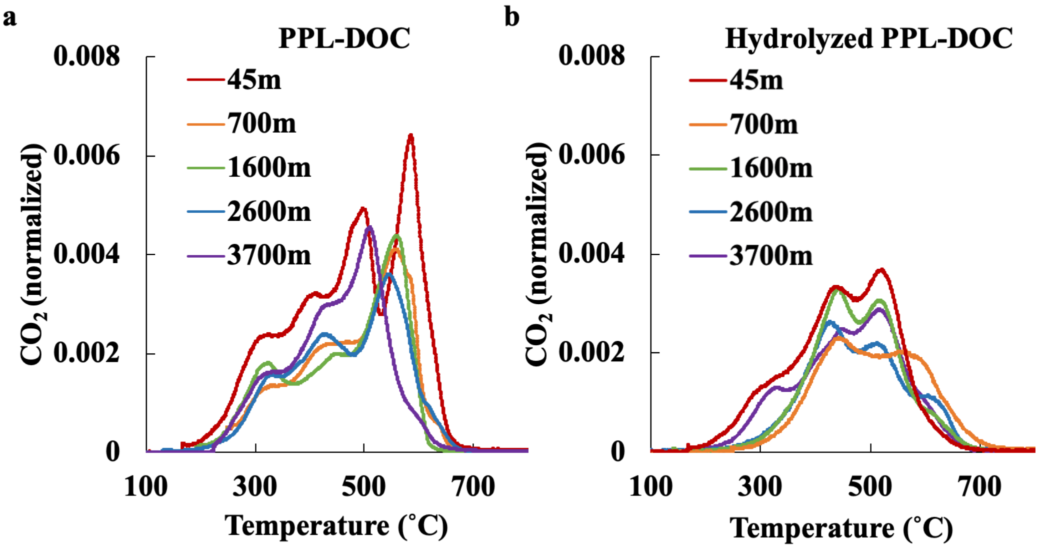

Figure 5.2. Serial thermal oxidation (thermograms) of PPL-DOC before and after acid hydrolysis. Thermograms of PPL-DOC from five depths at Station M (**a**). CO_2 concentrations were scaled based on DOC concentration assuming uniform extraction efficiencies. Thermograms of the same samples after hydrolysis, scaled to predicted yields, show marked changes (**b**). Samples become more similar to each other and to deep DOM following hydrolysis and re-extraction onto the PPL resin.

The pyrolysis/oxidation of organic carbon that occurs during RPO is monitored as a 'thermogram,' which tracks the evolution of CO_2 as temperature increases (Rosenheim et al. 2008). Previous studies have demonstrated that thermograms integrate the activation energies of all compounds in a sample, and thus are unique to the combination of molecules present (Rosenheim et al. 2008; Plante 2013; Williams et al. 2014; Hemingway et al. 2017b). Thermograms of Station M samples showed discernible depth-related differences (Figure 5.2a).

To interrogate the range in $\Delta^{14}C$ values (i.e., $\Delta^{14}C$ diversity) within a sample, six CO_2 fractions were collected during RPO analyses of PPL-DOC from three depths. Contrary to what has been observed for other environmental organic carbon samples (Rosenheim and Galy 2012; Plante 2013; Hemingway et al. 2019) and what would be predicted based on the current model of DOC cycling, thermal fractions of PPL-DOC did not exhibit substantial $\Delta^{14}C$ diversity (Zigah et al. 2015) (Figure 5.3, blue bars). For example, none of the CO_2 fractions collected from the 45 m sample had modern $\Delta^{14}C$-DOC signatures, whereas RPO fractions of surface HMW DOC have been shown to contain modern carbon (Figures S5.1 and S5.2) as would be anticipated from bulk HMW DOC $\Delta^{14}C$ signatures (Repeta and Aluwihare 2006; Zigah et al. 2017; Broek et al. 2017, 2020).

Given that shallower Station M thermograms contained distinct thermal features that might be expected to reflect the addition of new material from photosynthesis and its subsequent removal at depth (Figure 5.2a), the <100 ‰ range in $\Delta^{14}C$ values among RPO fractions (Figure 5.3, blue bars) at each depth, was unexpected. However, serial UV oxidation, when applied with the purpose of examining $\Delta^{14}C$-DOC diversity, has similarly failed to directly detect endmember $\Delta^{14}C$ values in surface marine DOC (Beaupré and Druffel 2012; Follett et al. 2014). If distinct molecules and/or functional groups oxidize at particular temperatures, then the observed overlap in $\Delta^{14}C$ values requires that unique populations of molecules are composed of a mixture of $\Delta^{14}C$ signatures whose average value is similar across the thermogram. Partial oxidation of compounds along the temperature ramp is also possible and appears to be supported by the observed heterogeneity in $\delta^{13}C$ values across fractions (Figures S5.3-10 and S5.12). Since the $\delta^{13}C$ signature of marine DOC is not expected to show significant diversity, the observed variations in $\delta^{13}C$ are interpreted to reflect thermal oxidation of different functional groups that may be derived from distinct biosynthetic pathways (Hayes 1993). Such an interpretation is consistent with the thermogram "separating" distinct chemical structures in DOC. A similar $\delta^{13}C$ trend has also been observed in thermograms of riverine POC and marine HMW DOC (Hemingway et al. 2017b) (Figures S5.1 and S5.2). Partial oxidation within a temperature bin and accompanying redistribution of remaining carbon along the activation energy spectrum may also be required to explain the observed thermogram and isotope distribution. Charring in particular has been documented during RPO and could contribute to the high temperature peak that is most prominent in the surface ocean (Figure 5.2a, S5.3-4) (Williams et al. 2014). This potential for reorganization highlights a possible issue with "dissolved" black carbon isolation methods that utilize only thermal oxidation, because thermally resistant carbon that was not present in the original sample can be generated during this process. Thus, recently published results showing that black carbon isolated via high temperature oxidation does not have a radiocarbon signature significantly different from that of bulk PPL may misrepresent black carbon cycling, at least within the DOC pool (Qi et al. 2020).

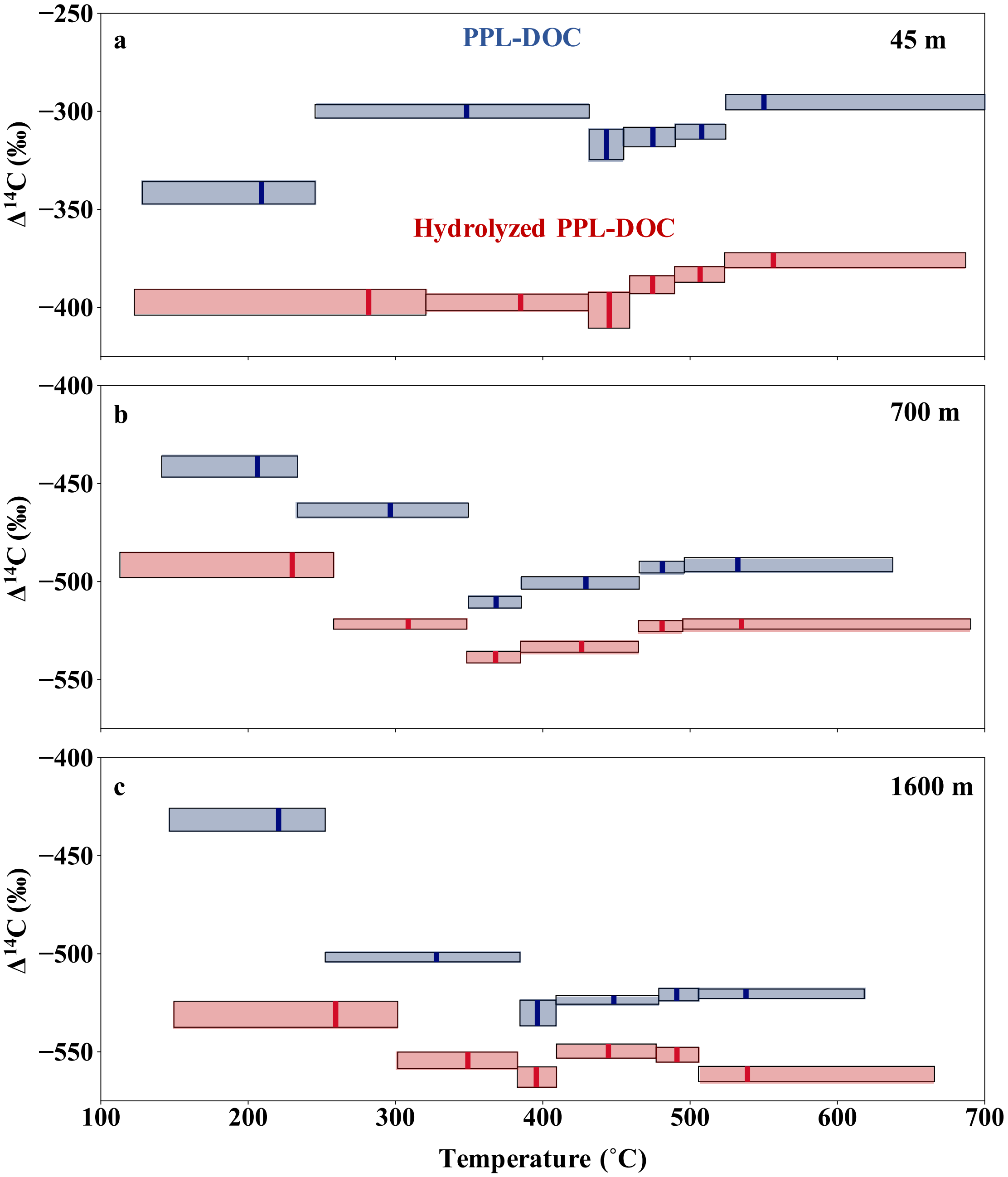

Figure 5.3. Radiocarbon measurements of individual thermal fractions. Bulk PPL-DOC is shown in blue and hydrolyzed PPL-DOC in red for (**a**) 45 m, (**b**) 700 m, and (**c**) 1600 m. Boxes span the temperature range (horizontally) and the mean $\Delta^{14}C$ value ± 1 standard deviation (vertically) for each fraction. The line inside each box indicates the carbon weighted average temperature for that fraction. Note the different scale for the 45 m sample.

Isolation of ubiquitous, ^{14}C-depleted DOC with a vertical Δ^{14}C gradient

Previous work has shown that the Δ^{14}C diversity in DOC can be revealed by chemical degradation techniques, such as acid hydrolysis (Repeta and Aluwihare 2006; Arakawa et al. 2017). Therefore, PPL-DOC was subjected to hydrochloric acid hydrolysis followed by re-extraction onto PPL resin, which isolated a more ^{14}C-depleted component (Figure 5.1b). The change in Δ^{14}C following the acid hydrolysis ($\Delta\Delta^{14}$C) revealed that ^{14}C-enriched, acid-labile material was present at several depths. A crude mass balance indicated that PPL-DOC lost from each depth during the hydrolysis had Δ^{14}C values significantly more enriched than the bulk value and similar to local Δ^{14}C-DIC reported in previous studies (Table S5.2). Yields for the hydrolysis reaction were precisely determined for PPL-DOC samples from other locations in the Eastern Pacific where ample material was available. These results showed that the hydrolysis removed a greater fraction of carbon from surface (30-40%) compared with deep ocean (10-20%) PPL-DOC (Table S5.5). This is consistent with previously reported vertical decreases in acid-labile polar compounds including dissolved sugars and amino acids (Repeta and Aluwihare 2006; Kaiser and Benner 2009; Helms 2012). The carbon to nitrogen ratio (C:N) of all samples increased following hydrolysis and re-extraction, indicating the removal of N-rich material, a characteristic generally associated with more labile DOM (Aluwihare et al. 2005) (Table S5.5).

The observed change after hydrolysis, both in terms of Δ^{14}C and thermogram shape, was greatest in the 45 m sample, consistent with the presence of more recently produced and acid-labile DOC in the surface ocean (Figures 5.1b and 5.22b). Additionally, the thermograms of hydrolyzed residues resembled each other closely and were more similar to the deepest PPL-DOC sample (Figures 5.2, 5.4a), and the extent to which acid hydrolysis altered each thermogram was well-correlated with the change in Δ^{14}C values (Figure 5.4b). Such a shift toward a “core” thermogram has previously been observed for soil organic matter subjected to acid fumigation (Plante 2013). In addition to being more similar across depths, thermogram peak shapes for the hydrolysis residue are less defined and they occupy a narrower thermal range (Figure 5.2b) suggesting fewer distinct functional groups than the bulk.

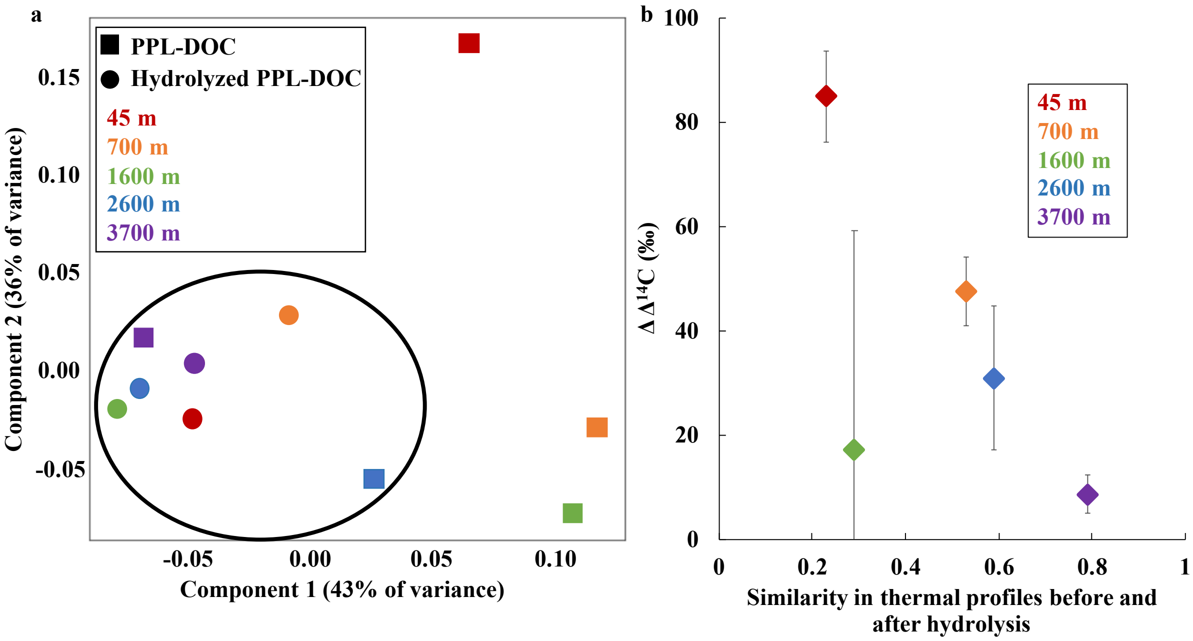

Figure 5.4. Comparison of PPL-DOC thermograms and Δ^{14}C before and after acid hydrolysis. Sample thermograms become more similar to each other and to deep DOM following hydrolysis and re-extraction on the PPL as shown by a Principal Coordinate Analysis (PCA) in (**a**). The black circle emphasizes the similarity between hydrolyzed samples and deep PPL-DOC. Hydrolysis alters the chemistry and radiocarbon of PPL-DOC samples (**b**), where a greater change in the thermal profile is strongly correlated with a greater change in the radiocarbon (Δ^{14}C of the corresponding hydrolysis residue minus Δ^{14}C PPL-DOC; $\Delta\Delta^{14}$C). Error bars correspond to propagated uncertainty in radiocarbon measurements.

The convergence of PPL-DOC thermograms from hydrolysis residues toward unhydrolyzed PPL-DOC from the deepest depths (Figures 5.2 and 5.4) is taken as evidence that the similar features in these thermograms do not result from hydrolysis-induced rearrangement of structures in PPL-DOC. Instead, the removal of compounds following the hydrolysis and re-extraction apparently exposes the core thermogram of a DOC component that is present throughout the water column and dominates the bulk PPL-DOC at depth. Each thermogram is a result of the entire mixture of components within the sample and its shape results from a non-linear combination of the thermal reactivities of that unique mixture of compounds (Williams et al. 2014). This is why thermograms with similar shapes provide strong evidence of compositional similarity. Fraction collections were completed for hydrolyzed samples from 45, 700, and 1600 m, and maximum radiocarbon diversity within hydrolysis residues was 39 ‰, compared to 100 ‰ for PPL-DOC. All fractions showed a decrease in Δ^{14}C compared to their counterpart in PPL-DOC over the same temperature range (Figure 5.3), which indicated that diverse functional groups were present in both the PPL-DOC that was removed following the hydrolysis and the hydrolysis residue. The decrease in Δ^{14}C across all fractions following hydrolysis further confirmed that ^{14}C-enriched (contemporary) and ^{14}C-depleted components overlap to some extent in their structural features.

Despite the shift toward a core thermogram, the hydrolyzed 45 m sample remained >100 ‰ more enriched than deeper samples (Figure 5.1b). Whereas the compositional uniformity of hydrolysis residues supported the presence of a ubiquitous DOC component (i.e., compositionally similar DOC present throughout the water column), this component did not have a vertically uniform Δ^{14}C signature. The observed vertical Δ^{14}C gradient is consistent with all other Δ^{14}C-DOC investigations to date, where no fraction in the surface ocean has been directly shown to possess a Δ^{14}C signature as depleted as Δ^{14}C-DOC in the deep ocean (Druffel et al. 1992; Repeta and Aluwihare 2006; Beaupré and Druffel 2012; Follett et al. 2014; Walker et al. 2016; Zigah et al. 2017; Broek et al. 2017, 2020). Based on the current paradigm, this vertical Δ^{14}C gradient would be interpreted as reflecting the addition of chemically similar, but new DOC at the surface, which enriches the $\Delta^{14}C$ signature of ubiquitous DOC that is mixed up from the deep ocean.

A new hypothesis for marine DOC cycling

Interpreting the vertical chemical and isotopic characteristics of ubiquitous DOC in the context of the current paradigm leaves many questions unanswered. In fact, such an interpretation cannot explain either the inventory, or the $\Delta^{14}C$ signature, of this component. The observations presented in this study could instead be explained by a pre-aged component that enters the ocean and ages further as it moves along the path of deep ocean circulation, similar to what is observed for dissolved inorganic carbon (DIC). We can approximate the ^{14}C-age gradient of the ubiquitous component by comparing the 45 m and 2500 m hydrolysis residues from Station M (i.e., -385 and -537‰, respectively; Table S5.1). This results in an age gradient of ~2300 radiocarbon years. A similar calculation for DIC using comparable depths at Station M (in this case 85 and 2532 m; Table S5.2) results in an age difference of ~2200 radiocarbon years, not significantly different from that of the hydrolysis residue. This model is distinct from the previous paradigm in that it requires the background component to have a non-uniform $\Delta^{14}C$-DOC signature that is also changing with time. Furthermore, any removal of ubiquitous DOC along the path of ocean circulation would not modify the $\Delta^{14}C$ signature of the remaining fraction. This proposed model is consistent with the $\Delta^{14}C$ and concentration gradients observed for DOC in the deep ocean (Druffel et al. 1992; Druffel and Bauer 2000; Beaupré et al. 2020; Broek et al. 2020). Note that such a model does not preclude dilute components of DOC exhibiting different trends with depth.

$\Delta^{14}C$ signatures presented here for the ubiquitous component have other important implications. If we revise the depleted endmember to -400 ‰ in the surface ocean, then in order to satisfy measured bulk Δ^{14}C-DOC we would predict a larger background component, closer to 75 % of the DOC, or around 50 μM at Station M (compared to the typically assumed concentration of 36 μM C). Globally, this would suggest a 40 % increase in the surface ocean (upper 200 m) refractory DOC reservoir and consequent decrease in the surface ocean labile DOC reservoir of approximately 12 Pg of C. A lower contribution from contemporary photosynthesis is more consistent with measurements of surface DOC drawdown by microbial communities, where incubation studies have not observed DOC concentrations to drop below 50 μM (Carlson et al. 2004; Letscher et al. 2015). This revision together with the overall vertical decrease in DOC concentrations (e.g. Figure 5.1a), would also suggest that the ubiquitous component is removed during its transit to the deep ocean along with contemporary DOC, though at a slower rate.

This interpretation suggests that two independent DOC cycles are operating in the ocean – one that involves DOC derived from contemporary photosynthesis and a second that involves the ubiquitous component. Such a hypothesis is consistent with observations showing that the isotope mixing model for DOC is decoupled above and below ~300 m at Station M (Beaupré and Aluwihare 2010; Beaupré et al. 2020). Previous estimates of carbon flux through the DOC reservoir assumed that the average age of >5,000 radiocarbon years for DOC in the deep ocean reflected its accumulation in the ocean following production by photosynthesis. In contrast, this new paradigm would explain the measured Δ^{14}C signature of DOC not by assuming a residence time longer than the overturning circulation of the ocean, but by invoking a pre-aged source of DOC to the upper ocean, followed by aging of this DOC in the deep ocean before removal. In consequence, this revision would increase the removal rate for ^{14}C-depleted DOC to approximately 0.2-0.3 Pg DOC per year, which results in a residence time that is consistent with the faster DOC removal rates inferred from early photochemical studies (Mopper et al. 1991). Deep ocean removal processes may also be important, and hydrothermal processes and particle interactions have been put forward as potential sinks for refractory DOC in the deep ocean (Druffel and Williams 1990; Lang et al. 2006; Hawkes et al. 2015; Shah Walter et al. 2018), yet the extent of their contributions remains far from constrained (Beaupré et al. 2019). There are several possible sources of pre-aged DOC to the upper ocean including sediments of continental shelves (Druffel et al. 1998; Komada et al. 2013), riverine input (Coppola and Druffel 2016; Coppola et al. 2018), and atmospheric deposition (Yu et al. 2018). Sediments are the most likely source of this widespread pre-aged component (Mopper et al. 1991), which requires that carbon previously thought to have been sequestered in sediments is re-entering the water column and being oxidized.

Applying this method to surface DOC collected in different ocean basins, including in the Southern Ocean near sites of deep-water formation where no ^{14}C gradient would be expected for ubiquitous DOC, should help to constrain the $\Delta^{14}C$ signature of the ubiquitous fraction in the surface ocean. Furthermore, demonstrating synchrony in the $\Delta^{14}C$ gradient of hydrolysis resistant PPL-DOC and DIC along the path of deep ocean circulation together with modelling efforts could effectively demonstrate ongoing aging of the ubiquitous component. Finally, further efforts to constrain the relevant sources and sinks of marine DOC will be necessary.

Results presented here, along with observations from all other $\Delta^{14}C$-DOC studies to date, suggest that there is a structurally uniform fraction that dominates PPL-DOC throughout the water column but that no component in the surface ocean is as ^{14}C-depleted as its counterpart in the deep ocean. The latter observation is fundamentally at odds with the whole-ocean two-component model that has long dominated this field of study. It is time that we examined the possibility that the surprisingly advanced radiocarbon-age of DOC is not conferred simply by DOC accumulation in the water column over many thousands of years, but from the input of pre-aged DOC to the upper ocean.

Acknowledgements

We would like to thank the captain and crew of the *R/V Western Flyer* as well as Christine Huffard, Christina Preston, and Erich Rienecker for help with sample collection. We are grateful to the staff at NOSAMS, particularly Mark Kurz and Alan Gagnon for help with sample analysis logistics. We also thank Yury Kiselev for help with data processing. Funding for this work came from NSF grants OCE 1736656 and OCE 1555375 and from the NOSAMS Graduate Student Internship Program. KLS was funded by the David and Lucile Packard Foundation.

Additional Acknowledgements

Chapter 5, is currently being formulated into a manuscript that will be submitted for publication. “It’s about time: a new perspective on marine dissolved organic radiocarbon”. Margot White, Tran Nguyen, Irina Koester, Mary C. Lardie Gaylord, J. Michael Beman, Kenneth Smith, Ann McNichol, Steven Beaupré, and Lihini Aluwihare. The dissertation author was the primary investigator and author of this paper.

References

Aluwihare, L.I., Repeta, D.J., Pantoja, S., Johnson, C.G., 2005. Two chemically distinct pools of organic nitrogen accumulate in the ocean. Science (80-.). 308, 1007–1010. https://doi.org/10.1126/science.1108925

Aluwihare, L.I., Repeta, D.J.D., 1999. A comparison of the chemical characteristics of oceanic DOM and extracellular DOM produced by marine algae. Mar. Ecol. Prog. Ser. 186, 105–117. https://doi.org/10.3354/meps186105

Arakawa, N., Aluwihare, L.I., Simpson, A.J., Soong, R., Stephens, B.M., Lane-Coplen, D., 2017. Carotenoids are the likely precursor of a significant fraction of marine dissolved organic matter. Sci. Adv. 3, e1602976. https://doi.org/10.1126/sciadv.1602976

Bauer, J.E., Druffel, E.R.M., Williams, P.M., Wolgast, D.M., Griffin, S., 1998. Temporal variability in dissolved organic carbon and radiocarbon in the eastern North Pacific Ocean. J. Geophys. Res. Ocean. 103, 2867–2881. https://doi.org/10.1029/97JC02545

Beaupré, S.R., Aluwihare, L., 2010. Constraining the 2-component model of marine dissolved organic radiocarbon. Deep Sea Res. Part II Top. Stud. Oceanogr. 57, 1494–1503.

Beaupré, S.R., Druffel, E.R.M., 2012. Photochemical reactivity of ancient marine dissolved organic carbon. Geophys. Res. Lett. 39. https://doi.org/10.1029/2012GL052974

Beaupré, S.R., Druffel, E.R.M., 2009. Constraining the propagation of bomb-radiocarbon through the dissolved organic carbon (DOC) pool in the northeast Pacific Ocean. Deep. Res. Part I Oceanogr. Res. Pap. 56, 1717–1726. https://doi.org/10.1016/j.dsr.2009.05.008

Beaupré, S.R., Kieber, D.J., Keene, W.C., Long, M.S., Maben, J.R., Lu, X., Zhu, Y., Frossard, A.A., Kinsey, J.D., Duplessis, P., Chang, R.Y.W., Bisgrove, J., 2019. Oceanic efflux of ancient marine dissolved organic carbon in primary marine aerosol. Sci. Adv. 5. https://doi.org/10.1126/sciadv.aax6535

Beaupré, S.R., Walker, B.D., Druffel, E.R.M., 2020. The two-component model coincidence: Evaluating the validity of marine dissolved organic radiocarbon as a stable-conservative tracer at Station M. Deep Sea Res. Part II Top. Stud. Oceanogr. 104737. https://doi.org/10.1016/j.dsr2.2020.104737

Broek, T.A.B., Walker, B.D., Guilderson, T.P., McCarthy, M.D., 2017. Coupled ultrafiltration and solid phase extraction approach for the targeted study of semi-labile high molecular weight and refractory low molecular weight dissolved organic matter. Mar. Chem. 194, 146–157. https://doi.org/10.1016/J.MARCHEM.2017.06.007

Broek, T.A.B., Walker, B.D., Guilderson, T.P., Vaughn, J.S., Mason, H.E., McCarthy, M.D., 2020. Low Molecular Weight Dissolved Organic Carbon: Aging, Compositional Changes, and Selective Utilization During Global Ocean Circulation. Global Biogeochem. Cycles 34.

https://doi.org/10.1029/2020GB006547

Carlson, C.A., Giovannoni, S.J., Hansell, D.A., Goldberg, S.J., Parsons, R., Vergin, K., 2004. Interactions among dissolved organic carbon, microbial processes, and community structure in the mesopelagic zone of the northwestern Sargasso Sea. Limnol. Oceanogr. 49, 1073–1083. https://doi.org/10.4319/lo.2004.49.4.1073

Coppola, A.I., Druffel, E.R.M., 2016. Cycling of black carbon in the ocean. Geophys. Res. Lett. 43, 4477–4482. https://doi.org/10.1002/2016GL068574

Coppola, A.I., Wiedemeier, D.B., Galy, V., Haghipour, N., Hanke, U.M., Nascimento, G.S., Usman, M., Blattmann, T.M., Reisser, M., Freymond, C. V., Zhao, M., Voss, B., Wacker, L., Schefuß, E., Peucker-Ehrenbrink, B., Abiven, S., Schmidt, M.W.I., Eglinton, T.I., 2018. Global-scale evidence for the refractory nature of riverine black carbon. Nat. Geosci. 11, 584–588. https://doi.org/10.1038/s41561-018-0159-8

de Jesus, R.P., 2008. Natural abundance radiocarbon studies of dissolved organic carbon (DOC) in the marine environment. University of California San Diego.

Dittmar, T., Koch, B., Hertkorn, N., Kattner, G., 2008. A simple and efficient method for the solid-phase extraction of dissolved organic matter (SPE-DOM) from seawater. Limnol. Oceanogr. Methods 6, 230–235. https://doi.org/10.4319/lom.2008.6.230

Druffel, E.R.M., Bauer, J.E., 2000. Radiocarbon distributions in Southern Ocean dissolved and particulate organic matter. Geophys. Res. Lett. 27, 1495–1498. https://doi.org/10.1029/1999GL002398

Druffel, E.R.M., Griffin, S., 2015. Radiocarbon in dissolved organic carbon of the South Pacific Ocean. Geophys. Res. Lett. 42, 4096–4101. https://doi.org/10.1002/2015GL063764

Druffel, E.R.M., Griffin, S., Bauer, J.E., Wolgast, D.M., Wang, X.C., 1998. Distribution of particulate organic carbon and radiocarbon in the water column from the upper slope to the abyssal NE Pacific Ocean. Deep. Res. Part II Top. Stud. Oceanogr. 45, 667–687. https://doi.org/10.1016/S0967-0645(98)00002-2

Druffel, E.R.M., Griffin, S., Wang, N., Garcia, N.G., McNichol, A.P., Key, R.M., Walker, B.D., 2019. Dissolved Organic Radiocarbon in the Central Pacific Ocean. Geophys. Res. Lett. 46, 2019GL083149. https://doi.org/10.1029/2019GL083149

Druffel, E.R.M., Williams, P.M., 1990. Identification of a deep marine source of particulate organic carbon using bomb 14C. Nature 347, 172–174. https://doi.org/10.1038/347172a0

Druffel, E.R.M.M., Williams, P.M., Bauer, J.E., Ertel, J.R., 1992. Cycling of dissolved and particulate organic matter in the open ocean. J. Geophys. Res. 97, 15639. https://doi.org/10.1029/92JC01511

Follett, C.L., Repeta, D.J., Rothman, D.H., Xu, L., Santinelli, C., 2014. Hidden cycle of dissolved organic carbon in the deep ocean. Proc. Natl. Acad. Sci. U. S. A. 111, 16706–16711. https://doi.org/10.1073/pnas.1407445111

Hansell, D.A., Carlson, C.A., Repeta, D.J., Schlitzer, R., 2009. Dissolved organic matter in the ocean: a controversy stimulates new insights. Oceanography. https://doi.org/10.2307/24861036

Hawkes, J.A., Rossel, P.E., Stubbins, A., Butterfield, D., Connelly, D.P., Achterberg, E.P., Koschinsky, A., Chavagnac, V., Hansen, C.T., Bach, W., Dittmar, T., 2015. Efficient removal of recalcitrant deep-ocean dissolved organic matter during hydrothermal circulation. Nat. Geosci. 8, 856–860. https://doi.org/10.1038/ngeo2543

Hayes, J.M., 1993. Factors controlling 13C contents of sedimentary organic compounds: Principles and evidence, Marine Geology.

Hedges, J.I., Oades, J.M., 1997. Comparative organic geochemistries of soils and marine sediments. Org. Geochem. https://doi.org/10.1016/S0146-6380(97)00056-9

Helms, J., 2012. Spectroscopic Characterization of Dissolved Organic Matter: Insights into Composition, Photochemical Transformation and Carbon Cycling. Chem. Biochem. Theses Diss. https://doi.org/10.25777/1y3p-e444

Hemingway, J.D., Rothman, D.H., Grant, K.E., Rosengard, S.Z., Eglinton, T.I., Derry, L.A., Galy, V. V., 2019. Mineral protection regulates long-term global preservation of natural organic carbon. Nature 570, 228–231. https://doi.org/10.1038/s41586-019-1280-6

Hemingway, J.D., Rothman, D.H., Rosengard, S.Z., Galy, V. V., 2017. Technical note: An inverse method to relate organic carbon reactivity to isotope composition from serial oxidation. Biogeosciences 5099–5114. https://doi.org/10.5194/bg-14-5099-2017

Kaiser, K., Benner, R., 2009. Biochemical composition and size distribution of organic matter at the Pacific and Atlantic time-series stations. Mar. Chem. 113, 63–77. https://doi.org/10.1016/j.marchem.2008.12.004

Komada, T., Burdige, D.J., Crispo, S.M., Druffel, E.R.M., Griffin, S., Johnson, L., Le, D., 2013. Dissolved organic carbon dynamics in anaerobic sediments of the Santa Monica Basin. Geochim. Cosmochim. Acta 110, 253–273. https://doi.org/10.1016/j.gca.2013.02.017

Lang, S.Q., Butterfield, D.A., Lilley, M.D., Paul Johnson, H., Hedges, J.I., 2006. Dissolved organic carbon in ridge-axis and ridge-flank hydrothermal systems. Geochim. Cosmochim. Acta 70, 3830–3842. https://doi.org/10.1016/j.gca.2006.04.031

Lechtenfeld, O.J., Kattner, G., Flerus, R., McCallister, S.L., Schmitt-Kopplin, P., Koch, B.P., 2014. Molecular transformation and degradation of refractory dissolved organic matter in the Atlantic and Southern Ocean. Geochim. Cosmochim. Acta 126, 321–337.

https://doi.org/10.1016/j.gca.2013.11.009

Letscher, R.T., Knapp, A.N., James, A.K., Carlson, C.A., Santoro, A.E., Hansell, D.A., 2015. Microbial community composition and nitrogen availability influence DOC remineralization in the South Pacific Gyre. Mar. Chem. 177, 325–334. https://doi.org/10.1016/j.marchem.2015.06.024

Loh, A.N., Bauer, J.E., Druffel, E.R.M., 2004. Variable ageing and storage of dissolved organic components in the open ocean. Nature 430, 877–881. https://doi.org/10.1038/nature02780

Mopper, K., Zhou, X., Kieber, R.J., Kieber, D.J., Sikorski, R.J., Jones, R.D., 1991. Photochemical degradation of dissolved organic carbon and its impact on the oceanic carbon cycle. Nature 353, 60–62. https://doi.org/10.1038/353060a0

Plante, A.F., 2013. Distribution of Radiocarbon Ages in Soil Organic Matter by Thermal Fractionation. Radiocarbon 55, 1077–1083. https://doi.org/10.2458/azu_js_rc.55.16310

Qi, Y., Fu, W., Tian, J., Luo, C., Shan, S., Sun, S., Ren, P., Zhang, H., Liu, J., Zhang, X., Wang, X., 2020. Dissolved black carbon is not likely a significant refractory organic carbon pool in rivers and oceans. Nat. Commun. 11, 1–11. https://doi.org/10.1038/s41467-020-18808-8

Repeta, D.J., Aluwihare, L.I., 2006. Radiocarbon analysis of neutral sugars in high-molecular-weight dissolved organic carbon: Implications for organic carbon cycling. Limnol. Oceanogr. 51, 1045–1053. https://doi.org/10.4319/lo.2006.51.2.1045

Rosenheim, B.E., Day, M.B., Domack, E., Schrum, H., Benthien, A., Hayes, J.M., 2008. Antarctic sediment chronology by programmed-temperature pyrolysis: Methodology and data treatment. Geochemistry, Geophys. Geosystems 9. https://doi.org/10.1029/2007GC001816

Rosenheim, B.E., Galy, V., 2012. Direct measurement of riverine particulate organic carbon age structure. Geophys. Res. Lett. 39, n/a-n/a. https://doi.org/10.1029/2012GL052883

Shah Walter, S.R., Jaekel, U., Osterholz, H., Fisher, A.T., Huber, J.A., Pearson, A., Dittmar, T., Girguis, P.R., 2018. Microbial decomposition of marine dissolved organic matter in cool oceanic crust. Nat. Geosci. 11, 334–339. https://doi.org/10.1038/s41561-018-0109-5

Stuiver, M., Quay, P.D., Ostlund, H.G., 1983. Abyssal water carbon-14 distribution and the age of the world oceans. Science (80-.). 219, 849–851. https://doi.org/10.1126/science.219.4586.849

Walker, B.D., Beaupré, S.R., Guilderson, T.P., McCarthy, M.D., Druffel, E.R.M., 2016. Pacific carbon cycling constrained by organic matter size, age and composition relationships. Nat. Geosci. 9, 888–891. https://doi.org/10.1038/ngeo2830

Williams, E.K., Rosenheim, B.E., McNichol, A.P., Masiello, C.A., 2014. Charring and nonadditive chemical reactions during ramped pyrolysis: Applications to the characterization of sedimentary and soil organic material. Org. Geochem. 77, 106–114. https://doi.org/http://dx.doi.org/10.1016/j.orggeochem.2014.10.006

Williams, P.M., Druffel, E.R.M.M., 1987. Radiocarbon in dissolved organic matter in the central North Pacific Ocean. Nature 330, 246–248. https://doi.org/10.1038/330246a0

Yu, M., Guo, Z., Wang, X., Eglinton, T.I., Yuan, Z., Xing, L., Zhang, H., Zhao, M., 2018. Sources and radiocarbon ages of aerosol organic carbon along the east coast of China and implications for atmospheric fossil carbon contributions to China marginal seas. Sci. Total Environ. 619–620, 957–965. https://doi.org/10.1016/j.scitotenv.2017.11.201

Zigah, P.K., McNichol, A.P., Xu, L., Johnson, C., Santinelli, C., Karl, D.M., Repeta, D.J., 2017. Allochthonous sources and dynamic cycling of ocean dissolved organic carbon revealed by carbon isotopes. Geophys. Res. Lett. https://doi.org/10.1002/2016GL071348

Zigah, P.K., Repeta, D.J., McNichol, A.P., Beaupré, S.R., Xu, L., Aluwihare, L.I., Hemingway, J.D., 2015. Constraining the Radiocarbon Distribution Within Major Components of Marine Dissolved Organic Carbon, in: American Geophysical Union, Fall Meeting.

Supplementary Information

Methods

PPL-DOC Extraction and Hydrolysis

PPL-DOC extraction

Samples were collected during a cruise aboard the *R/V Western Flyer* to Station M off the coast of central California in April 2018 (34^o 50'N, 123^o 00'W; 4100 meters depth). 30-40 L of seawater were collected at five depths ranging from 45 meters to 3700 meters. Water was then acidified to pH 2 using trace metal grade hydrochloric acid (HCl). 1 g PPL cartridges (Bond Elut, Agilent) were first activated overnight with liquid chromatography/mass spectrometry (LC/MS) grade methanol and then rinsed with LC/MS grade water, LC/MS grade methanol and LC/MS grade water adjusted to pH 2 using trace metal grade HCl. The acidified seawater was passed through the PPL cartridges under gravitational pressure over multiple days (Dittmar et al. 2008; Petras et al. 2017). Typically, 5 L of seawater was extracted with one 1 g PPL cartridge. Before eluting the PPL resin and immediately following the extraction, the cartridge was rinsed with three column volumes of pH 2 LC/MS grade water and dried under ultra-high purity nitrogen gas. Organic matter retained on the cartridge was then eluted with 10 mL of methanol/1 g PPL cartridge (PPL-DOC) and stored at -20 °C. Seawater for total organic carbon concentration [TOC] and dissolved organic carbon concentration [DOC] (i.e., seawater pre-filtered through combusted GF/F (Whatman corporation)) analysis was collected into combusted 40-mL borosilicate vials, immediately acidified to pH 2 using trace metal grade 12 N HCl (Fisher Scientific), capped with acid-washed vial caps with septa, and stored at room temperature until measurement.

Acid Hydrolysis

Each extracted PPL-DOC sample was divided in half. One half was dried extensively to remove methanol and then subjected to a 2 M acid hydrolysis. Briefly, the organic matter was transferred to an ampoule with 2 mL of 2 M hydrochloric acid and sealed under a nitrogen atmosphere before being placed in an oven at 80°C for 18 hours. Following hydrolysis, the sample was diluted with LC/MS grade water adjusted to pH 2 with trace metal grade HCl and then re-extracted onto a PPL cartridge as described above. The organic matter retained by the cartridge was then eluted in methanol and dried down for frozen storage. This sample is described as the hydrolysis residue of PPL-DOC.

Sample Analysis

Total and Dissolved Organic Carbon

Acidified samples for [TOC] and [DOC] were stored at room temperature in the dark until analyzed via high-temperature combustion on a Shimadzu 500 V-CSN/TNM-1 (Shimadzu Corp, Kyoto, Japan) at the Scripps Institution of Oceanography, La Jolla, CA. The TOC analyzer was modified from the manufacturer's design as described below. The Shimadzu combustion oven contained a quartz column filled with platinum (Pt) catalyst beads. Combustion columns were pre-conditioned on 40 - 100 injections of filtered (0.2 µm) seawater until the baseline of measured carbon was stable. A magnesium perchlorate water-trap was placed prior to the halogen trap and changed daily. CO_2-free carrier gas was used to pre-condition the column, and ultra-high purity grade O_2 gas was delivered to the instrument as the carrier gas during sample analysis. Each acidified TOC sample was sparged for two minutes and measured following high-temperature combustion at 680° C. During analysis, five 100 µL injections were made from a single sample reservoir, and samples were reanalyzed when the % CV of the best 3 injections was >5%. TOC measurements were calibrated using an 8-point calibration curve between 10 and 100 μM C of potassium phthalate in Milli-Q water. Milli-Q water and a reference water sample were analyzed every 10 samples. Reference standards were obtained from NSF-supported deep Florida Strait (Batch 6FS – 2006; Dennis Hansell, RSMAS, University of Miami). The expected concentration range for Batch reference materials is provided at http://www.rsmas.miami.edu/groups/biogeochem/. Further details of sample analysis details and data verification protocols can be found at cce.lternet.edu/research.

Ramped Pyrolysis Oxidation (RPO)

Ramped pyrolysis oxidation (RPO) was performed at the National Ocean Sciences Accelerator Mass Spectrometry (NOSAMS) facility in Woods Hole, MA, USA. Samples were transferred while dissolved in a small amount of methanol into quartz cups (pre-combusted at 850 °C, 1 hour) and then dried down under ultra-high purity nitrogen gas. Thorough drying is crucial for removing any residual methanol that can influence the carbon isotopic signature. Samples were further dried in an oven at 50°C for multiple days in an attempt to remove all methanol. Each quartz cup containing a single sample was then placed inside the RPO reactor. The RPO instrument continuously heats organic carbon, monitors evolved CO_2, and traps CO_2 for isotope analysis. RPO methodology has been described previously and further information describing the detailed protocol can be found in other publications (Rosenheim et al. 2008; Hemingway et al. 2017b). In summary, all samples were operated in oxidation mode (carrier gas 92% He, 8% O2) with a flow rate of 35 ml min^{-1} and a ramp rate of either 20 or 5 °C min^{-1}. Six fractions were collected during each 5 °C min^{-1} ramp. In total we ran ten 20 °C min^{-1} ramps and six 5 °C min^{-1} ramps of samples from Station M (half with PPL-DOC, the other half hydrolyzed PPL-DOC). It must be noted that the amount of sample initially present as well as instability in the ramp rate can have a significant effect on the shape of the thermogram. This is a potential concern as we compare thermograms generated from various sample sizes of organic carbon.

High molecular weight (HMW) DOC thermographs and isotope signatures of isolated fractions are shown in Figure S5.1 (2 m, 8°N, 110°W) (KA0701.1) and Figure S5.2 (450 m, 10.69°N, 97.17°) (KA0701.13) for comparison to PPL-DOC (Beaupre and Aluwihare, unpublished). Thermographs were generated from CO_2 evolved as the temperature was ramped at 5°C/min. The fractions were collected and processed for isotope measurements following the protocols for PPL-DOC above. The HMW DOC samples were isolated from seawater following ultrafiltration according to Meador et al., 2007 and represented between 15% (450 m) to 25% (2 m) of the total DOC at these sites and depths. These samples are presented as a comparison to PPL-DOC, where HMW DOC is well known to be enriched in ^{14}C compared to the bulk.

All bulk and RPO fraction isotope measurements were performed at NOSAMS. Stable carbon isotope compositions were measured on CO_2 gas using a dual-inlet isotope ratio mass spectrometer (IRMS), with resulting ^{13}C content expressed in $\delta^{13}C$ per mil (‰) notation relative to Vienna Pee Dee Belemnite (VPDB). Radiocarbon measurements were completed via accelerator mass spectrometry (AMS) following standard graphitization methods (McNichol et al. 1994).

A note about calculating yields

Determining accurate yields following PPL extraction as well as acid hydrolysis of Station M samples was hampered by the limited amount of sample available for RPO. We were not able to determine accurate yields because the priority was to keep samples as clean as possible for the isotope measurements and to maximize sample amounts available for RPO. As such, transfer efficiencies between steps were typically below 100%. We did determine hydrolysis yields for a different set of samples, extracted and processed identically to Station M samples. Their hydrolysis yields and sampling locations are listed in Table S5.4.

Error and Uncertainty

Radiocarbon blanks associated with PPL extraction were less than 1 µg of carbon per cartridge and have previously been determined to have a $\Delta^{14}C$ value of −998 ± 1 ‰ (Lechtenfeld et al. 2014; Lewis et al. 2020). Samples were not corrected for PPL blanks because the resulting change in $\Delta^{14}C$ was well within measurement uncertainty.

A blank was measured for the acid hydrolysis and subsequent re-extraction onto the PPL cartridge and was determined to be 8 µg C (0.67 µmol) with a $\delta^{13}C$ of -26 ‰. This blank was less than 0.05 % of the mass of each sample, and sample $\delta^{13}C$ values overlapped with that of the blank. Therefore, error introduced from the hydrolysis blank to the $\delta^{13}C$ values of samples (≤ *ca.* 0.04 ‰) was smaller than the IRMS instrument uncertainty (ca. ± 0.1 ‰). Due to the small size of the hydrolysis blank, the $\Delta^{14}C$ values of the RPO fractions (Table S5.4) would not have been affected over the range of possible $\Delta^{14}C$ values for the blank.

The amount of CO_2 for each RPO fraction, their $\delta^{13}C$ values, and Fm values were corrected for blank carbon contributions from the RPO system. Ultimately, $\Delta^{14}C$ values following blank correction were identical within the error of the NOSAMS measurements. $\delta^{13}C$ was additionally corrected to ensure ^{13}C mass balance, after Hemingway et al.,(2017a) using the 'ramped pyrox' python package developed by Hemingway et al., (2017b) and available online at http://pypi.python.org/pypi/rampedpyrox. For samples which were processed both on fast and slow ramps (45 m, 700 m, 1600 m) (Table S5.3), the mass balance radiocarbon results were used in combination with the 'bulk' results from the fast ramps to estimate error. For the remaining two depths (2600 and 3700 m), error is based on analysis error reported by NOSAMS. All errors were propagated using standard practices.

Although we corrected the RPO data using the blanks reported in Hemmingway et al. (2017a) (resulting corrections of no more than 3 ‰ for any sample), we found that when paired samples of different carbon amounts were analyzed by RPO (13.5 μg vs 88 μg; 36.5 vs 148 μg; 36.5 vs 95 μg) (Table S5.3), their uncorrected $\Delta^{14}C$ signatures (of each pair) were identical within the error of the measurement (Tables S5.3 & S5.4). These data suggest minimal contamination was introduced during the RPO measurement and even during the processing of PPL-DOC samples for RPO, such as the various drying steps for methanol removal, because any contamination should have disproportionately impacted the smaller samples. This assumes that the $\Delta^{14}C$ signature of the contamination introduced from the RPO system is distinct from that of the samples. It is still likely that contamination was not significant because the $\Delta^{14}C$ signatures of PPL-DOC samples ranged for -295 ± 5 to -513 ± 10‰ yet none of these samples exhibited signs of contamination. Additionally, $\delta^{13}C$ signatures of pairs also showed no significant signs of contamination.

Residual methanol may be contributing to the first fraction collected for some of the samples when this fraction was small (~50 μg, see Tables S5.3 & S5.4), but this contamination did not affect the bulk isotope measurements which were made on larger samples, which did not have anomalous $\delta^{13}C$ values. In order to avoid any issues associated with residual methanol, we recommend a water rinse followed by freeze drying of the samples in future studies.

Data Analysis

Data were processed using the ‘ramped pyrox’ python package developed by Hemingway et al., 2017b and available online as noted above. Activation energy distributions were calculated for all samples using the suggested parameters, for example, a constant ω value of 1010 s^{-1}. The one significant difference was that in lieu of the Tikhonov regularization described in Hemingway et al., 2017b we used a constant λ value of 0.2. Activation energy distributions were compared using Pearson's Product-Moment Correlation, and these results are plotted in Figure 5.4b. Comparison of activation energy distributions was visualized using a principal component analysis (PCA) and these results are shown in Figure 5.4a.

A note on the Δ^{14}C distribution of SPE-DOC vs. bulk DOC

We observed that Δ^{14}C values for PPL-DOC overlapped tightly with those of bulk DOC at Station M. This agreement was taken as evidence that PPL-DOC encompasses the range of Δ^{14}C values present in total DOC, and therefore, should be representative of the ^{14}C distribution in DOC (Lechtenfeld et al. 2014; Broek et al. 2017, 2020). Such an assumption is complemented by previous studies (including some from our own lab), which showed that solid phase extraction (SPE-DOC) using similar resins (HP-20) and methanol elution, isolated DOC with Δ^{14}C values that approximated bulk DOC in the surface ocean (de Jesus 2008; Coppola et al. 2015; Broek et al. 2017), and contained both modern and ^{14}C-depleted fractions (de Jesus 2008).

However, if DOC that is *not* extracted by PPL has Δ^{14}C values that are significantly different from the bulk then it is possible that PPL-DOC does not contain the Δ^{14}C endmembers. Such a finding would be particularly relevant if the non-extracted DOC was significantly ^{14}C-depleted compared to the bulk, as this could indicate that the low radiocarbon endmember is missing from PPL-DOC. Our data cannot constrain the Δ^{14}C value of non-extracted PPL-DOC. However, the ^{14}C signature of PPL-DOC decreases with depth indicating that strongly ^{14}C-depleted DOC is extractable by PPL at depth. Zigah et al. (2017) measured non-extractable DOC directly and found that Δ^{14}C values for non-extracted DOC at depth (i.e., hydrophilic low molecular weight DOC (LMW) in that paper) were significantly more depleted than the bulk. It is critical to note that their non-extracted DOC (hydrophilic LMW) was not more depleted in the surface (-304‰) than the hydrolysis residue of PPL-DOC from the current study (-381±5 to -390±1‰, Table S5.4). Such an observation further confirms that indeed, surface PPL-DOC contains the range of $\Delta^{14}C$ values expected for surface DOC. However, in the deep ocean, the hydrolysis residue of PPL-DOC mimics that of bulk DOC and does not approach the extremely low values reported by Zigah et al. (2017) for hydrophilic DOC (-762‰ versus -553±12‰ for the lowest value observed in the current study (Table S5.4)). However, the extremely depleted $\delta^{13}C$ values for their same samples, which have not been previously *measured* for marine DOC raise some concerns that need to be addressed with further studies. Furthermore, Zigah et al. (2017) also measured more ^{14}C-enriched high molecular weight (HMW) DOM in the deep ocean than has been observed in other studies (e.g. Broek et al., 2017; Loh et al., 2004; Repeta and Aluwihare, 2006; Walker et al., 2016), and this is relevant because it constrains the $\Delta^{14}C$ mass balance. In contrast, results from Broek et al., 2020 *do not* suggest that the non-extracted DOC pool is more ^{14}C depleted, but rather that its $\Delta^{14}C$ is essentially indistinguishable from the bulk value. Based on the lack of definitive data, we choose the most-simple explanation for Figure 5.1c, that PPL-DOC adequately captures the ^{14}C distribution in DOC. What is not controversial is that PPL-DOC and non-extractable DOC both exhibit a vertical ^{14}C gradient (Broek et al., 2020, 2017; Zigah et al., 2017, Figure 5.1b).

Table S5.1. Characteristics of DOC sampled at Station M in this study. DOC concentrations reflect total DOC in the water column. DOM for isotope measurements was isolated using solid phase extraction PPL cartridges.

Depth (m)	**[DOC]** (μM)	**Δ^{14}C** (‰)		**δ^{13}C** (‰)	
		PPL-DOC	**hydrolyzed PPL-DOC**	**PPL-DOC**	**hydrolyzed PPL-DOC**
45	66.6 ± 1.6	-300 ± 6	-385 ± 6	-23.5 ± 0.1	-24.6 ± 0.3
700	40.5 ± 1.1	-483 ± 8	-506 ± 14	-23.2 ± 0.1	-24.3 ± 0.1
1600	38.9 ± 1.3	-507 ± 9	-524 ± 40	-23.4 ± 0.2	-22.3 ± 0.1
2600	37.9 ± 1	-490 ± 3	-537 ± 7	-22.3 ± 0.1	-23.4 ± 0.1
3700	41.2 ± 1	-514 ± 2	-522 ± 4	-23.0 ± 0.1	-23.5 ± 0.1

Table S5.2. Average measured concentrations and Δ^{14}C values of bulk DOC as well as Δ^{14}C values of DIC at Station M between 1991 and 2004. Reproduced from Beaupré and Druffel, 2009.

Depth (m)	**[DOC]** (μM)	**DOC Δ^{14}C** (‰)	**DIC Δ^{14}C** (‰)
24 ± 2	71.0 ± 4.8	-272 ± 24	53 ± 20
85 ± 1	58.0 ± 4.8	-309 ± 33	44 ± 22
455 ± 9	42.5 ± 1.6	-453 ± 28	-117 ± 13
728 ± 35	39.3 ± 1.4	-495 ± 18	-166 ± 28
1619 ± 23	37.3 ± 1.4	-552 ± 10	-233 ± 11
2532 ± 89	37.3 ± 2.4	-553 ± 12	-244 ± 4
3502 ± 46	38.2 ± 1.2	-556 ± 12	-243 ± 8
4052 ± 45	38.3 ± 2.9	-552 ± 17	-231 ± 9

Table S5.3. Isotope measurements of RPO fractions from bulk PPL samples at Station M. Reported $\Delta^{14}C$ and $\delta^{13}C$ values have been corrected for the RPO blank after Hemmingway et al. (2017a). Dashes indicate where a measurement was not made. Asterisks denote possible methanol contamination. Uncertainty for all $\delta^{13}C$ is ± 0.1‰.

Fract. #	$T_{initial}$ (°C)	T_{final} (°C)	T_{avg} (°C)	**C** (µmol)	**% C**	**Fm**	**Age** (^{14}C yr)	$\Delta^{14}C$ (‰)	$\delta^{13}C$ (‰)
					Depth = 45 m				
1	109	245	209	4.81	5.47	0.6640*	3,300*	-341 ± 6*	-30.4*
2	245	432	348	32.5	37.0	0.7057	2,800	-300 ± 3	-24.7
3	432	455	443	4.82	5.48	0.6887	3,000	-317 ± 8	-23.0
4	455	490	475	7.42	8.43	0.6925	2,950	-313 ± 5	-22.6
5	490	524	508	18.1	20.6	0.6953	2,920	-310 ± 4	-22.1
6	524	800	550	20.3	23.0	0.7105	2,760	-295 ± 3	-22.3
total	**-**	**-**	**437**	**88.0**	**100**	**0.7003**	**2,870**	**-305 ± 13**	**-23.6**
bulk	**-**	**-**	**469**	**13.5**	**-**	**0.7104**	**2,750**	**-295 ± 5**	**-23.5**
					Depth = 700 m				
1	110	234	206	4.51	3.05	0.5633	4,610	-441 ± 6	-28.5
2	234	349	296	26.0	17.5	0.5409	4,940	-463 ± 4	-24.8
3	349	385	368	13.6	9.16	0.4935	5,670	-510 ± 3	-24.8
4	385	465	429	38.1	25.8	0.5035	5,510	-501 ± 3	-
5	465	496	481	25.8	17.4	0.5116	5,380	-493 ± 3	-22.6
6	496	800	532	40.0	27.0	0.5128	5,360	-491 ± 3	-
total	**-**	**-**	**431**	**148**	**100**	**0.5149**	**5,330**	**-489 ± 9**	**-**
bulk	**-**	**-**	**469**	**36.8**	**-**	**0.5272**	**5,140**	**-477 ± 3**	**-23.2**
					Depth = 1600 m				
1	100	252	221	4.38	4.62	0.5731	4,480	-431 ± 6	-29.2
2	252	385	328	23.7	25.0	0.5024	5,530	-502 ± 2	-24.8
3	385	409	396	6.37	6.70	0.4737	6,000	-530 ± 7	-24.4
4	409	479	448	26.3	27.7	0.4804	5,890	-523 ± 2	-22.4
5	479	506	491	12.7	13.4	0.4831	5,840	-521 ± 3	-22.2
6	506	800	538	21.5	22.6	0.4833	5,830	-521 ± 3	-22.0
total	**-**	**-**	**431**	**95.0**	**100**	**0.4908**	**5,720**	**-513 ± 10**	**-23.3**
bulk	**-**	**-**	**457**	**36.5**	**-**	**0.5036**	**5,510**	**-500 ± 3**	**-23.5**

Table S5.4. Isotope measurements of RPO fractions from hydrolyzed PPL samples. Reported $\Delta^{14}C$ and $\delta^{13}C$ values have been corrected for the RPO blank after Hemmingway et al. (2017a). Dashes indicate where a measurement was not made. Stars denote possible methanol contamination.

Fract. #	$T_{initial}$ (°C)	T_{final} (°C)	T_{avg} (°C)	**C** (µmol)	**%C**	**Fm**	**Age** (^{14}C yr)	$\Delta^{14}C$ (‰)	$\delta^{13}C$ (‰)
Depth = 45 m									
1	123	321	234	4.477	9.29	0.6073*	4,020*	-398±6*	-31.7*
2	321	431	372	14.76	30.6	0.6075	4,010	-397±4	-26.3
3	431	459	450	4.675	9.70	0.6035	4,060	-401±9	-25.9
4	459	490	479	5.672	11.8	0.6166	3,890	-388±5	-23.6
5	490	524	513	7.553	15.7	0.6218	3,820	-383±4	-23.3
6	524	800	563	11.05	22.9	0.6292	3,730	-376±4	-22.2
total	**-**	**-**	**451**	**48.19**	**100**	**0.6154**	**3,900**	**-390±14**	**-25.0**
bulk	**-**	**-**	**444**	**11.87**	**-**	**0.6238**	**3,791**	**-381±5**	**-24.2**
Depth = 700 m									
1	110	258	230	4.407	2.38	0.5130	5,350	-491±6	-28.0
2	258	348	309	24.622	13.3	-	-	-	-
3	348	385	368	14.151	7.64	0.4653	6,150	-538±3	-25.0
4	385	465	426	43.634	23.6	0.4706	6,050	-533±3	-24.6
5	465	495	481	23.064	12.5	0.4813	5,870	-523±3	-24.1
6	495	800	535	75.371	40.7	0.4822	5,860	-522±3	-22.1
total	**-**	**-**	**455**	**185.2**	**100**	**N/A**	**N/A**	**N/A**	**N/A**
bulk	**-**	**-**	**497**	**7.352**	**-**	**0.4980**	**5,601**	**-506±9**	**-24.3**
Depth = 1600 m									
1	100	302	259	4.724	8.68	0.4727	6,000	-531±7	-29.0
2	302	383	349	10.137	18.6	0.4496	6,420	-554±4	-25.3
3	383	409	395	5.215	9.58	0.4408	6,580	-563±5	-24.7
4	409	477	445	13.950	25.6	0.4542	6,340	-549±4	-
5	477	506	491	7.700	14.1	0.4523	6,370	-551±4	-22.8
6	506	800	539	12.707	23.3	0.4423	6,540	-561±4	-21.9
total	**-**	**-**	**434**	**54.43**	**100**	**0.4506**	**6,400**	**-553±12**	**N/A**
bulk	**-**	**-**	**471**	**11.36**	**-**	**0.5090**	**5,424**	**-495±5**	**-22.3**

Table S5.5. Results from repeat hydrolysis experiment. Six additional PPL samples from a range of depths and locations were hydrolyzed using the same procedure used for the Station M samples in order to constrain differences in C yield. Stable carbon, but not radiocarbon, measurements were made on these samples. Uncertainty for all δ^{13}C is ± 0.1‰. Locations of each station are shown in Figure S5.4.

Depth (m)	**[TOC]** (µM)	**δ^{13}C (‰)**		**C:N**		**Yield from PPL DOM (%)**	
		PPL	hydrolyzed	PPL	hydrolyzed	C	N
24.7°N, -113.3°E							
655	39.2 ± 1	-21.8	-21.8	26 ± 1	34 ± 2	89 ± 5	68 ± 4
1485	36.8 ± 1	-21.9	-21.7	27 ± 2	35 ± 2	90 ± 5	70 ± 4
2469	36.4 ± 1	-22.2	-22.1	28 ± 2	37 ± 2	86 ± 5	65 ± 4
-0.71°N, -110°E							
30	58.5 ± 1	-22.3	-22.5	28 ± 2	39 ± 2	67 ± 4	49 ± 3
3700	40.4 ± 1	-22.3	-22.2	32 ± 2	37 ± 2	70 ± 4	60 ± 4
-13°N, -103°E							
40	79.9 ± 2	-22.7	-22.7	30 ± 2	42 ± 2	66 ± 4	48 ± 3

Table S5.6. Additional samples from the eastern tropical North Pacific. Seven additional PPL samples from a range of depths were analyzed on the RPO. Stable carbon and radiocarbon measurements were made on these samples. Uncertainty for all $\delta^{13}C$ is ± 0.1‰.

Depth (m)	**[TOC] (μM)**	**C isotopes (‰)**	
		$\delta^{13}C$	**$\Delta^{14}C$**
	32°N, -120°E		
684	40.1 ± 1	-22.8	-497 ± 3
	27°N, -115°E		
49	64.5 ± 1	-23.8	-295 ± 5
	16°N, -110°E		
50	77.5 ± 2	-24.2	-257 ± 3
140	48.5 ± 1	-23.5	-394± 4
500	42.4 ± 1	-23.8	-461 ± 3
1782	37.3 ± 1	-23.4	-540 ± 3
3157	37.4 ± 1	-24.0	-521 ± 3

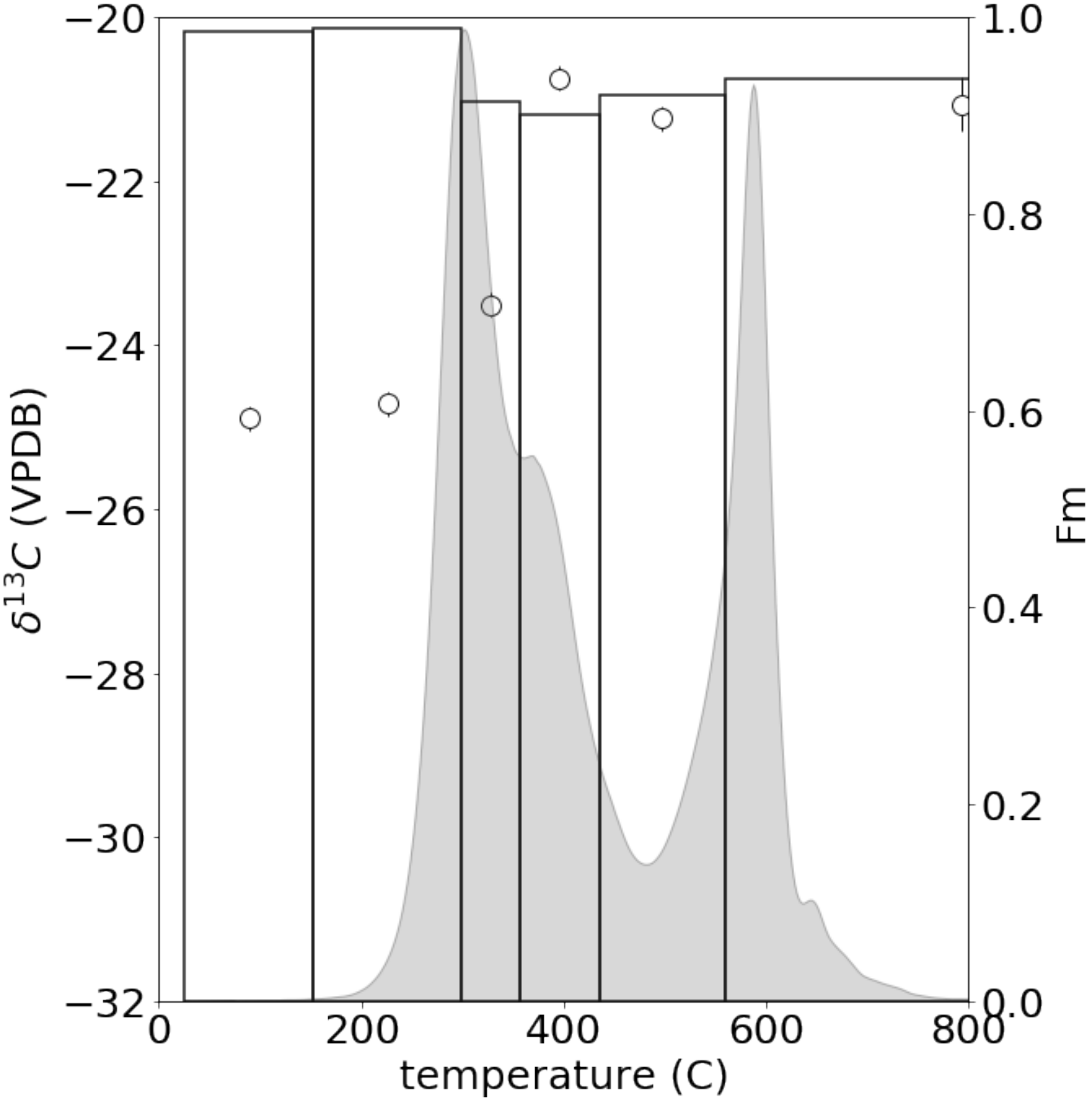

Figure S5.1. Thermogram of 2 m HMW DOC from Station KA0701.1 in the Eastern Equatorial Pacific Ocean. The bars indicate the fraction modern and the circles show the stable carbon isotope measurements. The bulk radiocarbon for this sample is -66 ‰ and the bulk $\delta^{13}C$ is -23.1 ‰. The thermogram in grey is scaled to the most enriched Fm value. This is the case for all thermograms below as well.

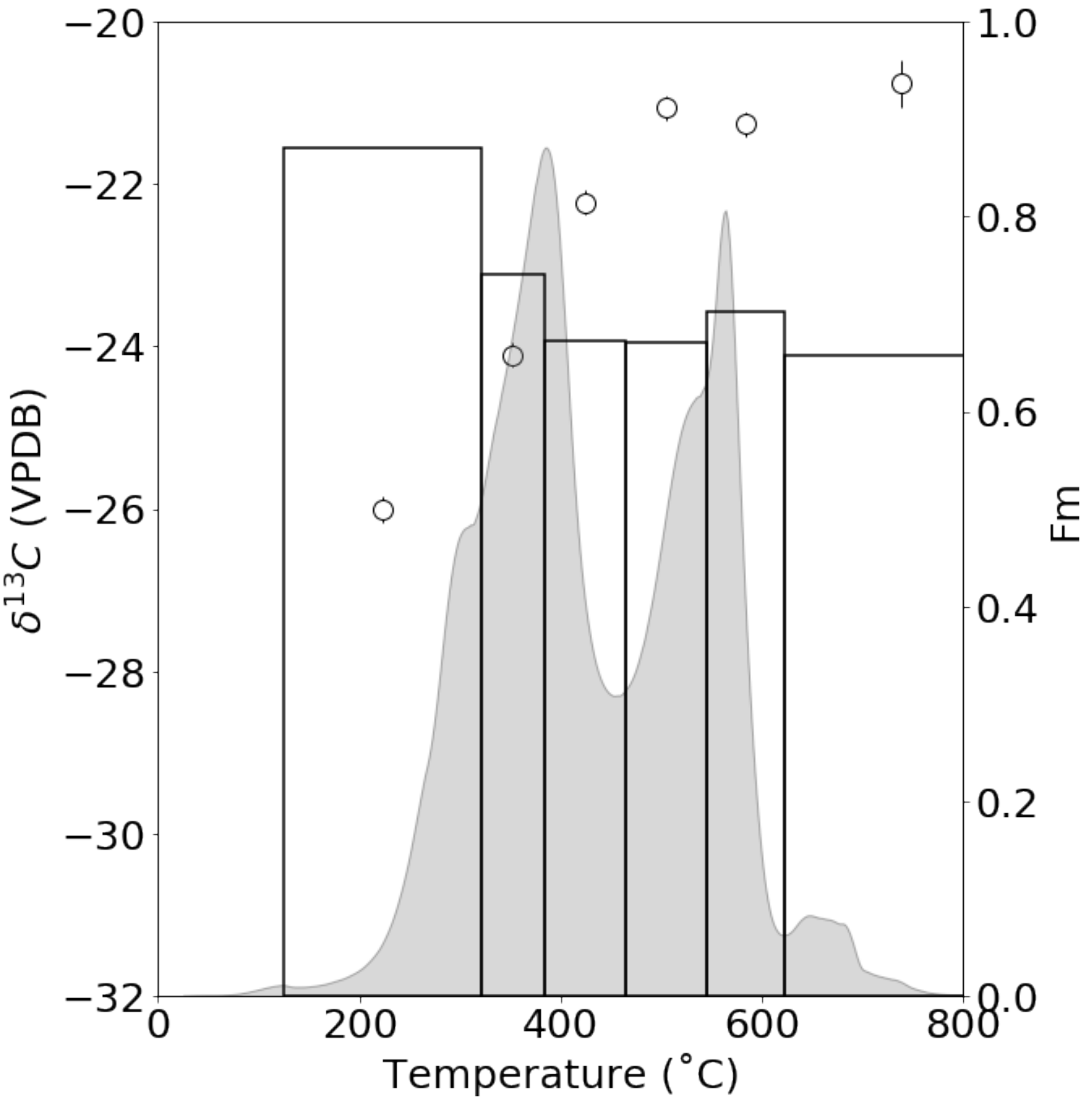

Figure S5.2. Thermogram of 450 m HMW DOC from Station KA0701.13 in the Eastern Equatorial Pacific Ocean. The bars indicate the fraction modern and the circles show the stable carbon isotope measurements. The bulk radiocarbon for this sample is -242 ‰ and the bulk $\delta^{13}C$ is -22.9‰.

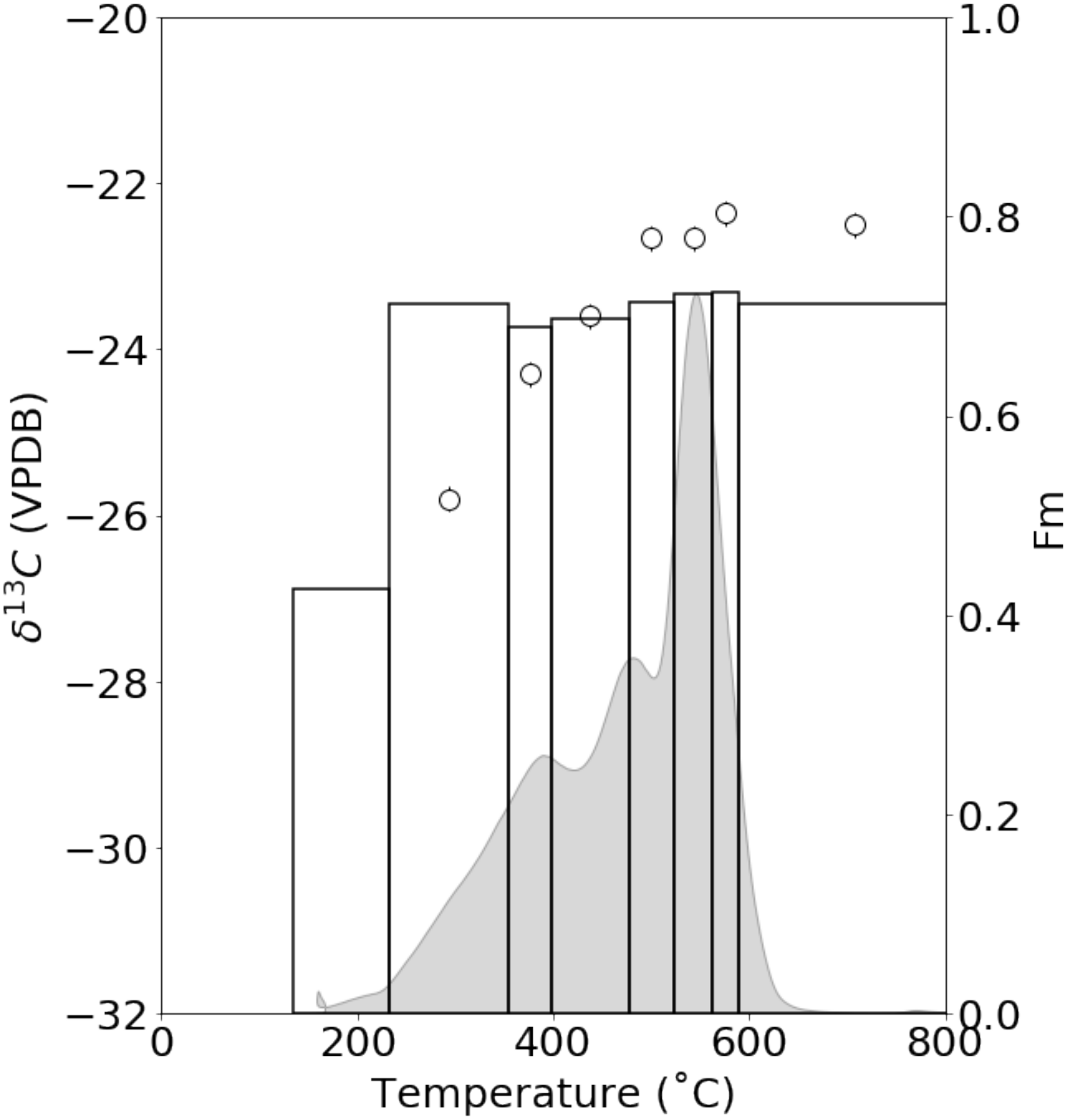

Figure S5.3. Thermogram from 49 m at 27°N, -115 °E in the Eastern North Pacific. DOC concentration was 64.5 ± 1 µM. The first fraction shown here almost certainly had methanol contamination.

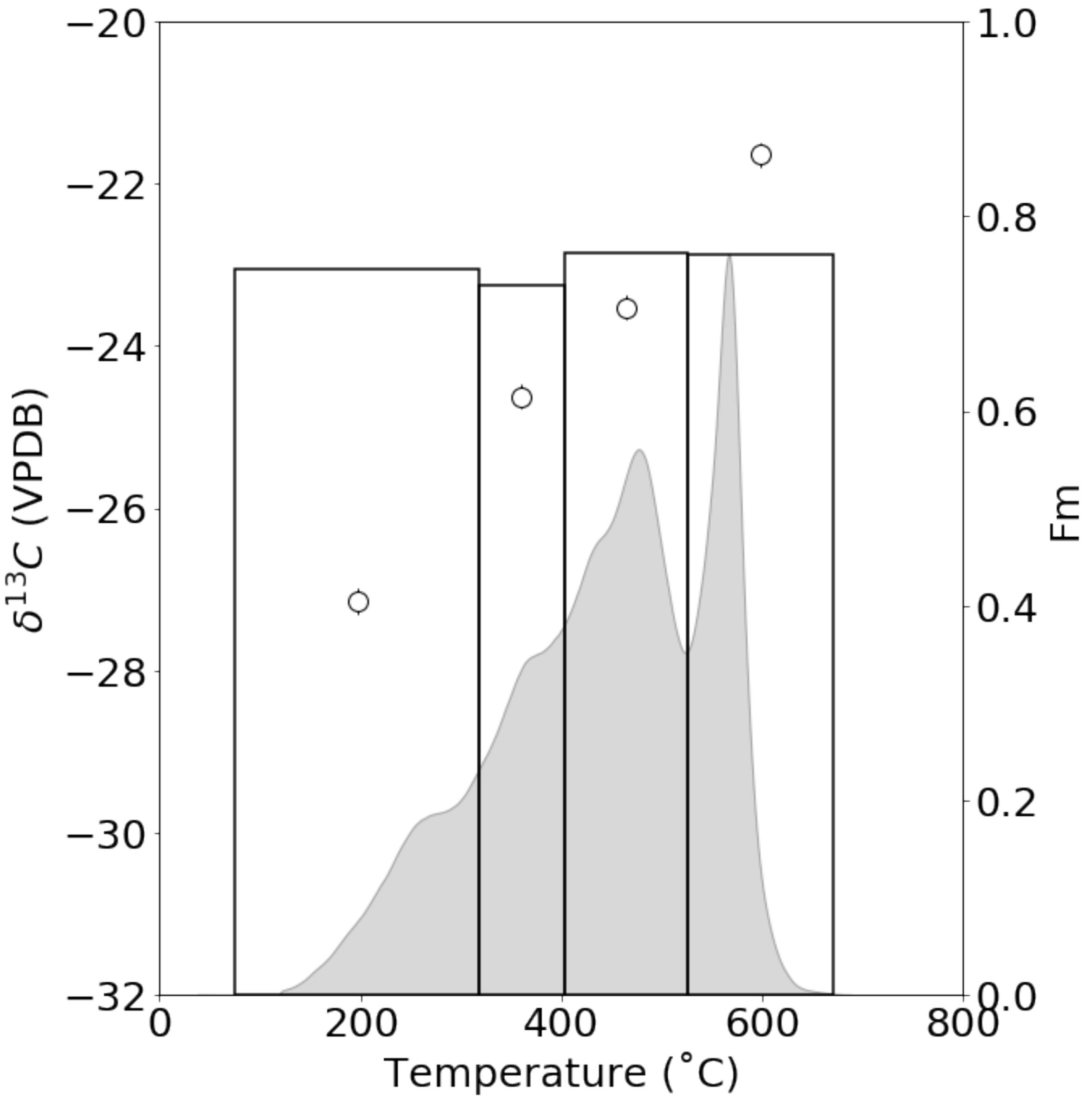

Figure S5.4. Thermogram from 49 m at 16°N, -110 °E in the Eastern Tropical North Pacific. DOC concentration was 77.5 ± 2 μM.

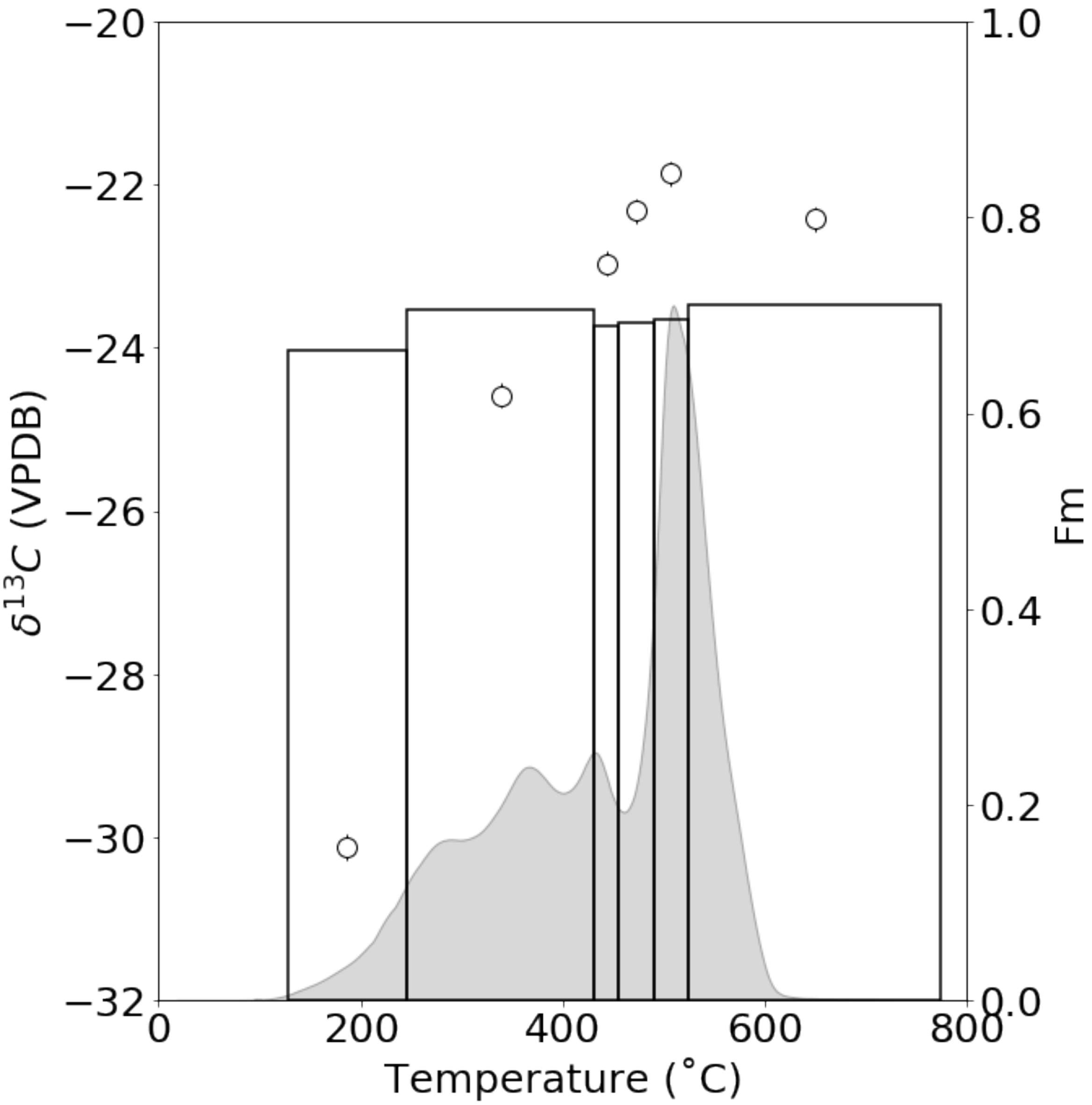

Figure S5.5. Thermogram of PPL DOM from 45 m at Station M.

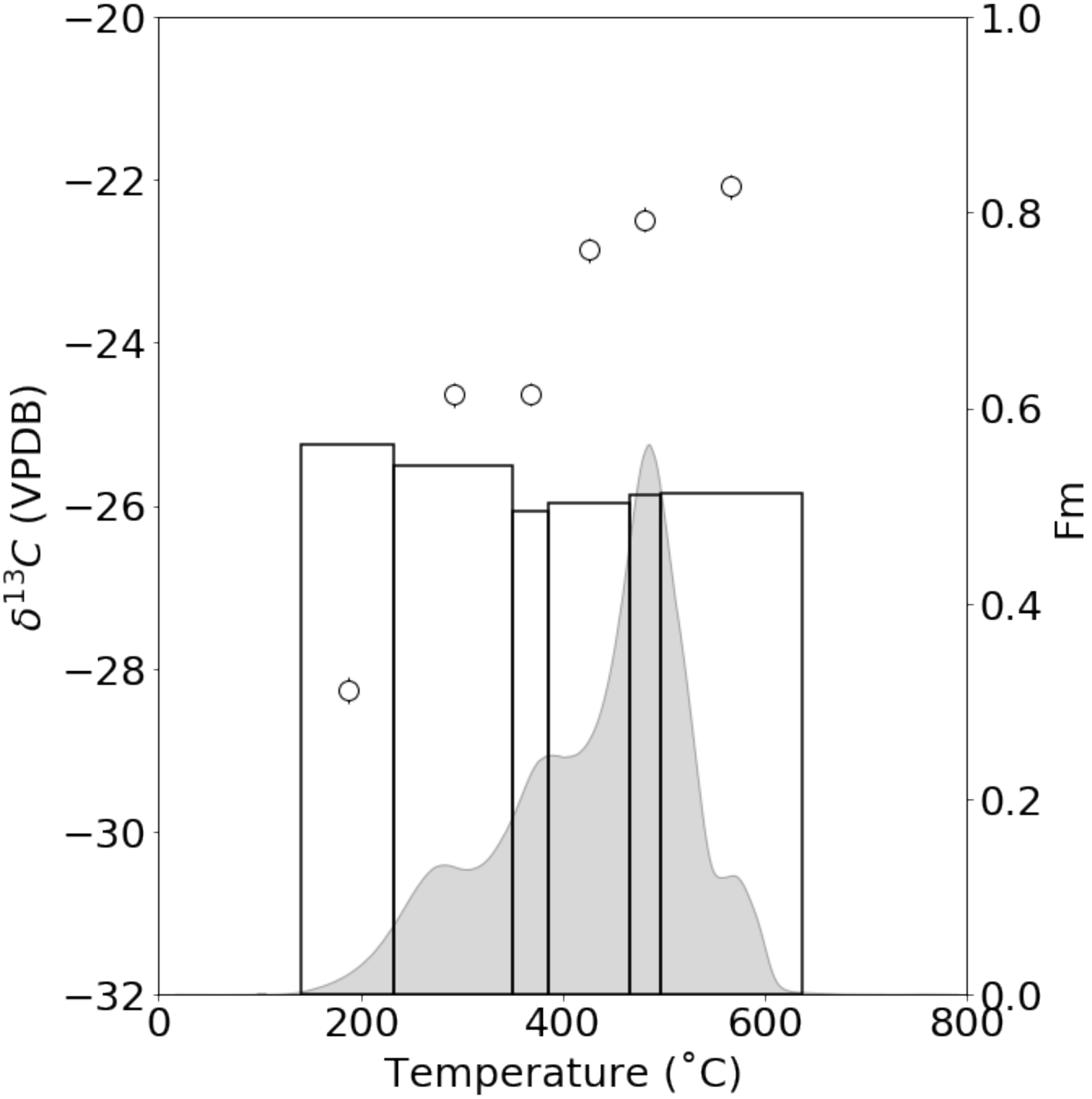

Figure S5.6. Thermogram of PPL DOM from 700 m at Station M.

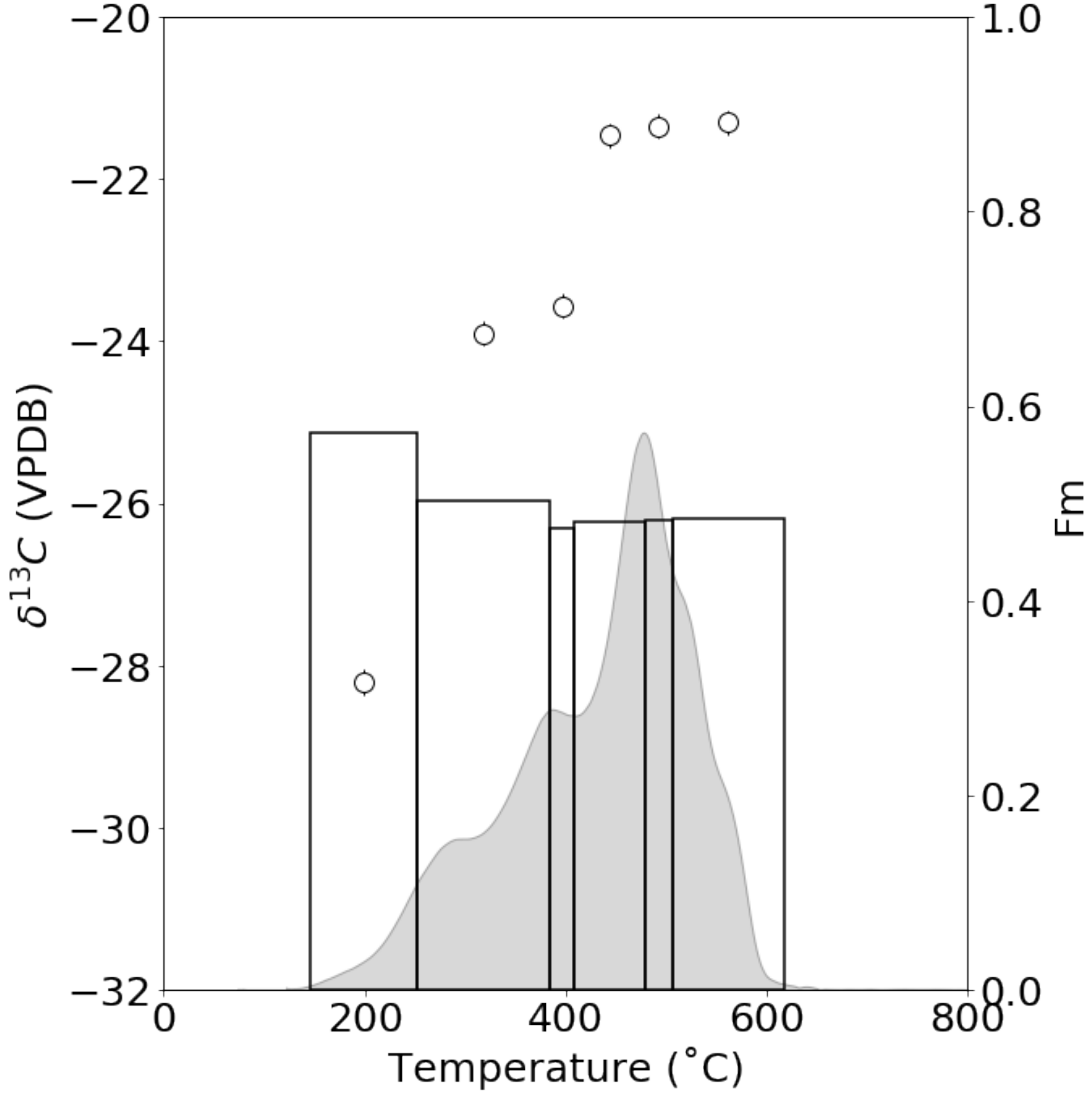

Figure S5.7. Thermogram of PPL DOM from 1600 m at Station M.

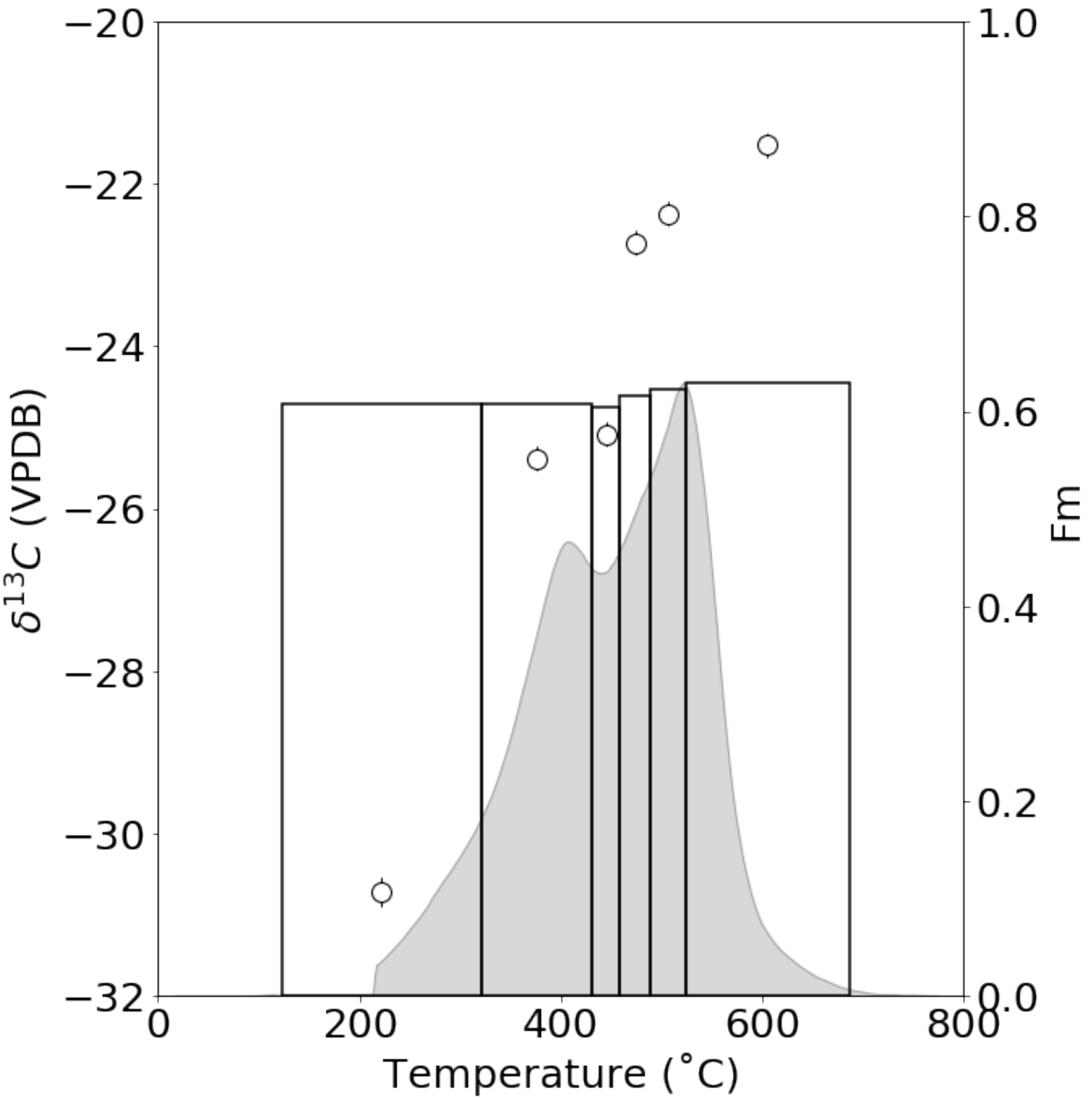

Figure S5.8. Thermogram of acid hydrolyzed PPL DOM from 45 m at Station M.

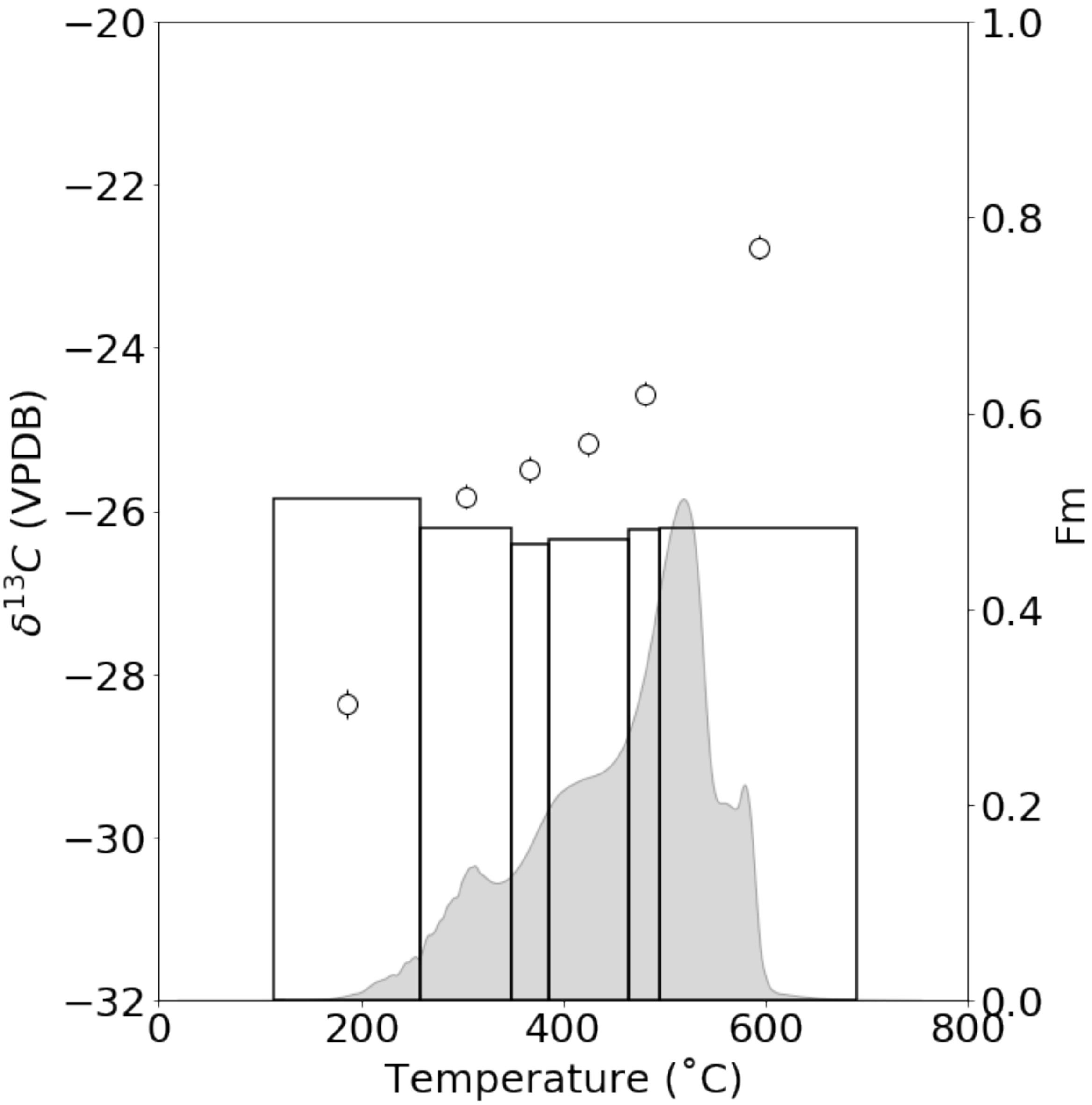

Figure S5.9. Thermogram of acid hydrolyzed PPL DOM from 700 m at Station M.

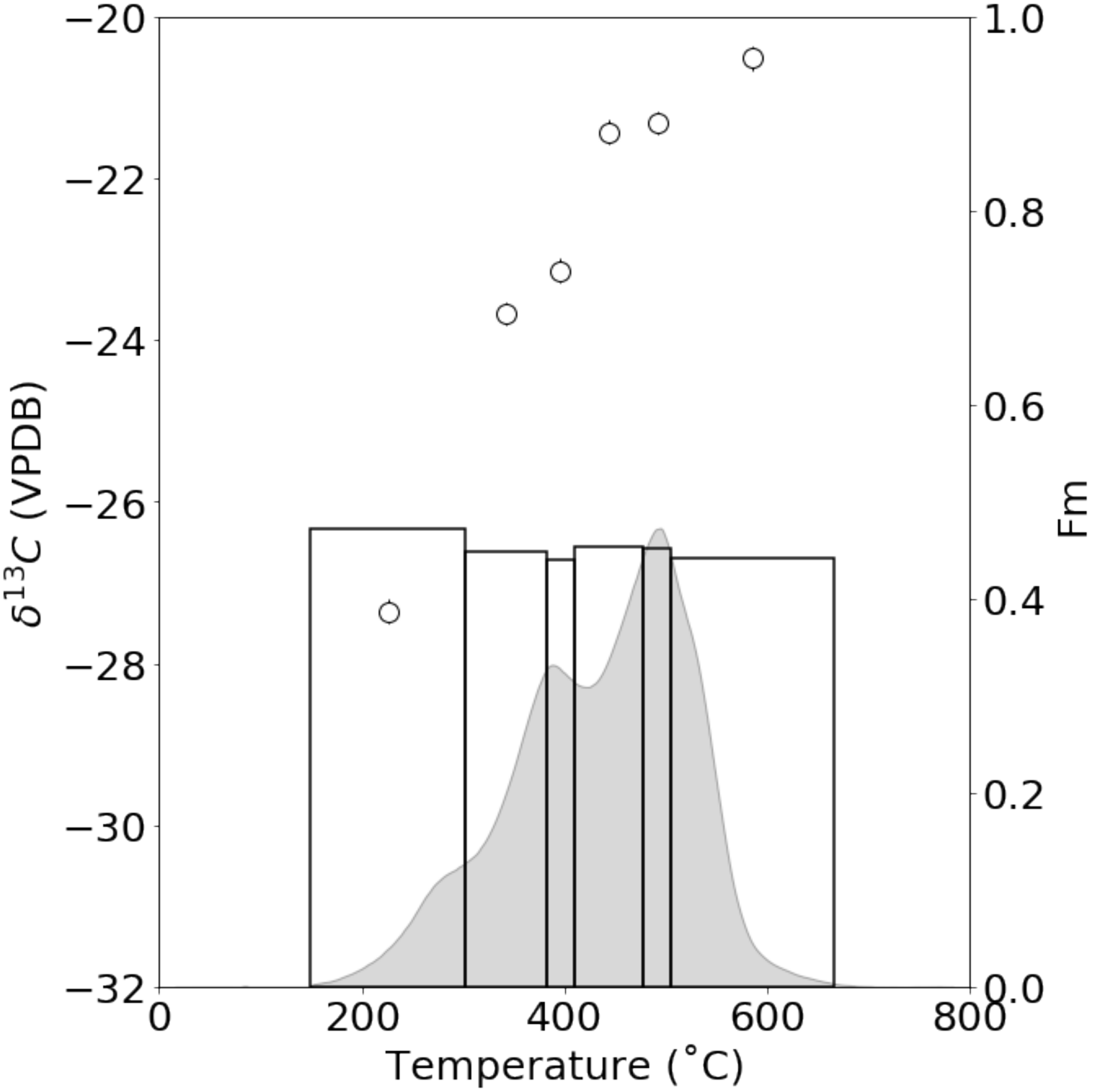

Figure S5.10. Thermogram of acid hydrolyzed PPL DOM from 1600 m at Station M.

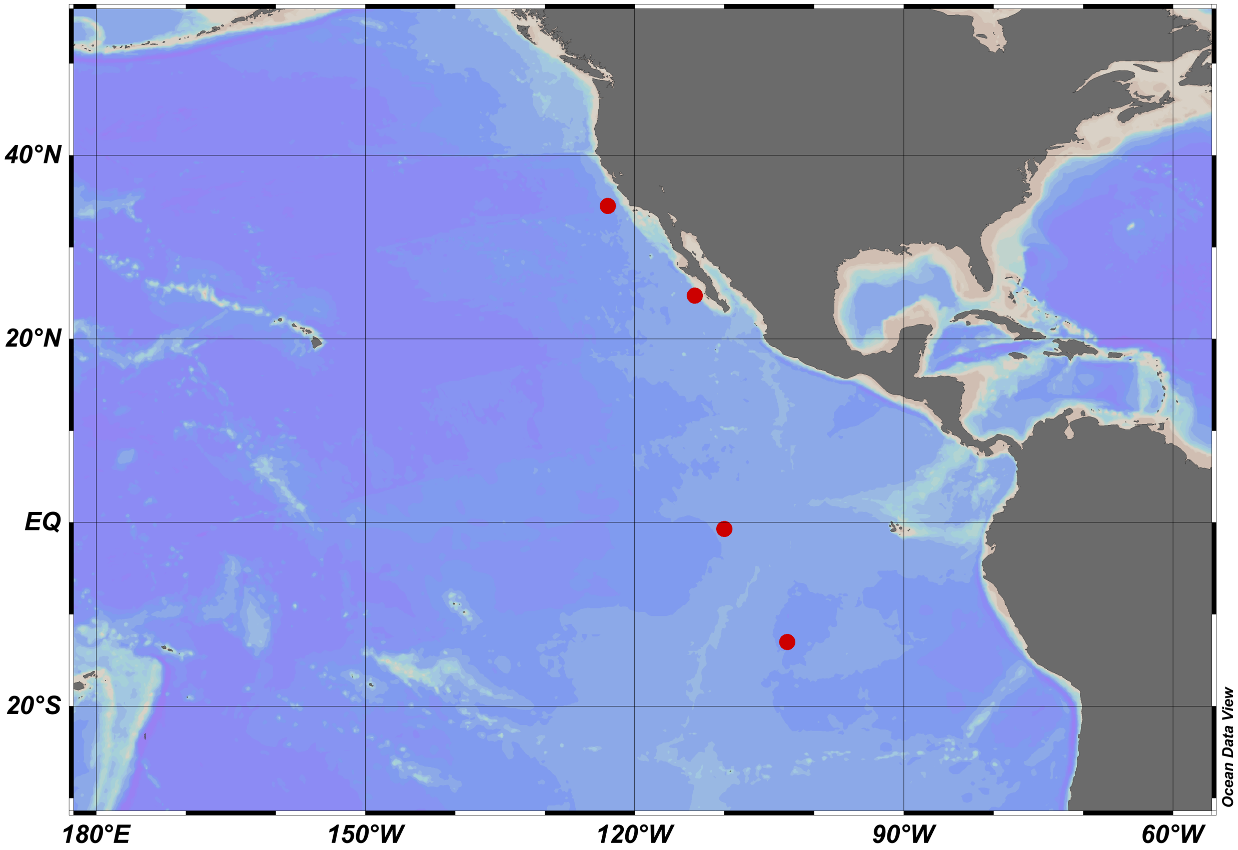

Figure S5.11. Location of Station M and three stations used for repeat hydrolysis experiment. Stations in the Southern Hemisphere were sampled during GOSHIP P18 in November-December 2016.

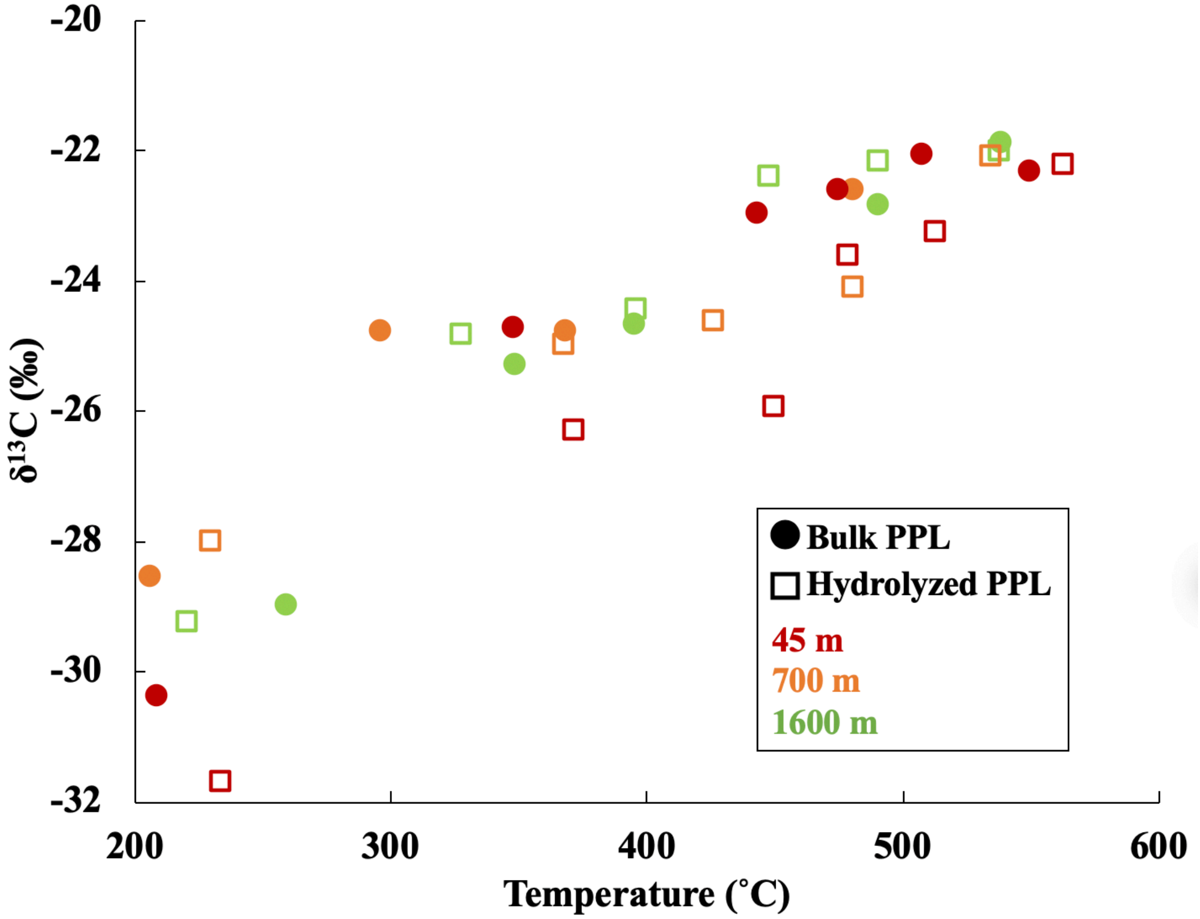

Figure S5.12. δ^{13}C values for all fractions from Station M. The temperature value is the C-weighted average temperature for that fraction.

References

Broek, T.A.B., Walker, B.D., Guilderson, T.P., McCarthy, M.D., 2017. Coupled ultrafiltration and solid phase extraction approach for the targeted study of semi-labile high molecular weight and refractory low molecular weight dissolved organic matter. Mar. Chem. 194, 146–157. https://doi.org/10.1016/J.MARCHEM.2017.06.007

Broek, T.A.B., Walker, B.D., Guilderson, T.P., Vaughn, J.S., Mason, H.E., McCarthy, M.D., 2020. Low Molecular Weight Dissolved Organic Carbon: Aging, Compositional Changes, and Selective Utilization During Global Ocean Circulation. Global Biogeochem. Cycles 34. https://doi.org/10.1029/2020GB006547

Coppola, A.I., Walker, B.D., Druffel, E.R.M., 2015. Solid phase extraction method for the study of black carbon cycling in dissolved organic carbon using radiocarbon. Mar. Chem. 177, 697–705. https://doi.org/10.1016/j.marchem.2015.10.010

de Jesus, R.P., 2008. Natural abundance radiocarbon studies of dissolved organic carbon (DOC) in the marine environment. University of California San Diego.

Dittmar, T., Koch, B., Hertkorn, N., Kattner, G., 2008. A simple and efficient method for the solid-phase extraction of dissolved organic matter (SPE-DOM) from seawater. Limnol. Oceanogr. Methods 6, 230–235. https://doi.org/10.4319/lom.2008.6.230

Hemingway, J.D., Galy, V. V., Gagnon, A.R., Grant, K.E., Rosengard, S.Z., Soulet, G., Zigah, P.K., McNichol, A.P., 2017a. Assessing the blank carbon contribution, isotope mass balance, and kinetic isotope fractionation of the ramped pyrolysis/oxidation instrument at nosams. Radiocarbon 59, 179–193. https://doi.org/10.1017/RDC.2017.3

Hemingway, J.D., Rothman, D.H., Rosengard, S.Z., Galy, V. V., 2017b. Technical note: An inverse method to relate organic carbon reactivity to isotope composition from serial oxidation. Biogeosciences 5099–5114. https://doi.org/10.5194/bg-14-5099-2017

Lechtenfeld, O.J., Kattner, G., Flerus, R., McCallister, S.L., Schmitt-Kopplin, P., Koch, B.P., 2014. Molecular transformation and degradation of refractory dissolved organic matter in the Atlantic and Southern Ocean. Geochim. Cosmochim. Acta 126, 321–337. https://doi.org/10.1016/j.gca.2013.11.009

Lewis, C.B., Walker, B.D., Druffel, E.R.M., 2020. Isotopic and optical heterogeneity of solid phase extracted marine dissolved organic carbon. Mar. Chem. 103752. https://doi.org/10.1016/j.marchem.2020.103752

Loh, A.N., Bauer, J.E., Druffel, E.R.M., 2004. Variable ageing and storage of dissolved organic components in the open ocean. Nature 430, 877–881. https://doi.org/10.1038/nature02780

McNichol, A.P., Osborne, E.A., Gagnon, A.R., Fry, B., Jones, G.A., 1994. TIC, TOC, DIC, DOC, PIC, POC - unique aspects in the preparation of oceanographic samples for 14C-AMS. Nucl. Inst. Methods Phys. Res. B 92, 162–165. https://doi.org/10.1016/0168-

583X(94)95998-6

Meador, T.B., Aluwihare, L.I., Mahaffey, C., 2007. Isotopic heterogeneity and cycling of organic nitrogen in the oligotrophic ocean. Limnol. Oceanogr. 52, 934–947. https://doi.org/10.4319/lo.2007.52.3.0934

Petras, D., Koester, I., Da Silva, R., Stephens, B.M., Haas, A.F., Nelson, C.E., Kelly, L.W., Aluwihare, L.I., Dorrestein, P.C., 2017. High-Resolution Liquid Chromatography Tandem Mass Spectrometry Enables Large Scale Molecular Characterization of Dissolved Organic Matter. Front. Mar. Sci. 4, 405. https://doi.org/10.3389/fmars.2017.00405

Repeta, D.J., Aluwihare, L.I., 2006. Radiocarbon analysis of neutral sugars in high-molecular-weight dissolved organic carbon: Implications for organic carbon cycling. Limnol. Oceanogr. 51, 1045–1053. https://doi.org/10.4319/lo.2006.51.2.1045

Rosenheim, B.E., Day, M.B., Domack, E., Schrum, H., Benthien, A., Hayes, J.M., 2008. Antarctic sediment chronology by programmed-temperature pyrolysis: Methodology and data treatment. Geochemistry, Geophys. Geosystems 9. https://doi.org/10.1029/2007GC001816

Walker, B.D., Beaupré, S.R., Guilderson, T.P., McCarthy, M.D., Druffel, E.R.M., 2016. Pacific carbon cycling constrained by organic matter size, age and composition relationships. Nat. Geosci. 9, 888–891. https://doi.org/10.1038/ngeo2830

Zigah, P.K., McNichol, A.P., Xu, L., Johnson, C., Santinelli, C., Karl, D.M., Repeta, D.J., 2017. Allochthonous sources and dynamic cycling of ocean dissolved organic carbon revealed by carbon isotopes. Geophys. Res. Lett. https://doi.org/10.1002/2016GL071348

Chapter 6: Conclusions

This dissertation used measurements of natural abundance isotopes to address questions about marine nitrogen and organic carbon cycling in the modern ocean. As presented in the introduction **Chapter 1**, natural abundance isotopes are a valuable tool that can be applied to a variety of topics within chemical oceanography. In **Chapter 2** we used stable isotopes of nitrate to study the impact of the 2015-2016 El Niño event on nitrogen cycling in the sCCS region. This study provides the first set of nitrate isotope measurements comprehensive enough to assess the variability at the base of the food web, providing a valuable resource for interpretation of nitrogen isotope measurements in other reservoirs. We saw that during periods when the surface ocean warms, the sCCS experiences lower productivity, greater percent nitrate utilization and a greater contribution from nitrate regenerated in the surface ocean. We were also able to link these trends with indices such as net primary production and water column stratification that can be applied across the CalCOFI record. Additionally, we identified spatial and temporal variability in euphotic zone nitrate utilization associated with iron limitation as detected by a proxy that compares the ratios of nitrate and silicate. The observations presented in this chapter provide important insight into how this region will respond to warming linked to anthropogenic climate change.

Chapter 3 used nitrate isotopes to examine nitrogen cycling in a different context- the extent and location of denitrification in the seasonally suboxic bottom waters of the Santa Barbara Basin. Results from this chapter confirm that an unprecedented increase in water column denitrification in basin bottom waters in recent years has resulted in enrichment of nitrate isotopes and accumulation of nitrite. Comparison oxygen and nitrogen isotopes of nitrate demonstrated the significance of reoxidation of nitrite even under low oxygen conditions.

Evidence from the wider sCCS region implicates a long-term trend of decreasing oxygen concentrations in intermediate waters as the likely driver for these observed changes.

Chapter 4 continued our investigation of the low oxygen water column, but in a very different location- the largest anoxic marine zone in the world in the eastern tropical North Pacific. Nitrogen cycling in this region has been extensively documented, but our study focused on the production and processing of organic matter. We found that in general, our data can be best explained by the gradient of production and remineralization processes as well as water mass mixing, rather than by differences in oxygen concentration. We identified a unique pattern in fluorescent DOM that appears to be closely associated with intense remineralization of organic matter along the oxycline. In addition, we saw that oxygen consumption rates across oxygen gradients were related to DOM composition as reflected by its optical properties, suggesting a link between remineralization and chemical composition. Finally, we documented the impact of a recent category 4 hurricane which passed through the ETNP and resulted in intense vertical mixing and shoaling of the AMZ, potentially exacerbating low oxygen conditions by stimulating additional production.

Chapter 5 also focused on marine organic carbon cycling but used radiocarbon rather than stable isotope measurements to probe the long-term storage of DOC in the oceans. We attempted to evaluate the currently established model of marine DOC cycling which requires a well-mixed background pool to be present throughout the water column. However, based on our results and all available research, there is no direct evidence of a significant component of DOC in the surface ocean that is as depleted in ^{14}C as bulk DOC in the deep ocean. Thus, we proposed a new explanation for the advanced radiocarbon age of marine DOC, namely, a pre-aged source to the upper water column and subsequent aging along the path of thermohaline circulation. This revision to the current model of DOC cycling would revise the water column lifetime of marine DOC to only 2,300 years, approximately doubling the estimated flux of carbon through the deep ocean.